COMPUTATIONS ON FULLERENES: CHARACTERIZATION, REACTIVITY AND GROWTH

Laura Abella Guzman

UNIVERSITAT ROVIRA i VIRGILI

Computations on Fullerenes: Characterization, Reactivity and Growth

---

Laura Abella Guzman

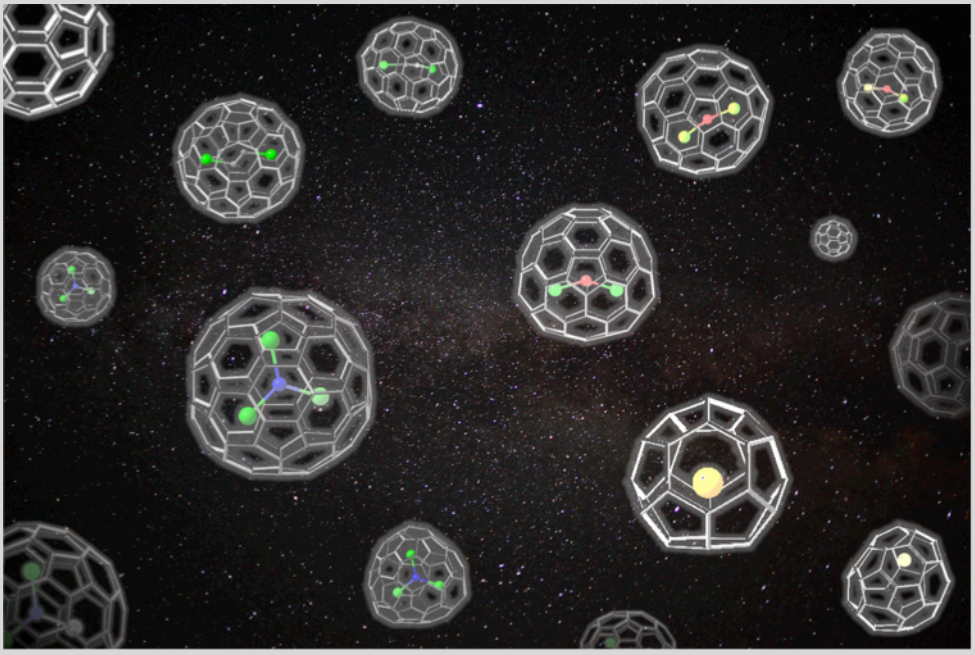

DOCTORAL THESIS
2017

UNIVERSITAT ROVIRA I VIRGILI
COMPUTATIONS ON FULLERENES: CHARACTERIZATION, REACTIVITY AND GROWTH
Laura Abella Guzman

Laura Abella Guzman

Computations on Fullerenes: Characterization, Reactivity and Growth

PhD Thesis

Supervised by
Dr. Antonio Rodríguez Fortea and Prof. Josep Maria Poblet Rius

Grup de Química Quàntica
Departament de Química Física i Inorgànica

UNIVERSITAT ROVIRA i VIRGILI

Tarragona, November 2017

UNIVERSITAT ROVIRA I VIRGILI
COMPUTATIONS ON FULLERENES: CHARACTERIZATION, REACTIVITY AND GROWTH
Laura Abella Guzman

UNIVERSITAT ROVIRA I VIRGILI
DEPARTAMENT DE QUÍMICA FÍSICA I INORGÀNICA

C/ Marcel.li Domingo 1- Campus Sescelades
43007- Tarragona SPAIN

Antonio Rodríguez Fortea, Professor Agregat del Departament de Química Física i Inorgànica de la Universitat Rovira i Virgili i Josep Maria Poblet Rius, Catedràtic del Departament de Química Física i Inorgànica de la Universitat Rovira i Virgili,

FEM CONSTAR que la present memòria, titulada

"Computations on Fullerenes: Characterization, Reactivity and Growth"

ha estat realitzada sota la nostra direcció al Departament de Química Física i Inorgànica de la Universitat Rovira i Virgili per Laura Abella Guzmán per a optar al títol de Doctor.

Tarragona, 30 d'agost de 2017

Dr. Antonio Rodríguez Fortea

Prof. Josep M. Poblet Rius

UNIVERSITAT ROVIRA I VIRGILI
COMPUTATIONS ON FULLERENES: CHARACTERIZATION, REACTIVITY AND GROWTH
Laura Abella Guzman

Acknowledgments / Agraïments

I would like to start this Thesis thanking all people that have contributed, helped and supported me during these years of PhD Thesis. Most people could think that it is the easiest part to write, but I do not think so. I am not very good at expressing all my feelings in a few lines; thus, it has taken me much more time than I expected. Although writing is not my strong point, I would try to do all my best.

En primer lloc, voldria agrair a aquelles dues persones que sense elles no hagués pogut fer el doctorat, els meus *jefes*, Josep M. i Toni. Encara recordo ara el dia que em vau proposar fer el doctorat en vosaltres i no disposàveu de beques de departament. No em vaig trencar massa el cap, tenia molt clar que si ho feia, havia de ser sota la vostra supervisió. Durant el transcurs de la meva vida m'he equivocat en moltes ocasions, però després d'aquests 4 anys de doctorat, puc dir que en aquella no ho vaig fer. Sou investigadors i persones tan diferents, que tenir-vos junts ha estat per mi un gran privilegi. La veritat és que els dos heu contribuït i lluitat per treure el millor de mi, ara bé, si ho heu aconseguit o no ja és cosa meva... Josep M., no et puc estar més agraïda després de tot el que has fet per mi, tan científicament com personalment, sincerament has estat com un pare dins la uni. En tot moment has estat pendent de mi, en la formació, decisions, salut... en fi, he estat tota una afortunada de tenir-te! La teva sinceritat junt amb els teus consells, agradables o no, m'han ajudat més del que et pots arribar a pensar, encara que en moltes ocasions et pogués ficar mala cara... Després de totes les experiències viscudes durant aquests anys i, sobretot, en aquest darrer, em podria enrotllar molt més, però no acabaria mai. Això sí, crec que no tornaràs a anar a Xina tan ben acompanyat!! *jeje* Toni, *más de lo mismo*! Des de que et vaig tenir de professor d'Espectroscòpia a tercer de carrera, que vaig saber que volia que fossis tu el meu director de tesi! Que sàpigues que t'admiro moltíssim, tan com a investigador, persona i esportista! Les teves rectificacions, bronques, consells, xerrades... m'han ajudat a millorar en molts aspectes. Gràcies per preocupar-te sempre de tot i en ajudar-me amb tot el que has pogut. A més, és un plaer compartir en tu el *hobby* nº1, el *running*! Sempre fa il·lusió veure't entrenant o a les curses... Bé, finalment, agrair-vos per la vostra paciència, dedicació, motivació, suport i ajuda des de que vaig entrar al departament amb una beca de col·laboració fins ara. De tot cor, moltes gràcies a ambdós.

A la resta de membres sèniors del grup: Xavi, Jordi, Mar, Anna, Coen, Joan, Josep Manel i Rosa, us voldria agrair tots els vostres comentaris, crítiques, idees i discussions durant els seminaris, així com també dir que ha estat un plaer compartir estones durant les pauses del cafè, dinars, sopars, l'estada a la casa rural, etc. Sincerament, moltes gràcies per contribuir d'una manera o d'altra en aquesta etapa, sempre donant el millor de vosaltres. També, agrair a aquelles persones que són l'ànima del grup, en les que sense ells no podríem calcular, els informàtics: Jose, Elisenda i Moisés. Moltes gràcies per solucionar-

me sempre de manera instantània tots els problemes que he tingut amb l'ordenador, maginet, llac, io-chem, disc dur, virus, etc. Gràcies per la paciència que heu tingut i sempre rebrem amb un somriure.

Ja han passat una sèrie d'anys des de que vaig començar en aquest grup amb una beca de col·laboració l'any 2012. Ho compaginava amb l'últim any de carrera, així que em feia una mica de respecte i por a la vegada. Tot i això, a pesar d'estar sola a la sala de terminals, des d'un bon inici que em vaig sentir molt ben acollida per tots els membres del grup. Durant aquests cinc anys han passat moltes persones, amb qui he compartit més o menys temps, voldria agrair-lis a tots ells tot el que han fet per mi. Mireia i John, vam coincidir molt poquet, però suficient per transmetre'm tota l'alegria que porteu dins.

Un cop començar el màster ja vaig entrar a formar part del despatx 204, gràcies Xavi, Núria, Marc i Gian per fer-me un lloc al vostre costat i, sobretot, per ser-hi sempre, tan als bons com als mals moments. Xavi, *profe* de problemes d'Espectro i posterior gran amic, vas ser durant tot aquell temps l'alegria del despatx, encara recordo ara els teus *xistes*, les teves anècdotes, les tardes amb la música a *tope*... Núria, estic eternament agraïda per tot el que em vas ensenyar de ful·lerens, per confiar en mi en tot moment i per aguantar tots els meus rotllos, ets un encant. Marc, gràcies també per tenir la paciència d'ensenyar-me sempre tot el que et preguntava i d'aguantar les meves històries. Ha estat un plaer compartir *jefes* i articles, així com també partits de pàdel! Gian, encara que només vinguessis un dia per setmana, em va encantar tenir-te allà, ja que erets una caixa de sorpreses!

Els altres despatxos... Pablo J., vas ser un gran amic, el teu humor característic era el que donava vida en aquell passadís! Jess, gràcies per la teva hospitalitat, a veure si repetim un dinar com el del Delta! Pablo A., crec que ets una grandíssima persona, no oblido el *running* per les platges explicant-te els meus maldecaps, ni tampoc la cursa del Pont del Diable! Ximo, no et vèiem massa, però els moments que has estat han estat molt intensos! Sergi S., que no et desapareixi mai el teu somriure característic! Gerard A., el músic del grup, el que et sap girar la truita sense donar-te'n compte, encara no entenc com no vam guanyar a Girona! Per la resta, Pedro, Mariano, Pep, Gantulga i Ola, encara que no hem tingut molta relació sempre heu estat allí per qualsevol dubte o problema.

Avancem amb el temps... Gerard N., compartir feina i *hobby* no és molt comú, així com tampoc les sortides de bici parlant de feina! La vida del triatleta és sacrificada, però de moment ho sabem portar de la millor manera! M'has ensenyat moltes coses, ets una persona que sap de tot, així que no dubtis en tornar-me a trucar si et quedes penjat per aquestes carreteres! Magda, continua com fins ara, espero que tinguis molta sort en aquesta nova etapa de post-doc i també espero vindre't a veure algun finde! Diego, et vaig conèixer fent el famós màster, sent una de les persones amb qui millor em duia i, ja

des de llavors, que hem compartit moments de tot. Ets una gran persona, no ho dubtis i la il·lusió va ser meva al saber que sol·licitaves fer el doctorat a Tarragona. Quan tornem a la Gioconda? *Jeje* Almu, amb només un any al grup, has aportat molt més del que et pots arribar a imaginar, vas fer molt bé de venir a Tarragona i, sobretot, de venir a la casa rural quan no havies ni començat! Antonio, successor dels ful·lerens, tindràs èpoques en què tot sortirà i altres que no, però no et desanimis! Jiang Fang, I was in China twice, but I did not meet a girl like you. Try not to change your thoughts and learn a lot here. Marc, Khalid i José Alberto, els més nous del grup, que tingueu molta sort, tindreu molts alts i baixos durant aquests anys, però si he après alguna cosa és que sempre s'ha d'intentar treure el millor de cada fet, tan bo com dolent.

Menció especial als meus companys i amics de despatx. Zhong Ling, the hardest working member that I have never seen in the group. It has been a pleasure to meet you, and you know that you are welcome to come back wherever you want. I know that these years have not been very easy for you, but you have never given up. Thus, it is admirable! Good luck in China! Albert, una bellíssima persona, sempre has estat quan ho he necessitat, tan quan estava a Xina com aquí. Tan temps un al costat de l'altre ha donat per explicar-nos moltes històries, bones i no tan bones, i això ha fet que només amb el simple fet de mirar-nos o fer qualsevol gest, ja sabem del que parlem! Així que és un plaer poder comptar amb un amic com tu. Roser, sé que deixo els ful·lerens en molt bones mans, però si vols un consell, intenta no estressar-te tan... Tard o d'hora tot acaba sortint dona! D'altra banda, dóna gust saber que tinc una persona com tu al meu costat, amb qui tan hem parlat de ful·lerens, com de la vida privada o de simples bogeries. Gràcies per tot!

M'agradaria mencionar també als amics del màster de Química Teòrica i Computacional. Va ser un any força dur, però que ens hem vam sortir. Els dies a Girona i la nit per Tarragona seran dates que costaran d'oblidar. Sergi P., sort va ser meva de tenir-te de company i d'amic durant aquella etapa, les teves bromes, humor i ajuda van ser primordials per tirar endavant! Juan Carlos, sabes que no coincidimos mucho con los ideales y maneras de ver el mundo, pero aún así, sabía que podía contar contigo cuando lo necesitase. Alberto, mi mejor amigo del máster, des del primer día que nos conocimos, que me lo he pasado muy bien contigo. Tenemos pendiente un retorno a la Gioconda, o puede que mejor lo dejemos en salir por Tarragona, *jeje*.

Now, it's turn to thank people who met in China. First of all, I would like to express all my gratitude to my boss in Xiamen, Su-Yuan Xie. Thank you for giving me the opportunity of being in Xiamen University during more than three months. I really appreciate all you did for me when I was in Xiamen. Then, I could not forget Meilin, him secretary, who was always solving all my problems very quickly. Cong-Li, my best friend in China, thanks for all you did for me. I was very lucky to meet you, and finding you in Wuhan was amazing. Chopin, I do not know what I would have done without you in Xiamen. I was really happy

to see you again. I would like to wish all other people who I met there, and say thank you for all they did for me during those months.

Xina va ser una estada que per molt que ho vulgui no la podré oblidar mai, suposa un abans i un després a la meva vida, en la que sort és meva d'haver quedat com una anècdota més. Van ser tres mesos i mig molt molt durs, però on vaig aprendre moltíssim, no solament científicament, sinó com a persona i manera d'entendre la vida, d'apreciar-la i valorar-la. Només puc dir que infinites gràcies a tots aquells que d'una manera o d'altra vau estar en mi.

No podria deixar d'agrair als amics de la carrera, que veient-los més o menys a cadascú d'ells, m'han ajudat en tot moment. Núria, Elena, Lluis, Xavi i Marc, llàstima no haver anat de viatge de final de carrera en vosaltres, però m'emporto tots els moments que hem viscut plegats durant aquests anys, com menjars, festes, bodes, Vinaròs, filosofades... i les que ens queden! Mil gràcies per tot el que heu fet per mi, sempre recordaré aquell *Como si no hubiera un mañana*... Sincerament sou especials! Mireia i Aleix, encara que sent veïns ens veiem molt poc, sé que sempre puc comptar en vosaltres. Mireia, topar en tu el primer dia de la carrera, va ser el millor que em podia passar, llàstima que després et canviessis, però vas fer bé. Gràcies per transmetre'm tota l'alegria que portes dins! Josu i Fran, els 'amics de passadís', els millors amics de la uni, amb qui hem passat moltes estones penjades parlant de tantes tonteries, *cotilleos*, preocupacions... Josu, que sàpigues que no m'apostaré res més en tu, ja que sempre ho acabo perdent tot amb tu! Fran, si algun dia canvies de feina, que continuï sent d'investigació... sempre acabes encertant en les teves prediccions! *You know what I mean*! Durant aquests anys hi ha hagut moments de tot, gràcies per ser-hi sempre!

Encara que aquests darrers anys ens hem vist menys del que voldríem, també voldria donar les gràcies als amics de la colla de Móra per ser-hi en tot moment a pesar de la distància. Rubén, Pau, Nando, Marta, Meri, Gemma, Ali, Irene i Roger, sabem que cadascú fa la seva vida dins o fora del poble, però a veure si arriba el dia en què podem coincidir tots plegats!

Durant aquest darrer any i mig de doctorat, m'he endinsat al món del triatló, on he conegut persones que valen molt la pena i, amb les quals, hem passat moltes hores juntes, ja sigui entrenant o no. Per aquest motiu, m'agradaria mencionar-los. Natalia, Patri, Miguel i Albert, els pilars fonamentals, qui m'heu escoltat i aconsellat sempre. Ha estat un plaer coneixeu-us i poder compartir molts moments plegats. Joan G., Vadó, Ito, Rubén O., Xavi B., Joan R., Jorge, Rubén T,... desconnectar amb vosaltres m'ha fet créixer com a esportista, però també com a persona, gràcies!

Per acabar, les persones més fonamentals de la meva vida... Unes de les més importants, qui sense elles no estaria aquí, ni hagués aconseguit tot el que m'he proposat fins ara, els meus pares, Enric i Neus. Sabeu que no sóc molt expressiva, però estic molt més que agraïda per tot el que heu fet per mi, m'heu donat tot i més, i sempre, sempre, heu estat en tot moment al meu costat. Valoro els fets molt més del que us podeu arribar a imaginar, segurament us dic menys coses de les que us mereixeu, sé que no sóc una filla 10, però m'agradaria que ara us poguéssiu sentir una mica orgullosos de la vostra filla gran... com de la petita també! Ja que, sense ella no hagués tirat endavant en moltes ocasions. Agnès, germana, millor amiga i companya de pis, l'essència que tothom desitjaria tenir al seu costat. És l'única persona qui ha viscut de primeres la meva rutina, els meus problemes, satisfaccions, maldecaps, alegries,... bàsicament tot! Estic eternament agraïda de tot el que fas, de poder confiar en tu i de tenir-te al meu costat, que sàpigues que ets la millor germana que podia tenir! Pepo, el meu cunyat, qui em coneix d'allò més bé, i sap que si li contesto malament o li faig mala cara és perquè no estic bé. Gràcies per entendre aquests moments, ets un sol! Realment em sento una afortunada de tenir-vos a tots, us estimo molt.

I, com no, no podies faltar tu... David. Des del dia que ens vam conèixer, a aquella mitja marató de Miami, la qual em vas fer de llebre els últims 11 km, vaig pensar que series una persona molt especial per mi, i no només per fer-me pujar per primer cop al podi d'una classificació general femenina... El cert és que en poc temps, has passat a ser una de les persones més importants de la meva vida. Hem passat moments de tot tipus, m'has fet desconnectar completament el temps que no treballava, m'has ensenyat coses que desconeixia o que menys valorava, m'has fet tirar endavant encara que et digués que no podia, m'has complementat els punts més dèbils, etc. A pesar de totes les discrepàncies i baralles que podem tenir, m'agrada saber i sentir que et tinc al meu costat. Segurament t'ho dic menys del que et tocaria, però gràcies per tot el que has fet i fas per mi.

Segurament em deixo a molta gent a qui voldria agrair d'una manera o d'altra, però disculpeu-me. Crec que és un orgull poder comptar en tots vosaltres.

"*We don't know how strong we are, until being strong is the only choice we have*" Bob Marley

UNIVERSITAT ROVIRA I VIRGILI
COMPUTATIONS ON FULLERENES: CHARACTERIZATION, REACTIVITY AND GROWTH
Laura Abella Guzman

Als meus pares, Enric i Neus.
I, en especial, a l'Agnès i Cuco.

UNIVERSITAT ROVIRA I VIRGILI
COMPUTATIONS ON FULLERENES: CHARACTERIZATION, REACTIVITY AND GROWTH
Laura Abella Guzman

Contents

Acronyms

APP Adjacent Pentagon Pair
BE Bond Energies
BP86 Becke-Perdew 86 functional
B3LYP Becke 3-Parameter, Lee, Yang and Parr Functional
CCC Chlorinated Carbon Clusters
CCF Carbide Clusterfullerene
CF Clusterfullerene
CN Coordination Number
CPMD Car-Parrinello Molecular Dynamics
CV Collective Variable
DFT Density Functional Theory
EMF Endohedral Metallofullerene
FEM Free-Encapsulating Model
HOMO Highest-Occupied Molecular Orbital
IPR Isolated Pentagon Rule
LUMO Lowest-Occupied Molecular Orbital
MD Molecular Dynamics
MEP Molecular Electrostatic Potential
MS Mass spectrum
NCF Nitride Clusterfullerene
OCF Oxide Clusterfullerene
o-DCB ortho-Diclorobenzene
PBE Perdew, Burke, and Ernzerhof Functional
PES Potential Energy Surface
RRHO Rigid Rotor Harmonic Approximation
SOMO Singly Occupied Molecular Orbital
TS Transition State

UNIVERSITAT ROVIRA I VIRGILI
COMPUTATIONS ON FULLERENES: CHARACTERIZATION, REACTIVITY AND GROWTH
Laura Abella Guzman

Abstract

The overall goal of this Thesis is focused on the characterization, reactivity and growth of fullerenes. These young molecules are closed carbon cages formed by only hexagons and pentagons. Their formation has become one of the main interests in the scientific community since their discovery. Thus, the experimental detection of new families of endohedral metallofullerenes, Ti@C_{2n} and Sc_3N@C_{2n}, let us the choice of study their formation accurately. Different models have been proposed to predict their formation from graphite or amorphous carbon, but none of them are strictly convincing. This work gives support to the bottom-up mechanism as a model of fullerene formation. We have explored this mechanism by means of static DFT and Car-Parrinello molecular dynamics calculations for series of different endohedral fullerenes. A comprehensive exploration of the most favorable isomers, the potential energy surfaces associated with the successive C_2 insertions and the topologies of the involved structures, helped us to develop this project. The insertion of a C_2 unit to already formed EMF is always an exothermic/exergonic process and the free energy barriers for each step are attainable at temperature of fullerene formation (2000 K). The most abundant isomers of Ti@C_{2n} (2n=26-48) and Sc_3N@C_{2n} (2n=68-80) are formally linked by direct C_2 insertions and in a few cases by additional Stone-Wales transformations. In addition, from our Sc_2C_2@C_s(hept)-C_{88} calculations, we suggest that it could be a kinetically-trapped species derived from the recently reported Sc_2C_2@C_{2v}-C_{86}(9) via a direct C_2 insertion. Therefore, the present theoretical studies provide strong support for the CNG mechanism.

Sc_2O has demonstrated to be a good template for middle size fullerenes, between C_{70} and C_{82}, permitting to characterize many structures and determining different physical properties. The new metallic oxide clusterfullerenes, Sc_2O@T_d-C_{76}(19151), Sc_2O@C_{2v}-C_{80}(31922) and Sc_2O@C_{3v}-C_{82}(39717) have been isolated and characterized by mass spectrometry, UV-vis-NIR absorption spectroscopy, cyclic voltammetry, ^{45}Sc NMR spectroscopy, DFT calculations, and single-crystal X-ray diffraction. Our results show that the Sc_2O cluster transfers four electrons to the corresponding C_{2n} cage, $(Sc_2O)^{4+}$@$(C_{2n})^{4-}$.

Chlorination has emerged as a powerful tool in fullerene derivatives. Several C_{2n} families (2n=50,60,66,68,etc.) have been found to show cages exohedrally chlorinated. The reaction sites where chlorines are attached, the chlorination pathways and how chlorofullerenes are formed are issues that have been considered in recent years. Herein, we can find the following chlorofullerenes: $C_{66}Cl_{10}$, $C_{74}Cl_{10}$ and $C_{78}Cl_6$(C_5Cl_6). According to our results, low-energy neutral cages are the ones that are functionalized when a chlorine source is introduced in the arc. Chlorination would take place at a temperature significantly lower than 2000 K, once the neutral isomers were formed.

UNIVERSITAT ROVIRA I VIRGILI
COMPUTATIONS ON FULLERENES: CHARACTERIZATION, REACTIVITY AND GROWTH
Laura Abella Guzman

CHAPTER 1

Getting into the World of Fullerenes

UNIVERSITAT ROVIRA I VIRGILI
COMPUTATIONS ON FULLERENES: CHARACTERIZATION, REACTIVITY AND GROWTH
Laura Abella Guzman

CHAPTER 1

Getting into the World of Fullerenes

This chapter introduces the amazing world of Fullerenes to the reader, highlighting their fundamental aspects and one of the biggest headaches for the scientific area of these molecules; their formation. First, this introduction contains a brief description related to fullerenes: their discovery, different types, the most common properties, and some relevant applications. Afterwards, the two main hypothetical models of fullerene formation mechanisms established until now are described.

1.1. Fullerene Discovery

One of the most versatile elements in chemistry is carbon, which has been extensively studied by the scientific community. Depending how the carbon atoms are bonded, it can be found by different ways, termed allotropes of carbon. The two best-known allotropic forms are graphite and diamond. Interestingly, a new allotropic form of carbon appeared accidentally in 1985, known as Fullerenes.[1] These molecules are closed and empty carbon cages that contain only pentagonal and hexagonal rings and consist of a spherical or ellipsoid arrangement of dozens of carbon atoms.

The first fullerene discovered was the buckyball (Figure 1), being the most abundant and studied. It is also known as buckminsterfullerene, after the architect Buckminster Fuller, whose geodesic dome it resembles.[1,2] It was discovered in 1985 at Rice University in Houston by Richard Smalley, Robert Curl and Harry Kroto in an attempt to explain the pronounced abundance of the C_{60} cluster in their graphite laser vaporization experiment.[3] This proposal was subsequently confirmed in 1990, when

Krätschmer, Lamb, Fostiropoulos, and Huffman reported a method for the bulk production of C_{60} in an electric carbon-arc in a low-pressure atmosphere along with infra-red (IR) spectroscopic evidence for its structure.[3] Few years later, Smalley, Curl and Kroto won the 1996 Nobel Prize in Chemistry for their discovery.[4] Buckminsterfullerene or buckyball molecules are roughly spherical cages of 60 carbon atoms (C_{60}) arranged in interlocking hexagons and pentagons, like the patches on a soccer ball (Figure 1).

Figure 1. (Left) Geodesic Dome designed by Richard Buckminster Fuller in Montreal's Biosphere Environmental Museum (Canada). (center) A soccer ball. (right) The I_h-C_{60} fullerene representation.

Other fullerenes were discovered shortly afterwards with more and fewer carbon atoms, ranging from 28 up into the hundreds, though C_{60} remains the easiest to produce and consequently cheapest, with prices rising rapidly for the larger fullerenes. C_{70} was found to be the second more stable fullerene.[5]

The graphite laser vaporization results of Rohlfing *et al.*[6] are reproduced schematically in Figure 2, which shows ion signals from carbon clusters obtained by vaporizing graphite with a high-power laser, cooling and clustering the resulting carbon vapour in a beam of helium, and photoionizing the clusters so obtained for detection by time-of-flight mass spectrometry. The resulting carbon cluster mass distribution is seen to be distinctly bimodal, with both even and odd C_{2n} clusters in the range $2n \leq 25$, but only even C_{2n} clusters in the range $2n \geq 40$. Although these features are quite general, the details of this mass distribution can vary depending on the experimental conditions.

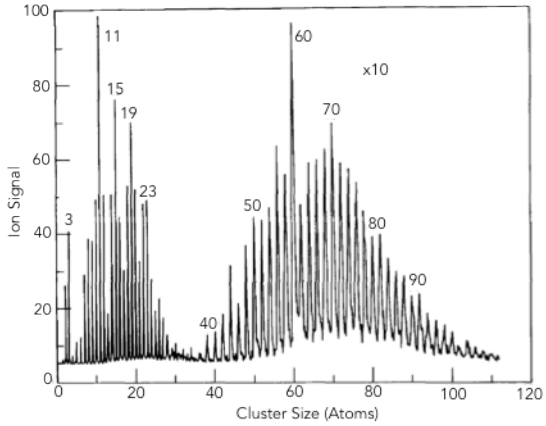

Figure 2. Schematic picture of the early graphite laser vaporization results of Rohlfing, Cox and Kaldor. The abscissa gives the carbon cluster size as the number of atoms 2n.[6]

Fullerenes occur only in small amounts naturally, but several techniques for producing them in greater amounts have been developed. Some techniques use a benzene flame to produce fullerenes.[4] Other techniques include the vaporization of graphite rods and catalytic chemical vapour deposition from ethanol vapour. In research laboratories, fullerenes are synthesized with the Krätschmer-Huffman machine by the arc-discharged method, unofficially know as "arcing" (Figure 3). By whatever methods fullerenes are synthesized, it is clear that carbon needs to be exposed to very high temperatures, and that condensation process of the carbon vapour or hydrocarbon fragments plays a crucial role for the self-assembly of the fullerene cages. From Laser Induced Fluorescence (LIF) experiments we know that C_2 and C_3 species are abundant in the laser plumes generated by graphite evaporation, and high level *ab initio* calculations have shown that macrocyclic rings dominate over linear carbon chains starting from C_{10}. Any fullerene synthesis operates under non-equilibrium conditions with a continuous energy input and carbon concentration (or pressure) gradient.[2]

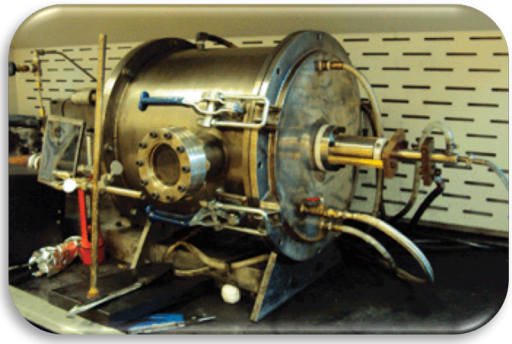

Figure 3. Krätschmer-Huffmann reactor or arc used for the synthesis of fullerenes. Courtesy of Prof. L. Echegoyen of Texas University at El Paso (UTEP).

After developing Krätschmer and Huffmann techniques, Kikuchi *et al*. confirmed the presence of larger fullerenes such as C_{76}, C_{78} and C_{84}, by using a preparative HPLC for isolation. Furthermore, cages of 60, 70, 76, 78, 82, 84, 90 and 96 have been extracted from carbon soot.[7] Aromatic and polycyclic compounds, such as PAHs, benzyl and phenyl, have also been used via pyrolysis as methods of syntheses.[4]

Since the buckminsterfullerene detection, many different studies about stability, reactivity, aromaticity and electronic structure have been carried out using several methodologies and approximations.[8]

1.2. Number of Isomers & Nomenclature

In theory, an infinite number of fullerenes can exist. Their structure is based on that each carbon atom is bonded to three other atoms, i.e. sp^2 hybridised, to give a closed spherical cage of five- and six-membered rings. However, there is the possibility of finding four- and seven-membered rings in some less abundant cases. This bonding framework forms a polyhedron with an atom at each vertex, a bond along each edge and a ring in each face.[3]

The C_{2n} cage containing only pentagonal and hexagonal rings can encompass an enormous number of different isomers at each nuclearity (2n). Despite the fact that there are so many possible fullerene isomers, it is sometimes possible to guess the most stable (and therefore chemically relevant) C_{2n} fullerene cage simply by

experimenting with molecular models. Computational chemists predict the most stable C_{2n} isomers with electronic structure methods, and investigate general trends. The number of fullerene isomers increases very rapidly with 2n, as shown in Table 1. The spiral algorithm allows us to predict the total number of isomers for a given number of 2n.[3]

Table 1. Number of isomers presents on a fullerene cage of 2n atoms.

2n	Isomers	2n	Isomers
20	1	60	60
30	3	70	8149
40	40	80	31924
50	271	90	99918

One of the best-known properties of polyhedra is Euler's theorem,[9] which states that the number of vertices (υ), edges (*e*), and faces (*f*) in a spherical polyhedron are related by

$$\upsilon + f = e + 2 \qquad \text{(Eq.1)}$$

For a polyhedron corresponding to a fullerene C_n, the number of vertices is $\upsilon = n$ and the number of edges is $e = 3n/2$. The number of faces is therefore $f = n/2 + 2$, as in any spherical polyhedron with trivalent vertices. If the number of pentagons is defined as *p* and the number of hexagons as *h*, the total number of vertices is then

$$(5p + 6h)/3 = n \qquad \text{(Eq.2)}$$

and the total number of faces is

$$p + h = n/2 + 2 \qquad \text{(Eq.3)}$$

The solution of which is $p = 12$ and $h = n/2 - 10$. Therefore C_n fullerenes contain 12 five- and $(n/2 - 10)$ six-membered rings. The smallest fullerene is the dodecahedron C_{20}, formed by only 12 pentagons. There is at least one fullerene for each even number of C atoms n≥20, with the sole exception of C_{22} because it is impossible to construct 22-vertex polyhedron with 12 pentagons and one hexagon.

One useful property of polyhedra is that they can be flattened onto a plane in such a way that the edges intersect only at the vertices. The vertices of the graph represent atoms, and the edges represent bonds, just as they do in the polyhedron. The stretching operation transforms a three-dimensional polyhedral representation that

contains the same bonding connectivity information. Figure 4 shows this sort of fullerene graph, known as Schlegel diagram.

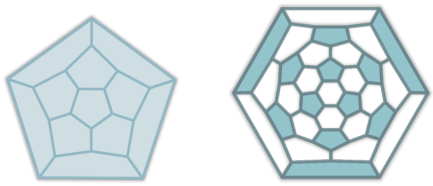

Figure 4. C_{20} (left) and I_h-C_{60} (right) Schlegel diagrams. Pentagons are represented in blue.

Fowler and Manolopoulos developed a nomenclature accepted by the whole community of scientists working in this field. Each carbon cage is labeled by a number according to the spiral algorithm and by its symmetry. For example, I_h-C_{60}(1812) would be the nomenclature for I_h-C_{60}.

Raghavachari proposed a nomenclature to know the arrangement of the pentagons in a fullerene. The neighbour index scheme is a six-component vector of the form (p_0,p_1,p_2,p_3,p_4,p_5), where p_k denotes the number of pentagons with neighbour index k, i.e. with k adjacent pentagons.[10] For example, all 12 pentagons in I_h-C_{60} have neighbour index 0, corresponding to the signature (12, 0, 0, 0, 0, 0) and the pentagon neighbour index signature of the unique D_{3h}-C_{26} fullerene is (0, 0, 0, 6, 6, 0). The sum of the six entries in the signature is always 12, which is simply the total number of pentagons. In addition, using the Raghavachari indices, the total number of pentagon adjacencies (N_p) can be calculated by using the following equation:

$$N_p = \frac{1}{2}\sum_{k=1}^{5} k\, p_k \qquad \text{(Eq.4)}$$

1.3. The Isolated Pentagon Rule (IPR)

The stability of fullerenes can be attributed to a balance between π electronic stability and steric strain.[3] The single most important consequence of steric strain in the fullerenes is the isolated-pentagon rule (IPR), which was proposed by Kroto in 1987. This rule states that the most stable fullerenes are those in which all the pentagons are isolated by hexagons (Figure 5).[11] Only the systems with 2n≥60 are able to follow this

rule and they have two different bond types: [6,6] bonds which are those situated between two hexagonal rings, and [5,6] bonds between an hexagonal and a pentagonal ring. In contrary, non-IPR structures have another sort of bond: [5,5], which are those situated between two pentagonal rings (Figure 6).

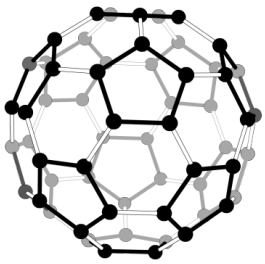

Figure 5. The I_h-C_{60} cage. All pentagons are isolated by hexagons and they are represented in black.

The deviation from the planarity induced by the presence of pentagons in the structure is responsible for the strain energy that is often used to explain the stability of different fullerene cages. Surface curvature partially destroys the π -overlap between adjacent carbon atoms decreasing the aromaticity of the fullerene.[12] The most stable isomers are expected to have the lowest number of pentagon adjacencies. This is known as the pentagon adjacency penalty rule (PAPR).

Fullerenes smaller than C_{60} unavoidably have adjacent pentagons, these carbon cages are known as non-IPR structures. The number of fused-pentagons is variable from 2 to 12, with different patterns of adjacencies (Figure 7). Smaller fullerenes have much higher strain energy in the carbon surface and are highly reactive. This high reactivity also precludes their more conventional chemical syntheses using procedures that give C_{60}. C_{50} fullerene is the smallest carbon cage without three directly or sequentially fused pentagons and should have less strain energy than other smaller fullerenes.

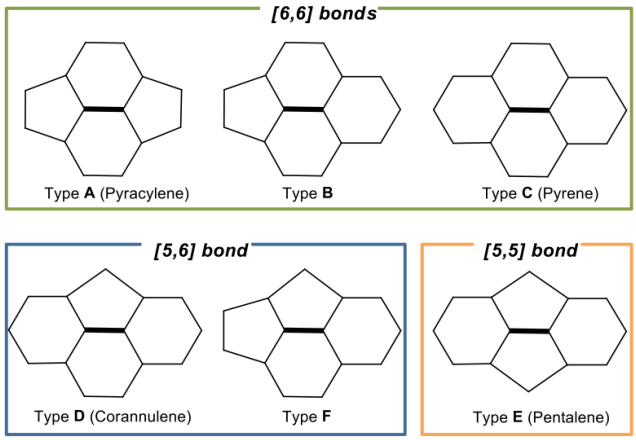

Figure 6. All different C-C bonds types in IPR fullerenes (A-D types) and two additional types found in the non-IPR (F and E types). The bold line determines the considered C-C bond.[13]

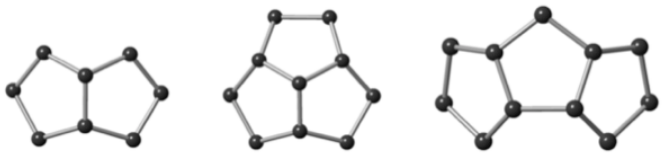

Figure 7. Some basic fused-pentagon patterns in non-IPR cages. (left) Adjacent pentagon pair. (center) Triply-fused pentagons with a 5,5,5 central C atom. (right) Triply-fused pentagons without any 5,5,5 C atom.

1.4. Types of Fullerenes

Different types of fullerenes have been synthesized, isolated and characterized so far. They can be classified according to the type of external derivatization, the internal encapsulated atoms or the heteroatoms that replace some of the C atoms in the cage framework. In this thesis we focus on two of them: endohedral metallofullerenes and exohedral fullerenes.

1.4.1. Endohedral Metallofullerenes (EMF)

Endohedral metallofullerenes are formed when a single metal atom or a metal cluster is encapsulated inside the fullerene cage. The endohedral fullerenes are represented as $M@C_n$ where the symbol @ is used to define that the left-marked atom or cluster is encapsulated inside of the right-indicated fullerene-cage. This special symbolism is widely accepted and is what we will use in this work, although it is different from the IUPAC nomenclature.

We have studied several endohedral metallofullerenes, such as those that contain a single Ti atom or Sc_2O and Sc_3N clusters. But other metals can be encapsulated inside the cages such as zirconium, hafnium, scandium, lanthanides, and uranium, among many others. Figure 8 shows two important endohedral metallofullerenes. $La@C_{60}$ is the first discovered EMF (1985);[14] later Dorn and co-workers reported in 1999 the synthesis, characterization and isolation of the endohedral $Sc_3N@C_{80}$.[15] This cage is the most stable endohedral synthesized and the third fullerene in terms of abundance, after C_{60} and C_{70}.[15]

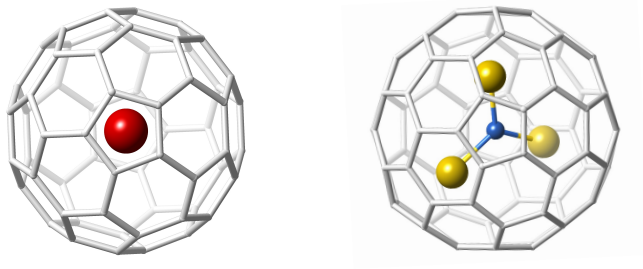

Figure 8. Two types of endohedral metallofullerenes, La@C_{60} (left) and Sc_3N@C_{80} (right).

We consider as small fullerene cages those that have from 28 to 50 carbon atoms. All of them are non-IPR isomers because of the impossibility of constructing an IPR cage with 12 pentagons surrounded by hexagons with less than 60 atoms.

Due to the strain energy for the non-IPR cages which is larger than for larger IPR isomers, these small cages present a very high curvature and huge instability.

In 1992, Scuseria and co-workers reported experimental evidences of a prominent peak of U@C_{28} and this led them to the conclusion that U was trapped inside the C_{28} cage. *Ab initio* calculations showed that C_{28} could be stabilized inserting a tetravalent atom such as Si, Ge, Ti, Zr and Hf. Moreover, they reported the experimental confirmation of the presence of Zr@C_{28} and Hf@C_{28} and a very weak signal for Ti@C_{28}.[16] C_{28}, which presents two isomers, has been considered so far to be the smallest fullerene to encapsulate one atom. However, Kroto and co-workers have detected Ti@C_{26} in a recent study.[17]

1.4.2. Exohedral Fullerenes

A minor part of the present work is also dedicated to exohedral fullerenes, also called exofullerenes. These molecules have additional atoms, ions or clusters attached to their outer spheres, resulting in an external derivatization of the carbon cage. The first exohedral fullerene synthesized was 1,2-$C_{60}(OsO_4(4\text{-t-Bu}C_5H_4N_2)_2)$ by Hawkins and co-workers.[18] This thesis is based on the study of one kind of halogenated fullerenes, the chlorinated fullerenes. Fullerenes can be chlorinated by introducing chlorines in the chaotic violent graphite arc discharge or by reacting with inorganic chlorides at high temperature. Numerous fullerenes chlorides, both with IPR or non-IPR cages have been produced in the past dozen years.[19] In the presence of CCl_4, a modified Krätschmer-Huffman arc discharge has been applied to synthesize smaller non-IPR chlorofullerenes such as D_{5h}-$C_{50}(271)Cl_{10}$ in 2004[20] (Figure 9) and $C_{54}(540)Cl_8$,

$C_{56}(864)Cl_{12}$, $C_{56}(913)Cl_{10}$ and $C_{56}(916)Cl_{12}$ later.[20-22] Larger fullerenes from C_{60} to C_{108} have been produced as chlorofullerenes in radio-frequency furnace[23] and solvothermal reactions as well. For example, in the past years, $C_{56}(916)Cl_{12}$,[24] $C_{72}(11188)Cl_4$,[25] and $C_{68}(6094)Cl_8$,[26] have been synthesized in a radio-frequency furnace starting from graphite in the presence of CCl_4.

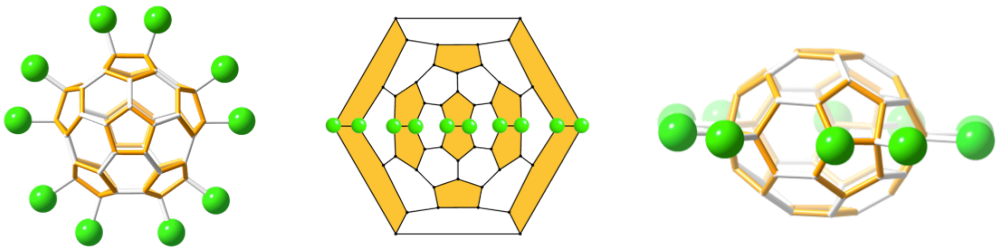

Figure 9. Representations in 2- and 3-dimensions of $C_{50}Cl_{10}$ fullerene.

1.5. The Most Relevant Applications

The discovery of fullerenes has rapidly attracted the attention of the scientific community. Their novel properties have created high expectations on their applications. During the last decades, the most prominent applications of fullerenes have been devoted to different fields, the most redundant are those related in medicine and material science.

A field under constant development is biomedicine. Fullerenes are organic molecules, which do not show signs of toxicity, so it allows them being doable in biomedical applications. The first fullerene-based drug formed, $Gd_3N@I_h\text{-}C_{80}(7)$, was developed by Dorn and co-workers as contrast agent in Magnetic Resonance Imaging or MRI.[18]

Due to the electronic motion in the most spherical cages and the huge electron affinity of these systems, endohedral metallofullerenes can be found in solar cells field. Thus, organic photovoltaics are another of the very promising fields. New fullerene-based cells are reversible, metastable, and have ultra fast mobility, as shown in several published studies. Thus, a good alternative to the current organic solar cells is appeared.

Other applications were also predicted on endohedrals metallofullerenes due to their chemical and physical properties. Superconductors, metallofullerenes lasers or nanomemory devices are some examples.

Day after day, new endohedral metallofullerenes are synthesized providing to the field new molecules with new features that can provide different applications. Therefore, innovative applications could be appeared in the following years.

1.6. Hypothetical Models of Fullerene Formation

How carbon atoms find their locations during the growth of these highly symmetric structures in the chaotic environment of cooling carbon vapour had puzzled experimentalists and theoreticians for a long time. Proposed fullerene growth models typically invoke small carbon clusters to account for fullerene formation, however, in very different and often conflicting ways.

Several theories about the formation mechanisms of fullerenes have been published, among them the "party line",[27] the "pentagon road",[28] the "fullerene road",[7] the "ring-stacking",[7,29] and the "ring fusion spiral zipper".[30,31] All of these models are based on the same concept, i.e. growing up from intermediate structures and additions of small C_x units in a thermodynamic equilibrium. But, none of these hypothetical mechanisms has been strictly confirmed. Up to date the most prominent models for the formation of fullerenes are the "shrinking hot giant" and the "closed network growth" mechanisms, focused on the extrusion/addition of C_2 units, respectively. Nowadays, the formation of fullerenes is still one enigma to be solved in this field.

1.6.1. Shrinking Hot Giant Road

This mechanism was proposed from quantum chemical molecular dynamics (QM/MD) simulations of hot carbon vapor in a non-equilibrium environment by Irle and Morokuma.[4] This road consists of two parts: a "size-up" part, where giant fullerenes are self-assembled by the interplay of dynamics and chemistry of hot polyyne chains in carbon vapour leading to exothermic, more or less curved π-stabilized sp^2-networks, and a "size-down" part, where these giant, vibrationally excited cages shrink down to the size of C_{70} and C_{60}.[32,33]

Giant fullerenes growth occurs in three stages under non-equilibrium dynamic conditions. First, nucleation of polycyclic structures takes place from entangled polyyne chains. This step is followed by growth, which utilizes the familiar ring condensation of carbon chains and rings attached to the hexagons and pentagons. The final step is characterized by the cage closure.

In the size-down part, larger fullerene cages are energetically preferable due to their lower steric strain energy. However, the giant fullerenes are produced "hot", in a vibrationally highly excited state, due to the rapid gain of energy by cage closure, and this energy has to be dissipated, either by unimolecular decomposition or collision with other carbon clusters or carrier gas atoms. Their simulations reveal that newly produced giant fullerenes inevitably shrink to smaller sizes, a process that is obviously related to the environmental temperature and the duration of heat exposure. The formation by repeated C_2 elimination reactions is particularly carried out in low carbon density environments.[34]

The same authors, Irle and Morokuma, also remarked that fullerenes with a number of atoms lower than 100 tend to grow, as observed in molecular dynamics simulations at constant temperature and constant carbon density.[34] The C_2 ejection and insertion rates depend strongly on the concentration of available carbon outside the cages: A larger number of free carbons increases the growth rate, whereas a smaller number increases the shrinking rate. Kinetic models provided an interpretation of the driving force of the shrinking process and the prevalence of C_{60} and C_{70} over other fullerenes.[32,33]

It is worth remarking here that other authors proposed the top-down mechanism. Recently, Chuvilin *et al.* demonstrated the transformation of graphene into a fullerene cage by electron beam irradiation in transmission electron microscopy studies.[35] Then, Balch, Olmstead, Dorn and co-workers interpreted the transformation of larger EMFs (C_{84} / C_{80}) via the loss of C_2 units and SW transformation.[36] They isolated and characterized a metallofullerene proposed to be a key intermediate in the top-down formation of EMFs from graphite.

1.6.2. Closed Network Growth (CNG)

Kroto *et al.* have recently reported a new mechanism for the growth of fullerenes.[17] They revealed that fullerenes self-assemble through a closed network growth (CNG) mechanism by incorporation of atomic carbon and small carbon clusters, as C_2 molecule. Growth by C and C_2 incorporation is demonstrated for C_{60}, C_{70}, C_{76}, C_{78}, C_{84} and the endohedral metallofullerenes, $La_2@C_{80}$, $Gd@C_{82}$,[37] $Ti@C_{2n}$[38] and $Sc_3N@C_{2n}$.[39] C_{60} exposed to the characteristic high synthesis temperature achieved by laser

ablation, results predominantly in C_{60} with only very minor amounts of C_{58}, C_{56}, or C_{54}, and a very low abundance of clusters larger than 60 carbon atoms. In contrast, in the presence of carbon vapor under the same conditions, remarkable amounts of C_{60+2n} species are observed, with C_{70} being formed at a higher relative abundance because of the IPR nature of the isomer.[17]

The ingestion of single C atoms into the C_{60} cage catalyses bond rearrangements that would be more difficult and probably unattainable without such an ingestion (Figure 10). Subsequent C ejection leads to another C_{60} cage. A new C ingestion leads to the formation of C_{62} (Figure 10).

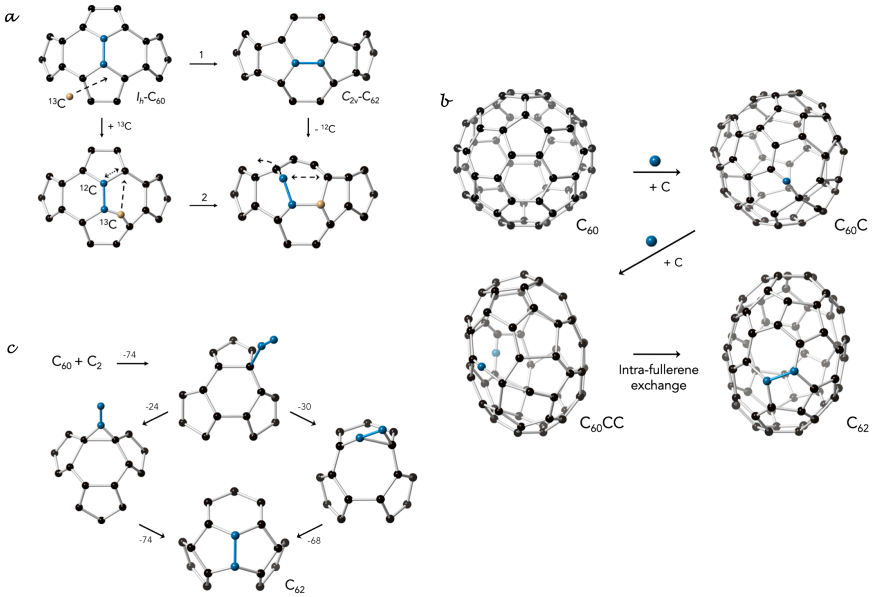

Figure 10. Mechanisms proposed by Kroto *et al.* for growth processes. a) Exposure to ^{13}C-enriched carbon vapour. b) Ingestion of atomic carbon. c) Direct C_2 ingestion (Energies in kcal·mol^{-1}).

Besides, two carbon atoms can separately insert into C_{60} to form a $C_{60}CC$ species, essentially C_{60} with two carbon adatoms. The locations of the two carbon adatoms change as they interchange throughout the C_{60} cage by the mechanism shown in Figure 10. Their movement through the fullerene terminates as the adatoms meet to form a bond resulting in a structural conversion to the ground-state fullerene C_{62}, the same structure produced by direct C_2 addition (Figure 10). Direct C_2 ingestion into I_h-

C_{60} proceeds via a series of metastable intermediates, forming a heptagon-containing fullerene as shown in Figure 10.

In addition, it has recently been reported that a heptagon-containing clusterfullerene could play an important role in the bottom-up mechanism. Echegoyen, Poblet and co-workers proposed the heptagon-containing cage $Sc_2C_2@C_{88}$ to be a likely intermediate in the CNG mechanism once C_2 insertion takes place into the thermodynamic $Sc_2C_2@C_{86}$ cage.[40] Furthermore, the first characterized heptagon-containing metallofullerene, $LaSc_2N@C_{80}$, potentially can form by either carbon loss or gain.[41]

1.7. Isomerisation Paths

A striking characteristic of fullerenes as a class is the huge number of isomers corresponding to the formula C_{2n}. It seems likely that under the violent conditions of graphite vaporization the isomers can interconvert, allowing conversion of thermodynamically unfavourable cages to the few favoured structures. We discuss here two likely isomerisation paths.

1.7.1. Stone-Wales Rearrangement

Since the essential difference between fullerene isomers lies in the distribution of the pentagons, this hypothesis implies that there should be a mechanism for motion of pentagons on the fullerene surface. One such mechanism, which is called Stone-Wales transformation, is described now.[42]

To perform the transformation it is first necessary to find a place on the surface of the fullerene polyhedron where two hexagons and two pentagons meet in a pyracylene patch (Figure 6). Figure 11 shows the patch of the fullerene surface involved in the Stone-Wales (SW) transformation between general fullerene isomers. If such a patch exists, the Stone-Wales bond can be twisted, breaking two of its neighbouring bonds and making two more, thereby swapping pentagons and hexagons, and producing a rotated patch within the same perimeter of 12 atoms and 12 bonds. The product is still a fullerene and is in general different from the starting isomer, though it is possible for the initial and final fullerenes to be enantiomeric or even conceivably identical. Any single SW transformation is reversible and so links isomers in a well-defined way. Given the complete set of fullerene isomers of a particular C_{2n} it is straightforward to generate all possible SW interconversions and so to construct a map of isomerisation allowed under this mechanism. The smallest fullerene to support the SW is D_2-C_{28}(1).

The Stone-Wales transformation is expected to be a high-energy process, as predicted by computations (higher than 100 kcal·mol^{-1}).[43]

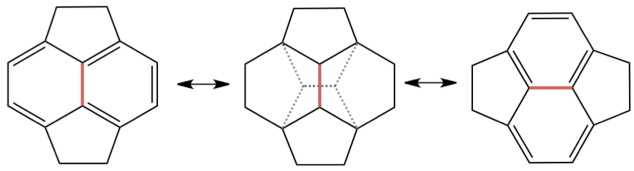

Figure 11. Schematic representation of the Stone-Wales transformation.

1.7.2. The Azulene-Naphtalene Arrangement

Heilbronner *et al.* reported isomerisation of the unsubstituted azulene molecule to naphthalene in 1947. Three years later, they concluded that this rearrangement was "...essentially homogeneous and monomolecular" in the gas phase over the temperature range 370-430 °C. The transformation of azulene to naphthalene is a very simple but exciting and beautiful example of the rearrangement of a nonbenzenoid to a benzenoid aromatic structure (Figure 12).[44] The thermal process has been the subject of intensive experimental investigations.[45] Numerous ^{13}C-labeling studies on azulene have been conducted to explore the reaction mechanisms. From the patterns obtained for the scrambling of the carbon atoms, different reaction mechanisms have been inferred, including unimolecular pathways and those initiated by the formation of radical adducts.

This kind of rearrangement can also take place in the fullerene surface, mainly in formation processes. The combination of a pentagon-heptagon (5:7) can generate a hexagon-hexagon (6:6) fusion.

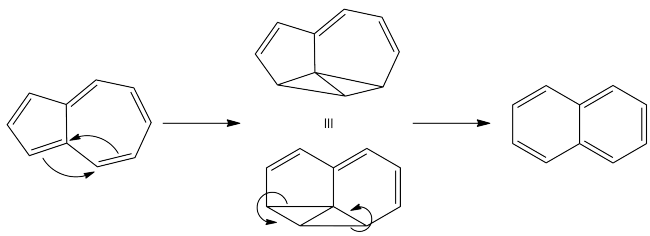

Figure 12. The azulene-naphtalene transformation.

1.8. References

(1) Kroto, H. W.; Heath, J. R.; O'Brien, S. C.; Curl, R. F.; Smalley, R. E. *Nature* **1985**, *318*, 162.
(2) Rodríguez-Fortea, A.; Irle, S.; Poblet, J. M. *Wiley Interdiscipl. Rev. Comput. Mol. Sci.* **2011**, *1*, 350.
(3) Fowler, P. W.; Manolopoulos, D. E. *An atlas of fullerenes* Oxford Univ. Press, Oxford (UK), **1995**.
(4) Irle, S.; Zheng, G.; Wang, Z.; Morokuma, K. *J. Phys. Chem. B* **2006**, *110*, 14531.
(5) Kratschmer, W.; Lamb, L. D.; Fostiropoulos, K.; Huffman, D. R. *Nature* **1990**, *347*, 354.
(6) Rohlfing, E. A.; Cox, D. M.; Kaldor, A. *J. Chem. Phys.* **1984**, *81*, 3322.
(7) Wakabayashi, T.; Achiba, Y. *Chem. Phys. Lett.* **1992**, *190*, 465.
(8) Chaur, M. N.; Melin, F.; Ortiz, A. L.; Echegoyen, L. *Angew. Chem. Int. Ed.* **2009**, *48*, 7514.
(9) Lakatos, I. *Proofs and refutations* Cambridge Univ. Press, Cambridge (UK), **1976**.
(10) Raghavachari, K. *Chem. Phys. Lett.* **1992**, *190*, 397.
(11) Kroto, H. W. *Nature* **1987**, *329*, 529.
(12) Chen, Z. F.; King, R. B. *Chem. Rev.* **2005**, *105*, 3613.
(13) Campanera, J. M., PhD Thesis "Theorethical Characterization of Metallofullerenes", Universitat Rovira i Virgili, **2003**.
(14) Heath, J. R.; Obrien, S. C.; Zhang, Q.; Liu, Y.; Curl, R. F.; Kroto, H. W.; Tittel, F. K.; Smalley, R. E. *J. Am. Chem. Soc.* **1985**, *107*, 7779.
(15) H. C. Dorn; S. Stevenson; G. Rice; T. Glass; K. Harich; F. Cromer; M. R. Jordan; J. Crae; E. Hadju; R. Bible; M. M. Olmstead; K. Maitra; Fisher, A. J.; A. L. Balch *Nature* **1990**, *401*, 55.
(16) Guo, T.; Smalley, R. E.; Scuseria, G. E. *J. Chem. Phys.* **1993**, *99*, 352.
(17) Dunk, P. W.; Kaiser, N. K.; Hendrickson, C. L.; Quinn, J. P.; Ewels, C. P.; Nakanishi, Y.; Sasaki, Y.; Shinohara, H.; Marshall, A. G.; Kroto, H. W. *Nat. Chem.* **2012**, *3*, 855.
(18) Hawkins, J. M.; Meyer, A.; Lewis, T. A.; Loren, S.; Hollander, F. J. *Science* **1991**, *252*, 312.
(19) Tan, Y. Z.; Xie, S. Y.; Huang, R. B.; Zheng, L. S. *Nat. Chem.* **2009**, *1*, 450.
(20) Xie, S.-Y.; Gao, F.; Lu, X.; Huang, R.-B.; Wang, C.-R.; Zhang, X.; Liu, M.-L.; Deng, S.-L.; Zheng, L.-S. *Science* **2004**, *304*, 699.
(21) Tan, Y. Z.; Li, J.; Zhu, F.; Han, X.; Jiang, W. S.; Huang, R. B.; Zheng, Z.; Qian, Z. Z.; Chen, R. T.; Liao, Z. J. *Nat. Chem.* **2010**, *2*, 269.

(22) Tan, Y.-Z.; Han, X.; Wu, X.; Meng, Y.-Y.; Zhu, F.; Qian, Z.-Z.; Liao, Z.-J.; Chen, M.-H.; Lu, X.; Xie, S.-Y.; Huang, R.-B.; Zheng, L.-S. *J. Am. Chem. Soc.* **2008**, *130*, 15240.
(23) Mueller, A.; Ziegler, K.; Amsharov, K. Y.; Jansen, M. *Eur. J. Inorg. Chem.* **2011**, *2*, 268.
(24) Ziegler, K.; Mueller, A.; Amsharov, K. Y.; Jansen, M. *Chem. Asian J.* **2011**, *6*, 2412.
(25) Ziegler, K.; Mueller, A.; Amsharov, K. Y.; Jansen, M. *J. Am. Chem. Soc.* **2010**, *132*, 17099.
(26) Amsharov, K. Y.; Ziegler, K.; Mueller, A.; Jansen, M. *Chem. Eur. J.* **2012**, *18*, 9289.
(27) Zhang, Q. L.; O'Brien, S. C.; Heath, J. R.; Liu, Y.; Curl, R. F.; Kroto, H. W.; Smalley, R. E. *J. Phys. Chem.* **1986**, *90*, 525.
(28) Smalley, R. E. *Acc. Chem. Res.* **1992**, *25*, 98.
(29) Ueno, Y.; Saito, S. *Phys. Rev. B* **2008**, *77*, 085403.
(30) Helden, G. V.; Gotts, N. G.; Bowers, M. T. Physics & Chemistry of Fullerenes: A Reprint Collection, **1993**; Vol. 1, p. 52.
(31) Schwarz, H. *Angew. Chem. Int. Ed. Engl.* **1993**, *32*, 1412.
(32) Fedorov, A. S.; Fedorov, D. A.; Kuzubov, A. A.; Avramov, P. V.; Nishimura, Y.; Irle, S.; Witek, H. A. *Phys. Rev. Lett.* **2011**, *107*, 175506.
(33) Curl, R. F.; Lee, M. K.; Scuseria, G. E. *J. Phys. Chem. A* **2008**, *112*, 11951.
(34) Saha, B.; Irle, S.; Morokuma, K. *J. Phys. Chem. C* **2011**, *115*, 22707.
(35) Chuvilin, A.; Kaiser, U.; Bichoutskaia, E.; Besley, N. A.; Khlobystov, A. N. *Nat. Chem.* **2010**, *2*, 450.
(36) Zhang, J.; Bowles, F. L.; Bearden, D. W.; Ray, W. K.; Fuhrer, T.; Ye, Y.; Dixon, C.; Harich, K.; Helm, R. F.; Olmstead, M. M.; Balch, A. L.; Dorn, H. C. *Nat. Chem.* **2013**, *5*, 880.
(37) Sebetci, A.; Richter, M. *J. Phys. Chem. C* **2010**, *114*, 15.
(38) Mulet-Gas, M.; Abella, L.; Dunk, P. W.; Rodriguez-Fortea, A.; Kroto, H. W.; Poblet, J. M. *Chem. Sci.* **2015**, *6*, 675.
(39) Mulet-Gas, M.; Abella, L.; Cerón, M. R.; Castro, E.; Marshall, A. G.; Rodríguez-Fortea, A.; Echegoyen, L.; Poblet, J. M.; Dunk, P. W. *Nat. Commun.* **2017** *(in press).*
(40) Chen, C.-H.; Abella, L.; Ceron, M. R.; Guerrero-Ayala, M. A.; Olmstead, M. M.; Powers, X. B.; Balch, A. L.; Poblet, J. M.; Echegoyen, L. *J. Am. Chem. Soc.* **2016**, *138*, 13030.
(41) Zhang, Y.; Ghiassi, K. B.; Deng, Q.; Samoylova, N. A.; Olmstead, M. M.; Balch, A. L.; Popov, A. A. *Angew. Chem. Int. Ed.* **2015**, *54*, 495.
(42) Stone, A. J.; Wales, D. J. *Chem. Phys. Lett.* **1986**, *128*, 501.
(43) Cioslowski, J. *Electronic Structure Calculations on Fullerenes and Their Derivatives* Oxford Univ. Press, Oxford (UK), 1995.
(44) Scott, L. T. *Acc. Chem. Res.* **1982**, *15*, 52.

(45) Stirling, A.; Iannuzzi, M.; Laio, A.; Parrinello, M. *ChemPhysChem* **2004**, *5*, 1558.

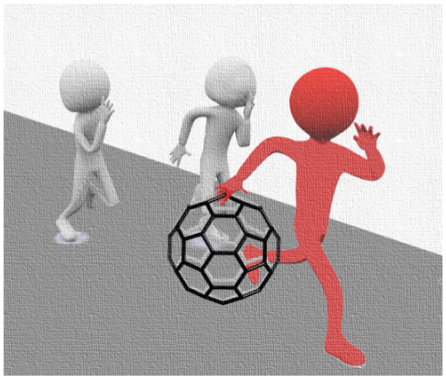

CHAPTER 2

Goals of this Thesis

UNIVERSITAT ROVIRA I VIRGILI
COMPUTATIONS ON FULLERENES: CHARACTERIZATION, REACTIVITY AND GROWTH
Laura Abella Guzman

CHAPTER 2

Goals of this Thesis

Thanks to experiments and computations working together, research on fullerenes has significantly advanced during the last few years. Most part of our research has been carried out in collaboration with different experimental groups. We aimed to understand and rationalize their experiments on fullerenes. Thus, we designed several models and strategies in order to achieve these goals, which are specifically described below.

Chapter 4 | Growth of Endohedral Metallofullerenes

This work has been done in collaboration with Prof. Harry Kroto and Prof. Paul Dunk (Florida State University) and Prof. Luis Echegoyen (University of Texas at El Paso).

The formation of fullerenes has become one of the main interests in the scientific community since their discovery. Thus, the experimental detection of new families of endohedral metallofullerenes ($Ti@C_{2n}$, $Sc_2C_2@C_{2n}$ and $Sc_3N@C_{2n}$) aroused us the curiosity of their growth. Although it was quite a challenge, we undertook with enthusiasm this project. The main objectives were:

- ✗ Understand how $M@C_{2n}$ (M = metal or metal cluster) families are formed.
- ✗ Propose a possible process of fullerene formation mechanism based on C_2 insertions into the most favourable isomers for each size by making use of the DFT methodology.

- ✗ Analyze the potential energy surface associated with the successive C_2 ingestions and the topologies of the involved structures.

- ✗ Reproduce the endofullerene formation shown in experiments by making use of the Car-Parrinello molecular dynamics.

- ✗ Compare our proposed process of growth against the top-down mechanism.

Chapter 5 | Identifying an Extended Oxide Clusterfullerene Family

This work has been done in collaboration with Prof. Ning Chen (Soochow University at Suzhou).

The detection and isolation of new metallofullerenes, $Sc_2O@C_{2n}$, by Prof. Chen at Soochow University encouraged us to perform a computational study for the characterization of new isomers. The main goals in order to rationalize and characterize the species detected were:

- ✗ Validate the ionic model for the oxide clusterfullerenes.

- ✗ Explore the most appropriate cage for $Sc_2O@C_{76}$, $Sc_2O@C_{80}$, and $Sc_2O@C_{82}$.

- ✗ Simulate the absorption spectrum and the electrochemical properties for the $Sc_2O@C_{2n}$ family.

- ✗ Analyze the movement of Sc_2O cluster in different C_{2n} cages at room temperature and temperature of fullerene formation.

- ✗ Identify the most favorable structure for $Sc_3O@C_{80}$ and explain its electronic structure and its low abundance in experiments.

Chapter 6 | On the Formation of Chlorofullerenes

This work has been done in collaboration with Prof. Su-Yuan Xie (Xiamen University).

After the synthesis and detection of some chlorinated fullerenes by Prof. Xie group at Xiamen University, we decided to start a new project working with these exohedral

fullerenes. Their formation and the reason of the chlorinated sites were our main curiosities. Thus, we aimed to:

- ✗ Find the main factors that take place in fullerene chlorination.
- ✗ Identify why some cages are or not chlorinated.
- ✗ Analyse the effect of the temperature in the formation of chlorofullerenes.
- ✗ Explain why chlorine atoms are attached in the corresponding sites in C_1-$C_{74}(14049)Cl_{10}$.
- ✗ Study the formation mechanism for the doubly functionalized cage C_{2v}-$C_{78}Cl_6(2)(C_5Cl_6)$ based on static DFT methodology and Car-Parrinello MD simulations.

UNIVERSITAT ROVIRA I VIRGILI
COMPUTATIONS ON FULLERENES: CHARACTERIZATION, REACTIVITY AND GROWTH
Laura Abella Guzman

CHAPTER 3

Computational Methods

UNIVERSITAT ROVIRA I VIRGILI
COMPUTATIONS ON FULLERENES: CHARACTERIZATION, REACTIVITY AND GROWTH
Laura Abella Guzman

CHAPTER 3

Computational Methods

This work is based on theoretical and computational chemistry, which is fundamental in the elucidation of structures and properties of fullerenes. The fast evolution of the improvements in computer hardware, and the algorithms and mathematical techniques gave rise to a new way of doing science besides experimental and theoretical studies, thus the computational science emerged. This chapter contains a brief description of the methodologies used in this Thesis.

3.1. Introduction

Computational chemistry is simply the application of chemical, mathematical and computing skills to the solution of interesting chemical problems, such as properties of molecules or simulated experimental results. There are three different methodologies: *ab initio*, semi-empirical and molecular mechanics methods. In developing this work, we used the first one that is based on solving the Schrödinger equation. So, we discarded to use semi-empirical methods that are based on the Hartree-Fock formalism with some empirical parameters obtained from experimental works, and molecular mechanics methods, which are based on the classical physics to predict the behaviour of the atoms and molecules.

The computer codes used are mainly the Amsterdam Density Functional (ADF) and the Car-Parrinello Molecular Dynamics (CPMD),[1] whose methodology is an approach to

perform *ab initio* molecular dynamics (AIMD). Both methods are based on Density Functional Theory (DFT) methodology[2] in order to achieve the best balance between accuracy and computational cost.

3.2. Density Functional Theory (DFT)

Nowadays, the Density Functional Theory is the most used methodology to study molecular systems of medium and large size with metal atoms. Hohenberg and Kohn (HK) proposed this methodology in 1964. The basis for DFT is the proof by them that the ground state electronic energy is determined completely by the electron density ρ. In other words, there exists a one-to-one correspondence between the electron density of a system and the energy.[2] Two theorems were enunciated:

"Any observable magnitude of a stationary non-degenerated ground state can be calculated exactly from its electronic density."

"The electronic density of a stationary non-degenerated ground state can be calculated exactly determining the density that minimizes the energy of the ground state."

DFT is based on the electronic density, not the wave function.[2] The significance of the HK theorems is perhaps best illustrated by comparing it with the wave function approach. A wave function for an *N* electron system contains 4*N* variables; three spatial and one spin coordinates for each electron. The electron density is the square of the wave function, integrated over *N*-1 electron coordinates and each spin density only depends on three spatial coordinates, independent of the number of electrons. With an increase of the *N* number, or size system, the complexity of the wave function increases too, while the electron density maintain the same number of variables. The problem is that, however, different electron density produces different ground state energy, the functional connecting these two parameters is not well known: designing it is the goal of DFT methods.[3,4]

The application of self-consistent methodology to the DFT, developed by Kohn and Sham in 1965, has emerged as an important first-principles computational method to predict chemical properties accurately and to analyse and interpret these in convenient and simple chemical terms. This success is based on the suggestion that the electron kinetic energy should be calculated from an auxiliary set of orbitals used for representing the electron density.[5] The exchange-correlation energy, E_{xc}, is the only unknown functional, and even relatively crude approximations for this term provide

quite accurate computational models. So, the problem is how to calculate the part of energy that comes from this exchange-correlation potential. Good approximations to the exchange-correlation energy are required. The energy expression can be written as equation 1. Exact kinetic energy functional calculated from the Slater determinant is denoted by T_S, the Coulomb repulsion energy is given by J[ρ], and nuclei-electron energy is written by E_{Ne}[ρ].

$$E_{DFT}[\rho] = T_s[\rho] + E_{Ne}[\rho] + J[\rho] + E_{xc}[\rho] \quad \text{(Eq.1)}$$

There exist several approximations, the simplest one, but a very useful, is the Local Density Approximation (LDA). At the next level the so-called non-local or Generalized Gradient Approximations (GGA) is found. An improved version of the latter is the meta-GGA approximation.

In the LDA it is assumed that the density locally can be treated as a uniform electron gas, or equivalently that the density is a slowly varying function. Contributions to the correlation and to the exchange are usually treated separately. The exchange energy for a uniform electron gas is given by the Dirac formula.

$$E_X^{LDA}[\rho] = -C_X \int \rho^{4/3}(r)\, dr \quad \text{(Eq.2)}$$

Various possibilities exist for the correlation energy. This LDA approximation works very well in systems in which the density is maintained approximately constant. For atoms and molecules where the density variations are important, uniform electron gas approximation in infinitesimal volumes is applied. It is assumed that the exchange-correlation effects are local and depend only on the value of electron density at each point.

When the α and β densities are not equal, the Local Spin Density Approximation (LSDA) replaces LDA. Therefore, the energy is reformulated as equation 3.

$$E_X^{LSDA}[\rho] = -2^{1/3} C_X \rho^{1/3} \int [\rho_\alpha^{4/3} + \rho_\beta^{4/3}]\, dr \quad \text{(Eq.3)}$$

The evolution of LDA to GGA is marked by the aim of introducing density gradients $\nabla\rho(r)$ into the description of exchange and correlation effects. This takes into account the value of the density at each point and how it varies around each point. One of the earliest and most popular GGA exchange correction was proposed by Becke (B or B88).[6] Regarding to the correlation part, the functional of Perdew,[7] and that of Lee, Yang, and Parr are among the most popular ones.[8]

Potentially more accurate than the GGA functionals are the meta-GGA. In this sort of functionals the exchange-correlation energy functional contains not only the density

and its gradient, but also the kinetic energy density $\tau(r)$, or the Laplacian of the density $\nabla^2\rho(r)$.

Another improvement of the exchange-correlation functionals has derived in the development of the hybrid GGA functionals. The exchange part of this exchange-correlation potential is in these hybrid models the exact exchange of the HF method. In contrary, the correlation part comes from the DFT treatment. This makes that these methods are a hybrid between DFT and HF. The problem is that the HF exchange potential does not take into account the dynamical correlation, so a new term of dynamical correlation must be added into the functional and this is made through the adiabatic connection. There are several functionals that have been reported since now such as O3LYP and B3PW91,[9] though the most popular is B3LYP.[10]

3.3. Molecular Dynamics (MD)

Molecules cannot be always represented by static structures, many of these and their properties are in fact "dynamic". Molecular dynamics methods are deterministic simulations and their properties are calculated as time averages. Moreover, it determines a trajectory that specifies how the position and the velocities of the particles vary with the time, by integrating the equations of motion: Newton's equations. The ratio and the direction of atoms movement is determined by forces, which can be calculated in two ways:

Classical Mechanics → Classical Molecular Dynamics

Quantum Mechanics → *Ab Initio* Molecular Dynamics

Classical Mechanics methods are based on balls and springs model, so atoms are represented by balls (softness), and bonds are springs (stiff). It is a model without electrons, so Schrödinger equation cannot be solved. In contrast, Quantum Mechanics methods deal with electrons, solving the Schrödinger equation, i.e. considering the electronic structure.

To develop this study we decided to work with *Ab Initio* MD (Car-Parrinello MD) because:

- In the course of the fullerene formation, the electronic structure/bonding pattern changes importantly.

- We deal with systems at very high temperatures/pressures for which no experimental data is available.
- Our systems are small (maximum ninety carbon atoms).
- The systems need to be treated in a rigorous and accurate way.

3.4. Ab Initio Molecular Dynamics (AIMD)

The basic idea of every *ab initio* molecular dynamics method is to compute forces acting on the nuclei from electronic structure calculations that are performed "on-the-fly" as the molecular dynamics trajectory is generated. The electronic variables are considered to be active and explicit degrees of freedom in the course of the simulation.[5,11]

Assuming that the Born-Oppenheimer approximation holds (electrons are moving in the field of fixed nuclei), *ab initio* molecular dynamics (AIMD) can be viewed as a series of DFT calculations at different instants of time, each one for a different set of atomic positions $\{R_N\}$. The basic AIMD procedure consists of repeating two main steps:[12]

- ✗ For a given set of atomic coordinates $\{R_N\}$, the total energy E^{DFT} is calculated by minimizing the density functional.
- ✗ The Newton's equations of motion are solved to obtain the new nuclear coordinates.

3.5. Car-Parrinello Molecular Dynamics (CPMD)

A first-principles molecular dynamics (MD) simulation will generate a trajectory of our initial coordinates by propagating this starting set of coordinates and velocities according to Newton's second law equation, using an "on-the-fly" calculated DFT potential energy, by a series of finite time steps. When using direct dynamics with electronic structure methods one needs a very well converged wave function at each time step and this makes the procedure computationally expensive, the so-called Born-Oppenheimer molecular dynamics (BOMD). This is required to accomplish energy conservation over the whole simulation length.

The improvement made by Car and Parrinello (CP) shows that it is not necessary to fully converge the wave function in each time step. After having determined a converged wave function at the first point, the essence of Car-Parrinello method is to

let the orbitals evolve simultaneously with the changes in nuclear positions. This can be achieved by including the wave function parameters as variables with fictitious masses in the dynamics, analogous to the nuclear positions and masses. Since this involves generalized variables, the Lagrange functions for describing the evolution of a system with both "real" (nuclear/electronic) and "fictitious" (method parameters) degrees of freedom is quite general, and is for example also used in force field methods incorporating fluctuating charges and/or polarization.

The CP method is a kind of *ab initio* MD approach where the electrons are treated quantum mechanically while the nuclear motion is treated classically. The latter implies that for example zero point vibrational effects are not included, nor can nuclear tunnelling effects be described; this requires fully quantum methods.

The simulation time step for CP simulation is shorter (0.1-0.2 fs) compared to BOMD (0.5-2 fs), in order to describe properly the faster movement of the electrons.[11,13]

Therefore, the basic CPMD procedure is the same as for AIMD, except that:[12]

- The electronic energy only needs to be calculated at the beginning of the simulation, because the electrons also evolve in time, following the nuclear motion.
- The equations of motion have to be integrated for both nuclei and electrons.
- In each MD step we obtain a new set of orbital coefficients, besides the new nuclear positions.
- In a Car-Parrinello MD, it is computationally convenient to use plane waves (PW) as the basis set in which the Kohn and Sham (KS) orbitals are expanded. Plane waves require the use of pseudopotentials to describe the effect of the core electrons.[12]

3.6. Metadynamics

Metadynamics is a novel molecular dynamics based technique aimed at enhancing the sampling of the phase space and at estimating the free energy landscape.[14,15] The algorithm is based on a dimension reduction, defining a set of *collective variables* (*s*) which enclose the essential modes associated with the transitions in the analysed process.

Let us consider a system of atomic coordinates *x*, which is moving under an interatomic potential V(*x*), Figure 1. In a standard molecular dynamics simulation the system is oscillating in one of the minima of the energy surface and the crossing to the other

minima is rather unlikely, because the barrier is higher than the thermal energy (1/2 k_b T). In order to accelerate the exploration of the phase space we can use metadynamics. This technique is based on defining a collective variable s which is an explicit function of a subset of coordinates *x'* [*s* = f(*x* ')], i.e. a distance or a coordination number.

The metadynamics simulation starts in one of the minima of the energy surface. At the beginning of the simulation the force acting on the system is given by the gradient of the potential V, see eq. 4:

$$f_i^V = -\frac{\partial V}{\partial r_i} \quad \text{(Eq.4)}$$

After a time interval *t'*, a small Gaussian-like repulsive potential term (V') is added, centred at the value of *s* at time *t'* (Figure 1b). This is repeated every time interval *t'* along the MD simulation, such that at a time *t* the total potential is the sum of the interatomic potential V and the sum of the V' terms added up to that time, see eq. 5 and 6:

$$V_T = V + V_G \quad \text{(Eq.5)}$$

$$V_G = \sum_{t'} w \exp\left(-\frac{[s(t)-s(t')]^2}{2(\Delta s)^2}\right) \quad \text{(Eq.6)}$$

where *w* is the height of the Gaussian potential term, Δs is its width and V_G is the history-dependent potential (i.e. the number of Gaussian terms added depends on the time passed). As a consequence, the force acting on the system is now the sum of V and V_G, equation 7:

$$f_i^{V_r} = f_i^V + f_i^{V_G} = -\frac{\partial V}{\partial r_i} - \frac{\partial V_G}{\partial r_i} \quad \text{(Eq.7)}$$

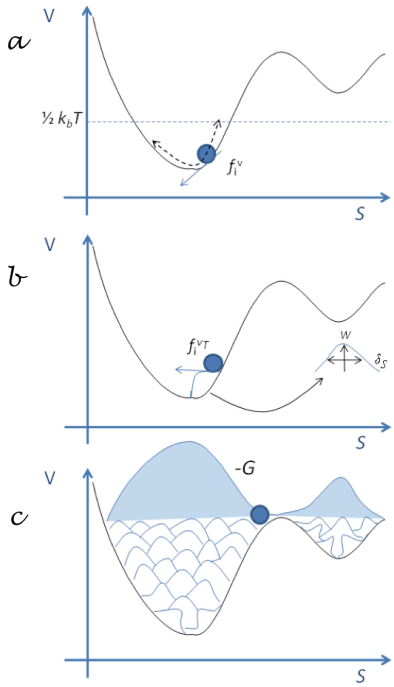

Figure 1. a) Standard molecular dynamics simulation. The system evolves following the interatomic potential V, and thus the force acting on the system is f_i^V (eq. 4). b) Metadynamics simulation. The system evolves following the modified potential (eq. 5), and thus the force acting on the system is $f_i^{V_T}$ (eq. 7). c) End of metadynamics and reconstruction of the free energy surface (G).

The added potentials V' progressively counterbalance the underlying free energy (Figure 1), thus penalizing the regions of the phase space already explored. As a result, the system tends to escape from already visited points to another energy minimum through the nearest and lowest-in-energy transition state. Hence, *metadynamics can accelerate the exploration of the phase space and the observation of rare events*. In other words, provided that the collective variables are properly chosen, the system will evolve by the same pathway that would have explored in a longer standard molecular dynamics.

3.7. Thermochemistry

Gibbs free energy (G), needed to take into account the thermal effects on the stability of fullerene cages, is defined in terms of entropy (S) and enthalpy of the system (H),

where G = H – TS. The entropy and the enthalpy of a set of particles can be determined through the statistical mechanics by means of the partition function. The partition function for one particle is denoted by *q* and is defined as the sum of the exponential terms with all possible quantum states (equation 8). For an N particle system, the partition function is *Q* (equation 9 and 10).

$$q = \sum_{i=states}^{\infty} e^{-\varepsilon_i/kT} \quad \text{(Eq.8)}$$

$$Q = q^n \quad \text{(Eq.9)}$$

$$Q = \frac{q^n}{N!} \quad \text{(Eq.10)}$$

The partition function can also be described as a sum of the energy levels by introducing the *g* degeneracy factor.

$$q = \sum_{i=levels}^{\infty} g_i \, e^{\varepsilon_i/kT} \quad \text{(Eq.11)}$$

Thermodynamic functions as the enthalpy (H), entropy (S), and Gibbs free energy (G) can be calculated:

$$H = U + PV = kT^2 \left(\frac{\partial \ln Q}{\partial T}\right)_V + kTV \left(\frac{\partial \ln Q}{\partial V}\right)_T \quad \text{(Eq.12)}$$

$$S = \frac{U-A}{T} = kT \left(\frac{\partial \ln Q}{\partial T}\right)_V + k \ln Q \quad \text{(Eq.13)}$$

$$G = H - TS = kTV \left(\frac{\partial \ln Q}{\partial V}\right)_T - kT \ln Q \quad \text{(Eq.14)}$$

If we assume that the energy can be written as a sum of terms, the partition function can be described as a dot product of terms:

$$\varepsilon_{tot} = \varepsilon_{trans} + \varepsilon_{rot} + \varepsilon_{vib} + \varepsilon_{elec} \quad \text{(Eq.15)}$$

$$q_{tot} = q_{trans} q_{rot} q_{vib} q_{elec} \quad \text{(Eq.16)}$$

For each partition function contributions, the sum over all the quantum states is done. However, the partition functions, due to their negative exponential form can be truncated.

3.8. Construction of all the C_{2n} Cage Isomers

All geometries of carbon cages developed in this work are obtained using the *fullgen code* by Gunnar Brinkmann. Using this code, we are capable of creating all sizes of cages with the appropriate symmetries and the sorting according to the spiral algorithm.[16,17]

3.9. Computational Details

Both electronic structure calculations and molecular dynamics simulations have been performed in the present work. Regarding to the electronic structure calculations, we used the program Amsterdam Density Functional (ADF code).[18,19] The electronic density was provided by the local density approximation using Becke's[6,20] gradient corrected exchange-correlation functional, and Vosko, Wilk, Nusair (VWN)[21] parametrization for correlation, corrected with Perdew's functional (BP86). Electrons for all atoms were described with Slater-type basis function of triple-ζ polarization quality. We have included scalar relativistic corrections by means of the zeroth-order regular approximation (ZORA) formalism.[10] Some calculations have also been performed including dispersion corrections by the method of Grimme.[22]

The MD simulations have been performed by means of the CPMD program.[1,23] The description of the electronic structure is based on the expansion of the valence electronic wave functions into a plane wave basis set, which is limited by an energy cutoff of 40 Ry. The interaction between the valence electrons and the ionic cores is treated through the pseudopotential (PP) approximation (Martins-Troullier type). PBE was selected as density functional. In simulations with Ti and Sc atoms, we had to include the nonlinear core corrections (NLCC) in the Martins-Troullier PP. We use a fictitious electron mass of 800 a.u. The Nosé-Hoover thermostat for the nuclear degrees of freedom was used to maintain the temperature as constant as possible. In all simulations, the wave function is converged at the beginning of the MD run. Most of the simulations were carried out in a cubic cell with a side length of 15 Å. Periodic boundary conditions were used in all simulations.

Most simulations have been done in three main steps: initialization, equilibration and production. The first one starts the dynamics at one temperature. The second step is equilibration, we maintain the temperature and we want to stabilize the energy. Once stabilized energy, third step is production where temperature is kept constant and the system evolves to each a minimum of energy. The time of each simulation is not the same; it depends on cluster size, type of dynamics or time for equilibration.

The "fictitious" kinetic energy of the electrons is a parameter that has to be controlled in a Car-Parrinello simulation. If it does not oscillate around a constant value, the Car-Parrinello approximation is not valid. We have checked this point in all of our simulations (Figure 2). On the other hand, temperature oscillates around a target value during an NVT Car-Parrinello MD simulation using the Nosé-Hoover thermostat (see for example Figure 2, right).

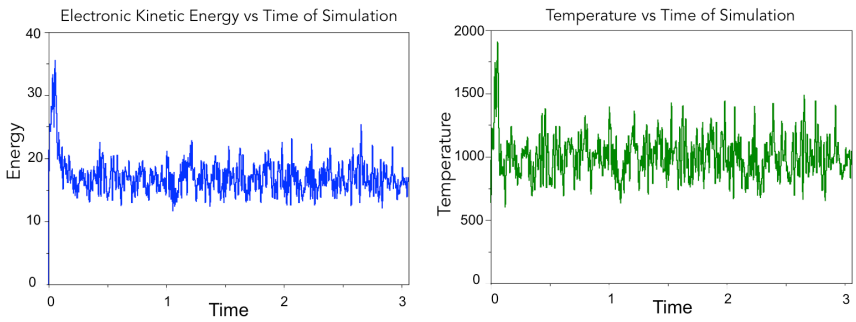

Figure 2. (left) "Fictitious" kinetic energy (in kcal·mol^{-1}) of the electrons during one MD simulation (time in ps). (right) Temperature (in Kelvin) in the course of dynamics (time in ps).

3.10. References

(1) CPMD. http://www.cpmd.org./; Copyright IBM Corp. 1990– 2015, Copyright MPI für Festkörperforschung Stuttgart 1997-2001.
(2) Jensen, F. *Introduction to Computational Chemistry*, Wiley, 1999.
(3) Parr, R. G.; Yang, W. *Density Functional Theory*, Oxford Univ. Press, Oxford (UK), 1989.
(4) Koch, W.; Holthausen, M. *A Chemist's Guide to Density Functional Theory*, Wiley-VCH, 2000.
(5) Marx, D.; J., H. *Ab initio Molecular Dynamics: Basic Theory and Advanced Methods* Cambridge Univ. Press, Cambridge (UK), 2009.
(6) Becke, A. D. *Phys. Rev. A* 1988, *38*, 3098.
(7) Perdew, J. P. *Phys. Rev. B* 1986, *33*, 8822.
(8) Lee, C. T.; Yang, W. T.; Parr, R. G. *Phys. Rev. B* 1988, *37*, 785.
(9) Becke, A. D. *J. Chem. Phys.* 1993, *98*, 1372.
(10) Becke, A. D. *J. Chem. Phys.* 1993, *98*, 5648.
(11) Marx, D.; Hutter, J. *NIC Series* 2000, *1*, 301.
(12) Alfonso, M., PhD Thesis "Study of the Reactivity of Catalases by Means of Ab Initio Molecular Dynamics", Universitat Autònoma de Barcelona, 2009.
(13) Vilà, L., PhD Thesis "Assembly and Properties of Polyoxometalates: A Theoretical Point of View", Universitat Rovira i Virgili, 2011.
(14) Laio, A.; Parrinello, M. *Proc. Natl. Acad. Sci. USA* 2002, *99*, 12562.
(15) Laio, A.; Gervasio, F. L.; VandeVondele, J.; Sulpizi, M.; Rothlisberger, U. *J. Phys. Chem. B* 2004, *108*, 7963.
(16) Brinkmann, G.; Goedgebeur, J.; McKay, B. D. *J. Chem. Inf. Mod.* 2012, *52*, 2910.
(17) Brinkmann, G.; Delgado-Friedrichs, O.; Lisken, S.; Peeters, A.; Cleemput, N. V. *Match-Commun. Math. Co.* 2010, *63*, 533.
(18) Baerends, E. J.; Ellis, D. E.; Ros, P. *ADF 2013.01; SCM:Amsterdam* 2013.
(19) Velde, G. t.; Bickelhaupt, F. M.; Baerends, E. J.; Guerra, C. F.; Gisbergen, S. J. A. v.; Snijders, J. G.; Ziegler, T. *J. Comput. Chem.* 2001, *22*, 932.
(20) Becke, A. D. *J. Chem. Phys.* 1986, *84*, 4524.
(21) Vosko, S. H.; Wilk, L.; Nusair, M. *Can. J. Phys.* 1980, *58*, 1200.
(22) Grimme, S.; Ehrlich, S.; Goerigk, L. *J. Comput. Chem.* 2011, *32*, 1456.
(23) Car, R.; Parrinello, M. *Phys. Rev. Lett.* 1985, *55*, 2471.

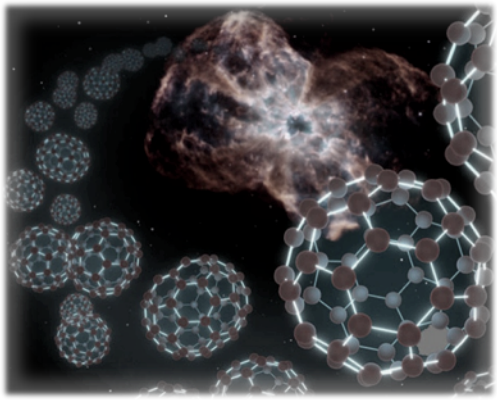

CHAPTER 4

Growth of Endohedral Metallofullerenes

Related Publications:

Small Endoheral Metallofullerenes: Exploration of the Structure and Growth Mechanims in the Ti@C_{2n} (2n=26-50) Family
Mulet-Gas, M.; Abella, L.; Dunk, P. W.; Rodríguez-Fortea, A.; Kroto, H.; Poblet, J.M. *Chem. Sci.* **2015**, 6, 675.

A Zigzag Sc_2C_2 Carbide Cluster inside a [88]Fullerene Cage with One Heptagon $Sc_2C_2@C_s$(hept)-C_{88}: A Kinetically-Trapped Fullerene Formed by C_2 Insertion?
Chen, C.H.; Abella, L.; Cerón, M. R.; Guerrero-Ayala, M.; Rodríguez-Fortea, A.; Olmstead, M. M.; Powers, X. B.; Balch, A.; Poblet, J. M.; Echegoyen, L. *J. Am. Chem. Soc.* **2016**, 138, 13030.

Transformation of Graphite into Cluster-Encapsulated Cages
Mulet-Gas, M.; Abella, L.; Cerón, M. R.; Castro, E.; Marshall, A. G.; Rodríguez-Fortea, A.; Echegoyen, L.; Poblet, J. M.; Dunk, P. W. *Nat. Commun.* **2017** (in press).

CHAPTER 4

Growth of Endohedral Metallofullerenes

Since the discovery of fullerenes, tremendous advances have been made in the field of nanoscience. However, the formation of these molecules still remains as a mystery. Several hypothetical models have been established to elucidate their formation from graphite or amorphous carbon, but none of them are strictly convincing. During the last few years, many experiments of fullerene growth have been developed. Thus, it allowed us to study their formation accurately. This chapter gives support to the bottom-up mechanism as a model of fullerene formation. This is part of the work in collaboration with the experimental groups of Prof. Dunk at the Florida State University (FSU) and Prof. Echegoyen at University of Texas at el Paso (UTEP).

4.1. Introduction

Since the discovery of C_{60} in 1985 by applying laser technology for the evaporation of graphite,[1] tremendous advances have been made in the science of fullerenes and related compounds. Although soon after the discovery of C_{60} the first endohedral fullerene La@C_{60} was detected,[2] the characterization in 1999 of a Sc_3N inside a cage with 80 carbons represented a qualitative change in the science of this new family of compounds; $Sc_3N@I_h$-C_{80} was found as the third most abundant fullerene after C_{60} and C_{70}.[3] During the last twenty years, the number of known endohedral fullerenes has been constantly growing and carbon cages are able to encapsulate trimetallic nitrides, metallic oxides, metallic sulfides, metallic carbides, as well as up to three individual metal atoms.[4-9] Electron transfer from the internal cluster to the carbon cage, which

preferentially concentrates on the pentagonal rings, together with the maximum separation of the twelve pentagons and the metal-cage interaction in non-IPR cages, help to understand and predict the observed endohedral compounds.[10,11] It is worth mentioning that despite the complexity of the presumed formation mechanisms, in general the observed and predicted cages always coincide, and that the most favourable *thermodynamic* isomer is usually observed.

In all synthetic procedures of carbon nanoforms, carbon needs to be exposed to very high temperatures,[12-14] and the condensation process of carbon units seems to play a crucial role for the self-assembly of the fullerene cages.[15-17] Several models have been suggested to explain the formation of fullerenes, as shown in the Introduction. Top-down formation proposals have been predominantly advanced to explain fullerene synthesis over the past decade.[18-21] On the basis of mass spectrometry information from previous experiments, fullerenes are believed to be in formation from atomic carbon or small clusters. In 2012, Kroto *et al.* shed new light on the fundamental processes that govern self-assembly of carbon networks, showing that fullerenes self-assemble through a closed network growth (CNG) mechanism by incorporation of C_2 and atomic carbon.[22] C_2 molecule has been confirmed to play the most important role in fullerene growth, as deduced from experimental and theoretical results. Endo and Kroto advanced the mechanism of C_2 ingestion in 1992 (Figure 1).[23] According to this, the growth process is the transformation from one hexagonal ring into two fused pentagonal rings by insertion of a C_2 unit. One drawback of this model would be that the new fullerene violates the isolated pentagon rule, but fullerenes below C_{60} cannot obey this rule. In other words, small fullerenes can be obtained by C_2 insertion according to Figure 1, but larger fullerenes need at least one bond rearrangement to achieve an IPR structure.

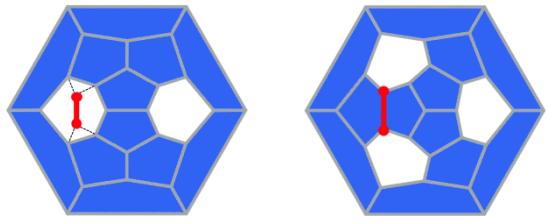

Figure 1. Schlegel representation of D_{3h}-C_{26}(1) and T_d-C_{28}(2) showing that the latter can be obtained from the former by ingestion of a C_2 unit (red) as proposed by Endo and Kroto. Insertion does not take place in a single step, but through several intermediates.

Less is known about the formation of endohedral fullerenes. The origin of clusterfullerenes produced by plasma synthesis and associated formation processes remains unclear. However, it is more or less assumed that their formation mechanisms should not be rather different from those of empty cages. Bottom-up formation of empty cage fullerenes has been studied by laser-based plasma cluster source techniques.[24] Very recently, single metal-encapsulated cages or mono-metallofullerenes, $M@C_{2n}$ (M = metal), were investigated and a metal in the reaction path is found to dramatically alter self-assembly processes.[25]

Recently isolated structures suggest that either top-down or bottom-up mechanistic processes may explain their fullerene formation.[26] Interestingly, a heptagon-containing clusterfullerene, $Sc_2C_2@C_{88}$, was recently proposed to form by C_2 insertion into a known $Sc_2C_2@C_{86}$ cage.[27] The first characterized heptagon-containing metallofullerene, $LaSc_2N@C_{80}$, potentially can form by either carbon loss or gain.[28]

Understanding how endohedral metallofullerenes form is essential to solve the huge mystery unrevealed in this field until now. In this chapter, we study the growth of different endohedral metallofullerenes families by use of comprehensive quantum chemical investigations. In particular, we propose the bottom-up mechanism for the families studied of $Ti@C_{2n}$ (2n = 26-50),[29] $Sc_2C_2@C_{2n}$ (2n = 86-90)[30] and $Sc_3N@C_{2n}$ (2n = 68-80).[31]

4.2. Small EMFs: the $Ti@C_{2n}$ (2n=26-50) Family

The experimental detection of the new family of endohedral metallofullerenes $Ti@C_{2n}$ (2n = 26-50) is the starting point of this work (Figure 2). All of them are non-IPR isomers because of the impossibility of constructing an IPR cage with 12 pentagons surrounded by hexagons with less than 60 atoms. The FT-ICR-MS obtained shows that $Ti@C_{26}$ is the smallest detected cage, and $Ti@C_{28}$ and $Ti@C_{44}$ present the highest intensity and stability. Once computed all the possible isomers for each of the $Ti@C_{2n}$ detected, we started to analyse their formation step by step focused on the direct C_2 ingestion and, in few cases, subsequent structure rearrangements.

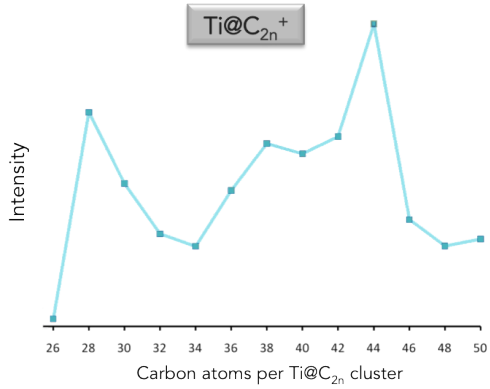

Figure 2. FT-ICR-MS spectra obtained by Kroto and co-workers for $Ti@C_{2n}^{+}$.[14]

4.2.1. The $Ti@C_{26}$ to $Ti@C_{28}$ Transformation

Kroto and co-workers, within their Closed Network Growth mechanism, proposed two possible paths to form C_{62} from C_{60} and C_2 insertion.[22] Both paths were investigated here for the transformation of $Ti@C_{26}$, the smallest EMF detected so far, to $Ti@C_{28}$, which could be the very first step in fullerene-to-fullerene conversion. In addition, this step can be accurately modelled and provides understanding for the transformations that take place for larger species. We found that direct C_2 ingestion into the only possible isomer of $Ti@C_{26}$ proceeds via a series of intermediates. The C_2 molecule can be inserted in one of the three equivalent hexagons that D_{3h}-C_{26}(1) has (Figure 1).

4.2.1.1. Free Energy Profile

The mechanism proposed by Kroto and co-workers is based on the fact that a C_2 molecule reacts to one [5,5,6] carbon atom of the selected hexagon, forming a first intermediate I1, in which the C_2 unit is attached to the $Ti@C_{26}$ surface through one C atom (Figure 3). In this first step, no transition state (TS) is found. The Gibbs free energy difference between I1 and reactants is -31 kcal·mol^{-1}, so C_2 attachment is a favourable process.

From the corresponding C_{62} intermediate, Kroto and co-workers proposed two pathways to reach the same product. In the current work, we focused on one of them, which was characterized to have the most stable intermediate. This second intermediate I2 contains a seven-membered ring and it was characterized by its huge stability. A transition state TS1, in which the attached C_2 unit is forming a C-C-C angle

of 134.3 degrees, was found to connect I1 and I2. The barrier to overcome this transition state is only 19 kcal·mol^{-1}.

The final step corresponds to the closure of the cage, where C_2 is finally inserted in the fullerene cage forming two fused pentagons in the original hexagon, as proposed by Endo and Kroto.[23] The free energy barrier to overcome this transition state TS2 is 106 kcal·mol^{-1} and the Gibbs free energy difference for this last step is -44 kcal·mol^{-1}. Although this barrier is rather large, it is rather easily overcome at the temperatures in which fullerenes are formed (> 1000 K). The entire insertion process is clearly exergonic (Figure 3). No significant differences existed in the free energy profile if dispersion corrections were included or not.

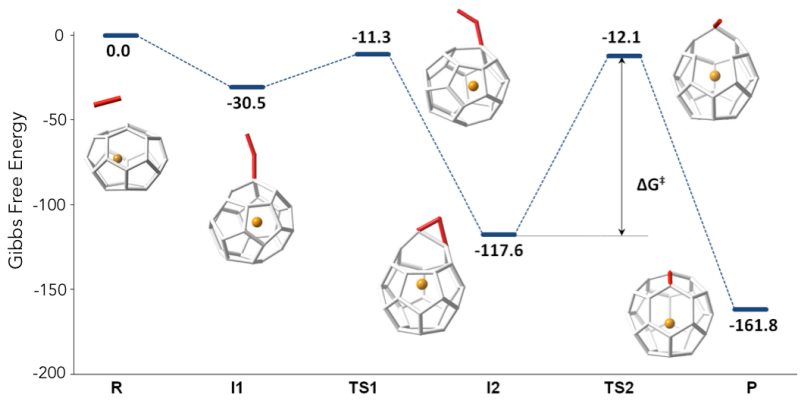

Figure 3. Gibbs free energy profile at 1000 K (in kcal·mol^{-1}) for the formation of Ti@C_{28} from Ti@C_{26} and C_2 ingestion.

The second path proposed by Kroto and co-workers was also studied.[22] The only difference with respect to the mechanism explained before was that a second intermediate with higher energy was found, I2'. In fact, for the Ti@C_{28} system under study, this stationary point was not a true intermediate, but a transition state that connected I2 and its symmetrical structure (Figure 4).

Gibbs free energy profiles at different temperatures between 1000 and 3000 K have been calculated to simulate the conditions in which fullerenes are formed. Similar shapes for the free energy profiles are obtained at different temperatures. Increasing temperature, however, the profiles are shifted to higher free energies with respect to

reactants, i.e. less exergonic, mainly due to the negative entropy change associated to the first step, from reactants to I1 (Figure 5).

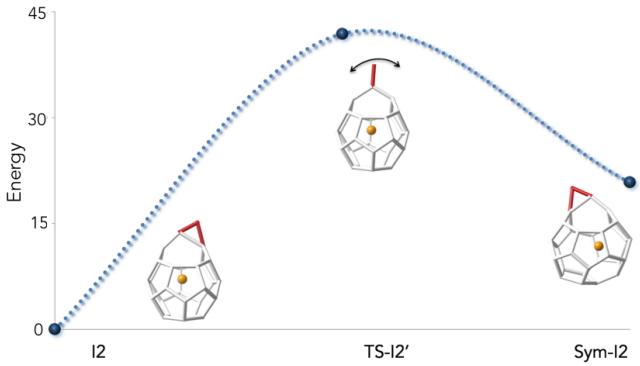

Figure 4. Energy profile (in kcal·mol^{-1}) for the pathway that connects I2 and its symmetrical structure, Sym-I2. The two structures are connected through transition state TS-I2'. The structures of I2, Sym-I2, and TS-I2' are also shown in the profile. For the TS-I2' structure, the arrow describes the motion of the C atom in the normal mode with the imaginary frequency.

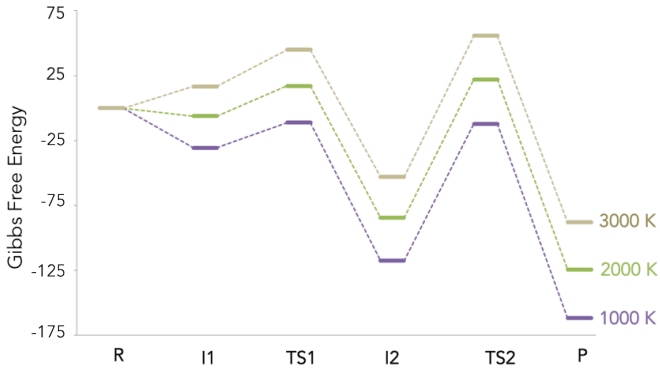

Figure 5. Gibbs free energy profiles (in kcal·mol^{-1}) at different temperatures (1000, 2000 and 3000 K) for the formation of Ti@C_{28} from Ti@C_{26} and C_2.

We have also studied the successive insertion of atomic carbon proposed by Kroto and co-workers as a second possible cage growth process for empty fullerenes.[22] Two carbon atoms were inserted separately into Ti@D_{3h}-C_{26} to form the Ti@C_{26}CC intermediate (Figure 6). The first carbon ingestion to a [5,5,6] carbon atom led to

intermediate Ti@C_{26}C I1', which presented a heptagon. There was no transition state in this step and the relative free energy at 1000 K with respect to reactants was -83 kcal·mol^{-1}. The subsequent C insertion took place on another [5,5,6] carbon atom and led to intermediate Ti@C_{26}CC I1'', which was characterized to have two heptagonal rings (Figure 6). The free energy of formation of I1'' with respect to I1' is -84 kcal·mol^{-1}. Intermediate I1'' showed at 1000 K somewhat lower free energy, 14 kcal·mol^{-1}, than the first intermediate from C_2 insertion mechanism I1. Once Ti@C_{26}CC I1'' was formed, structural rearrangement to form I2, the second intermediate found for C_2 insertion, might take place through transition state TS1' with a free energy barrier of 64 kcal·mol^{-1} at 1000 K. The last step from I2 to products was the same as for the C_2 insertion mechanism. Both paths are compared in Figure 6.

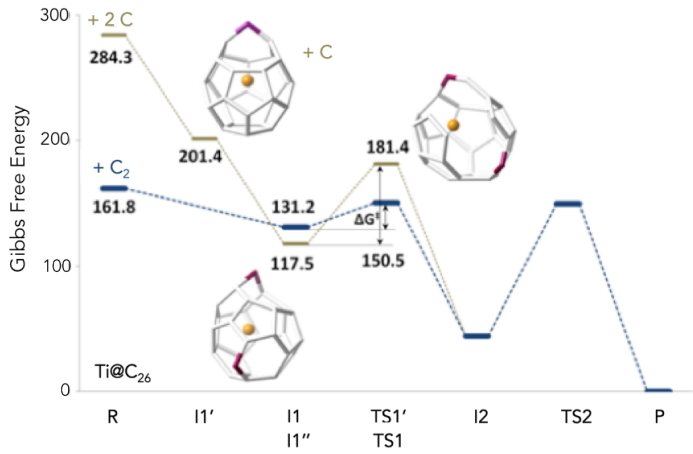

Figure 6. Free energy profiles at 1000 K (in kcal·mol^{-1}) for the formation of Ti@C_{28} from Ti@C_{26}. The profiles for the C_2 and the two successive C atom insertion mechanisms are represented with blue and grey lines, respectively.

4.2.1.2. Car-Parrinello MD Simulations

Besides the careful inspection of the potential energy surface and the free energy surfaces at different temperatures, we have gone beyond the *static* analysis by simulating the ingestion of a C_2 molecule in the Ti@C_{26} cage using Car-Parrinello molecular dynamics. The CNG mechanism, namely those structures shown in Figure 3,

was followed until I2, but any of the many simulated trajectories could overcome the second barrier associated to TS2.

I2 is a rather stable intermediate and could not evolve to product at the short time scale of our simulations (tens of ps). In fact, it was basically because the barrier to reach the product is around 100 kcal·mol^{-1} at 1000 and 2000 K. In some trajectories, we observed geometries near TS2, but the system had not enough energy to overcome the barrier and reach the product (movie M1). As a consequence, we deemed necessary to accelerate the dynamics at that point to observe such a rare event within our limited timescale of few ps.

On one hand, the metadynamics method was used, which also allowed us to estimate the free energy barrier for the rare event.[32-34] Several successful metadynamics runs at 1000 K using different initial conditions and different sets of collective variables, coordination numbers of the atoms involved in the bond formation or some of their C−C distances (Figure 7), provided an estimation for the free energy barrier of 104 kcal·mol^{-1}, in good agreement with the results obtained from the static electronic structure calculations.

In particular, for some metadynamics two coordination numbers (CN) are used. The first coordination number, CN 1, is involved in the [5,5] bond formation, and the second one, CN 2, follows the breaking of the triangular cycle. For other metadynamics runs, one C-C distance (DIST) is also used as collective variable (CV).

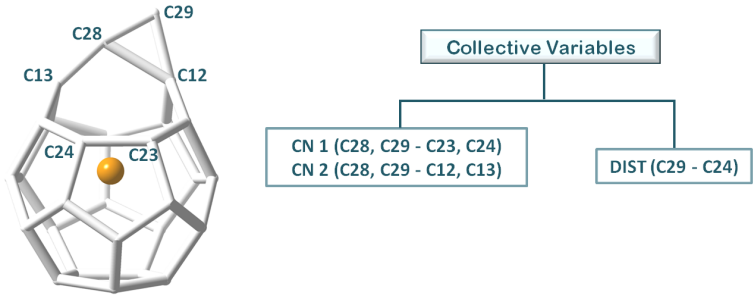

Figure 7. Sets of collective variables used in different metadynamics at 1000 K. Carbon atoms involved in the collective variables are labeled in the intermediate **I2**. Carbon atoms involved in each set are indicated next to the type of the CVs.

The presence of an inert gas is required for the synthesis of fullerenes.[22] Elucidating the role of this inert gas in EMF formation is important to gain insight about a likely

formation mechanism. Perturbations on intermediate I2 as a consequence of some external effects, as for example, collisions with the carrier gas (He or Ar atoms), as well as C_2 molecules or C atoms were also simulated. In a first and rougher approximation, the initial velocities of some C atoms, those involved in the cage closure, were increasingly modified as if they were activated by collisions with other atoms. At some point, we were able to observe the closure of the cage, that is, the formation of Ti@C_{28}.

We also simulated collisions between I2 and one atom of the carrier gas (He or Ar), a C atom or a C_2 molecule, at different initial conditions. Formation of the Ti@C_{28} cage was observed in most of the cases, but for collisions with a single C atom. In these cases, the atom was incorporated to the carbon framework, either forming a C–C stick attached to the cage like an "octopus leg" or forming a more closed Ti@C_{29} structure. Collisions with He atoms at velocities that were around 20000 m/s, i.e. kinetic energies around 9 eV, were seen to be successful to close the Ti@C_{28} cage (Figure 8 and movie M2). Even though a very tiny fraction of He atoms should present such high kinetic energies at 2000-3000 K according to the Maxwell-Boltzmann velocity distribution, we have to keep in mind that conditions during fullerene formation are far from equilibrium.

To know the velocity of the colliding atom (He or Ar), we plot its velocity along the trajectory (see Figure 8). The rather constant velocity just before the collision is arbitrarily considered to be its velocity (black circle in Figure 8).

In general, velocities of He atoms were found to be larger than Ar atoms for both processes growth and shrinkage (as expected for similar temperatures because He is much lighter than Ar).

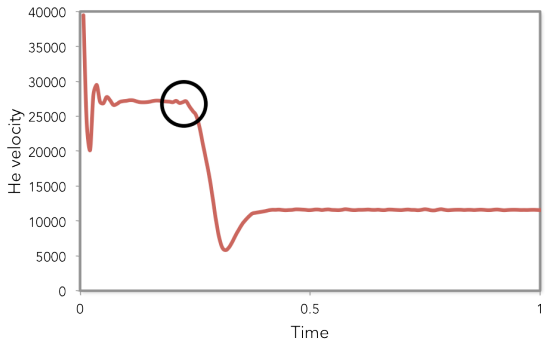

Figure 8. Variation of He velocity (in $m \cdot s^{-1}$) during the Car-Parrinello MD simulation. The time/velocity of the collision is represented by the black circle. Time in ps.

4.2.2. Closed Network Growth (CNG) Mechanism From C_{26} to C_{48}

According to the CNG formation of fullerenes, we propose a general mechanism for the growth of the cages from Ti@C_{26} to Ti@C_{48} based on successive C_2 ingestions, in analogy to that recently proposed by Zhao and Nagase for empty C_{2n} fullerenes,[35] based on the ideas of Fowler and Manolopoulos.[36] The growth mechanism, represented in Figure 9, relates the most abundant isomers for each Ti@C_{2n} family from 2n = 26 to 48 through simple C_2 insertions and, in some cases, Stone-Wales (SW) rearrangements. Minimization of pentagon adjacencies is not the sole criterion for EMFs growth because for larger carbon cages the stabilization due to charge transfer can reverse the relative stabilities.

The first step, shown in Figure 9, relates cages D_{3h}-C_{26}(1) and T_d-C_{28}(2). Once the C_2 is ingested into the hexagon, two fused pentagons are formed (the new bond is remarked in red in Figure 9). Next, insertion of an additional C_2 unit into the T_d-C_{28}(2) cage leads to the formation of C_{2v}-C_{30}(3). Further growth proceeds by inserting C_2 molecules successively to give D_3-C_{32}(6), C_2-C_{34}(5) and D_{2d}-C_{36}(14), as for the hollow cages.[35] This latter isomer is the second most abundant Ti@C_{36} after D_{6h}-C_{36}(15). These two cages are intimately related by a single SW rearrangement (the bond that rotates is marked in green in Figure 9 and the mechanism is shown in Figure 10 and movie M3). Although SW transformations show rather large free energy barriers, 111 kcal·mol^{-1} in the present case, they might be easily overcome at T > 1000 K. Moreover, previous theoretical and experimental reports find for hollow C_{60} that such rearrangements could be carbon-catalysed leading to atom exchange.[22,37,38] For Ti@C_{36}, the free energy barrier for the carbon-catalyzed transformation between cages D_{2d}-C_{36}(14) and D_{6h}-C_{36}(15) drops significantly to only 36 kcal·mol^{-1}. The insertion of a carbon atom in Ti@D_{2d}-C_{36}(14) cage leads to the first intermediate, INT-1, in the carbon-catalyzed bond rearrangement mechanism. Once the transition state is overcome, it reaches the second intermediate, INT-2 (Figure 10).Thus, carbon-catalysed bond rearrangements could be a process involved in metallofullerene formation. It is important to remark here that the two cages D_{2d}-C_{36}(14) and D_{6h}-C_{36}(15) yield, after C_2 insertion, the most abundant Ti@C_2-C_{38}(17) isomer. Ti@D_2-C_{40}(38) is then obtained and would evolve to Ti@D_3-C_{42}(45), the most abundant Ti@C_{42} isomer, after successive C_2 ingestions. That species then grows to Ti@D_2-C_{44}(75), which is the second most stable Ti@C_{44} isomer, but with almost zero molar fraction for the full range of temperatures compared to the most abundant Ti@D_2-C_{44}(89). An alternative formation path to reach Ti@D_2-C_{44}(89) is through the Ti@C_1-C_{42}(33) precursor, formed by SW rearrangement of the initially formed Ti@D_3-C_{42}(45) species. C_2 insertions into Ti@D_2-C_{44}(89) and Ti@D_2-C_{44}(75) lead to Ti@C_1-C_{46}(114) and Ti@C_2-C_{46}(109), respectively, which are among the most abundant Ti@C_{46} isomers at high temperatures, and are also related by a SW transformation. Additionally, Ti@C_1-

C_{46}(114) is related to the most abundant Ti@C_2-C_{46}(116) isomer by a single SW rearrangement. Finally, the two most abundant Ti@C_{48} isomers, Ti@C_1-C_{48}(196) and Ti@C_2-C_{48}(199), are formed by direct C_2 insertion into these Ti@C_{46} isomers. Therefore, the present mechanistic proposal relates the most abundant isomers of the Ti@C_{2n} series (2n = 26-48) by successive C_2 insertions and a few number of SW rearrangements, in line with the CNG mechanism.

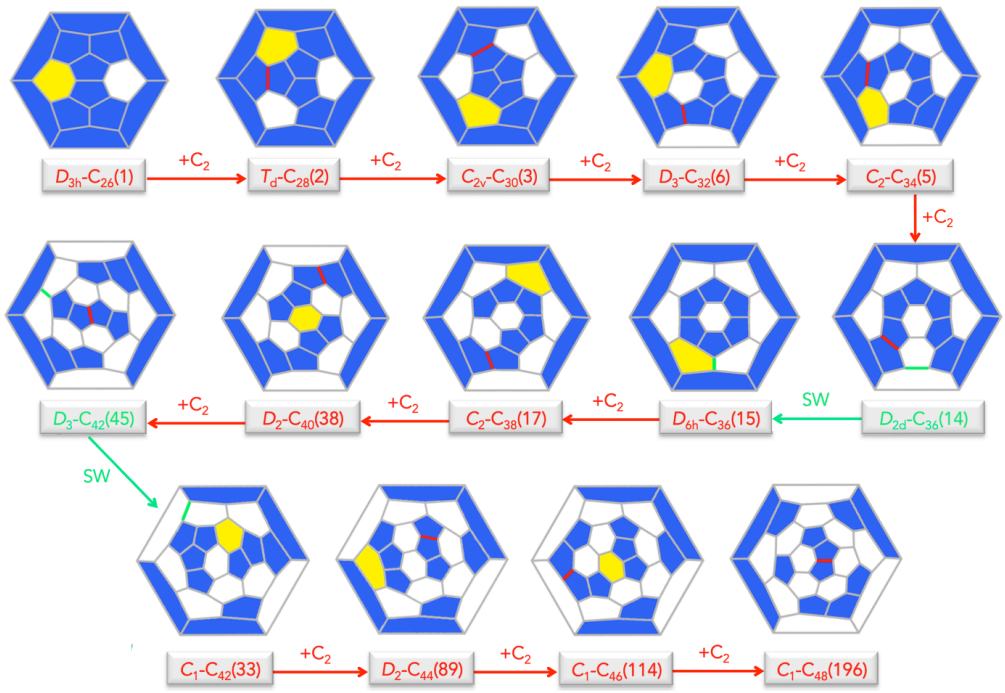

Figure 9. Schlegel diagrams connecting the most abundant isomers of each Ti@C_{2n} family. The hexagons where C_2 inserts are highlighted in yellow; the formed C-C bonds are in red and the bonds that rearrange (Stone-Wales) are in green. Most of the lowest-energy isomers are linked through a C_2 insertion and only few of them are related by Stone-Wales transformations (cages C_{36} and C_{42}).

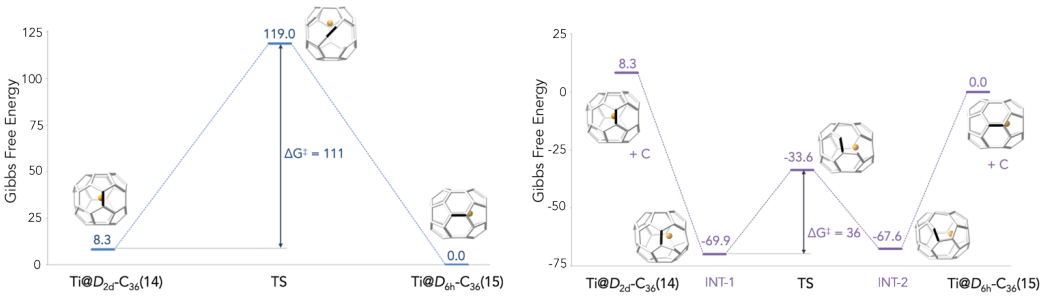

Figure 10. Gibbs free energy profiles (in kcal·mol^{-1}) comparing (left) the conventional Stone-Wales rearrangement, and (right) the carbon-catalyzed bond rearrangement leading to atom exchange. Stone-Wales transformations for Ti@D_{2d}-C_{36}(14) isomer to Ti@D_{6h}-C_{36}(15) isomer. All the geometries for both mechanisms are shown in the figure.

The stationary points and energetic profiles for these Ti@C_{2n} + C_2 → Ti@C_{2n+2} processes were also characterized (2n = 28-46). Free energy profiles are totally equivalent to that found for 2n = 26 (Table 1 and Figure 11). Analogous geometries for the intermediates, I1 and I2, and transition states, TS1 and TS2, were observed. In general, I2 is much more stable than I1 and the barrier (TS2) that connects I2 and product was much higher than the one that connects I1 and I2 (TS1). These barriers (50-100 kcal·mol^{-1}), while somewhat high, are attainable at temperatures larger than 1000 K.

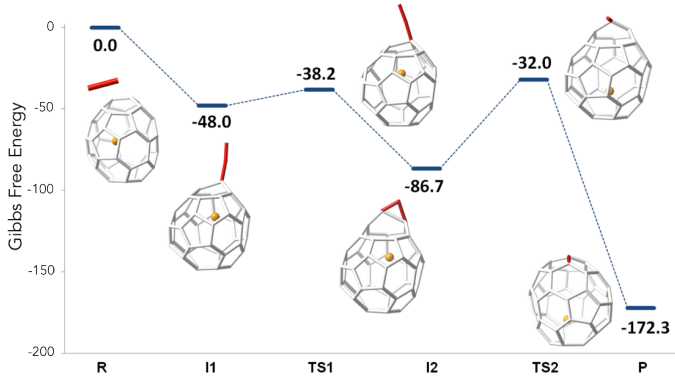

Figure 11. Gibbs free energy profile at 1000 K (in kcal·mol^{-1}) for the formation of Ti@C_{44} from Ti@C_{42} and C_2 ingestion. Free energy barrier, TS2, is found to be 54.7 kcal·mol^{-1} in this mechanism. All the intermediates, I1 and I2, and transition states, TS1 and TS2, which are shown in the profile, are equivalent to those found for Ti@C_{26} to Ti@C_{28}.

Interestingly, lower free energy barriers are found for larger cages. Free energy barriers from Car-Parrinello metadynamics calculations are in good agreement with static calculations (Table 1). Reaction free energies at 1000 K are around -150 kcal·mol^{-1} and show significant differences depending on the size of the cage. Low reaction free energies, in absolute values, might be related to those processes that have the most stable reactants. The less exergonic reaction energies were found for the formation of Ti@C_{30} and Ti@C_{46}. Therefore, Ti@C_{28} and Ti@C_{44} are predicted to be rather stable species.

The transition states and the associated free energy barriers for non-catalyzed and carbon-catalyzed SW transformations on different Ti@C_{2n} (2n = 36 and 42) were also characterized. We find that the barriers for these particular catalyzed processes can be readily overcome at the high temperature required for metallofullerene synthesis.

Table 1. Reaction energies and free energies for the Ti@C_{2n} + C_2 → Ti@C_{2n+2} processes.[a)]

$C_{2n} + C_2 \rightarrow C_{2n+2}$	$\Delta E(P)$[b)]	$\Delta E(I2)$[c)]	$\Delta E^{\ddagger}$[d)]	$\Delta G(P)$[e)]	$\Delta G(I2)$[e)]	$\Delta G^{\ddagger}$[e)]	$\Delta G(P)-\Delta G(I2)$[e)]	$\Delta G^{\ddagger}$[f)]
26→28	-207.4	-130.5	79.2	-161.8	-117.6	105.5	-44.2	104
28→30	-175.0	-115.8	83.6	-124.9	-72.3	83.7	-52.6	83
30→32	-190.7	-132.9	83.6	-130.4	-88.8	78.5	-41.6	76
32→34	-203.3	-122.5	61.6	-152.6	-81.3	63.5	-71.3	-
34→36	-197.6	-109.8	62.9	-153.1	-72.7	63.8	-80.4	-
36→38	-203.0	-115.5	34.5	-150.2	-73.1	41.9	-77.1	-
38→40	-198.8	-121.2	50.9	-153.4	-80.0	52.1	-73.4	-
40→42	-214.1	-126.3	50.0	-159.7	-78.7	50.2	-81.0	54
42→44	-218.8	-124.6	52.6	-172.3	-86.7	54.7	-85.6	61
44→46	-185.6	-100.7	62.4	-137.0	-58.5	60.0	-78.5	50
46→48	-201.4	-105.2	49.2	-151.2	-62.6	48.1	-88.6	-

a) See Figure 11 for the reaction profile. All energies are in kcal·mol^{-1}; b) Reaction energy for the process Ti@C_{2n} + C_2 → Ti@C_{2n+2}; c) Relative energy of intermediate with respect to reactants; d) Energy barrier corresponding to the step I2 → Product; e) Gibbs free energies at 1000K. f) Free energy barriers for the successful metadynamics.

4.2.3. CNG vs Shrinking Mechanisms

Insertions of C_2 to small C_{2n} cages (2n = 26-48) are thermodynamically favourable processes, as reaction free energies show (Table 1). The barriers for the CNG mechanism are easily attainable at the rather high temperatures of formation of fullerenes. As a consequence, shrinking of these small C_{2n} cages by loss of C_2 units are rather unfavourable endergonic processes. Moreover, if cage shrinking were to take place through the same mechanism as ingestion (Figure 11), significantly much larger barriers of around 140 kcal·mol^{-1} would have to be surmounted to reach I2. Therefore, from the free energy profiles at the formation temperatures of fullerenes, bottom-up growth by C_2 ingestion is thermodynamically (reaction free energies) and kinetically (free energy barriers) more favourable than top-down shrinkage by C_2 loss for these small Ti@C_{2n} fullerenes (2n = 28-48).

To gain more insight about the bottom-up and shrinking mechanisms, we have simulated the collisions of several Ti@C_{2n} (2n = 28, 30, 44 and 48) with the buffer gas (He or Ar) at different initial conditions. In this way we have accelerated the closure of the I2 intermediate in the bottom-up growth, and the extrusion of a single C atom for the top-down shrinkage. Both are key steps in the two mechanisms, but they are very rare events that cannot be observed by standard Car-Parrinello molecular dynamics simulations at the time scale (tens of ps) that we can simulate. To observe successful cage shrinkage events, the required kinetic energy for the carrier gas is much higher than for bottom-up growth, in correlation with the values of the free energy barriers. For example, He atoms with kinetic energies of around 13 eV were needed to collide with the optimized I2 structure to obtain Ti@C_{28}, whereas He atoms with energies up to around 33 eV and greater were required to shrink Ti@C_{30} (Figure 12). These results correspond to simulations using initial structures optimized at 0 K.

Interestingly, when distorted structures from MD simulations were considered as initial structures, the energy to close I2 drops to 9 eV, while that to shrink Ti@C_{30} was mainly kept at 32 eV. It should be pointed out here that more than one hundred and twenty MD runs where He atoms collided with different velocities and orientations with respect to the carbon cage were performed to simulate the shrinking mechanism for Ti@C_{30}, and only seven of them led to the extrusion of a C atom from the closed fullerene (6%). On the other hand, about one hundred runs were done to simulate the bottom-up mechanism for the Ti@C_{28} system. In this case, around half of the collisions led to the closure of the fullerene from intermediate I2. Kinetic energies of ~13 eV could seem at first sight rather huge – the free energy barrier to close the carbon cage is 4.5 eV. However, the He atom kept an energy of ~3 eV after collision, so a total of ~10 eV are transferred from the He to the cage.

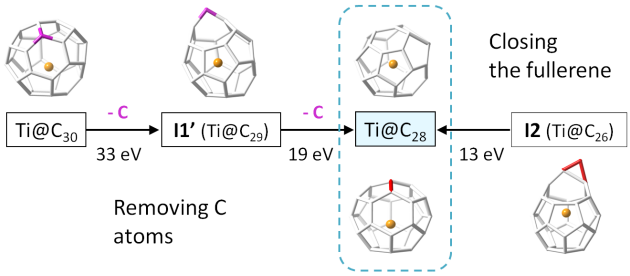

Figure 12. Collision kinetic energies involved in the closure of I2 Ti@C_{28} (right); and the shrinkage of Ti@C_{30} by successive removal of two C atoms (left).

Energies much larger than the barrier were always found necessary for the event to take place. The extra energy (~5 eV) is mainly dissipated through the vibrational modes. When distorted structures were considered, the collisions were seen to be more effective with appreciably less energy dissipation through vibrations (~2 eV, Figure 13). As the size of the cage increases the barrier to close the cage decreases. Consequently present results clearly support that larger cages can be formed at lower temperatures. For example, for C_{48} kinetic energies for the He atom of about 9 eV (8 eV for distorted structures) were needed to overcome a barrier of 2.1 eV (Figure 13).

When collisions with much more energetic He atoms were simulated (of the order of keV, as in CID experiments) release of C_2 units from Ti@C_{2n} systems (2n = 30 and 38) were observed, as found in experiments.[24] Analogous results were obtained when the carrier gas is Ar, although in all simulations, larger kinetic energies for the colliding atom were needed.

Finally, we remark that in all the dynamics that simulate the shrinking process, we have found that the excess of energy, dissipated essentially as vibrational energy, is much higher (>20 eV) than in the closing step of the carbon cage.

In summary, the free energy profiles for cage growth and shrinkage and the Car-Parrinello simulations of the collisions with the carrier gas indicate that Ti@C_{2n} (2n=28-48) should be mainly formed by bottom-up growth of smaller cages rather than top-down shrinkage of larger systems. These findings are in agreement with experimental results that show carbon cages grow in high-temperature environments of carbon vapor and helium gas, i.e. in fullerene synthesis conditions.

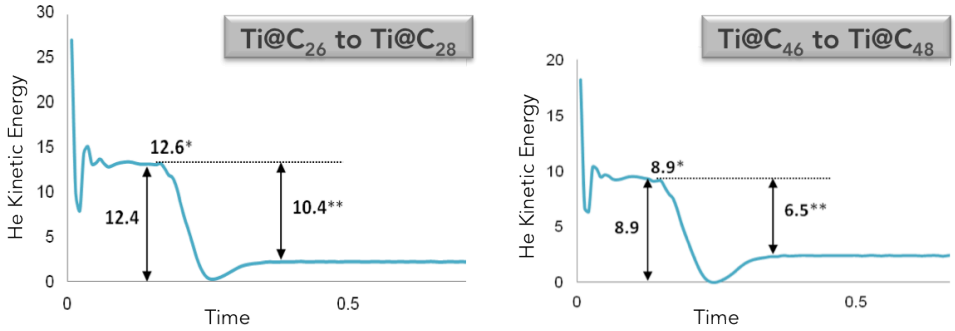

Figure 13. Kinetic energy (in eV) of the He atom during the MD run simulating the collision to I2 in (left) Ti@C_{26} to Ti@C_{28} system, and (right) Ti@C_{46} to Ti@C_{48} system. The average of these kinetic energies (KE) are listed in ref 29. * Kinetic energy for the He atom required to close the fullerene cage. ** Kinetic energy transferred to the carbon cage as a consequence of the collision. Time in ps.

4.3. A New Heptagon Structure: $Sc_2C_2@C_s$(hept)-C_{88}

A non-isolated pentagon rule metallic carbide clusterfullerene containing a heptagonal ring, $Sc_2C_2@C_s$(hept)-C_{88}, was isolated from the raw soot obtained by electric arc vaporization of graphite rods packed with Sc_2O_3 and graphite powder in a modified Krätschmer-Huffman arc-discharge reactor under a helium atmosphere.

Four isomers of Sc_2C_{90} were found, but only $Sc_2C_2@C_s$(hept)-C_{88} was obtained in a reasonable yield and was relatively easy to isolate.[30] The heptagon structure was purified by multistage high-performance liquid chromatography (HPLC), cocrystallized with Ni−(octaethylporphyrin), and characterized by single-crystal X-ray diffraction.

The diffraction data revealed a zigzag Sc_2C_2 unit inside an unprecedented C_s(hept)-C_{88} carbon cage containing 13 pentagons, 32 hexagons, and 1 heptagon. There is only one abutting pair of pentagons, which is adjacent to the heptagon. Figure 14 shows the structure of the endohedral fullerene as determined from single crystal X-ray diffraction of the black cocrystal $Sc_2C_2@C_s$(hept)-C_{88}·Ni(OEP)·2(C_7H_8). The Sc_2C_2 unit has a planar, zigzag structure, rather than the more common, folded butterfly arrangement found in other carbide containing endohedral fullerenes. The two-scandium ions are situated near the centers of hexagons on the inside of the carbon cage.

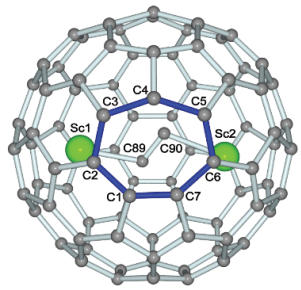

Figure 14. A view of the structure of $Sc_2C_2@C_s$(hept)-C_{88}.

4.3.1. Computational Analysis of $Sc_2C_2@C_s$(hept)-C_{88} and Other Sc_2C_{90} Isomers

To assess the stability of the crystallographic structure and to propose likely cages for the other three detected Sc_2C_{90} isomers, DFT computations were done. Besides the $Sc_2C_2@C_{88}$ carbide clusterfullerenes (CCFs), classical dimetallic endohedral fullerenes of the type $Sc_2@C_{90}$ were also considered. Note that for IPR cages, the truncated nomenclature of Fowler and Manolopoulos is written.

4.3.1.1. Looking for the Most Appropriate Isomers

For the C_{88} cage, there are 81738 possible isomers, but only 35 of them follow the isolated pentagon rule (IPR). Given the formal transfer of four electrons from Sc_2C_2 to the C_{88} cage, described as $(Sc_2C_2)^{4+}@(C_{88})^{4-}$, we have computed the tetraanions for all the C_{88} IPR cages (35) and non-IPR isomers with up to two adjacent pentagon pairs (APP): 368 APP1 and 2304 APP2. The lowest-energy tetraanionic cages, within a range of 23 kcal·mol^{-1}, were selected and the corresponding $Sc_2C_2@C_{88}$ structures were optimized at BP86/TZP level (Table 2).

On the other hand, there are 99918 isomers for the C_{90} cage, and only 46 of them satisfy the IPR. In this case, the electronic structures of the $Sc_2@C_{90}$ metallofullerenes result from a formal transfer of six electrons from the metal atoms to the cage, $(Sc_2)^{6+}@(C_{90})^{6-}$. Thus, we have computed the energies of the hexaanions for all cages with two or less adjacent pentagon pairs: 46 IPR, 544 APP1 and 3454 APP2 isomers. The lowest hexaanionic cages (less than 10 kcal·mol^{-1}) were chosen and optimized as $Sc_2@C_{90}$ metallofullerenes (Table 2).

Table 2. Relative energies and HOMO-LUMO (H-L) gaps for the selected isomers of C_{88} and C_{90} in the corresponding anionic and endohedral forms.[a,b)]

Isomer	C_{90}^{6-}	$Sc_2@C_{90}$	H-L gap
$Sc_2@C_2$-C_{90}(44)	4.3	0.0	0.773
$Sc_2@C_2$-C_{90}(42)	9.2	4.5	0.567
$Sc_2@C_2$-C_{90}(43)	0.0	5.0	0.548
$Sc_2@C_1$-C_{90}(21)	9.9	9.9	0.410
Isomer	C_{88}^{4-}	$Sc_2C_2@C_{88}$	**H-L gap**
$Sc_2C_2@D_2$-C_{88}(35)	0.0	2.1	0.751
$Sc_2C_2@C_s$-C_{88}(32)	8.5	3.6	0.709
$Sc_2C_2@C_1$-C_{88}(26)	7.2	8.7	0.810
$Sc_2C_2@C_s$(hept)-C_{88} (2)[b]	15.0	10.4	0.738
$Sc_2C_2@C_1$-C_{88}(78749)	19.0	12.2	0.683
$Sc_2C_2@C_1$-C_{88}(74790)	19.4	12.7	0.731
$Sc_2C_2@C_1$-C_{88}(70333)	23.0	13.1	0.531
$Sc_2C_2@C_s$(hept)-C_{88} (1)[b]	15.0	18.8	0.625

[a)] Energies in kcal·mol^{-1}, H-L gaps in eV. [b)] Same isomer, but different cluster orientation is shown in parenthesis for $Sc_2C_2@C_s$(hept)-C_{88}.

The IPR isomers D_2-C_{88}(35) and C_2-C_{90}(43) were found to be the lowest-energy C_{88}^{4-} and C_{90}^{6-} anions, respectively (Table 2). It should be noted that the crystallographically characterized $Sm_2@D_2$-C_{88}(35) with an internal $(Sm_2)^{4+}$ unit utilizes the D_2-C_{88}(35) cage. Although the lowest-energy EMF corresponds to the IPR di-metallic $Sc_2@C_2$-C_{90}(44), the next most stable isomers are the CCFs $Sc_2C_2@D_2$-C_{88}(35) at only 2.1 kcal·mol^{-1} and $Sc_2C_2@C_s$-C_{88}(32) at 3.6 kcal·mol^{-1}. The X-ray characterized structure, $Sc_2C_2@C_s$(hept)-C_{88} (1), once optimized, was found to be at 18.8 kcal·mol^{-1}. The optimized Sc-C distances are 2.17 Å for Sc1-C89, 3.37 Å for Sc1-C90, 2.69 Å for Sc2-C89 and 2.10 Å for Sc2-C90, in rather good agreement with the X-ray data.[30] Interestingly, a second minimum in which the Sc_2C_2 cluster is perpendicular with respect to the orientation found in the X-ray structure, $Sc_2C_2@C_s$(hept)-C_{88} (2), is found at a lower energy (10.4 kcal·mol^{-1}, Table 2 and Figure 15).

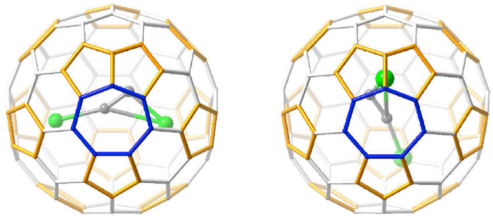

Figure 15. Optimized structures of $Sc_2C_2@C_s$(hept)-C_{88} with two different orientations of the internal dimetallic carbide. Orientation 1 is the one found in the X-ray structure; orientation 2, with the cluster rotated around 90 degrees, is 8.4 kcal mol^{-1} lower in energy than 1. Pentagons are highlighted in orange and the heptagon in blue.

4.3.1.2. Thermodynamic and Entropy Control

The molar fractions of the lowest-energy $Sc_2C_2@C_{88}$ and $Sc_2@C_{90}$ isomers as a function of the temperature were also computed using the rigid rotor and harmonic oscillator (RRHO) approximation and the related free-encapsulated model (FEM) as proposed by Slanina (Figure 16).[39,40]

For $Sc_2C_2@C_s$(hept)-C_{88}, we have considered the X-ray structure, $Sc_2C_2@C_s$(hept)-C_{88} (1). Both approximations predict $Sc_2C_2@D_2$-C_{88}(35) as the most abundant isomer for temperatures lower than 1000 K. Another IPR carbide clusterfullerene, $Sc_2C_2@C_s$-C_{88}(32) was found to be the second most abundant isomer up to 1000 K and the most abundant one at higher temperatures (T > 1000 K).

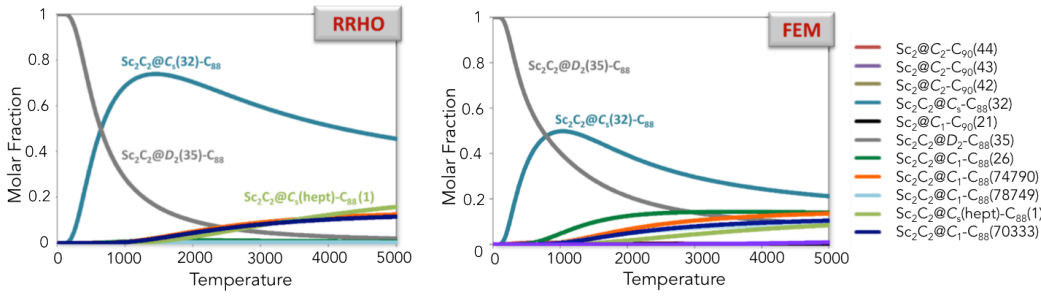

Figure 16. Predicted molar fractions within RRHO and FEM approximations as a function of temperature for the selected $Sc_2@C_{90}$ and $Sc_2C_2@C_{88}$ isomers.

The abundance of the X-ray characterized structure, $Sc_2C_2@C_s$(hept)-C_{88} (1), increases slightly at high temperatures, but remains less than 10% at temperatures of fullerene formation (2000 - 3000 K). Although the X-ray structure does not correspond to the theoretically computed most stable orientation of the Sc_2C_2 unit at the present level of calculation, both orientations are practically degenerate at high temperatures (the free energy difference at 2000 K is only 3 kcal mol^{-1}).

The molar fractions of classical dimetallofullerenes are negligible in the whole range of temperatures. According to these results, isomers $Sc_2C_2@C_s$-C_{88}(32) and $Sc_2C_2@D_2$-C_{88}(35) are likely to be among the other three isomers of Sc_2C_{90} found experimentally but not isolated. We confirmed that the relative stabilities of $Sc_2C_2@C_s$(hept)-C_{88}, $Sc_2C_2@D_2$-C_{88}(35) and $Sc_2C_2@C_s$-C_{88}(32) isomers do not depend on the computational settings. Other density functionals (PBE, B3LYP and M06) or the introduction of dispersion corrections results in similar predictions for their relative stabilities (Table 3).

Table 3. Relative energies (in kcal·mol^{-1}) for $Sc_2C_2@C_s$(hept)-C_{88}, $Sc_2C_2@D_2$-C_{88}(35) and $Sc_2C_2@C_s$-C_{88}(32) isomers using different packages (ADF, G09 and CPMD), density functionals (BP86, PBE, B3LYP,M06) and dispersion corrections (Dispersion Grimme 3).

Isomer	ADF BP86	ADF BP86/G3	ADF PBE/G3	G09 B3LYP	G09 M06	CPMD (Sc; BP86, C; PBE)
$Sc_2C_2@D_2$(35)-C_{88}	0.0	0.0	0.0	0.0	0.0	0.0
$Sc_2C_2@C_s$(32)-C_{88}	1.2	1.1	1.7	1.2	1.2	2.9
$Sc_2C_2@C_s$(hept)-C_{88}	16.4	15.8	16.7	19.7	20.7	16.6

4.3.1.3. Validity of the Ionic Model

The frontier molecular orbitals of $Sc_2C_2@C_s$(hept)-C_{88} confirm that there is a formal transfer of four electrons from the Sc_2C_2 unit to the C_{88} cage, i.e., $(Sc_2C_2)^{4+}@(C_{88})^{4-}$ (Figure 17). The HOMO and the LUMO are mainly localized on the cage.

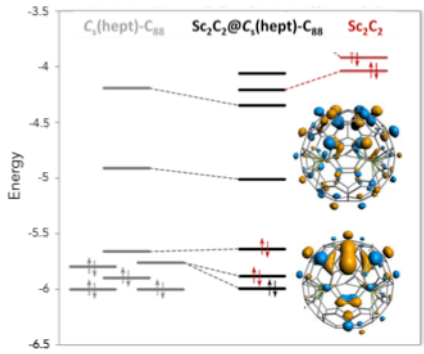

Figure 17. Orbital interaction diagram for Sc_2C_2@C_s(hept)-C_{88} isomer.

4.3.1.4. Electrochemical and UV-vis-NIR Properties

We have analyzed the electrochemical properties for some possible Sc_2C_{90} candidates (Table 4). The results for Sc_2C_2@C_s(hept)-C_{88} are in agreement with the experimental data.[30] The first oxidation and reduction potentials are computed (experimental value in parenthesis) to be 0.34 V (0.38 V) and -0.70 V (-0.78 V), respectively. The predicted EC gap is 1.03 V, which compares well with the experimental value (1.16 V).

Table 4. Computed oxidation and reduction potentials, electrochemical (EC) gaps (in V) and HOMO-LUMO (H-L) gaps (in eV) for selected Sc_2C_{90} isomers.

Isomer	$E^{2+/+}$	$E^{+/0}$	$E^{0/-}$	$E^{-/2-}$	$E^{-/3-}$	$E^{-/4-}$	EC	H-L gap
Sc_2C_2@D_2-C_{88}(35)	0.79	0.30	-0.80	-1.26	-2.32	-2.81	1.10	0.74
Sc_2C_2@C_s-C_{88}(32)	0.67	0.20	-0.91	-1.38	-2.37	-2.89	1.12	0.71
Sc_2C_2@C_1-C_{88}(26)	0.67	0.14	-1.06	-1.50	-2.23	-2.67	1.19	0.83
Sc_2C_2@C_1-C_{88}(74790)	0.83	0.27	-0.91	-1.37	-2.21	-2.64	1.18	0.79
Sc_2@C_2-C_{90}(44)	0.53	-0.03	-0.81	-1.98	-	-	0.78	0.78
Sc_2C_2@C_s(hept)-C_{88}	0.87	0.34	-0.70	-1.15	-2.27	-2.76	1.03	0.65
Experimental	-	0.38	-0.78	-1.73	-2.02	-2.27	1.16	

The computed UV-vis-NIR spectrum using time-dependent (TD) DFT for the Sc_2C_2@C_s(hept)-C_{88} isomer shows transitions at 622, 770, 903, 1183 and 1302 nm (Figure 18).

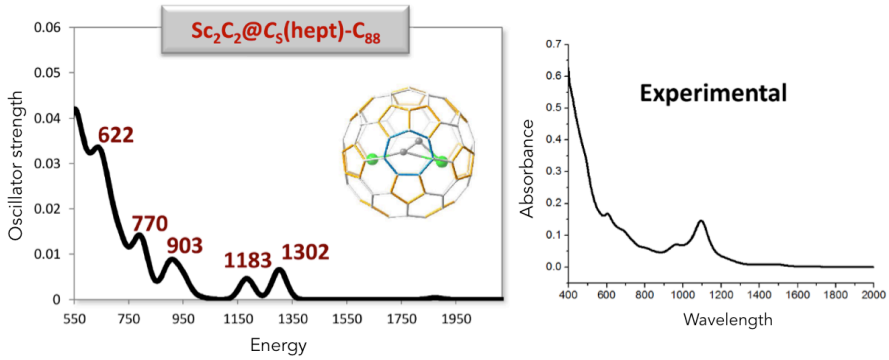

Figure 18. Calculated and experimental UV-vis-NIR absorption spectra for $Sc_2C_2@C_s$(hept)-C_{88} isomer.

4.3.1.5. Car-Parrinello MD Simulations

Car-Parrinello molecular dynamics simulations of $Sc_2C_2@C_s$(hept)-C_{88} (1) at room temperature and at temperatures of fullerene formation (2000 K) were also done to gain more insight about the motion of the Sc_2C_2 cluster inside the C_s(hept)-C_{88} fullerene. The Sc_2C_2 unit essentially keeps the original orientation for trajectories that last 30 ps at room temperature (Figure 19).

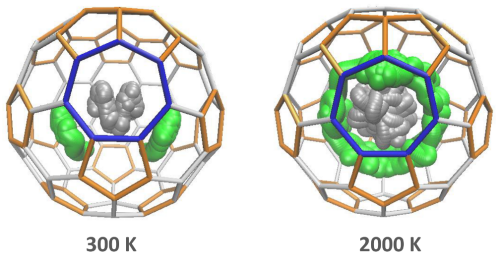

Figure 19. Motion of the Sc_2C_2 cluster inside the C_s(hept)-C_{88} cage along the Car-Parrinello simulation at 300 K (30 ps) and 2000 K (20 ps). Pentagons are highlighted in orange and heptagon in blue.

The average of the Sc-C distances in the Sc_2C_2 unit reasonably matches the value found by X-ray crystallography.[30] However, at 2000 K, the mobility of the scandium carbide in the cage is much higher, which led to the observation of another stable

orientation of the cluster inside the cage, the abovementioned $Sc_2C_2@C_s$(hept)-C_{88} (2). The cluster changes the initial orientation to finally get the optimal one in only 3.6 ps. The much higher mobility of the cluster at high temperatures is clearly shown in Figure 19.

4.3.2. How is $Sc_2C_2@C_s$(hept)-C_{88} Formed?

At this point, we wondered about the formation of this unique non-classical heptagon-containing EMF, which might provide valuable insight about the formation mechanism of endohedral fullerenes. Recently, Echegoyen, Balch and co-workers synthesized, isolated and characterized the carbide clusterfullerene $Sc_2C_2@C_{2v}$-C_{86}(9).[27] Interestingly, a direct relationship between the X-ray characterized structures of $Sc_2C_2@C_{2v}$-C_{86}(9) and $Sc_2C_2@C_s$(hept)-C_{88} has been found. Isomer $Sc_2C_2@C_s$(hept)-C_{88} could have been formed by a simple C_2 insertion on $Sc_2C_2@C_{2v}$-C_{86}(9) (Figure 20). When a C_2 unit is added at the selected hexagon, one hexagon, one heptagon and two fused pentagons are formed in the new structure (Figure 20). The process is highly favorable at 0, 300 and 2000 K. $Sc_2C_2@C_{2v}$-C_{86}(9) is found to be the lowest-energy (thermodynamic) isomer of the $Sc_2C_2@C_{86}$ family, followed by $Sc_2C_2@C_{2v}$-C_{86}(15) at 4.7 kcal·mol^{-1}.

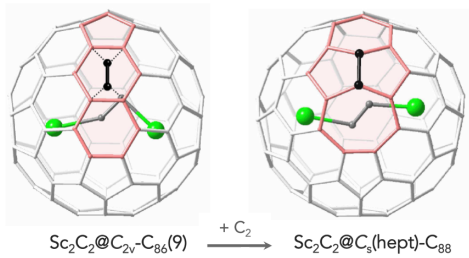

Figure 20. Structural relationship between $Sc_2C_2@C_{2v}$-C_{86}(9) and $Sc_2C_2@C_s$(hept)-C_{88} by a C_2 insertion. The motif that is involved in the transformation is highlighted in pink. The inserted C_2 unit is highlighted in black.

We have confirmed that the orientation of the Sc_2C_2 cluster inside the C_{2v}-C_{86}(9) cage is (i) the one with the lowest energy among all those other orientations analyzed and (ii) the most frequent one in a 40-ps Car-Parrinello MD trajectory at 2000 K (Figure 21). In

addition, the computed molar fractions (both RRHO and FEM approximations) predict the lowest-energy isomer $Sc_2C_2@C_{2v}$-C_{86}(9) to be the most abundant in the complete temperature range, i.e. the thermodynamic isomer, with $Sc_2C_2@C_{2v}$-C_{86}(15) as the second most abundant isomer.[30]

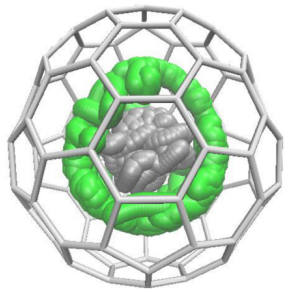

Figure 21. Motion of the Sc_2C_2 cluster inside the C_{2v}-C_{86}(9) cage during the simulation at 2000 K (around 40 ps).

4.3.2.1. Studying the C_2 Insertions

To shed light on the formation mechanism of $Sc_2C_2@C_s$(hept)-C_{88}, we analyzed all the possible single C_2 insertions to the tetraanionic cages C_{2v}-C_{86}(9) and C_{2v}-C_{86}(15) that lead to classical and non-classical heptagon-containing C_{88} fullerenes. Figure 22 shows the two types of additions analyzed.

We found that cage C_s(hept)-C_{88}, the one found by X-ray crystallography to contain the Sc_2C_2 cluster, is the lowest-energy cage among all the different possibilities. Two classical APP1 cages and a heptagon-containing cage are at 7, 8 and 11 kcal mol^{-1}, respectively; the other cages are found at 20 and 80 kcal·mol^{-1} (Figure 23).

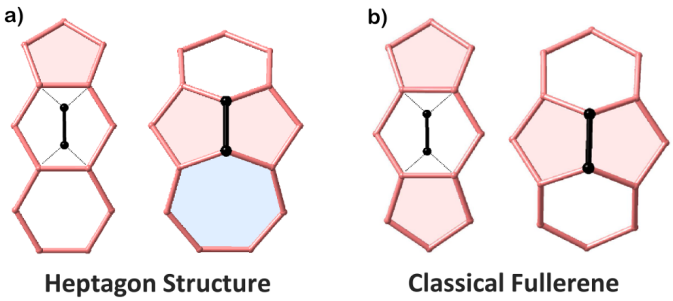

Figure 22. C_2 insertion on a hexagon forming a) a heptagon-containing cage; or b) a classical fullerene. Pentagons are colored in pink, hexagons in white and heptagon in blue.

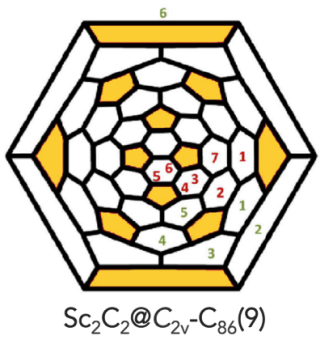

Isomer	C_{88}^{4-}
IPR 32	-6.4
IPR 35	**-14.9**
Hept formation	
Ins1	25.0
Ins2	32.5
Ins3	11.3
Ins4	68.2
Ins5	70.9
Ins6	21.3
Ins7 (Hept)	**0.0**

Isomer	C_{88}^{4-}
CF formation	
Ins1	8.3
Ins2	34.5
Ins3	25.9
Ins4	40.2
Ins5	6.7
Ins6	22.9

Figure 23. Schlegel diagram of $Sc_2C_2@C_{2v}$-C_{86}(9) with the number of positions where C_2 can be inserted. Red numbers indicate the formation of the heptagon structure (Hept formation) and green numbers the classical fullerene (CF formation). The energies of the structures formed are shown in tables in kcal·mol^{-1}. 'Ins' is the abbreviation of the inserted position according to the Schlegel diagram.

4.3.2.2. Why is $Sc_2C_2@C_s$(hept)-C_{88} Detected and Isolated?

Once the heptagon-containing EMF is formed, why is it detected and isolated? The likely answer to this query is that this non-classical cage cannot evolve easily to a more stable classical IPR or non-IPR cage. At least *four bond* rearrangements are required to obtain some APP1 and APP2 isomers, such as C_1-C_{88}(70333), C_1-C_{88}(78749), C_1-C_{88}(81690), C_1-C_{88}(66771), C_1-C_{88}(66889), and C_1-C_{88}(66708). A minimum of five

rearrangements are needed to transform the cage structure of C_s(hept)-C_{88} into the IPR D_2-C_{88}(35) cage.

It is worth remarking that these rearrangements require high energies, i.e. energy barriers around 150 kcal·mol^{-1}. Although lower free energy barriers are needed for these transformations at higher temperatures (around 125 kcal·mol^{-1} at 2000 K), it is still difficult and rather unlikely to overcome many of them (Figure 24). In addition, insertion of a C_2 unit leads to Sc_2C_2@C_2-C_{90}(43), one of the computed lowest-energy Sc_2C_2@C_{90} isomers. Therefore, Sc_2C_2@C_s(hept)-C_{88} is very likely a *kinetically-trapped intermediate*, the most stable among the possible C_{88} non-classical cages, in a bottom-up growth process from Sc_2C_2@C_{2v}-C_{86}(9).

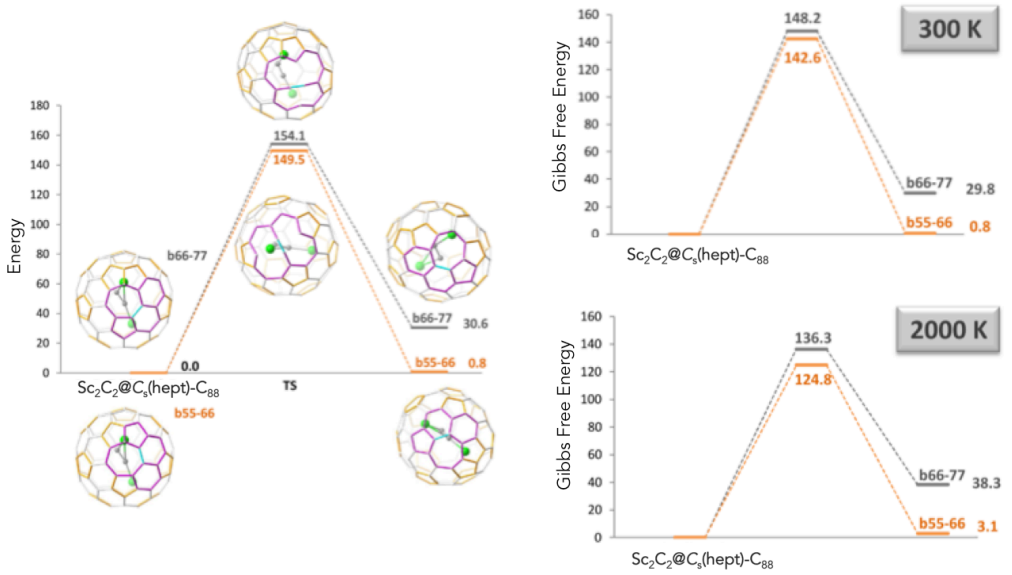

Figure 24. (left) Energy profile (in kcal·mol^{-1}) of the first rearrangement that can be observed from Sc_2C_2@C_s(hept)-C_{88} isomer. The bonds involved in the rearrangement are marked in cyan; b66-77 in gray line and b55-66 in orange line. (right) Gibbs free energy profiles (in kcal·mol^{-1}) of the first rearrangement that can be observed from Sc_2C_2@C_s(hept)-C_{88} isomer at room temperature and at 2000 K. The two possible bonds that can rearrange are marked (b66-77 is in gray and b55-66 in orange).

4.3.2.3. The Case of $LaSc_2N$@C_s(hept)-C_{80}

In order to further test the generality of these findings and to test the validity of the mechanistic interpretations and conclusions, we performed a similar analysis with the first observed EMF containing a heptagon, $LaSc_2N$@C_s(hept)-C_{80}.[28] Remarkably, a

simple C_2 insertion of the type depicted in Figure 22a to the non-IPR $LaSc_2N@C_2$-C_{78}(22010), as shown in Figure 25, leads to the reported heptagon-containing endohedral cage. This non-IPR EMF is at less than 4 kcal·mol^{-1} from the lowest-energy IPR isomer $LaSc_2N@D_{3h}$-C_{78}(5), but similar abundances for the two isomers are predicted at T > 2000 K.[30]

The other heptagon-containing fullerene synthesized thus far by the carbon arc process, C_{68}(hept)Cl_6, can be also directly obtained from the C_{66}(4169) precursor through a C_2 insertion of the type described in Figure 22a,[41] in perfect agreement with a growth mechanism involving a heptagon-containing cage as an intermediate. This was earlier proposed for empty pristine fullerenes in 2001.[42]

In addition, very recently, Fowler and co-workers have shown that the preferred nitride EMFs of the C_{78}, C_{80} and C_{82} cages are interconnected by a network of C_2 insertions/extrusions and Stone-Wales isomerization steps in which non-classical one-heptagon structures may play a significant role.[43] To the best of our knowledge the only pair of EMFs that can be related by a simple C_2 addition where both have been isolated and characterized so far are $Sc_2S@C_s$-C_{72}(10528)[44] and its potential precursor in a bottom-up growth, $Sc_2S@C_2$-C_{70}(7892).[26] In contrast to the heptagon-containing EMFs, the C_{70} and C_{72} cages encapsulating a Sc_2S do not exhibit non-classical heptagon structures at sufficiently low energies. All C_2 insertions of the type shown in Figure 22a on the C_2-C_{70}(7892) tetraanion are above 26 kcal·mol^{-1} relative to the energy of the observed C_s(10528)-C_{72} isomer, which is the optimal C_2 insertion of type b in Figure 22.

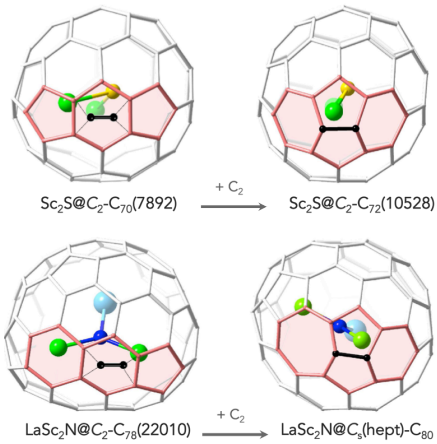

Figure 25. Potential precursors for the observed $LaSc_2N@C_s$(hept)-C_{80} and $Sc_2S@C_s$(10528)-C_{72} EMFs in a bottom-up growth mechanism.

4.3.3. Supporting the Bottom-up Growth

To date, the main experimental support for the bottom-up growth mechanism was reported by Kroto and co-workers, who demonstrated that empty and EMFs grow in the presence of a rich carbon vapor atmosphere.[22,25] A plausible interpretation compatible with the formation of the two heptagon-containing EMFs known so far, $Sc_2C_2@C_s$(hept)-C_{88} and $LaSc_2N@C_s$(hept)-C_{80}, as well as the classical non-IPR $Sc_2S@C_s$-C_{72}(10528), from *low-energy* precursors and *single* C_2 insertion steps is presented. The main difference between these two non-classical EMFs is that while $LaSc_2N@C_s$(hept)-C_{80} is highly stabilized by the presence of the cluster, which fits rather well inside this cage, C_s(hept)-C_{88} is already rather stable as a tetraanion.

The present interpretation is also in accord with the pioneering theoretical work of Hernandez and co-workers,[42] who showed that fullerenes may grow via heptagon intermediates without any Stone-Wales rearrangements. Although the extrusion of C atoms from an already closed fullerene is much more energetically demanding than forming the fullerene by a bottom-up mechanism,[29] it has been found that C_2 extrusion from *non-classical* carbon cages is favorable at very low carbon-vapor concentrations.[21] This means that the formation of a fullerene, classical or non-classical, could also follow a *top-down* mechanism,[20] but it is important to remark that to remove a C_2 unit from a classical fullerene, IPR or non-IPR, does not seem competitive when there is enough carbon vapor concentration in the atmosphere.

Maybe in the following years new evidence will emerge that will help elucidate the formation and growth mechanisms of fullerenes. The carbon cage diversity of EMFs will likely be important to characterize such mechanisms.

4.4. Growth of $Sc_3N@C_{2n}$ (2n=68-80) Family

Plasma synthesis techniques are used to construct many forms of carbon materials and compounds, and in particular, nitride clusterfullerenes, $M_3N@C_{2n}$ (M = metal, C_{2n} = even numbered cage), which are among the most intensively studied form of molecular nanocarbon. The chemical processes that result in the synthesis of nitride clusterfullerene compounds, however, are unknown because *in situ* analyses are not possible by conventional arc plasma discharge techniques.

Very recently, Prof. Dunk investigated metallic nitride clusterfullerene self-assembly for the first time by laser vaporization of metal- and nitrogen-doped graphite.[31] The Sc_3N cluster initially nucleates formation of smaller cages, and thereafter, larger species

primarily self-assemble through carbon insertion reactions. In contrast to mono-metallofullerenes, the Sc_3N cluster is too large to nucleate cage sizes of C_{60} or smaller. Therefore, the smallest carbon cages ($C_{2n} \leq 60$) are bypassed during clusterfullerene formation and thus high-value, medium-sized cages are more efficiently synthesized. The influence of cluster and cage-size effects is elucidated by molecular behaviour analysis of distinct clusterfullerenes under representative physicochemical synthesis conditions. The small, pentalene-containing $Sc_3N@D_3$-C_{68} compound is explicitly demonstrated to transform through a bottom-up mechanism into $Sc_3N@C_{80}$.

The molecular behaviour of defined $Sc_3N@C_{2n}$ in carbon plasma provides mechanistic insight into the origin of $Sc_3N@C_{2n}$ produced from bulk starting materials, as well as structural effects with respect to nanocarbon reactions that operate during self-assembly. It is known that charge transferred from the Sc_3N cluster to the cage resides at the most strained carbon atoms in the structure.[10] Therefore, negative charge is preferentially located at pentagon fusions. $Sc_3N@D_3$-C_{68} possesses three sets of double-fused pentagons (pentalene motifs), whereas all pentagons are isolated for $Sc_3N@I_h$-C_{80}. Figure 26 shows the reaction products formed after exposure of isomerically pure, pre-existing $Sc_3N@D_3$-C_{68} to carbon plasma in a low pressure He atmosphere. Bottom-up growth into larger $Sc_3N@C_{2n}$ (C_{2n} = 70-94) compounds is unambiguously observed. Under the present conditions, $Sc_3N@C_{70}$ exhibits the largest relative abundance. However, the much larger-sized $Sc_3N@C_{80}$ compound is also observed and exhibits an enhanced magnitude, indicating that the very stable $Sc_3N@I_h$-C_{80} clusterfullerene is formed.

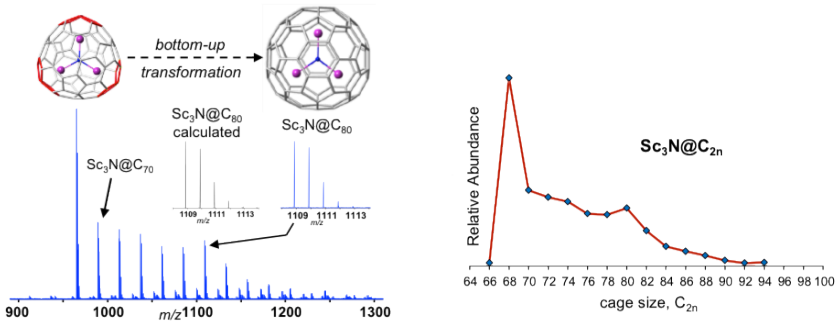

Figure 26. (left) Bottom-up growth of $Sc_3N@C_{68}$ into $Sc_3N@C_{80}$ and larger $Sc_3N@C_{2n}$ clusterfullerenes are formed from $Sc_3N@D_3$-C_{68} by carbon insertion reactions after reaction with carbon plasma (10mj/pulse). (right) Growth distribution for $Sc_3N@C_{68}$ + nC_2.

Pre-existing $Sc_3N@D_3$-C_{68} was studied without exposure to carbon vapour to examine its molecular behaviour under the high energy conditions of synthesis. Surprisingly, $Sc_3N@C_{70}$, a bottom-up growth product, is the most abundant molecular reaction product, even without the presence of carbon plasma generated from graphite, suggesting that carbon insertion reactions can be favoured in low carbon density, high-energy conditions. Consequently, these results provide additional evidence that the smallest $Sc_3N@C_{2n}$ (C_{2n} = C_{62}-C_{66}) are not formed from larger $Sc_3N@C_{2n}$ during self-assembly from a carbon plasma containing Sc and N.

4.4.1. Computational Analysis for the Transformations of C_{68} into C_{80}

As mentioned, it is very challenging to decipher the formation mechanisms of carbon nanoforms, such as metallofullerenes. From a theoretical perspective, computational studies that have aimed to understand self-assembly by means of molecular dynamics have generally concluded that high symmetry fullerenes are the result of a top-down mechanism, whereby large cages spontaneously assemble and then smaller cages, such as I_h-C_{60}, form by repeated C_2 elimination reactions, particularly in low carbon density environments.[19] However, Dunk et al. have recently shown that the small non-IPR fullerene, $Sc_3N@D_3$-C_{68}(6140) grows into larger $Sc_3N@C_{2n}$ upon exposure to carbon vapor in the gas phase, and importantly, the much larger $Sc_3N@C_{80}$ species is formed.

Further, isomerically pure $Sc_3N@I_h$-C_{80}(31924) does not readily undergo C_2 elimination processes under the present characteristic clusterfullerene synthesis conditions. Although C_2 loss can take place in the gas phase, and will be necessary to accurately describe a comprehensive mechanism, it is an arduous process. Based on the present experimental results, we focus on identification of bottom-up, cage-to-cage reaction pathways by use of DFT calculations, with an ultimate goal to unravel how the high symmetry, IPR I_h-C_{80}(31924) clusterfullerene cage may form from the much smaller, non-IPR D_3-C_{68}(6140) structure that contains three sets of fused pentagons.

4.4.1.1. C_{68} to C_{72}: Initial Growth Steps

$Sc_3N@D_3$-C_{68} is clearly demonstrated to transform into $Sc_3N@C_{70}$ after exposure to carbon vapor generated from graphite, which involves the overall incorporation of C_2 into the caged network. That nanocluster is also among the most abundant NCFs formed by laser vaporization of Sc- and N-doped graphite.[31] Interestingly, the only $Sc_3N@C_{70}$ species that has been isolated is C_{70}(7854).[45]

To discern a reaction path for the $Sc_3N@D_3$-C_{68} to $Sc_3N@C_{70}$ transformation, all possible topological C_2 insertions were analyzed for the D_3-C_{68}(6140) cage in the

hexaanionic form, C_{2n}^{6-}, to account for charge transfer from the encapsulated Sc_3N cluster to the cage. Six isomers of C_{70} can be generated by direct C_2 insertion (Figure 27) without the involvement of Stone-Wales (SW) bond rearrangements. The two lowest energy product structures, shown in Figure 28a-b, are found to be associated with very exothermic energies (Table 5). C_{70}(7886) exhibits a classical structure comprised of pentagons and hexagons, whereas C_{70}(hept) possesses a non-classical structure that contains a heptagon motif.

To date, $Sc_3N@C_{2v}$-C_{70}(7854) has been the only $Sc_3N@C_{70}$ species characterized,[45] which is related to C_{70}(7886) by more than three SW rearrangements and we find that it is -13.6 kcal·mol^{-1} lower in energy. Further, we find that the known cage C_{70}(7892), although encapsulated by Sc_2S rather than Sc_3N, is 2.3 kcal·mol^{-1} higher in energy than C_{70}(7886).[46] Therefore, these calculations suggest that the initial step in the growth from $Sc_3N@C_{68}$(6140) to $Sc_3N@C_{70}$ by a simple C_2 insertion favours the formation of a heptagon-containing fullerene, C_{70}(hept), or the pentalene-containing isomer, C_{70}(7886), prior to any structural rearrangements.

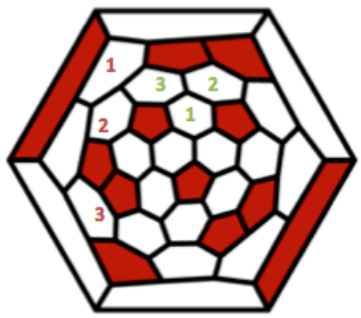

Isomer	C_{70}^{6-}
C_{2v} (7854)	0
C_2 (7892)	16.1
Hept formation	
ins1	57.9
ins2	25.5
ins3	47.5
CF formation	
ins1	36.1
ins2	36.4
ins3	13.8

Figure 27. Schlegel diagram of *D*$_3$-C_{68}(6140) with identified C_2 insertion sites that can form the heptagon (Hept formation) or the classical fullerene (CF formation) C_{70} structures described in this work. Red numbers indicate the formation of the heptagon structure and green numbers the classical fullerene. The energies of the structures formed are shown in kcal·mol^{-1}. Note that 'Ins' is the abbreviation for the inserted position according to the Schlegel diagram.

The proposed mechanism for the $Sc_3N@C_{70}$ to $Sc_3N@C_{72}$ step is focused on a C_2 unit that reacts with one [5,6,6] carbon atom at a hexagon of C_{70}, forming intermediate I1, in which one C atom of the C_2 molecule is attached to the cage (Figure 29). An extensive investigation of all possible C_2 insertions into hexagons and heptagons of these structures was performed (Figure 30). We find that the energy profiles for these

cage growth transformations are similar. Table 5 shows that reaction energies are somewhat lower, but remain very exothermic. Thus, the formation of the proposed C_{70} and C_{72} growth structures are favourable based on thermodynamic considerations. There is no transition state (TS) for this first step. The energy difference between I1 and the reactants is -62.1 kcal·mol^{-1} for C_{70}(7886) and -84.1 kcal·mol^{-1} for C_{70}(hept).

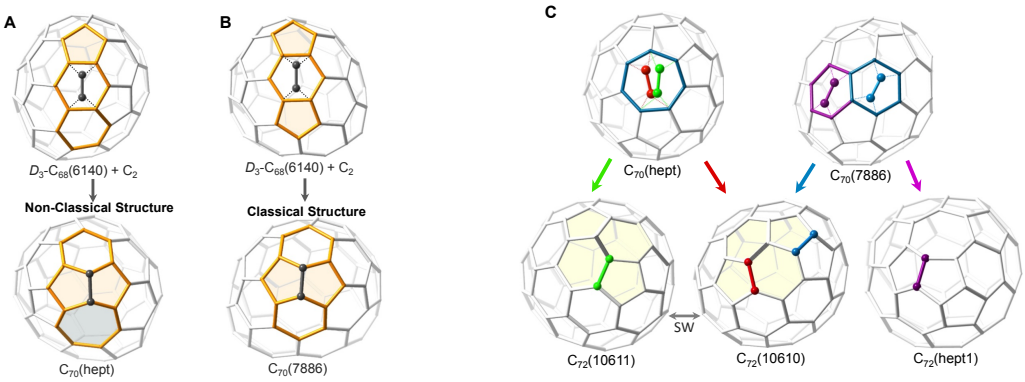

Figure 28. (left) C_2 insertion on a hexagon forms a pentalene giving a classical fullerene (B) or a heptagon-containing cage. (A) These structures are the lowest energy hexaanionic isomers obtained from direct addition of C_2 to D_3-C_{68}(6140). (right) Structures of the most favourable isomers formed by C_2 insertion and rearrangement for the C_{70} to C_{72} growth step. Reaction energies for hexaanions and clusterfullerenes are given in Table 5.

The second intermediate, I2, is characterized by its high stability and contains an eight-membered ring for C_{70}(hept), whereas I2 for C_{70}(7886), which is more stable (23.0 kcal·mol^{-1}), exhibits a heptagonal ring. Both intermediates, I1 and I2, are connected by a transition state TS1. The barrier to overcome this first transition state is rather low, 9.1 kcal·mol^{-1} for C_{70}(7886) and 7.9 kcal·mol^{-1} for C_{70}(hept). The last step of the mechanism corresponds to the closure of the cage. The C_2 unit is finally inserted in the fullerene cage through a second transition state (TS2) and two fused pentagons in the original hexagon are formed (i.e., a pentagon and a hexagon are formed from C_2 insertion into a heptagon). The energy barrier to overcome this last step is 49 kcal·mol^{-1} for C_{70}(7886) and 47 kcal·mol^{-1} for C_{70}(hept). Both barriers can be surpassed at typical temperature range of fullerene formation (>1000 K). Therefore, the entire C_2 insertion process is a highly favourable exothermic process. The associated Gibbs free energy is computed to be about -110 kcal·mol^{-1}, still a very exergonic energy. No significant change is observed between electronic and free energies for the closure of the cage.

Table 5. Reaction energies (in kcal·mol^{-1}) in hexaanion and endohedral form for the $Sc_3N@C_{2n}$ + C_2 ---> $Sc_3N@C_{2n+2}$ processes.

Reaction	C_{2n}^{6-}	$Sc_3N@C_{2n}$	Reaction	C_{2n}^{6-}	$Sc_3N@C_{2n}$
$C_{68} \rightarrow C_{70}$			**$C_{72} \rightarrow C_{74}$**		
6140 → hept	-182.6	-167.9	10528 → 13333	-221.0	-188.5
6140 → 7886	-194.5	-179.3	**$C_{74} \rightarrow C_{76}$**		
$C_{70} \rightarrow C_{72}$			hept1 → 17765	-223.2	-211.6
hept → 10611	-242.6	-210.7	13400 → 17512	-200.8	-198.9
hept → 10610	-226.4	-207.0	13400 → hept1	-194.3	-190.4
7886 → 10610	-214.5	-195.7	13295 → hept3	-193.0	-188.5
7886 → hept1	-206.4	-176.7	13290 → hept3	-202.2	-194.3
7854 → hept2	-194.0	-177.6	13333 → 17490	-213.1	-217.2
$C_{72} \rightarrow C_{74}$			**$C_{76} \rightarrow C_{78}$**		
10611 → 13400	-200.4	-192.5	17765 → hept1	-205.0	-219.8
10611 → hept1	-180.4	-171.9	17512 → hept1	-200.9	-175.7
10610 → 13391	-207.6	-177.3	hept3 → 22010	-226.3	-223.2
10610 → hept1	-196.5	-175.6	17490 → 22010	-211.1	-202.7
hept1 → 13400	-224.7	-215.1	**$C_{78} \rightarrow C_{80}$**		
hept2 → 13295	-231.5	-211.2	hept1 → 31923	-257.1	-227.2
hept2 → 13290	-222.3	-205.4	22010 → hept	-217.5	-213.2

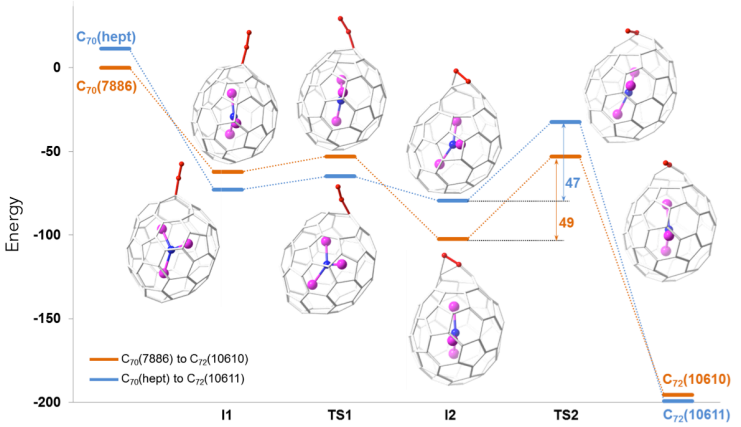

Figure 29. Energy profiles (in kcal·mol^{-1}) for the $Sc_3N@C_{70}$(7886) to $Sc_3N@C_{72}$(10610) (orange) and $Sc_3N@C_{70}$(hept) to $Sc_3N@C_{72}$(10611) (blue) transformations.

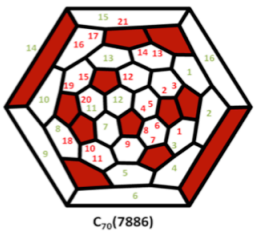

Isomer	C_{72}^{6-}
C_s(10528)	0
Hept formation	
ins1	65.7
ins2	24.2
ins3	65.4
ins4	68.4
ins5	41.1
ins6	61.9
ins7	98.0
ins8	73.9
ins9	72.4
ins10	50.6
ins11	76.3
ins12	40.4
ins13	63.5
ins14	40.7
ins15	83.8
ins16	87.6
ins17	47.7
ins18	65.8
ins19	52.9
ins20	69.0
ins21	71.5

Isomer	C_{72}^{6-}
CF formation	
ins1	16.1
ins2	49.0
ins3	52.6
ins4	59.8
ins5	45.6
ins6	58.7
ins7	24.6
ins8	60.4
ins9	57.2
ins10	30.3
ins11	66.0
ins12	44.9
ins13	24.3
ins14	60.8
ins15	57.9
ins16	48.7

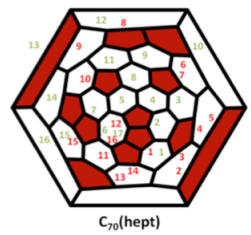

Isomer	C_{72}^{6-}
C_s(10528)	0
Hept formation	
ins1	75.1
ins2	64.4
ins3	81.8
ins4	74.2
ins5	87.5
ins6	61.3
ins7	88.3
ins8	80.5
ins9	90.1
ins10	92.5
ins11	55.0
ins12	59.3
ins13	65.6
ins14	77.4
ins15	101.0
ins16	53.5

Isomer	C_{72}^{6-}
CF formation	
ins1	63.4
ins2	96.3
ins3	67.1
ins4	66.3
ins5	41.6
ins6	16.3
ins7	61.0
ins8	74.2
ins9	65.7
ins10	47.6
ins11	53.4
ins12	66.5
ins13	77.3
ins14	50.8
ins15	69.2
ins16	61.0
ins17	0.0

Figure 30. Schlegel diagram of (left) C_{70}(7886) and (right) C_{70}(hept) with C_2 insertion sites that can form the heptagon (hept) or the classical fullerene (CF) C_{72} structures described in this work. Red numbers indicate the formation of the heptagon structure and green the classical fullerene. The energies of the structures formed are shown in kcal·mol^{-1}. Note that 'Ins' is the abbreviation for the inserted position according to the Schlegel diagram.

C_{72}(10610) or heptagon-containing C_{72}(hept1) is generated by C_2 insertion into a hexagonal face of C_{70}(7886). Interestingly, C_{72}(10610) can also be formed by a C_2 insertion into a heptagon of the non-classical C_{70} starting structure. That process can also lead to a closely related structure, C_{72}(10611). In fact, a single SW rearrangement connects isomers C_{72}(10611) and C_{72}(10610). We find that C_{72}(10611) is the most stable isomer, which has been previously isolated when encapsulating La_2 or Pr_2,[46] whereas C_{72}(10610) and C_{72}(hept1) are 16.1 and 24.2 kcal·mol^{-1} higher in energy.

Structures that possess two heptagons are not considered because such cages are very strained and are at least 53.5 kcal·mol^{-1} higher in energy than C_{72}(10611). The reaction energy values are slightly more exothermic for the C_{70} to C_{72} step than for the C_{68} to C_{70} step. Finally, reaction energies for all of the lowest energy isomers were investigated in the clusterfullerene form, $Sc_3N@C_{2n}$, for comparison to the hexaanionic energies. Table 6 shows that reaction energies are somewhat lower, but remain very exothermic. Thus, the formation of the proposed C_{70} and C_{72} (Figure 28) structures are favourable based on thermodynamic considerations.

Table 6. Reaction Energies for C_{68} to C_{72} Transformation[a)]

Step	C_{2n}^{6-}	$Sc_3N@C_{2n}$
D_3-C_{68}(6140) --> C_{70}(hept)	-182.6	-167.9
D_3-C_{68}(6140) --> C_{70}(7886)	-194.5	-179.3
C_{70}(hept) --> C_{72}(10611)	-242.6	-210.7
C_{70}(hept) --> C_{72}(10610)	-226.4	-207.0
C_{70}(7886) --> C_{72}(10610)	-214.5	-195.7
C_{70}(7886) --> C_{72}(hept1)	-206.4	-176.7
C_{72}(10611) --> C_{72}(10610)	+3.7	-1.8

[a)]Energies in kcal·mol^{-1}.

4.4.1.2. Bottom-up Reaction Paths to I_h-C_{80} (31924)

We have investigated global pathways to high symmetry C_{80} clusterfullerenes from $Sc_3N@D_3$-C_{68} based on this strategy for step-by-step cage formations of low energy isomers through C_2 insertions and bond rearrangements. Despite the complexity of the processes involved (Figure 31), it is extraordinary that several relatively simple pathways exist and are shown in Figure 32.

We have investigated global pathways from D_3-C_{68}(6140) to the archetypal clusterfullerene cage, I_h-C_{80}, as well as other medium-sized species such as D_{5h}-C_{80} and D_{3h}-C_{78} by use of the strategy described for the C_{68} to C_{72} transformation. Figure 31 shows the structures for a given cage size and their connections based on step-by-step formation of low energy isomers through C_2 insertions and rearrangements.

One of the features that we emphasize in Figure 31 is the complexity of the processes involved. Although we have used a simplified model that consists of carbon cages that react exclusively with C_2 units and use a minimal number of bond rearrangements, the number of potential reaction pathways is very high. Despite this complexity, it is extraordinary that several relatively simple pathways to high symmetry cages exist (Scheme 1 and Figure 32), which are comprised of six C_2 insertion reactions and two to three C_2 rearrangements.

Pathway 1: D_3-C_{68}(6140) → C_{70}(hept) → C_{72}(10611) → C_{74}(13400) → C_{76}(17512) → C_{78}(hept2) ⇔ C_{78}(22010) → C_{80}(hept) ⇔ I_h-C_{80}(31924)

Pathway 2: D_3-C_{68}(6140) → C_{70}(hept) → C_{72}(10611) → C_{74}(13400) → C_{76}(hept1) ⇔ C_{76}(17490) → C_{78}(22010) → C_{80}(hept) ⇔ I_h-C_{80}(31924)

Pathway 3: D_3-C_{68}(6140) → C_{70}(7886) → C_{72}(10610) → C_{74}(13391) ⇔⇔ C_{74}(13333) → C_{76}(17490) → C_{78}(22010) → C_{80}(hept) ⇔ I_h-C_{80}(31924)

Pathway 4: D_3-C_{68}(6140) → C_{70}(7886) → C_{72}(10610) ⇔⇔ C_{72}(10528) → C_{74}(13333) → C_{76}(17490) → C_{78}(22010) → C_{80}(hept) ⇔ I_h-C_{80}(31924)

Pathway 5: D_3-C_{68}(6140) → C_{70}(hept) → C_{72}(10611) → C_{74}(hept1) → C_{76}(17765) → C_{78}(hept1) → D_{5h}-C_{80}(31923)

Scheme 1. Selected pathways that link D_3-C_{68}(6140) to I_h-C_{80}(31924) and D_{5h}-C_{80}(31923) by carbon insertions via low energy isomers with a minimal number of C_2 structural rearrangements. The symbol → denotes a C_2 insertion, whereas ⇔ identifies a C_2 rearrangement.

In pathway 1, the first C_2 rearrangement occurs near the end of the route at C_{78}, whereas in pathway 2, isomerization takes place in a prior step, C_{76}(hept1) ⇔ C_{76}(17490). Both pathways share the same three initial steps, in which the growth of D_3-C_{68}(6140) starts with the formation of C_{70}(hept) and the subsequent capture of a second C_2 unit to yield C_{72}. However, C_{72}(hept1) is found to be 24.2 kcal·mol^{-1} higher in energy than C_{72}(10611). Therefore, the pathway through C_{72}(hept1) is thermodynamically less favorable. Interestingly, both pathways exhibit the final reaction sequence, C_{78}(22010) → C_{80}(hept) → I_h-C_{80}(31924), and C_{80}(hept) cage is the structure recently isolated and characterized as $LaSc_2N@C_{80}$(hept).[28] In addition, C_{78}(22010) has also been isolated as $M_3N@C_{78}$(22010) (M = Gd).[47]

Other routes can lead to the highly symmetric cage I_h-C_{80}(31924). In contrast to pathways 1 and 2 that emerge from the non-classical C_{70}(hept) structure, pathways 3 and 4 develop from a classical C_{70} isomer and each involve a total of three SW rearrangements. For example, in pathway 4, C_2 insertion into D_3-C_{68}(6140) forms the C_{70}(7886) cage, and thereafter, growth may progress through the "gateway" cage, C_{72}(10610), which evolves via two consecutive SW transformations to C_{72}(10528) and then to C_{74}(13333) by a subsequent C_2 insertion. In pathway 3, the C_{72}(10610) cage is also generated from C_{70}(7886); however, a direct C_2 reaction gives C_{74}(13391), which then undergoes two SW rearrangements to form C_{74}(13333). Pathways 3 and 4 result in the formation of icosahedral C_{80} by the same C_{74}(13333) to I_h-C_{80}(31924) reaction sequence as in pathways 1 and 2. We note that C_{72}(10528) has been characterized as the clusterfullerene, $Sc_2S@C_{72}$.[44] Strikingly, a sequence of six direct C_2 insertions without any SW rearrangements results in the D_{5h}-C_{80}(31923) isomer, as shown in pathway 5. The D_{3h}-C_{78} cage has a more indirect relationship to the D_3-C_{68}(6140)

precursor because it requires six SW transformations. Importantly, reaction energies for all routes are very exothermic, as shown in Table 5.

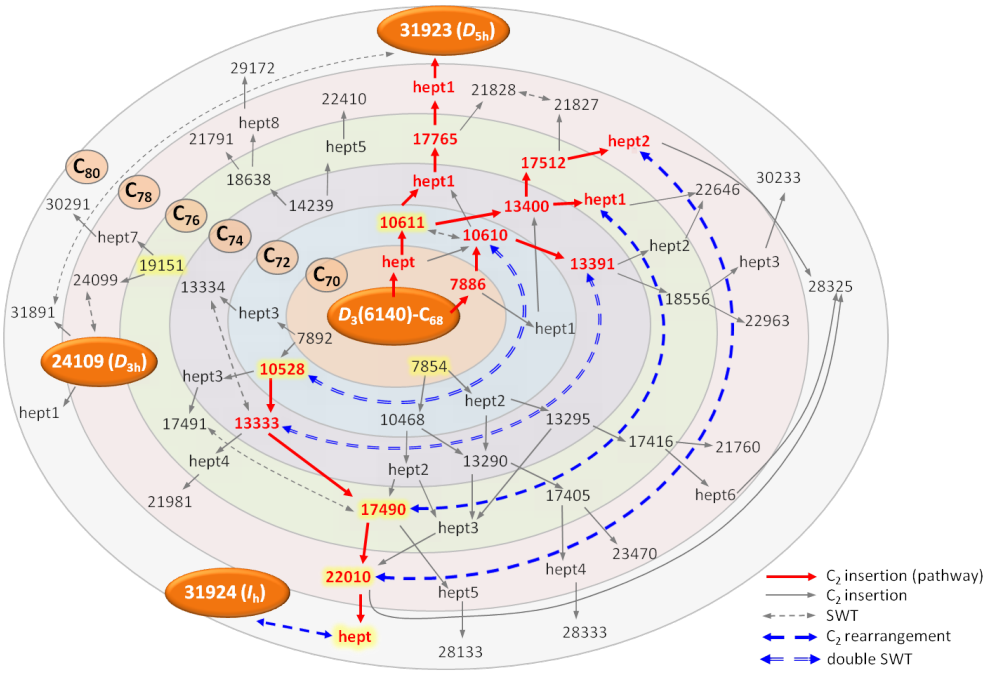

Figure 31. Schematic routes for the transformation from D_3-C_{68} to C_{80} cages in a bottom-up growth mechanism. Bold arrows represent pathways that yield I_h-C_{80} from D_3-C_{68} by simple C_2 insertions (red) and C_2 structural rearrangements (blue). Known endohedral cage isomers that have been structurally characterized are highlighted in yellow. See scheme 1 and Figure 32 for selected pathways.

Computed free energies at high temperatures (2000 K) confirm that all routes are very exergonic. It is likely that in the near future progress in the synthesis, isolation, and characterization of these predicted non-classical and classical gateway intermediates will be achieved.

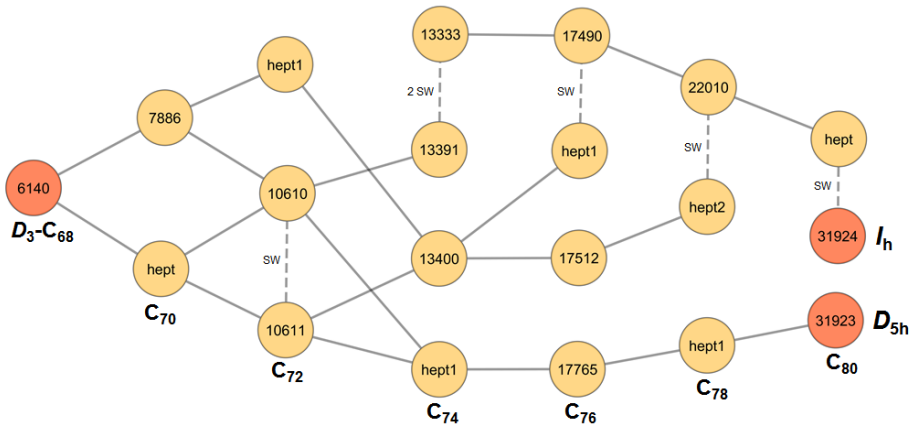

Figure 32. Reaction paths that form high symmetry C_{80} isomers (I_h, D_{5h}) from D_3-C_{68} through cage transformations that involve non-classical and classical cages. From those C_{72} isomers, reaction paths to high symmetry cages, I_h-C_{80} and D_{5h}-C_{80}, involve C_2 insertion reactions and two to three SW rearrangements through classical and non-classical cage intermediates.

4.4.1.3. Energy profiles for elementary steps

$Sc_3N@C_{72}$(10611) and $Sc_3N@C_{72}$(10610) are intimately related by a single Stone-Wales transformation (Figure 33). Although SW rearrangements show large energy barriers, they can be overcome at temperatures higher than 1000 K. In the present case, the energy barrier of the simple SW transformation is around 153-157 kcal·mol^{-1}. We have also studied the SW rearrangement mechanism that relates I2 of $Sc_3N@C_{70}$(7886) + C_2 to $Sc_3N@C_{72}$(10611). It is not a concerted mechanism because two transition states are found, TS2' and TS3'. The energy barrier that connects I2 and I3', i.e. when the rearrangement takes place in the open structure I2, is 120.7 kcal·mol^{-1}, and is lower than the direct SW found previously (~150-160 kcal·mol^{-1}). The last step is the closure of the cage; I3' is related to $Sc_3N@C_{72}$(10611) by a transition state TS3' that has a lower energy barrier (39.8 kcal·mol^{-1}) than TS2 (the transition state from direct C_2 insertion to C_{70}(hept) without a SW transformation). Thus, the isomerization process in I2 structures could be energetically more feasible than for closed cages.

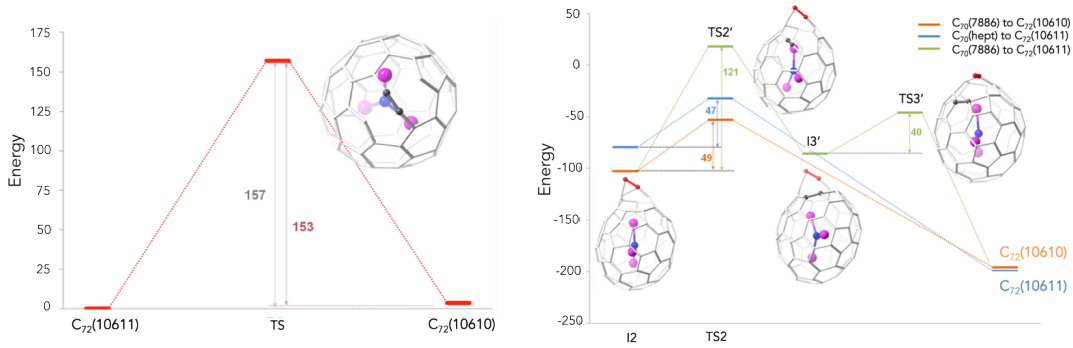

Figure 33. C_2 rearrangements for $Sc_3N@C_{72}$ formed from $Sc_3N@C_{70}$ during carbon insertion with conventional SW in closed fullerenes (left) and 'open structures' (right).

4.4.1.4. Car-Parrinello MD Simulations

We have shown that in the presence of C_2 units, a closed fullerene will tend to grow and that the mechanism may depend significantly on carbon density. At a low carbon concentration the insertion of C_2 could occur more or less as depicted in Figure 31, where C_2 insertions and rearrangements may be sequential. When the carbon density is very high, however, our molecular dynamics simulations suggest that the growth can be more chaotic, as shown in Figure 34.

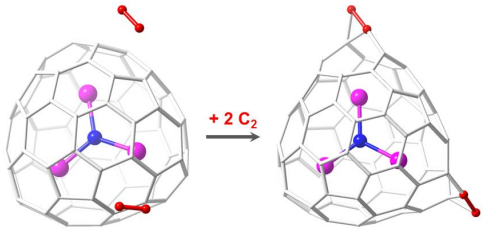

Figure 34. Molecular dynamics simulations show that after a few ps $Sc_3N@D_3$-C_{68}(6140) reacts with two C_2 units giving the structure shown on the right.

D_3-C_{68}(6140) rapidly evolves toward intermediates where two C_2 units are inserted before completing the closure of the cage. In this case, the growth paths are much less predictable. Further exploration is required to develop a detailed mechanism and will

be reported elsewhere. For example, additions of individual carbon atoms or C_3 may also be important in the growth process. We note that for a complete analysis of clusterfullerene formation, other factors need to be considered, such as atomic C and C_3 incorporation and perhaps some local C_2 loss events after bottom-up formation.

4.5. Conclusions

Recently, several mechanisms have been suggested to explain the formation of fullerenes. One of them involves the ingestion of a C_2 unit by an *already* formed fullerene. In this chapter, we have explored this mechanism by means of static DFT and Car-Parrinello molecular dynamics calculations for series of different endohedral fullerenes. By comprehensive exploration of the most favourable isomers, the potential energy surfaces associated with the successive C_2 insertions and the topologies of the involved structures, we conclude the following:

- ✗ The insertion of a C_2 unit to already formed EMF is always an exothermic/exergonic process, independent of the size, insertion site, or symmetry of the cage.

- ✗ The free energy barriers for each step are attainable considering the high temperature at which the processes occur.

- ✗ The most abundant Ti@C_{2n} (2n=26-48) isomers are formally linked by direct C_2 insertions and in a few cases by additional Stone-Wales transformations.

- ✗ Car-Parrinello MD simulations show that after the attack of a C_2 unit to one of the C atoms of the Ti@C_{2n} system, the formation of the second C-C bond that closes the cage is a very unlikely event at the time scale of our simulations, and must be accelerated using metadynamics or via an external collision, for example with He atoms that are present in the sample. Clearly, this is an extremely infrequent event that justifies the low abundance of small EMFs, only detected using especial spectroscopic techniques.

- ✗ Sc_2C_2@C_s(hept)-C_{88} is the first example of an endohedral carbide fullerene with a heptagon ring on the carbon cage and only the second endohedral fullerene to contain a heptagon. Calculations suggest that this endohedral fullerene

could be a kinetically-trapped species derived from the recently reported $Sc_2C_2@C_{2v}$-C_{86}(9) via a direct C_2 insertion.

- ✗ A simplified growth mechanism that proceeds by simple C_2 insertion reactions and rearrangements from $Sc_3N@D_3$-C_{68} to $Sc_3N@I_h$-C_{80} has been found.

- ✗ A diverse range of reaction paths are possible, however, in the presence of C_2, a closed fullerene tends to always capture carbon units. Interestingly, the iconic I_h-C_{80} cage can be formed from the much smaller D_3-C_{68} species via several routes that involve classical and heptagon-containing intermediates, and a minimal number of C_2 rearrangements. However, the extent of cages formed is not a result of thermodynamics, but rather is related to the carbon cage closure step, in which He gas is expected to play a significant role. Moreover, it is likely some of these predicted intermediates may be isolated and characterized by macroscopic synthesis methods in the future.

- ✗ In the presence of C_2 units, a closed fullerene will tend to grow and the mechanism may depend significantly on carbon density. At a low carbon concentration the insertion of C_2 could occur, where C_2 insertions and rearrangements may be sequential. When the carbon density is very high, however, our molecular dynamics simulations suggest that the growth can be more chaotic.

To sum up, the present theoretical studies provide strong support for the CNG mechanism proposed to explain the empirically observed growth of EMFs.[22] As the size of the carbon cages increases, the free energy barriers associated with C_2 insertion decrease and the collision kinetic energy required to close the cages also become smaller. The results imply that middle-sized endohedral metallofullerenes, 2n > 60, should have similar growth mechanisms. These results do not exclude shrinkage of fullerenes as an important process when the fullerenes abundance are high and the carbon vapour density is low, as Irle and Morokuma have demonstrated.[21] Thus, the endpoint in growth should be controlled by carbon density of the atmosphere surrounding a cage.

4.6. References

(1) Kroto, H. W.; Heath, J. R.; O'Brien, S. C.; Curl, R. F.; Smalley, R. E. *Nature* **1985**, *318*, 162.

(2) Heath, J. R.; Obrien, S. C.; Zhang, Q.; Liu, Y.; Curl, R. F.; Kroto, H. W.; Tittel, F. K.; Smalley, R. E. *J. Am. Chem. Soc.* **1985**, *107*, 7779.
(3) H. C. Dorn; S. Stevenson; G. Rice; T. Glass; K. Harich; F. Cromer; M. R. Jordan; J. Crae; E. Hadju; R. Bible; M. M. Olmstead; K. Maitra; Fisher, A. J.; A. L. Balch *Nature* **1990**, *401*, 55.
(4) Rivera-Nazario, D. M.; Pinzón, J. R.; Stevenson, S.; Echegoyen, L. A. *J. Phys. Org. Chem.* **2013**, *26*, 194.
(5) Chaur, M. N.; Melin, F.; Ortiz, A. L.; Echegoyen, L. *Angew. Chem. Int. Ed.* **2009**, *48*, 7514.
(6) Lu, X.; Feng, L.; Akasaka, T.; Nagase, S. *Chem. Soc. Rev.* **2012**, *41*, 7723.
(7) Popov, A. A.; Yang, S.; Dunsch, L. *Chem. Rev.* **2013**, *113*, 5989.
(8) Rodriguez-Fortea, A.; Balch, A. L.; Poblet, J. M. *Chem. Soc. Rev.* **2011**, *40*, 3551.
(9) Zhang, J. Y.; Stevenson, S.; Dorn, H. C. *Acc. Chem. Res.* **2013**, *46*, 1548.
(10) Rodriguez-Fortea, A.; Alegret, N.; Balch, A. L.; Poblet, J. M. *Nat. Chem.* **2010**, *2*, 955.
(11) Campanera, J. M.; Bo, C.; Poblet, J. M. *Angew. Chem. Int. Ed.* **2005**, *44*, 7230.
(12) Chai, Y.; Guo, T.; Jin, C. M.; Haufler, R. E.; Chibante, L. P. F.; Fure, J.; Wang, L. H.; Alford, J. M.; Smalley, R. E. *J. Phys. Chem.* **1991**, *95*, 7564.
(13) Shinohara, H.; Hayashi, N.; Sato, H.; Saito, Y.; Wang, X. D.; Hashizume, T.; Sakurai, T. *J. Phys. Chem.* **1993**, *97*, 13438.
(14) Adachi, G.-Y.; Imanaka, N.; Zhang, F. *Handbook on the Physics and Chemistry of Rare Earths*, 1991; Vol. 15.
(15) Wakabayashi, T.; Achiba, Y. *Chem. Phys. Lett.* **1992**, *190*, 465.
(16) Shvartsburg, A. A.; Hudgins, R. R.; Dugourd, P.; Gutierrez, R.; Frauenheim, T.; Jarrold, M. F. *Phys. Rev. Lett.* **2000**, *84*, 2421.
(17) Budyka, M. F.; Zyubina, T. S.; Ryabenko, A. G.; Muradyan, V. E.; Esipov, S. E.; Cherepanova, N. I. *Chem. Phys. Lett.* **2002**, *354*, 93.
(18) Irle, S.; Zheng, G. S.; Elstner, M.; Morokuma, K. *Nano Lett.* **2003**, *3*, 1657.
(19) Irle, S.; Zheng, G.; Wang, Z.; Morokuma, K. *J. Phys. Chem. B* **2006**, *110*, 14531.
(20) Zhang, J.; Bowles, F. L.; Bearden, D. W.; Ray, W. K.; Fuhrer, T.; Ye, Y.; Dixon, C.; Harich, K.; Helm, R. F.; Olmstead, M. M.; Balch, A. L.; Dorn, H. C. *Nat. Chem.* **2013**, *5*, 880.
(21) Saha, B.; Irle, S.; Morokuma, K. *J. Phys. Chem. C* **2011**, *115*, 22707.
(22) Dunk, P. W.; Kaiser, N. K.; Hendrickson, C. L.; Quinn, J. P.; Ewels, C. P.; Nakanishi, Y.; Sasaki, Y.; Shinohara, H.; Marshall, A. G.; Kroto, H. W. *Nat. Commun.* **2012**, *3*, 855.

(23) Endo, M.; Kroto, H. W. *J. Phys. Chem.* **1992**, *96*, 6941.
(24) Dunk, P. W.; Kaiser, N. K.; Mulet-Gas, M.; Rodriguez-Fortea, A.; Poblet, J. M.; Shinohara, H.; Hendrickson, C. L.; Marshall, A. G.; Kroto, H. W. *J. Am. Chem. Soc.* **2012**, *134*, 9380.
(25) Dunk, P. W.; Mulet-Gas, M.; Nakanishi, Y.; Kaiser, N. K.; Rodriguez-Fortea, A.; Shinohara, H.; Poblet, J. M.; Marshall, A. G.; Kroto, H. W. *Nat. Commun.* **2014**, *5*, 5844.
(26) Chen, N.; Mulet-Gas, M.; Li, Y. Y.; Stene, R. E.; Atherton, C. W.; Rodriguez-Fortea, A.; Poblet, J. M.; Echegoyen, L. *Chem. Sci.* **2013**, *4*, 180.
(27) Chen, C.-H.; Ghiassi, K. B.; Cerón, M. R.; Guerrero-Ayala, M. A.; Echegoyen, L.; Olmstead, M. M.; Balch, A. L. *J. Am. Chem. Soc.* **2015**, *137*, 10116.
(28) Zhang, Y.; Ghiassi, K. B.; Deng, Q.; Samoylova, N. A.; Olmstead, M. M.; Balch, A. L.; Popov, A. A. *Angew. Chem. Int. Ed.* **2015**, *54*, 495.
(29) Mulet-Gas, M.; Abella, L.; Dunk, P. W.; Rodriguez-Fortea, A.; Kroto, H. W.; Poblet, J. M. *Chem. Sci.* **2015**, *6*, 675.
(30) Chen, C. H.; Abella, L.; Ceron, M. R.; Guerrero-Ayala, M. A.; Rodriguez-Fortea, A.; Olmstead, M. M.; Powers, X. B.; Balch, A. L.; Poblet, J. M.; Echegoyen, L. *J. Am. Chem. Soc.* **2016**, *138*, 13030.
(31) Mulet-Gas, M.; Abella, L.; Cerón, M. R.; Castro, E.; Marshall, A. G.; Rodríguez-Fortea, A.; Echegoyen, L.; Poblet, J. M.; Dunk, P. W. *Nat. Commun.* **2017** *(in press).*
(32) Iannuzzi, M.; Laio, A.; Parrinello, M. *Phys. Rev. Lett.* **2003**, *90,* 238302.
(33) Laio, A.; Parrinello, M. *Proc. Natl. Acad. Sci. USA* **2002**, *99*, 12562.
(34) Laio, A.; Rodriguez-Fortea, A.; Gervasio, F. L.; Ceccarelli, M.; Parrinello, M. *J. Phys. Chem. B* **2005**, *109*, 6714.
(35) Dang, J. S.; Wang, W. W.; Zheng, J. J.; Zhao, X.; Osawa, E.; Nagase, S. *J. Phys. Chem. C* **2012**, *116*, 16233.
(36) Fowler, P. W.; Manolopoulos, D. E. *An atlas of fullerenes* Oxford Univ. Press, Cambridge (UK), 1995.
(37) Eggen, B. R.; Heggie, M. I.; Jungnickel, G.; Latham, C. D.; Jones, R.; Briddon, P. R. *Science* **1996**, *272*, 87.
(38) Ewels, C. P.; Heggie, M. I.; Briddon, P. R. *Chem. Phys. Lett.* **2002**, *351*, 178.
(39) Slanina, Z. k.; Lee, S.-L.; UhlÃ-k, F.; Adamowicz, L.; Nagase, S. *Theor. Chem. Acc.* **2007**, *117*, 315.
(40) Slanina , Z.; Nagase, S. *ChemPhysChem* **2005**, *6*, 2060.
(41) Tan, Y.-Z.; Chen, R.-T.; Liao, Z.-J.; Li, J.; Zhu, F.; Lu, X.; Xie, S.-Y.; Li, J.; Huang, R.-B.; Zheng, L.-S. *Nat. Commun.* **2011**, *2*, 420.
(42) Hernandez, E.; Ordejon, P.; Terrones, H. *Phys. Rev. B* **2001**, *63*, 193403.
(43) Gan, L. H.; Lei, D.; Fowler, P. W. *J. Comput. Chem.* **2016**, *37*, 1907.
(44) Chen, N.; Beavers, C. M.; Mulet-Gas, M.; Rodriguez-Fortea, A.; Munoz, E. J.; Li, Y. Y.; Olmstead, M. M.; Balch, A. L.; Poblet, J. M.; Echegoyen, L. *J. Am. Chem. Soc.* **2012**, *134*, 7851.

(45) Yang, S. F.; Popov, A. A.; Dunsch, L. *Angew. Chem. Int. Ed.* **2007**, *46*, 1256.
(46) Kato, H.; Taninaka, A.; Sugai, T.; Shinohara, H. *J. Am. Chem. Soc.* **2003**, *125*, 7782.
(47) Beavers, C. M.; Chaur, M. N.; Olmstead, M. M.; Echegoyen, L.; Balch, A. L. *J. Am. Chem. Soc.* **2009**, *131*, 11519.

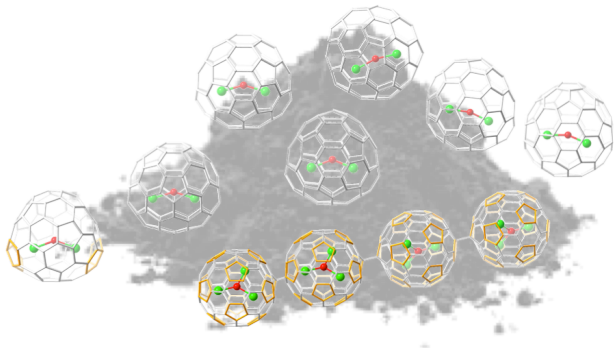

CHAPTER 5

Identifying an Extended

Oxide Clusterfullerene Family

Related Publications:

$Sc_2O@T_d(19151)$-C_{76}: Hindered Cluster Motion Inside a Tetrahedral Carbon Cage Probed by Crystallographic and Computational Studies
Yang, T.; Hao, Y.; Abella, L.; Tang, Q.; Li, X.; Wan, Y.; Rodríguez-Fortea, A.; Poblet, J. M.; Feng, L.; Chen, N. *Chem. Eur. J.* **2015**, 21, 1.

$Sc_2O@C_{2v}(5)$-C_{80}: Dimetallic Oxide Cluster Inside a C_{80} Fullerene Cage
Tang, Q.; Abella, L.; Hao, Y.; Li, X.; Wan, Y.; Rodríguez-Fortea, A.; Poblet, J. M.; Feng, L.; Chen, N. *Inorg. Chem.* **2015**, 54, 9845.

$Sc_2O@C_{3v}(8)$–C_{82}: A Missing Isomer of $Sc_2O@C_{82}$
Tang, Q.; Abella, L.; Hao, Y.; Li, X.; Wan, Y.; Rodríguez-Fortea, A.; Poblet, J. M.; Feng, L.; Chen, N. *Inorg. Chem.* **2016**, 55, 1926.

$Sc_3O@I_h(7)$-C_{80}: A Trimetallic Oxide Clusterfullerene Abundant in the Raw Soot
Abella, L.; Tang, Q.; Zhang, X.; Wang, Y.; Chen, N.; Poblet, J. M.; Rodríguez-Fortea, A. *J. Phys. Chem. C* **2016**, 120, 26159.

Current Status of Oxide Clusterfullerenes
Abella, L.; Wang, Y.; Rodríguez-Fortea, A.; Chen, N.; Poblet, J. M. *Inorg. Chim. Acta* **2017** (in press).

Dimerization of endohedral fullerene in a superatomic crystal
Voevodin, A. A.; Abella, L.; Castro Portillo, E.; Paley, D. W.; Campos, L. M.; Rodríguez-Fortea, A.; Poblet, J. M.; Echegoyen, L.; Roy, X. *Chem. Eur. J.* **2017** (in press).

CHAPTER 5

Identifying an Extended Oxide Clusterfullerene Family

The field of endohedral metallofullerenes has developed extraordinarily since the synthesis and characterization of $Sc_3N@I_h$-C_{80} in 1999, the third most abundant fullerene after C_{60} and C_{70}. During these almost two decades other clusterfullerenes have been trapped inside different IPR and non-IPR fullerenes. Sc_2O has demonstrated to be a good template for middle size fullerenes, between C_{70} and C_{82}, permitting to characterize many structures and determining different physical properties. This chapter will allow the reader to gain insight into the field of fullerenes containing scandium oxide clusters as well as into experimental and theoretical techniques used to characterize them. Part of this work is in collaboration with the group of Prof. Chen at the Soochow University (Suzhou, China).

5.1. Introduction

Among different synthetic methods, clusterfullerenes (CFs) have become the focus of the recent studies, due to their tunable encapsulated structures, high stabilities and relatively high yields. Since the discovery of La@C_{82} in 1991,[1] most of lanthanide metals have been entrapped into the fullerene cages in form of variable clusters. Very recently, Ti and V based CFs were also reported.[2-4] Various families of clusterfullerenes have been synthesized and characterized, such as nitride,[3,5-10] carbide,[11-18] hydrocarbide,[19] carbon nitride,[20] sulfide,[2,21-23] and oxide[24-29] families. Interestingly, the molecular structures of

nitride,[20] sulfide,[2,21-23] and oxide[24-29] families. Interestingly, the molecular structures of most of these CFs intend to follow a somewhat fixed template. For example, nitride clusterfullerenes (NCFs) family is one of the largest families of CFs. However, all the NCFs reported to date followed a trimetallic nitride template, which was first found and proposed by Dorn et al.[30] Sulfide clusterfullerenes (SCFs), on the other hand, follows a dimetallic sulfide template, in which two metal and one sulfur atom form the encapsulated cluster.[21]

However, oxide clusterfullerenes (OCFs) present versatile encapsulated structures that broke the template rule. The first reported OCF was $Sc_4O_2@I_h$-C_{80}(31924), followed by the discovery of $Sc_4O_3@I_h$-C_{80}(31924), which still remains the record as the CF with the largest cluster ever entrapped inside fullerenes.[29,31] These two OCFs shared the same I_h-C_{80} cage with a six-electron metal-to-cage charge transfer, similar to those found for NCFs. Interestingly, in 2010, Stevenson et al. reported a dimetallic OCF, $Sc_2O@C_s$-C_{82}(39715).[29] This OCF demonstrated similar structure and physicochemical properties as SCF $Sc_2S@C_s$-C_{82}(39715).[32] The above three structures reported by Stevenson et al. show that OCFs could be versatile both in the encapsulated clusters and the fullerene cages. However, the extensive family members of OCFs were yet to be explored.

Recently, the experimental group of Prof. Chen reported a novel synthetic method for the preparation of an extensive family of OCFs. With the introduction of CO_2 as oxygen source, a modified arc-discharging method was used and a large family of $Sc_2O@C_{2n}$ ($2n$=70-94) were produced and detected by mass spectrum (MS).[24] Followed by the successful synthesis, they were able to isolate $Sc_2O@C_2$-C_{70}(7892),[24] $Sc_2O@T_d$-C_{76}(19151),[28] $Sc_2O@D_{3h}$-C_{78}(24109), $Sc_2O@C_{2v}$-C_{78}(24107),[27] $Sc_2O@C_{2v}$-C_{80}(31922),[26] and $Sc_2O@C_{3v}$-C_{82}(39717),[25] the single crystal structures of all these OCFs were characterized for the first time and their physicochemical properties have been fully investigated.

In addition, a unique paramagnetic OCF, $Sc_3O@C_{80}$ was isolated and studied by DFT calculations.[33] It is the first discovered neutral paramagnetic species within the OCF family, which is isoelectronic to the anion of the prototypical nitride $Sc_3N@I_h$-C_{80}(31924). The tiny quantity of pure product acquired predicts the polymerization to be a favored process in this trimetallic oxide clusterfullerene. Somewhat related to this polimerization, Prof. Roy group has recently discovered a superatomic crystal of $Lu_3N@C_{80}$ in which the trimetallic clusterfullerene is dimerized in the solid state, presumably as a consequence of the electron transfer from the electron-rich superatom.[34]
This is the very first time that a large family of CFs with extensive cage structures has been fully characterized. The combined theoretical and experimental studies of these

structures show that the cages of these OCFs are correlated with each other. The orientations of the encapsulated dimetallic oxide clusters were also found to be affected by the cage structures. Furthermore, the influence of both cages and clusters on the electrochemical properties of these fullerenes were revealed. Thus, to better understand the correlation between molecular structures and physicochemical properties of the OCFs, in this work, we provided a detailed and comprehensive overview of the current studies of OCFs. The molecular structures and cluster dynamics of these OCFs were discussed extensively including the structures of some missing OCFs, such as $Sc_2O@C_{74}$, which were proposed and studied by DFT calculations. Based on these results, the structural connectivities between fullerene cages of $Sc_2O@C_{2n}$ (2n=70 to 82) were revealed. In addition, the electrochemical properties of these OCFs were summarized to understand the impact of the fullerene cages on their physicochemical properties.

In this chapter we report the combined experimental and computational work developed in order to study and identify some of the new scandium oxide clusterfullerenes, especially $Sc_2O@T_d$-C_{76}(19151), $Sc_2O@C_{2v}$-C_{80}(31922), $Sc_2O@C_{3v}$-C_{82}(39717), and $Sc_3O@C_{80}$.

5.2. Experimental Detection and Isolation

The experimental work was done by members of the research group of Prof. Chen at Soochow University. The scandium oxide clusterfullerenes were synthesized in a conventional Krätschmer-Huffman reactor with an atmosphere of helium and CO_2. The as-produced soot was Soxhlet-extracted with chlorobenzene and the raw extract was subjected to a multi-stage high-performance-liquid chromatography (HPLC) to isolate and purify most of the cages of $Sc_2O@C_{2n}$ family.

Two control experimental synthetic methods had been used to obtain OCFs. Only a trace of $Sc_2O@C_{82}$ was detected with a He/air or with pure He atmospheres. It seems that the introduction of CO_2 causes a significant increase of the relative yields of OCFs and supresses the generation of other clusterfullerenes, such as carbide and nitride clusterfullerenes. Therefore, until now, CO_2 is the best oxygen source for the production of OCFs.

In the present work, as shown in Figure 1, an extended series of scandium OCFs $Sc_2O@C_{2n}$ with cages ranging from C_{70} to C_{94} can be identified in the mass spectrum by

the method described above. $Sc_2O@C_{82}$ was found to be the most abundant fullerene obtained in the mixture of OCF family, and two fractions containing $Sc_2O@C_{82}$ as main products were discovered. Further separation and purification showed that the two purified fractions of $Sc_2O@C_{82}$ have notably different retention times on the same Buckyprep column, which suggests that they are two different isomers of $Sc_2O@C_{82}$.[35] Furthermore, the abundance of these two isomers in the obtained fullerene mixture was found to be equal under the current synthetic conditions. The second most abundant scandium oxide clusterfullerene was the $Sc_2O@C_{78}$, and in this case, also two isomers were separated and purified. $Sc_2O@C_{76}$ and $Sc_2O@C_{80}$ are the third and the fourth most abundant in the range of OCFs family with an estimated product yield of 33 and 20% of the $Sc_2O@C_{82}$, respectively.

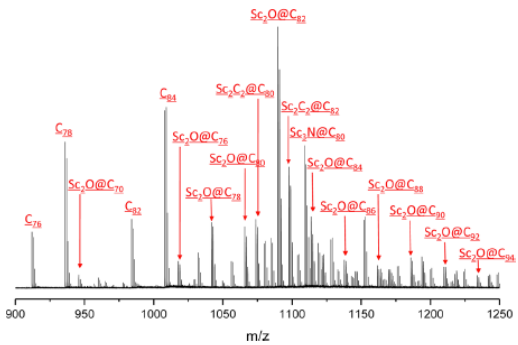

Figure 1. Mass spectra of the raw extract of $Sc_2O@C_{2n}$ (2n=70-94).

The mass characterization was done by matrix-assisted laser desorption/ionization time-of-flight (MALDI-TOF) mass spectrometry. The MALDI-TOF spectrum of the purified sample of the newest $Sc_2O@C_{82}$ isomer obtained shows a single peak at 1089.957 m/z. The MALDI-TOF spectrum of the isolated fractions of $Sc_2O@C_{76}$ and $Sc_2O@C_{80}$ show a single peak at 1018.028 and 1065.986 m/z. In all of these isomers, their molecular weights and their isotopic distributions of the experimental MALDI spectrum agree very well with the theoretical prediction.

The structures of $Sc_2O@C_{76,}$ $Sc_2O@C_{80}$ and $Sc_2O@C_{82}$ (II) were characterized via a single-crystal X-ray diffraction (XRD) study. Cocrystals of $Sc_2O@C_{2n}/[Ni^{II}(OEP)]$ (2n=76, 80, 82) suitable for X-ray analysis were obtained by slow diffusion of a benzene

solution of the corresponding $Sc_2O@C_{2n}$ into a $CHCl_3$ solution of [Ni^{II}(OEP)]. Other X-ray crystallography structures of this OCFs family have also been characterized, but other groups have studied them; $Sc_2O@C_{70}$, $Sc_2O@C_{78}$ and $Sc_2O@C_{82}$ (I).[24,27,29]

5.3. Elucidation of the $Sc_2O@C_{76}$ Structure

When experimentalists detect and isolate a new endohedral metallofullerene, one of the most challenging tasks for theoreticians is to elucidate which one of the thousands of possible isomers is the one found in the experiments. A comprehensive and extensive analysis combining experimental and computational works has to be considered to solve this problem, and sometimes it is not as easy as it could seem. In order to assign the correct isomer, we followed a designed computational strategy taking into account all the key factors that govern the stabilization of the endohedral metallofullerenes.

5.3.1. Looking for the Best C_{76} Candidates to Encapsulate Sc_2O

Besides the experimental characterization of $Sc_2O@C_{76}$, we have performed a computational study to assign the C_{76} cage symmetry. For a C_{76} cage there are 19151 isomers, but only two isomers (one D_{2h} isomer and one T_d isomer) follow the isolated pentagon rule.

We have computed (BP86/TZP) the energies of the tetraanions for all cages with two or less adjacent pentagon pairs (APP): 2 IPR isomers, 12 APP1 isomers and 134 APP2 isomers. The lowest-energy tetraanionic cages, within a range of 40 kcal·mol^{-1}, were selected and the corresponding $Sc_2O@C_{76}$ structures were optimized. Different orientations of the Sc_2O cluster in IPR and APP1 cages were taken into account.

An exhaustive analysis of some parameters for the IPR, APP1 and APP2 isomers was performed, such as the number of pyracylenes and the measure for the separation among the twelve pentagons present in a fullerene cage, provided by the Inverse Pentagon Separation Index.[36]

The IPR cage T_d-C_{76}(19151) was found to be, by a large difference, the lowest-energy tetraanion and the lowest-energy OCF as well (Table 1 and Figure 2). The non-IPR

C_{76}(19138), with a single APP, is the second most stable isomer for both tetraanion and OCF (at 13.7 kcal·mol^{-1}). These two cages show the lowest number of pyracylenes within the IPR and APP1 subsets as usually found for the most stable and characterized clusterfullerenes.[36,37] The third most stable $Sc_2O@C_{76}$ isomer, C_{76}(17459), which is not correlated with the third most stable tetraanion, is found at 20.2 kcal·mol^{-1}. The rest of OCFs are higher in energy, more than 22 kcal·mol^{-1}. The first non-IPR scandium oxide clusterfullerene isomer with two adjacent pentagon pairs is the C_{76}(17491) cage, which is quite high in energy (around 26.8 kcal·mol^{-1}).

Table 1. List of the relative energies (in kcal·mol^{-1}) for the lowest-energy isomers of C_{76}^{4-} and $Sc_2O@C_{76}$.[a]

Isomer	APP	C_{76}^{4-}	$Sc_2O@C_{76}$
19151	0	0.0	0.0
19138	1	15.5	13.7
17459	1	24.5	20.2
17750	1	31.8	22.7
17894	1	31.6	25.4
17418	1	30.9	25.6
17491	2	30.1	26.8
19142	1	29.5	28.3
17508	2	32.1	28.6
17490	2	19.8	29.8
17465	2	28.1	30.7
19150	0	32.9	31.0

[a]Isomer number according to the spiral algorithm of Fowler and Monopoulos. APP: number of adjacent pentagon pairs.

As a general trend for the lowest-energy isomers shown in Table 1, the relative stabilities of OCF (fourth column) are somewhat smaller than those of tetraanions (third column), which might indicate that the interactions between Sc_2O and non-IPR cages are more favorable than for IPR cages. This stabilization, however, is not enough to reverse the stability trend predicted by the ionic model, i.e. tetraanions, as found for other clusterfullerenes.[22]

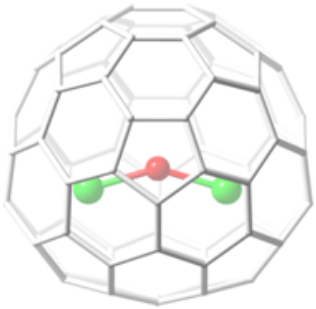

Figure 2. DFT-optimized structure for the lowest-energy $Sc_2O@C_{76}$ isomer, $Sc_2O@T_d$-C_{76}(19151). Scandium atoms are represented in green and oxygen atom in red.

The computations and analysis of the different isomers of C_{76}, in tetraanion and endohedral forms, lead us to select the T_d-C_{76}(19151) cage as the candidate isomer to encapsulate the Sc_2O cluster. Therefore, we suggest that $Sc_2O@T_d$-C_{76}(19151) is the isomer detected and isolated in the experiments. However, to confirm or discard the selection, a comparison between all the available experimental data and the computed properties is needed.

5.3.2. Formal Electron Transfer

Four electrons is the formal electron transfer for the $Sc_2O@C_{76}$, but it has to be confirmed. Thus, an analysis of the orbital interaction diagram for the endohedral fullerene from the corresponding C_{76} and Sc_2O fragments was performed to check it.

From an analysis of the frontier molecular orbitals of $Sc_2O@T_d$-C_{76}(19151), we can see the molecular orbitals of the clusterfullerene as a result of the interaction between the orbitals of each fragment, C_{76} and Sc_2O.

We have verified that a formal transfer of four electrons from Sc_2O to the C_{76} cage takes place, $(Sc_2O)^{4+}@(C_{76})^{4-}$, as shown in the orbital interaction diagram in Figure 3. The Highest Occupied Molecular Orbital (HOMO) and the Lowest-Unoccupied Molecular Orbital (LUMO) are mainly localized on the C_{76} framework, so the first oxidation and reduction take place in the cage.

Therefore, the electronic structure can be explained by the ionic model with a formal transfer of four electrons from the cluster to the cage, as for the rest of clusterfullerenes containing Sc_2X (X = O or S) known so far.[21,22,35,38]

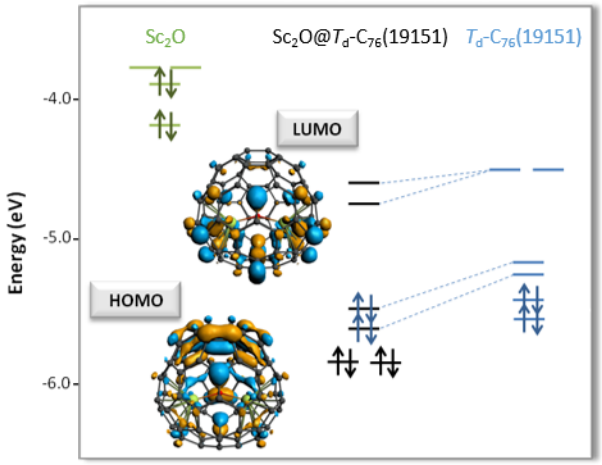

Figure 3. Orbital interaction diagram for $Sc_2O@T_d$-C_{76}(19151). The fragments Sc_2O and T_d-C_{76}(19151) are calculated with the geometry that they have in the OCF.

5.3.3. Thermal and Entropic Effects

Taking into account the possible effects of the high temperatures reached in the reactor during the fullerene synthesis, an analysis of the molar fractions was studied for the selected $Sc_2O@C_{76}$ isomers.

The molar fractions of the lowest-energy $Sc_2O@C_{76}$ isomers as a function of the temperature were computed using the rigid rotor and harmonic oscillator (RRHO) approximation and the related free-encapsulating model (FEM) as proposed by Slanina.[39,40] The difference between both approximations is the rotation of the cluster inside the cage. In case of FEM approximation, the cluster can move freely inside the spherical cage, so it would be the most suitable in case of the IPR cages, but not for the non-IPR isomers. Metal atoms or clusters are found near to the pentalenes motifs in non-IPR cages, so the movement inside the cage is much more restricted. This is the reason why RRHO approximation should be preferred when considering non-IPR isomers.

The two approximations predict $Sc_2O@T_d$-C_{76}(19151) as the most abundant isomer for the whole temperature range up to 4000 K (Figure 4). The abundance of isomer $Sc_2O@C_{2v}$-C_{76}(19138) increases slightly at very high temperatures, but only to around

15 and 5% of the total in FEM and RRHO approximations, respectively. This result is in striking contrast with the predictions made by Zhao, Nagase and co-workers for the detected, but not yet characterized $Sc_2S@C_{76}$, in which $Sc_2S@T_d$-C_{76}(19151) was the lowest-energy isomer at 0K, but an inversion of the relative abundances was observed at high temperatures.[41] Consequently, we consider the $Sc_2O@T_d$-C_{76}(19151) to be most stable and abundant isomer in the whole range of temperatures.

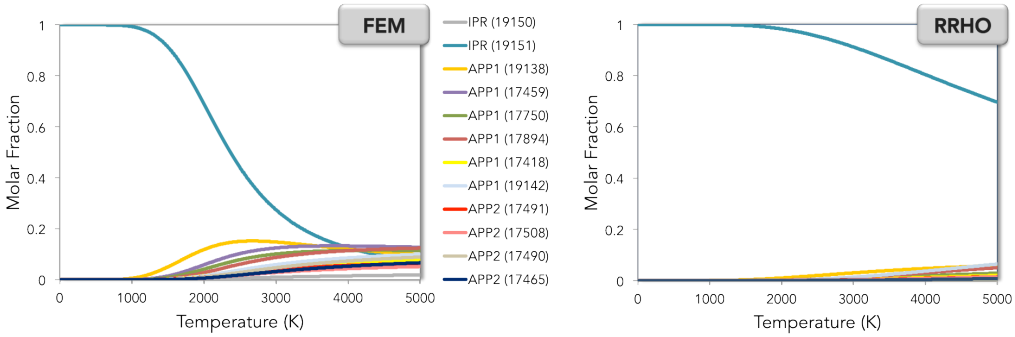

Figure 4. Predicted molar fractions within the FEM and RRHO approximations as a function of temperature for twelve different isomers of $Sc_2O@C_{76}$.

5.3.4. Electrochemical Studies

We have studied the electrochemistry for the $Sc_2O@T_d$-C_{76}(19151) and $Sc_2O@C_{2v}$-C_{76}(19138) isomers (Table 2). The computed HOMO-LUMO gaps are found to be 0.78 and 0.63 eV, respectively. Comparing the redox potentials and the electrochemical gaps for both C_{76} isomers, we assume that $Sc_2O@T_d$-C_{76}(19151) correlates better with the experimental electrochemistry data. The CV of $Sc_2O@T_d$-C_{76}(19151) exhibits five reduction peaks and one oxidation peak.[28] The first reduction process and oxidation process are electrochemically reversible, which agree with the theoretical results predicting that both the first reduction and the oxidation processes are cage based instead of cluster based. The second and third reduction peaks are essentially overlapping with each other and are obviously irreversible. The fourth reduction process, however, turned out to be electrochemically reversible again, which is a rare case in the study of electrochemical behaviour of the clusterfullerenes.[42,43]

Table 2. Computed (V vs Fc^+/Fc) first and second oxidation and reduction potentials, and electrochemical (EC) gaps for selected candidates of $Sc_2O@C_{76}$ along with the experimental values.[a)]

OCF	$E^{+/2+}$	$E^{0/+}$	$E^{0/-}$	$E^{-/2-}$	EC
C_{76}(19151)	0.71	0.15	-1.00	1.49	1.15
C_{76}(19138)	0.41	0.09	-0.98	-	1.07
Exp.	-	0.32	-0.91	-1.40	1.23

[a)]All redox potentials are given in V and orbital energies in eV; computed values in o-dichlorobenzene.

Up to the discovery of $Sc_2O@T_d$-C_{76}(19151), electrochemical studies of OCFs have been carried out for only two structures, $Sc_4O_2@I_h$-C_{80}(31924) and $Sc_2O@C_s$-C_{82}(39715).[31,32] $Sc_4O_2@I_h$-C_{80}(31924) demonstrated cluster-based electrochemical processes which agrees with the localization of the HOMO and LUMO orbitals on the oxide cluster.[31,44] $Sc_2O@C_s$-C_{82}(39715), on the other hand, shows cage-based redox processes.[32] The electrochemical behaviour of $Sc_2O@T_d$-C_{76}(19151) shows much more similarity to that of the $Sc_2O@C_s$-C_{82}(39715) rather than $Sc_4O_2@I_h$-C_{80}(31924). The computed HOMO and LUMO orbitals (Figure 3), as well as the spin density on the reduced and oxidized states of $Sc_2O@T_d$-C_{76}(19151) (Figure 5), confirm that the first reduction and oxidation of $Sc_2O@T_d$-C_{76}(19151) are also cage based processes. The computed first cathodic and first anodic potentials (-1.00 and 0.15 V), second cathodic potential (-1.49 V), as well as the electrochemical gap (1.15 V) agree reasonably well with experiment within the typical error found for other families of clusterfullerenes.[22,44]

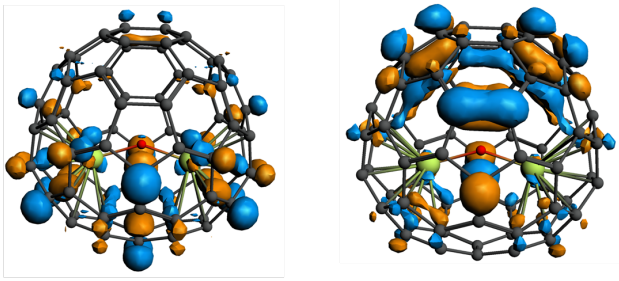

Figure 5. Spin density on the reduced (left) and oxidized (right) states of $Sc_2O@T_d$-C_{76}(19151).

5.3.5. UV-vis-NIR Absorption Spectroscopy

Although an UV-vis-NIR spectrum is not a conclusive result to determine the cage found in experiments, it is sometimes important to perform and use it because it helps in the characterization. The purified sample has a deep green colour in toluene and CS_2 solution (Figure 6) and was further characterized by UV-vis-NIR absorption. The characteristic features of this spectrum include major absorptions peaks at 651, 713, 836 nm along with two broad absorptions at 1136 and 1377 nm.

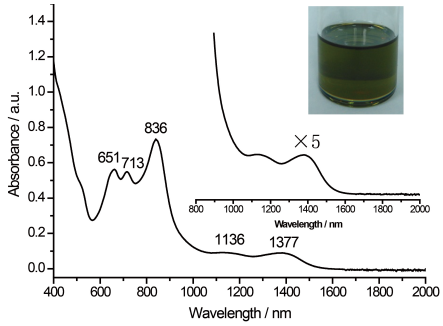

Figure 6. UV-vis-NIR absorption spectrum of $Sc_2O@T_d$-C_{76}(19151) in CS_2 solution; experimental. The insets show the enlarged spectral range (1000-1600 nm) and the photograph of $Sc_2O@T_d$-C_{76}(19151) dissolved in CS_2.

These features are very similar to those of reported $Lu_2@C_{76}$, suggesting an identical cage structure shared by the two endohedral fullerenes.[45] On the other hand, these absorption features are essentially different from those of the $DySc_2N@C_s$-C_{76}(17490), indicating a major difference on the cage symmetry and the charge transfer between the clusters and outside carbon cages.[46] On the basis of absorption onset at 1587 nm, the optical bandgap of this compound was estimated to be 0.79 eV. Using 1.0 eV as the limit to distinguish large and small band gap fullerenes, we can assign this isomer of $Sc_2O@T_d$-C_{76}(19151) to a small band gap fullerene. This bandgap is notably smaller than that of the $DySc_2N@C_s$-C_{76}(17490) (0.96 eV), again suggesting a major difference on the electronic structures of the two C_{76} based clusterfullerenes. On the other hand, although sharing the same cage symmetry, the bandgap for $Sc_2O@T_d$-C_{76}(19151) is larger than 0.69 eV for $Lu_2@T_d$-C_{76}, which verified again the significant impact of the encaged species on the electronic structures of the endohedral fullerenes. The

HOMO-LUMO gaps for these two endohedral fullerenes that share the same high-symmetry C_{76} cage correlate with the experimental optical bandgaps: 0.75 eV for $Sc_2O@T_d$-C_{76}(19151) and 0.45 eV for $Lu_2@T_d$-C_{76}(19151).

We computed the UV-vis-NIR spectrum using time-dependent (TD) DFT for both candidates of $Sc_2O@C_{76}$ isomers. The spectrum computed for $Sc_2O@T_d$-C_{76}(19151) agrees rather well with the experimental one. We have found the following transitions: 707, 763, 902, 1189 and 1480 nm, while the experimental ones were obtained at 654, 705, 833, 1150 and 1373 nm. On the other hand, the predicted transitions for 19138 isomer are: 655, 806, 1006, 1173 and 1708 nm, which do not correlate very well with the experimental one.

The TDDFT predictions for the most intense lowest-energy excitations in the absorption spectrum of the IPR cage, $Sc_2O@T_d$-C_{76}(19151), and the non-IPR cage $Sc_2O@C_{2v}$-C_{76}(19138) are listed in Table 3.

Table 3. TDDFT predictions for the most intense lowest-energy excitations in the absorption spectrum of $Sc_2O@T_d$-C_{76}(19151) and $Sc_2O@C_{2v}$-C_{76}(19138) isomers.

E(eV)	λ (nm)	*f* [a]	Leading configurations (%)[b]
$Sc_2O@T_d$-C_{76}(19151)			
0.838	1480	0.00605	HOMO → LUMO (98)
1.043	1189	0.00094	HOMO → LUMO +1 (96)
1.253	989	0.00578	HOMO -1 → LUMO +1 (94)
1.375	902	0.02563	HOMO -3 → LUMO (89)
1.625	763	0.02472	HOMO → LUMO +2 (74)
1.753	707	0.01161	HOMO -1 → LUMO +2 (91)
1.935	641	0.00459	HOMO -2 → LUMO +2 (92)
$Sc_2O@C_{2v}$-C_{76}(19138)			
0.726	1708	0.00505	HOMO → LUMO (99)
1.057	1173	0.00297	HOMO -1 → LUMO (99)
1.233	1006	0.00124	HOMO -2 → LUMO (98)
1.538	806	0.00123	HOMO -2 → LUMO +1 (85)
1.626	762	0.00543	HOMO -3 → LUMO (87)
1.760	705	0.00562	HOMO -1 → LUMO +2 (86)
1.892	655	0.00233	HOMO -3 → LUMO +1 (91)

[a] Only excitations with f (oscillator strength) > 0.001 are listed. [b] Contributions more than 70 %.

Therefore, we could assume that the computed UV-vis-NIR spectrum of $Sc_2O@T_d$-C_{76}(19151) using time-dependent DFT in the vis-NIR region (wavelengths larger than 500 nm) shows reasonable agreement with the experimental one (Figure 6), despite the limitations of the methodology, as found for the SCF family.[22,38]

5.3.6. Crystallographic Study

Cocrystal of $Sc_2O@C_{76}$/[Ni^{II}(OEP)] suitable for X-ray analysis has been successfully obtained by slow diffusion of a benzene solution of $Sc_2O@C_{76}$ into a $CHCl_3$ solution of [Ni^{II}(OEP)]. The molecular structure was resolved and refined in a monoclinic space group C2/m (No. 12). Figure 7 shows the structure of the endohedral fullerene and its relationship to the nickel porphyrin. In this case, the crystallographic data clearly indicate the presence of cage T_d-C_{76}(19151) in this endohedral structure despite the fact that the cage is disordered. To the best of our knowledge, this is the first report of the crystallographic observation of the T_d-C_{76} cage and a tetrahedral symmetry fullerene.

Inside the fullerene cage, two sets Sc_2O unit were identified. The Sc_2O unit is fully ordered relative to each cage orientation. This is different from what was obtained from the crystallographic studies of $Sc_2O@C_s$-C_{82}(39715), in which relative orientations between the cluster and cage are disordered. This difference suggests that, compared to that in the C_{82} cage, in a smaller C_{76} cage, the internal motion of Sc_2O might be more restrained. The performed computational study confirms that $Sc_2O@T_d$-C_{76}(19151) is the most abundant OCF, among the 19151 possible isomers of C_{76}, for the whole range of temperatures.

Optimized (DFT BP86/TZP) structural parameters very similar to those found for the X-ray structure were obtained; for example, 1.884 Å for the Sc−O distance and 146.9° for the Sc−O−Sc angle, to be compared with the values found from X-ray crystallography, 1.825-1.972 Å and 133.9°, respectively (Figure 2 and Figure 7).

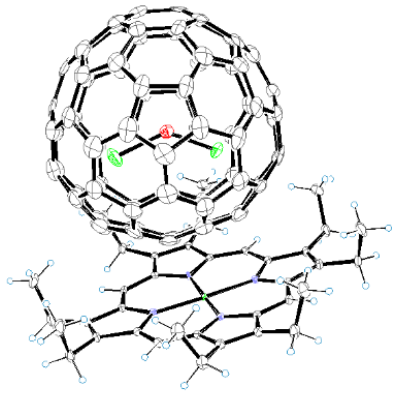

Figure 7. Ortep drawing of $Sc_2O@T_d$-C_{76}(19151)/[Ni^{II}(OEP)] with 25% thermal ellipsoids, showing the relationship between the fullerene cage and [Ni^{II}(OEP)]. Only the major cage orientation with 0.371 occupancy and the major Sc_2O unit with the same occupancy are shown. For clarity, the solvent molecules, minor cage orientation, and minor Sc_2O unit are omitted.

5.3.7. Flexibility of the Cluster

Car-Parrinello MD simulations at temperature of crystallographic determination (80 K), room temperature and temperature of fullerene formation (2000 K) were also done to gain more insight about the motion of the Sc_2O cluster inside the fullerene.[47]

For trajectories that last 14 ps, we have seen that the Sc_2O unit is moving inside the cage, with smaller or larger amplitudes depending on the simulation temperature (Figure 8). At 2000 K, the mobility of the Sc_2O unit to equivalent positions in the highly symmetric fullerene cage is much more evident, as shown in Figure 8. The average Sc-O-Sc angle for the trajectory at 80 K reasonably coincides with the value found by X-ray (MD: 130.0° vs exp: 133.9°), with oscillations of around 10°. Such oscillations become much more marked at higher temperatures, from 100 to 180° at 2000 K, confirming the high flexibility of the Sc_2O unit inside this cage. To help in the determination of the absolute structure of $Sc_2O@T_d$-C_{76}(19151), the two equally suggested orientations of Sc_2O by X-ray analysis were used as starting geometries for two additional Car-Parrinello simulations at 80 K. In one trajectory, the Sc_2O cluster essentially keeps the original (optimal) orientation during 7.2 ps. For the other, however, the cluster changes the initial orientation to finally get the optimal one in 1.5 ps, showing that for the isolated molecule there is only one minimum-energy

orientation. These results are in agreement with geometry optimizations at BP86/TZP level (Table 4).

Table 4. Relative energies (in kcal·mol^{-1}) of several orientations of $Sc_2O@T_d$-C_{76}(19151) isomer.

Isomer	Relative Energy	Isomer	Relative Energy
1	0.5	7	0.2
2	0.3	8	7.3
3	7.3	9	0.0
4	0.2	10	0.2
5	7.2	11	7.6
6	0.2	12	0.1

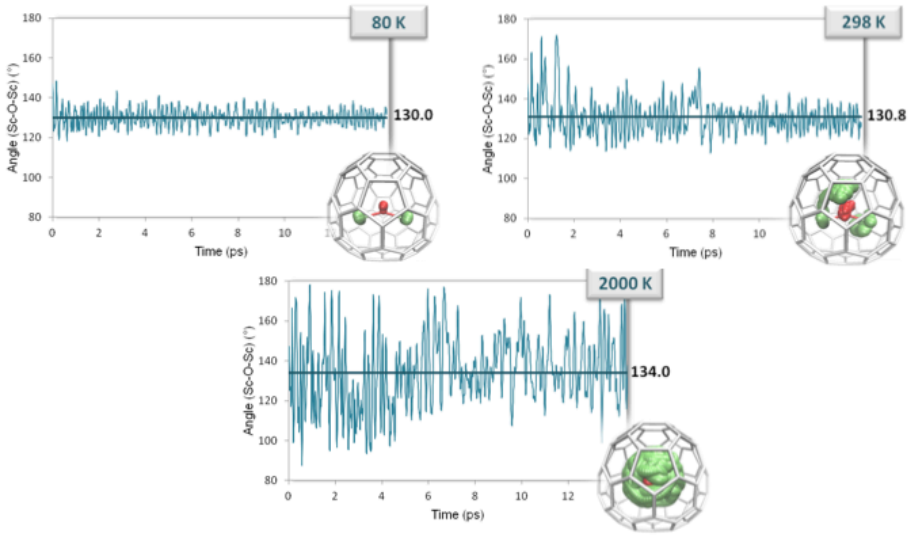

Figure 8. Representation of the motion of the Sc_2O cluster inside the T_d-C_{76} cage during 14 ps-long CPMD trajectories at 80, 298 and 2000 K, as well as the variation of the Sc-O-Sc angle (degrees) along the trajectories. The Sc-O-Sc angle averages are written next to the graphics.

5.4. Identification of $Sc_2O@C_{80}$ structure

In this section, the identification of a new scandium oxide clusterfullerene isolated and characterized by experimentalists is described. This is the case of the cage structure of $Sc_2O@C_{80}$, found in experiments by the group of Prof. Chen. The same strategy designed and explained previously for $Sc_2O@C_{76}$ is also used herein. The single crystal X-ray diffraction data for $Sc_2O@C_{80}$ was also obtained,[26] though it is also important to perform a comparison between the experimental data and computations.

5.4.1. Looking for the Best C_{80} Candidates to Encapsulate Sc_2O

Besides the experimental characterization of $Sc_2O@C_{2v}$-C_{80}(31922), our computations confirmed that the C_{2v}-C_{80}(31922) cage is the most favoured isomer to encapsulate the Sc_2O cluster. For a C_{80} cage there are 31924 isomers, but only seven of them follow the isolated pentagon rule. We assume that a formal transfer of four electrons takes place from the cluster to the cage, as for $Sc_2O@C_{82}$ and $Sc_2O@C_{76}$.

First, we have computed the energies of the tetraanions using DFT at BP86/TZP level for all cages with two or less adjacent pentagon pairs: 7 IPR isomers, 36 APP1 isomers and 415 APP2 isomers. The lowest-energy tetraanionic cages (less than 40 kcal·mol^{-1}) were selected and the corresponding structures of $Sc_2O@C_{80}$ were optimized at the same BP86/TZP level. Different orientations of the Sc_2O cluster in IPR cages were taken into account.

The IPR cage I_h-C_{80}(31924) was found to be the lowest-energy tetraanion, with isomers 31923 and 31922 within a range of less than 10 kcal·mol^{-1}. However, an energy inversion within the IPR isomers is observed when the Sc_2O cluster is encapsulated. In particular, $Sc_2O@D_{5h}$-C_{80}(31923) is found to be the lowest-energy OCF, followed by isomers 31922 and 31924 with relative energies smaller than 4 kcal·mol^{-1} (Table 5). The non-IPR OCFs with one or two APPs show significantly higher energies than IPR isomers.

Cages C_{2v}-C_{80}(31922), D_{5h}-C_{80}(31923) and I_h-C_{80}(31924) show the lowest number of pyracylenes within the IPR subset and the smallest electrostatic contributions to the bond energies, as usually found for the most stable and characterized cluster fullerenes. The optimized structures of isomers $Sc_2O@C_{2v}$-C_{80}(31922), $Sc_2O@D_{5h}$-C_{80}(31923), and $Sc_2O@I_h$-C_{80}(31924), are shown in Figure 9.

Table 5. Relative energies (in kcal·mol^{-1}) for the selected isomers of C_{80} in the tetraanion and endohedral forms.[a)]

Isomer	Sym	APP	C_{80}^{4-}	$Sc_2O@C_{80}$
31923	D_{5h}	0	4.2	0.0
31922	C_{2v}	0	10.4	3.2
31924	I_h	0	0.0	4.0
31876	C_1	1	32.9	11.6
28324	C_1	1	32.7	16.9
31891	C_1	1	32.1	27.4
29558	C_1	2	42.6	29.4
31920	C_{2v}	0	33.8	31.4
31891	C_{2v}	1	36.5	31.9
31921	D_3	0	41.9	32.8

[a)]Isomer number according to the spiral algorithm of Fowler and Manolopoulos.[32] APP: number of adjacent pentagon pairs.

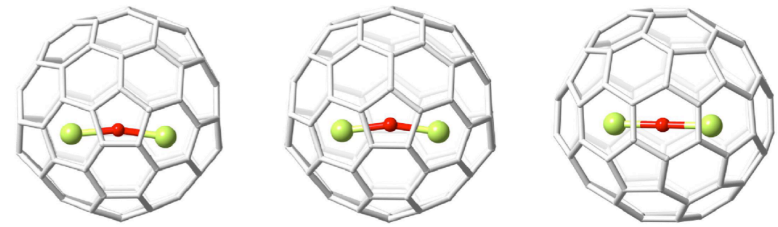

$Sc_2O@C_{2v}$-C_{80}(31922) $Sc_2O@D_{5h}$-C_{80}(31923) $Sc_2O@I_h$-C_{80}(31924)

Figure 9. DFT-Optimized structures of $Sc_2O@C_{2v}$-C_{80}(31922), $Sc_2O@D_{5h}$-C_{80}(31923) and $Sc_2O@I_h$-C_{80}(31924).

5.4.2. Checking the Formal Electron Transfer

We assume that for $Sc_2O@C_{2n}$ family four electrons are formally transferred from the trapped Sc_2O unit to the carbon cage, as previously reported and described for $Sc_2O@C_s$-C_{82}(39115) and $Sc_2O@T_d$-C_{76}(19151). In order to corroborate the charged transferred, an analysis of the frontier molecular orbitals was performed.

From the frontier molecular orbitals, we have reaffirmed that there is a formal transfer of four electrons from the Sc_2O unit to the C_{80} cage, i.e., the ionic model is described as $(Sc_2O)^{4+}@(C_{80})^{4-}$ (Figure 10).

As shown in Figure 10, the frontier orbitals, HOMO and LUMO, are mainly localized on the C_{80} framework. It means that the first oxidation and reduction take place in the cage. Therefore, the ionic model can also explain the electronic structure for $Sc_2O@C_{80}$ with a formal transfer of four electrons from the cluster to the cage, as the rest of $Sc_2O@C_{2n}$ compounds.

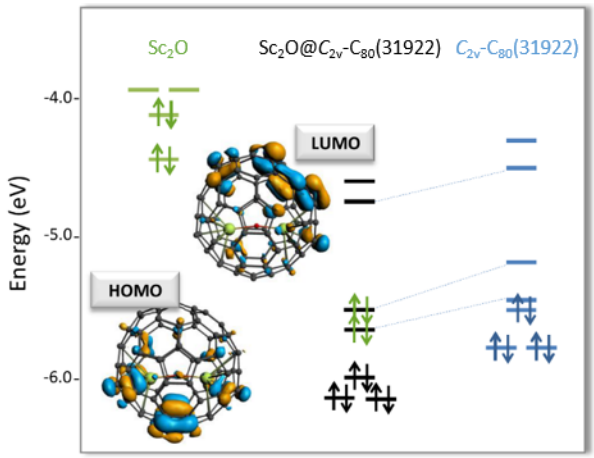

Figure 10. Orbital interaction diagram for $Sc_2O@C_{2v}$-C_{80}(31922). The fragments Sc_2O and C_{2v}-C_{80}(31922) are calculated with the geometry that they have in the OCF.

5.4.3. Thermal and Entropic Effects

Since the energy differences between the different isomers are small, the effect of the high temperatures at which fullerenes are formed can be critical to determine their relative stabilities and abundances.

Hence, we have also computed the molar fractions of these isomers as a function of the temperature (0-4000 K) using the rigid rotor and harmonic oscillator (RRHO)

approximation combined with the related free-encapsulating model (FEM) as proposed by Slanina (Figure 11).[39,40]

The two most abundant isomers are $Sc_2O@D_{5h}$-C_{80}(31923) and $Sc_2O@C_{2v}$-C_{80}(31922), which are related by a single Stone-Wales transformation (Figure 11, right).[26] $Sc_2O@D_{5h}$-C_{80}(31923) dominates at temperatures lower than 1300 K, but $Sc_2O@C_{2v}$-C_{80}(31922) becomes the most abundant isomer at higher temperatures (T > 1300 K). Thus, thermal and entropic contributions are relevant to rationalize the relative abundances of this family of OCFs, i.e. that the $Sc_2O@C_{2v}$-C_{80}(31922) isomer is the one observed in the experiments.

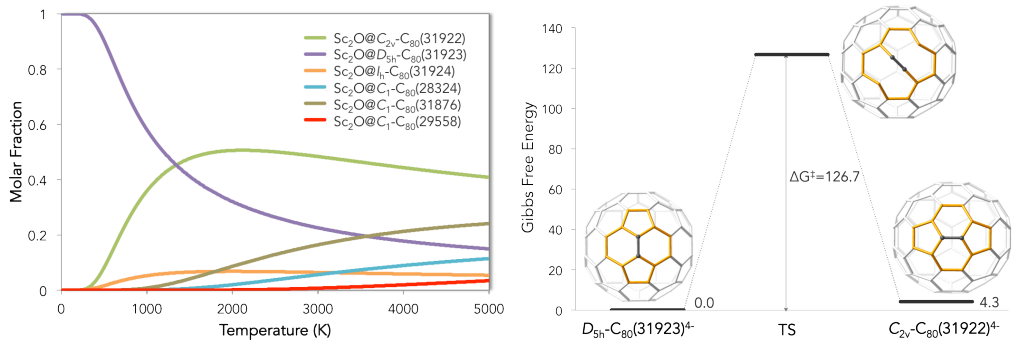

Figure 11. (left) Predicted molar fractions of the lowest-energy $Sc_2O@C_{80}$ isomers as a function of the temperature using the free-encapsulating model (FEM). (right) Free energy profile (in kcal·mol^{-1}) of the Stone-Wales transformation from D_{5h}-C_{80}(31923) to C_{2v}-C_{80}(31922) isomer in tetraanionic states. The free energy barrier is found to be 126.7 kcal·mol^{-1} at 2000 K (and the energy barrier at 0 K is 149.0 kcal·mol^{-1}).

5.4.4. Electrochemistry

The electrochemical properties of $Sc_2O@C_{2v}$-C_{80}(31922) were investigated first by cyclic voltammetry (Table 6). The CV of $Sc_2O@C_{2v}$-C_{80}(31922) shows five reduction and two oxidation peaks. The oxidation processes are completely reversible, which is similar to other OCFs.[24,31,35] On the contrary, the reduction processes, except for a semi-reversible fifth reduction process, are irreversible. In general, this overall redox pattern shows much more resemblance to the CV of $Sc_2C_2@C_{2v}$-C_{80}(31922) than to that of

$Sc_2O@T_d$-C_{76}(19151) and $Sc_2O@C_s$-C_{82}(39715), suggesting its frontier orbitals are more related to cage rather than the encapsulated cluster (frontier orbitals are mainly localized on the cage, Figure 10). The electrochemical gap of $Sc_2O@C_{80}$ is 1.13 V, which is almost identical to that of $Sc_2C_2@C_{2v}$-C_{80}(31922) (1.15 V) but smaller than those of other OCFs discovered so far.

Taking into account the most stable and abundant isomers of $Sc_2O@C_{80,}$ we have computed the oxidation and reduction potentials for $Sc_2O@C_{2v}$-C_{80}(31922) and $Sc_2O@D_{5h}$-C_{80}(31923) isomers (Table 6). Then, these results have been compared with the experimental ones. Both the oxidation and reduction potentials for $Sc_2O@C_{2v}$-C_{80}(31922) are much more similar to the experimental data than for $Sc_2O@D_{5h}$-C_{80}(31923).

Table 6. Experimental (Exp.) and computed oxidation and reduction potentials (in eV) for $Sc_2O@C_{2v}$-C_{80}(31922) and $Sc_2O@D_{5h}$-C_{80}(31923) isomers.

Isomer	$E^{2+/+}$	$E^{+/0}$	$E^{0/-}$	$E^{-/2-}$	EC gap	H-L gap	Bandgap
31922	0.767	0.244	-0.919	-1.438	1.16	0.78	
31923	-	0.284	-0.413	-	0.70	0.28	
Exp.	0.56	0.24	-0.89	-1.48	1.13		0.78

The computed HOMO-LUMO gaps for $Sc_2O@C_{2v}$-C_{80}(31922) and $Sc_2O@D_{5h}$-C_{80}(31923) are found to be 0.794 and 0.293 eV, respectively. The computed electrochemical (EC) gaps are 1.163 eV for the 31922 isomer and 0.697 eV for the 31923 isomer. The results for $Sc_2O@C_{2v}$-C_{80}(31922) are in much better agreement with the experimental ones than those for $Sc_2O@D_{5h}$-C_{80}(31923), the other isomer that is predicted to have a non-negligible abundance at high temperatures.

5.4.5. UV-vis-NIR Spectra

The purified sample presents a deep brown colour in CS_2 solution. Figure 12 shows that the overall absorption pattern of $Sc_2O@C_{2v}$-C_{80}(31922) closely resembles that of the $Sc_2C_2@C_{2v}$-C_{80}(31922).[48] Both of the spectra are featured by major absorptions at

ca. 650 nm and 800 nm. Since the UV-vis-NIR absorption has been universally acknowledged as the fingerprint signature to the assignment of the fullerene cages and their electronic structures, these results verified that the cage symmetry of $Sc_2O@C_{80}$ is identical to that of the $Sc_2C_2@C_{2v}$-C_{80}(31922). However, despite the overall resemblance, some notable differences have also been observed in two absorption spectra. Particularly, while the absorption spectrum of $Sc_2C_2@C_{2v}$-C_{80}(31922) demonstrates a triplet absorption peak at 656 nm, $Sc_2O@C_{2v}$-C_{80}(31922) shows a singlet absorption peak. Additionally, the minor absorption peak at 558 nm in the spectrum of $Sc_2O@C_{2v}$-C_{80}(31922) is not visible in the same absorption range in the spectrum of $Sc_2C_2@C_{2v}$-C_{80}(31922). The different endohedral clusters likely cause these differences. These differences suggest that, though sharing the same cage and electronic structure, the cluster-cage interactions in $Sc_2O@C_{2v}$-C_{80}(31922) and $Sc_2C_2@C_{2v}$-C_{80}(31922) are somewhat different, which leads to a noticeable impact on the energy distribution of frontier molecular orbitals and hence the excitation spectra.

The absorption onset of $Sc_2O@C_{2v}$-C_{80}(31922) is around 1585 nm, suggesting an optical gap of 0.78 eV. Optical gap roughly corresponds to the HOMO−LUMO gap and shows if molecule is kinetically stable or not. Using 1.0 eV as the limit to distinguish large and small bandgap, we can assign $Sc_2O@C_{2v}$-C_{80}(31922) as small bandgap molecule. This band gap is very close to 0.79 eV for $Sc_2O@T_d$-C_{76}(19151).

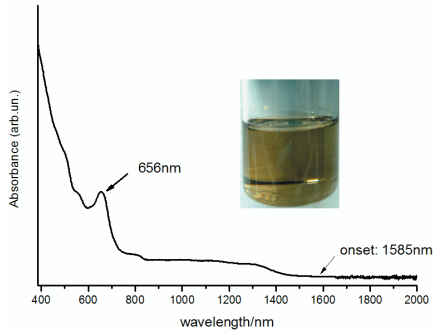

Figure 12. UV-vis-NIR spectrum of $Sc_2O@C_{2v}$-C_{80}(31922) in CS_2; inset shows the colour of $Sc_2O@C_{2v}$-C_{80}(31922) in CS_2 solution.

We have also computed the UV-vis-NIR spectrum using time-dependent (TD) DFT for the two $Sc_2O@C_{80}$ candidate isomers. While the experimental transitions have been obtained at 538~596, 656 and 766~850 nm, the computed values are the following;

transitions for $Sc_2O@C_{2v}$-C_{80}(31922) are 643, 683, 915, 967, 1017, 1199 and 1453 nm, and for $Sc_2O@D_{5h}$-C_{80}(31923) are 522, 527, 1348, 1692, 1825 and 1884 nm. In addition, the TDDFT predictions for the most intense lowest-energy excitations in the absorption spectrum for both selected IPR C_{80} cages have also been analyzed.[26] Therefore, the spectrum computed for $Sc_2O@C_{2v}$-C_{80}(31922) compares rather well with the experimental one (Figure 13).

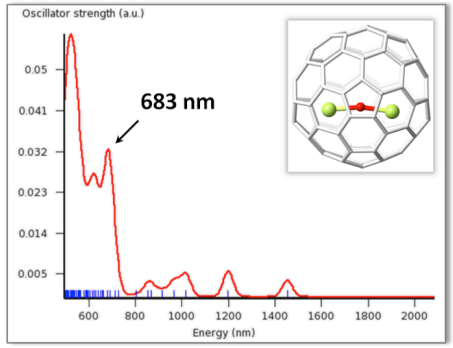

Figure 13. Computed UV-vis-NIR spectrum for $Sc_2O@C_{2v}$-C_{80}(31922) isomer.

All the results confirm $Sc_2O@C_{2v}$-C_{80}(31922) as the isolated OCF with formula $Sc_2O@C_{80}$. The other predicted isomer with lower abundance would be $Sc_2O@D_{5h}$-C_{80}(31923), but it shows a very low HOMO-LUMO gap, and consequently, very low kinetic stability, which makes it more difficult to isolate in case it were formed. It is true that both the experimental electrochemical properties and UV-vis-NIR spectrum for $Sc_2O@C_{80}$ and $Sc_2C_2@C_{2v}$-C_{80}(31922) show some differences, but they should be due to the different encapsulated cluster. The differences in the first oxidation and reduction potentials for $Sc_2O@C_{2v}$-C_{80}(31922) and $Sc_2C_2@C_{2v}$-C_{80}(31922) (around 150 mV) are larger than for other cluster fullerenes that share the same cage (usually the differences are less than 100 mV).[26] Since the two peaks are shifted the same value, the EC gap is almost the same for the oxide and the carbide CFs. Regarding their UV-vis-NIR spectra, the most significant features for the two CFs are reproduced by computations, in particular the spectral onset and the characteristic features between 600 and 700 nm.

5.4.6. Motion of the Sc_2O Cluster Inside the C_{80} Cage

Car-Parrinello MD simulations at room temperature and at a higher temperature nearer to conditions of fullerene formation (2000 K) for $Sc_2O@C_{2v}$-C_{80}(31922) have been done in order to gain more insight into the cluster behaviour inside the corresponding fullerene cage. We have seen that, at 2000 K, the Sc_2O unit is moving rather freely inside the fullerene cage during the short simulation time (15 ps), as supposed by the FEM model. At room temperature, we observe a significant motion of the cluster at the short time scale of the simulations (15 ps), which makes us infer that free rotation is operative on the NMR time scale. The motion of the Sc_2O unit during the Car-Parrinello MD trajectories at temperatures, 298 and 2000 K, is shown in Figure 14. Oscillations of the Sc-O-Sc angle are much more important at higher temperature. The average of the angle is 155° at 298 K and 146° at 2000 K. The standard deviations are 10° and 17°, respectively.

Figure 14. Representation of the motion of the Sc_2O cluster inside the C_{2v}-C_{80}(31922) cage during 15 ps at 298 (left) and 2000 K (right).

5.4.7. Crystallographic Data

The structure of $Sc_2O@C_{80}$ was characterized via a single-crystal X-ray diffraction (XRD) study. Cocrystals of $Sc_2O@C_{80}$/[Ni^{II}(OEP)] suitable for X-ray analysis were obtained by slow diffusion of a benzene solution of $Sc_2O@C_{80}$ into a $CHCl_3$ solution of [Ni^{II}(OEP)]. The molecular structure was resolved and refined in a C2/m (No. 12) space group. Figure 15 shows the X-ray structure of this OCF and its relationship with the adjacent [Ni^{II}(OEP)] moiety.

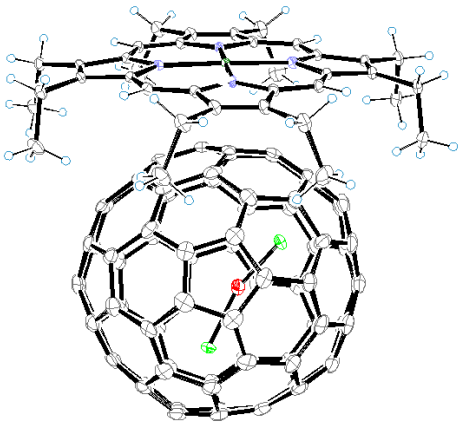

Figure 15. ORTEP drawing of $Sc_2O@C_{2v}$-C_{80}(31922)/[Ni^{II}(OEP)] with 30% thermal ellipsoids, showing the relationship between the fullerene cage and [Ni^{II}(OEP)]. For clarity, the solvent molecules, minor cage orientation, and minor Sc_2O unit are omitted.

The crystallographic data clearly suggest a C_{2v}-C_{80}(31922) cage with an endohedral Sc_2O cluster. Particularly, the C_{2v}-C_{80}(31922) cage is disordered in two orientations with fractional occupancies of 0.421 and 0.079, respectively, and only the major orientation is shown in Figure 15. Theoretical calculations also determine that the absolute structure of $Sc_2O@C_{2v}$-C_{80}(31922) is the one shown in Figure 15. The DFT-optimized structure of $Sc_2O@C_{2v}$-C_{80}(31922) presents the following Sc-O distances; 1.90 Å for Sc1 and 1.93 Å for Sc2, and the Sc1-O-Sc2 angle 164.2°, in rather good agreement with the X-ray data.[26] Therefore, we find that the DFT-optimized structure of $Sc_2O@C_{2v}$-C_{80}(31922) is very close to that of the X-ray model.

5.4.8. The Effect of the Cluster: Sc_2O versus Sc_2C_2

To this end, it is informative to compare the Sc_2O unit in $Sc_2O@C_{2v}$-C_{80}(31922)[Ni^{II}(OEP)] with the already reported Sc_2C_2 unit in $Sc_2C_2@C_{2v}$-C_{80}(31922)[Ni^{II}(OEP)] since either unit is rather fixed inside the corresponding C_{2v}-C_{80}(31922) cage.[15] A close observation reveals that the positions of the two major Sc sites in $Sc_2O@C_{2v}$-C_{80}(31922)·[Ni^{II}(OEP)] are almost identical: each site approaches the [6,6] bond of a pyracylene unit (fused six-membered rings with abutted pentagons) with the shortest Sc-cage contacts ranging from 2.23 to 2.25 Å. However, it shows differences from the previous observation of $Sc_2C_2@C_{2v}$-C_{80}(31922)[Ni^{II}(OEP)], in which one Sc atom is close to the [6,6] bond whereas the other approaches a hexagonal ring.[15] This observation is also consistent with the differences on their ^{45}Sc NMR spectra and suggests that, despite the close resemblance between the electronic structures of these two molecules, subtle differences do exist in their crystal structures as well as the interactions between the clusters and corresponding cages.[15]

On the other hand, despite the minor differences, for both EMFs the two Sc atoms within each cluster are still in the vicinity of pyracylene units. This might indicate that, for these dimetallic cluster fullerenes, there is a significant interaction between the metal and pyracylene unit. In fact, for C_{2v}-C_{80}(31922), 10 out of the 12 pentagons which are the faces that concentrate the negative charge,[36] are involved in the 9 pyracylene units that are present in the structure.

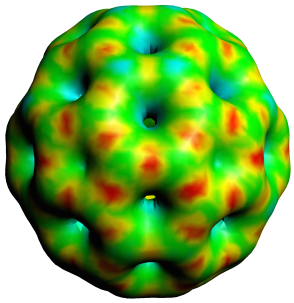

Figure 16. Molecular Electrostatic Potential for isomer C_{2v}-C_{80}(31922)$^{4-}$.

The computed molecular electrostatic potential (MEP) (Figure 16) for the cage tetraanion shows that, for both the Sc_2O and Sc_2C_2 clusters, one of the Sc ions binds to the most nucleophilic pyracylene unit and the second Sc ion is placed near other pyracylene while preserving the structure of the cluster. It thus confirms the remarkable ionic (electron transfer) interactions between the metals and the pyracylene units, which combine with the non-negligible covalent interactions also present in these OCFs.[42]

5.5. $Sc_2O@C_{3v}$-C_{82}(39717): A Missing Isomer of $Sc_2O@C_{82}$

The first dimetallic OCF was reported in 2010,[49] where two isomers were investigated by computational studies but only one of them, $Sc_2O@C_s$-C_{82}(39715) was discovered in the lab. To this end, the other predicted isomer, $Sc_2O@C_{3v}$-C_{82}(39717) remained missing from experimental studies. Now, with the finding of OCFs family (i.e., $Sc_2O@C_{2n}$, n=70-94) by using carbon dioxide as the oxygen source,[50] both C_{82} isomers, $Sc_2O@C_s$-C_{82}(39715) and $Sc_2O@C_{3v}$-C_{82}(39717), are also generated and in an equal abundance. The structure of $Sc_2O@C_{3v}$-C_{82}(39717) was characterized by single crystal X-ray diffraction.[25] As for other Sc sites, they show random locations inside the cage and it is not easy to further pair them or assign them to either cage. The presence of these multiple Sc sites seems to indicate a free rotation of the Sc_2O cluster inside the C_{3v}-C_{82}(39717) cage. Such a cluster movement is different from the situation found in $Sc_2O@C_s$-C_{82}(39715),[49] where the Sc_2O cluster is rotating along a band composed of 10

continuous hexagons, suggesting a major effect of cage structure on the cluster movement.

5.5.1. Confirming the Disordering of Sc_2O Inside the C_{3v}-C_{82}(39717)

In order to confirm that the Sc_2O cluster is disordered inside the C_{3v}-C_{82}(39717) cage, we calculated several orientations of Sc_2O for the selected cage. The optimization of those X-ray structures with the largest occupations factors showed a small displacement of the Sc_2O cluster associated with an enlargement of the Sc-O-Sc angle (Table 7 and Figure 17). The energies of these optimized structures are all rather similar, within 4 kcal mol^{-1}, and very similar to those found for the most-favored orientation of the cluster inside the C_{3v}-C_{82}(39717) cage (Figure 17).[49] Therefore, the cluster can rotate and change the Sc-O-Sc angle easily at rather low temperatures, as it is also confirmed by Car-Parrinello simulations (see below). The optimized angles are somewhat larger (around 160 degrees) than those found in the X-ray structure (130-150 degrees), which indicates considerable flexibility of the Sc_2O unit.

Table 7. Relative energies (E_{rel}) for the four different orientations of the Sc_2O cluster inside the C_{3v}-C_{82}(39717) cage derived from the crystallographic data. Ref corresponds to the lowest-energy orientation found in ref 35. Energies in kcal·mol^{-1} and angles in degrees.

Orientation	E_{rel}	Angle X-ray	Angle Opt
1	1.3	131.2	157.1
2	1.4	148.9	159.0
3	4.2	148.8	160.0
4	2.2	131.0	159.0
Ref	0.0		155.8

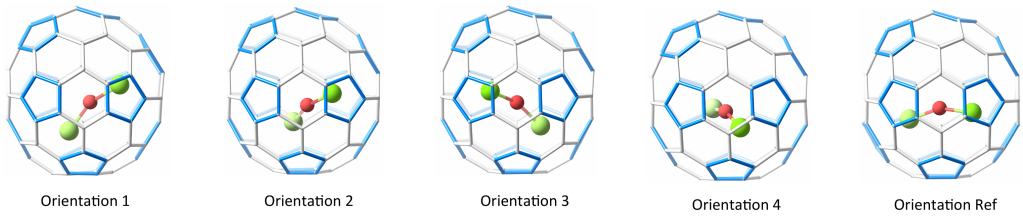

Figure 17. Representations of the optimized structures for the four different orientations of the $Sc_2O@C_{3v}$-C_{82}(39717) cage derived from the crystallographic data and for the lowest energy orientation found in ref 35.

5.5.2. Analysis of the Sc_2O Mobility by MD

Car-Parrinello simulations at 298 K and at high temperatures that mimic the conditions of fullerene formation (2000 K) show that, even at the low time scale of 50 ps, the Sc_2O cluster rotates freely inside the cage (Figure 18). In addition, significant changes of the Sc-O-Sc angle are observed; the average angle for each of the two simulations is 147 degrees and the standard deviations are 8 degrees at 298 K and 18 degrees at 2000 K. These results corroborate the high flexibility of the cluster inside C_{3v}-C_{82}(39717), as observed in other smaller cages.[28]

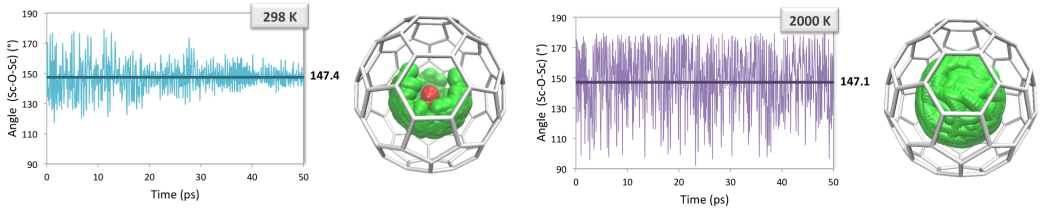

Figure 18. Motion of the Sc_2O cluster inside the C_{3v}-C_{82}(39717) cage along with the variations of the Sc-O-Sc angle from the Car-Parrinello simulation trajectories (50 ps) at 298 K and 2000 K.

5.5.3. Electrochemical Properties

We have computed the oxidation and reduction potentials for $Sc_2O@C_{3v}$-C_{82}(39717) taking into consideration the orientation of the cluster with the lowest energy. The results agree very well with the cyclic voltammogram measurements (Table 8). The computed oxidation potential, +0.45 V, is very similar to that found for the isoelectronic $Sc_2S@C_{3v}$-C_{82}(39717), 0.42 V, in line with their similar HOMO energies and in good agreement with experiments. On the other hand, it is significantly larger than the one for $Sc_2O@C_s$-C_{82}(39715), 0.19 V, which shows a much higher HOMO energy. The computed reduction potential for $Sc_2O@C_{3v}$-C_{82}(39717), -1.19 V, is appreciably more negative than that for $Sc_2S@C_{3v}$-C_{82}(39717), -1.07 V, a trend that is observed comparing their experimental cathodic potentials (-1.17 *vs* -1.04 V). This difference can be already seen, albeit much smaller, in the energies of their LUMOs (-3.96 vs. -3.98 eV). The predicted electrochemical (EC) gap, 1.64 V, also compares well with experiment, 1.71 V, within the error window of this methodology.[51,52] It is significantly larger than the one for $Sc_2S@C_{3v}$-C_{82}(39717), and is the largest for all the computed EC gaps in the OCF family.[24,28,53]

Table 8. Electronic parameters and redox potentials computed at BP86/TZP level in o-dichlorobenzene for $Sc_2O@C_{3v}$-C_{82}(39717) and $Sc_2O@C_s$-C_{82}(39715).

OCFs	HOMO	LUMO	H-L gap	E_{ox}	E_{red}	EC
C_{3v}-C_{82}(39717)	-5.19	-3.96	1.23	0.45	-1.19	1.64
C_s-C_{82}(39715)	-4.98	-4.16	0.82	0.19	-0.98	1.18

[a] Orbital energies in eV and potentials in V.

5.5.4. Computing the UV-vis-NIR Spectrum

The computed UV-vis-NIR spectrum from time-dependent DFT calculations in the vis-NIR region (wavelengths larger than 500 nm) shows reasonable agreement with the experimental one (Figure 19), despite the limitations of the methodology, as found for other OCFs.[24,28]

The TDDFT predictions for the most intense lowest-energy excitations in the absorption spectrum of the IPR cage, $Sc_2O@C_{3v}$-C_{82}(39717) were computed.[25] The first (HOMO → LUMO) transition appears at a rather high energy, 1.29 eV, in correlation with the large optical band gap (1.14 eV) measured for this OCF. The characteristic

feature at 884 nm (1.40 eV) might be assigned to the HOMO → LUMO+1 (predicted at 1.35 eV).

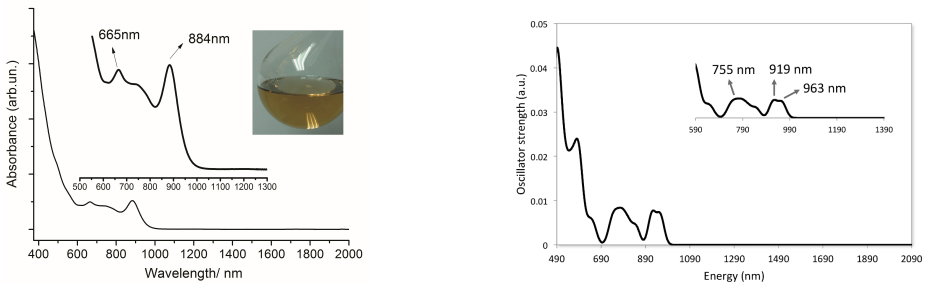

Figure 19. Experimental (left) and computed (right) UV-vis-NIR absorption spectrum of $Sc_2O@C_{3v}$-C_{82}(39717) in CS_2. The insets show the enlarged spectral range (500-1300 nm) and the photograph of $Sc_2O@C_{3v}$-C_{82}(39717) dissolved in CS_2.

5.6. The Extended $Sc_2O@C_{2n}$ Family

Several fullerenes containing a metal oxide cluster such as Sc_2O, Sc_4O_2, Sc_4O_3 have been synthesized and characterized by single-crystal X-ray crystallography.[26-29] The Sc_2O unit, which is the smallest endohedral cluster found inside fullerenes, along with M_2S and MCN clusters, and larger than endohedral monometal or dimetal units, has been found in a large number of carbon cages. Most of the cages in the range of 70-84 carbon atoms have been characterized by X-ray crystallography: $Sc_2O@C_2$-C_{70}(7892), $Sc_2O@T_d$-C_{76}(19151), $Sc_2O@C_{2v}$-C_{78}(24107), $Sc_2O@D_{3h}$-C_{78}(24109), $Sc_2O@C_{2v}$-C_{80}(31922), $Sc_2O@C_s$-C_{82}(39715) and $Sc_2O@C_{3v}$-C_{82}(39717). Their optimized structures are shown in Figure 20. The predicted cages for those $Sc_2O@C_{2n}$ that have not been isolated yet, $Sc_2O@C_s$-C_{72}(10528), $Sc_2O@D_{3h}$-C_{74}(14246), $Sc_2O@C_2$-C_{74}(13333), $Sc_2O@C_{2v}$-C_{84}(51575) and $Sc_2O@C_1$-C_{84}(51580) are also represented in Figure 20.

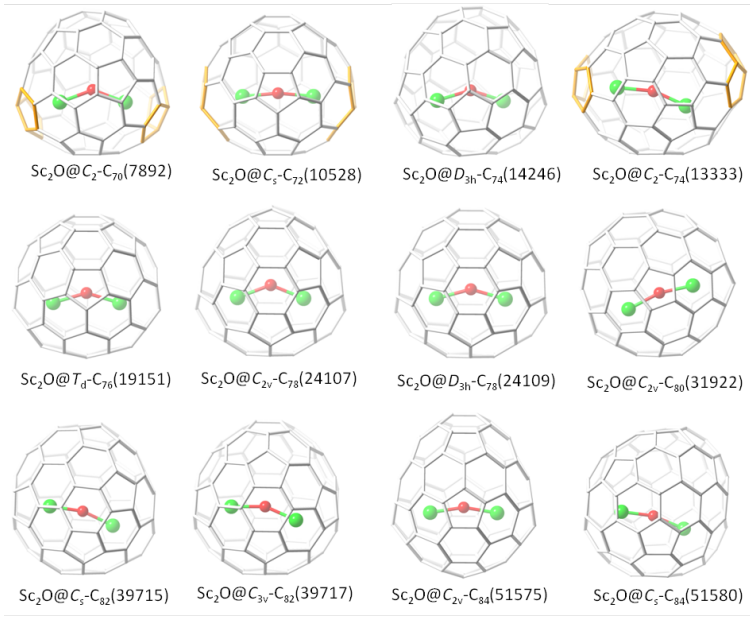

Figure 20. DFT-optimized structures of X-ray characterized and predicted most abundant isomers for each $Sc_2O@C_{2n}$ with 2n from 70 to 84.

5.6.1. Structural Characteristics of Sc_2O Cluster

The Sc_2O cluster always transfers four electrons to the fullerene cages, as we previously verified in this chapter. This kind of oxide cluster generally adopts a bent structure when it is encapsulated inside a fullerene. All $Sc_2O@C_{2n}$ isomers fulfill the isolated pentagon rule with the only exception of three of them, whose structures show the pentalene motifs highlighted in orange in Figure 20. These three non-IPR isomers have two adjacent pentagon pairs with the Sc atoms of the cluster pointing to them. For those IPR cages, different orientations of the Sc_2O unit can be found. The lowest energy orientation of the cluster for each isomer is shown in Figure 20.

Table 9 shows the most characteristic (computed and experimental) structural parameters for the $Sc_2O@C_{2n}$ family, such as distances and angles within the Sc_2O cluster. Although not always the two Sc-O bond lengths in the Sc_2O unit have the same value, the averages of both Sc-O distances in each $Sc_2O@C_{2n}$ cage are comparable among them, having a range of 1.880-1.927 Å.

Table 9. Computed and experimental (in parenthesis) X-ray values for Sc-O distances (in Å) and Sc-O-Sc angles (in degrees), the average of Sc-cage (Sc-C) distances (in Å) and the Sc-Sc distances (in Å) for the $Sc_2O@C_{2n}$ family.

Isomer	Sc1-O	Sc2-O	Sc-Sc	Sc-C	Sc-O-Sc
C_{70}(7892)	1.881	1.881	3.531	2.374	139.6
	(1.909)	(1.931)			(131.2)
C_{72}(10528)	1.928	1.926	3.830	2.452	167.0
C_{74}(14246)	1.888	1.892	3.614	2.397	146.0
C_{74}(13333)	1.923	1.876	3.747	2.402	161.0
C_{76}(19151)	1.883	1.884	3.611	2.421	146.9
	(1.972)	(1.825)			(133.9)
C_{78}(24107)	1.879	1.880	3.501	2.308	137.2
	(1.905)	(1.868)			(134.4)
C_{78}(24109)	1.887	1.887	3.633	2.320	148.7
	(1.903)	(1.979)			(135.2)
C_{80}(31922)	1.896	1.933	3.792	2.414	164.2
	(1.861)	(2.017)			(160.8)
C_{82}(39715)	1.881	1.911	3.747	2.379	162.2
	(1.867)	(1.943)			(156.6)
C_{82}(39717)	1.888	1.875	3.673	2.371	154.8
	(1.937)	(1.888)			(131.0-148.9)
C_{84}(51575)	1.883	1.881	3.714	2.400	161.3
C_{84}(51580)	1.905	1.873	3.746	2.385	165.0

Computed values, albeit somewhat smaller, are in good agreement with experimental ones. The Sc-O bond length is rather constant regardless of the cage size. The $Sc_2O@C_{3v}$-C_{82}(39717) and $Sc_2O@C_{2v}$-C_{80}(31922) isomers have the shortest and largest Sc-O distances, respectively (1.875 and 1.933 Å). The largest computed Sc-O-Sc angle is found in the hypothetical $Sc_2O@C_s$-C_{72}(10528) cage (167.0°). This largest Sc-O-Sc angle is consequence of the peculiar structure of this non-IPR cage. Both scandium atoms are pointing to the two pentalene motifs, thus the angle is less compressed than in other cages. Something similar happens to $Sc_2O@C_2$-C_{70}(7892), where the Sc-O-Sc angle (139.6 comp. and 131.2 degrees exp.) is mainly dictated by the position of the two pentalene motifs in the cage. The computed Sc-C distances are also rather constant regardless of the size of the cage, meaning that this cluster fits well inside cages in the range of C_{70} to C_{84}. As Table 9 shows, the largest Sc-O-Sc angles are found for larger cages, although still nonlinear geometries are commonly observed.

The variations of the Sc-O-Sc angle within the cluster among the $Sc_2O@C_{2n}$ family indicate that there is some kind of influence of the cage structure on the endohedral cluster shape. The dimetallic oxide cluster, Sc_2O, inside the carbon cages is extremely flexible, i.e., it can rotate freely inside the cage and the angular shape is very flexible. Thus, the shape and the size of the cages play a role in the Sc-O-Sc angle that the cluster adopts.

5.6.2. Looking for the Most Favorable $Sc_2O@C_{74}$ Isomer

All $Sc_2O@C_{2n}$ (2n=70-84) isomers have been computationally reported, with the only exception of $Sc_2O@C_{72}$ and $Sc_2O@C_{74}$. Both systems have not been isolated and purified up to now. C_s-C_{72}(10528) isomer was characterized to be the cage for encapsulating Sc_2S. As in the case of Sc_2O, the Sc_2S also transfer four electrons to the fullerene cage. Thus we assume that $Sc_2O@C_s$-C_{72}(10528) would be the most favourable cage for $Sc_2O@C_{72}$.

In case of C_{74} cage, there are 14246 isomers, but only one of them (D_{3h} symmetry) is an IPR structure. Prof. Chen recently detected the IPR isomer $Sc_2C_2@D_{3h}$-C_{74}(14246).[11] So again, four electrons are transferred from the cluster to the cage. Although we could consider the D_{3h}-C_{74}(14246) cage as the most appropriate cage to trap the Sc_2O, we wanted to analyse some APP isomers that maybe could fit better the Sc_2O unit. We have computed the energies of the tetraanions using DFT at BP86/TZP level for all C_{74} cages with two or less adjacent pentagon pairs: 1 IPR isomer, 3 APP1 isomers and 69 APP2 isomers. The lowest-energy tetraanionic cages of C_{74} (less than 13 kcal·mol^{-1}) were selected to be optimized at the BP86/TZP level in the endohedral form of $Sc_2O@C_{74}$ (Table 12). Isomers 14246 and 13333 are by far the most stable $Sc_2O@C_{74}$ endohedral metallofullerenes. Note that the IPR isomer, which is the most stable one, has the lowest encapsulation energy (-6.153 eV) and the smallest HOMO-LUMO gap (0.405 eV). The non-IPR isomer $Sc_2O@C_2$-C_{74}(13333), that was found at 3.4 kcal·mol^{-1}, shows a better encapsulation of the cluster to the cage (-8.099 eV) and a larger H-L gap (-0.941 eV). In addition, taking into account the energies of $Sc_2O@C_2$-C_{74}(13333), D_{3h}-C_{74}(14246), the lowest-energy C_{74} cage, and Sc_2O, the encapsulation energy would be -6.005 eV. This energy is 0.148 eV lower than the encapsulation energy of the IPR structure.

Table 12. Relative energies (in kcal·mol^{-1}) for tetraanions and $Sc_2O@C_{74}$ isomers, encapsulation energies (in eV) and HOMO-LUMO (H-L) gaps (in eV) for the selected isomers of C_{74} in the corresponding endohedral form.

Isomer	APP	Sym	C_{74}^{4-}	$Sc_2O@C_{74}$	Encapsulation Energy	H-L gap
14246	0	D_{3h}	0.0	0.0	-6.153	0.405
13333	2	C_2	1.4	3.4	-8.099	0.941
13290	2	C_2	9.1	16.2	-8.167	0.858
13295	2	C_2	11.6	19.0	-7.940	0.454
13384	2	C_1	12.2	21.4	-7.866	0.893

The optimized structures of isomers $Sc_2O@D_{3h}$-C_{74}(14246), $Sc_2O@C_2$-C_{74}(13333), $Sc_2O@C_2$-C_{74}(13290), $Sc_2O@C_2$-C_{74}(13295) and $Sc_2O@C_1$-C_{74}(13384) are shown in Figure 21.

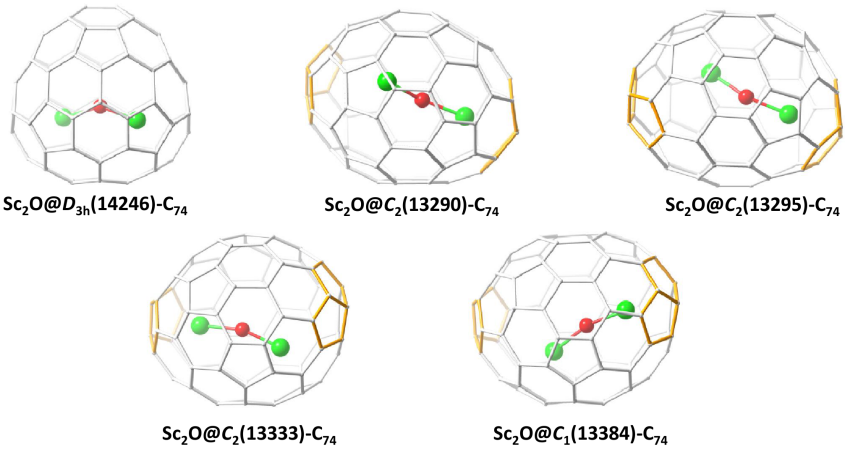

Figure 21. DFT-optimized cages of $Sc_2O@D_{3h}$-C_{74}(14246), $Sc_2O@C_2$-C_{74}(13333), $Sc_2O@C_2$-C_{74}(13290), $Sc_2O@C_2$-C_{74}(13295) and $Sc_2O@C_1$-C_{74}(13384) isomers.

The molar fraction in FEM and RRHO approximations for the corresponding $Sc_2O@C_{74}$ isomers are represented in Figure 22. The IPR structure, $Sc_2O@D_{3h}$-C_{74}(14246), is the most abundant isomer in the whole range of temperature in both models, followed by

the APP2 isomer $Sc_2O@C_2$-C_{74}(13333) that gets a maximum yield of around 40% in FEM approximation.

Taking into account that we only have the computational part for the $Sc_2O@C_{74}$ system, we can only predict that cages D_{3h}-C_{74}(14246) and C_2-C_{74}(13333) would be the most suitable isomers for encapsulating the Sc_2O moiety. Thus, up to now, we can not discard any of these two isomers.

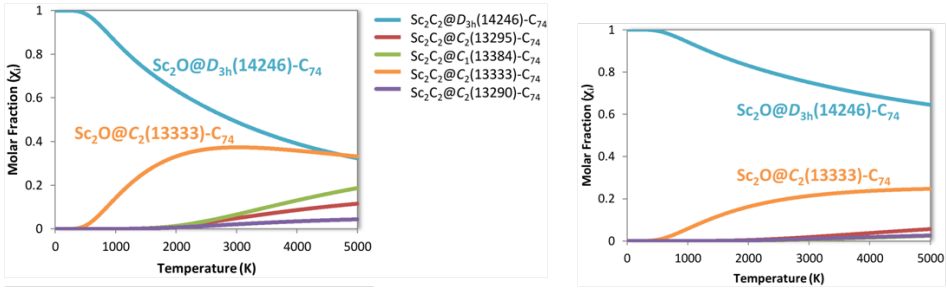

Figure 22. Representations of the molar fractions as a function of the temperature for the isomers of $Sc_2O@C_{74}$ using the rigid rotor and harmonic oscillator (RRHO) approximation (right) and the related free-encapsulating model (FEM) (left).

5.6.3. Cage Connectivity for $Sc_2O@C_{2n}$ Family (2n=70 to 82)

Although many efforts have been devoted to understand fullerene formation, the mechanism is still unclear and under debate, as mentioned in the above chapter.[54-58] Nowadays, it is assumed that in presence of a rich carbon atmosphere a closed fullerene can grow likely following a relatively simple mechanism.[59,60] At low carbon concentrations, it is likely that Stone-Wales (or similar) rearrangements are dominant and the less stable structures are transformed to give the thermodynamic product in most cases.

Figure 23 shows a growth scheme for the $Sc_2O@C_{2n}$ family through C_2 additions and SW transformations assuming the mechanism proposed by Endo and Kroto in the early nineties and denominated later as Closed Network Growth mechanism.[61-63] The critical point of this mechanism is that the fullerenes formed after a C_2 addition does not obey

the isolated pentagon rule due to the formation of two fused pentagonal rings. In particular, here we show that $Sc_2O@C_2$-C_{70}(7892) and $Sc_2O@C_{3v}$-C_{82}(39717) are linked by six C_2 insertions plus a few number of SW transformations for some of the isomers (Figure 23). The initial two cages C_2-C_{70}(7892) and C_s-C_{72}(10528) do not satisfy the IPR, but after the second insertion the most favorable isomers for each cage are of the IPR type and therefore it is needed at least one SW rearrangement to transform the non-IPR isomer into an IPR.

As mentioned, the first step relates cages C_2-C_{70}(7892) and C_s-C_{72}(10528) through a simple C_2 insertion (Figure 23). Once the C_2 unit is inserted into the selected hexagon of $Sc_2O@C_2$-C_{70}(7892), $Sc_2O@C_s$-C_{72}(10528) is formed. Although the C_s-C_{72}(10528) cage has been detected encapsulating Sc_2S, it has not been still found encapsulating a scandium oxide. However, it would also be the optimal isomer to capture Sc_2O. The next step is the formation of $Sc_2O@D_{3h}$-C_{74}(14246) from $Sc_2O@C_s$-C_{72}(10528) through the C_2 insertion and two SW transformations. D_{3h}-C_{74}(14246) has not been observed encapsulating Sc_2O neither, but it has been detected hosting a Sc_2C_2 cluster.[11] A detailed structural path from C_2-C_{70}(7892) to D_{3h}-C_{74}(14246) has been reported for $Sc_2S@C_{2n}$ by Fowler and co-workers.[64] Next step corresponds to the formation of $Sc_2O@T_d$-C_{76}(19151) from C_2 insertion into $Sc_2O@D_{3h}$-C_{74}(14246) followed by a SW transformation. Then, the two observed cages with 78 carbon atoms containing a Sc_2O cluster can be connected with $Sc_2O@T_d$-C_{76}(19151) by C_2 insertion plus one or two SW transformations. Indeed, these two cages, C_{78}(24109) and C_{78}(24107), are related by a single SW rearrangement.[27] The following step relates isomer $Sc_2O@C_{2v}$-C_{80}(31922) with $Sc_2O@C_{2v}$-C_{78}(24107) and $Sc_2O@D_{3h}$-C_{78}(24109) through a C_2 insertion and one or two SW transformations. Finally, the largest observed C_{82} cages, C_s-C_{82}(39715) and C_{3v}-C_{82}(39717) can be formally derived from $Sc_2O@C_{2v}$-C_{80}(31922), even though the cage with symmetry C_{3v} would require 4 SW transformations. Likely, $Sc_2O@C_{2v}$-C_{80}(31922) -> $Sc_2O@C_{2v}$-C_{82}(39717) occurs via non-classical intermediates containing a heptagonal ring.[12,65]

To summarize, the observed cages for OCFs are linked via C_2 insertions and few SW rearrangements. This is not specific for these OCFs since other clusterfullerenes containing tetravalent units, Sc_2S^{4+} or $Sc_2C_2^{4+}$, display rather similar connections. The greatest advantage of the $Sc_2O@C_{2n}$ family with respect to other families is the number of observed species that allow a more detailed analysis of the real links between the different species.

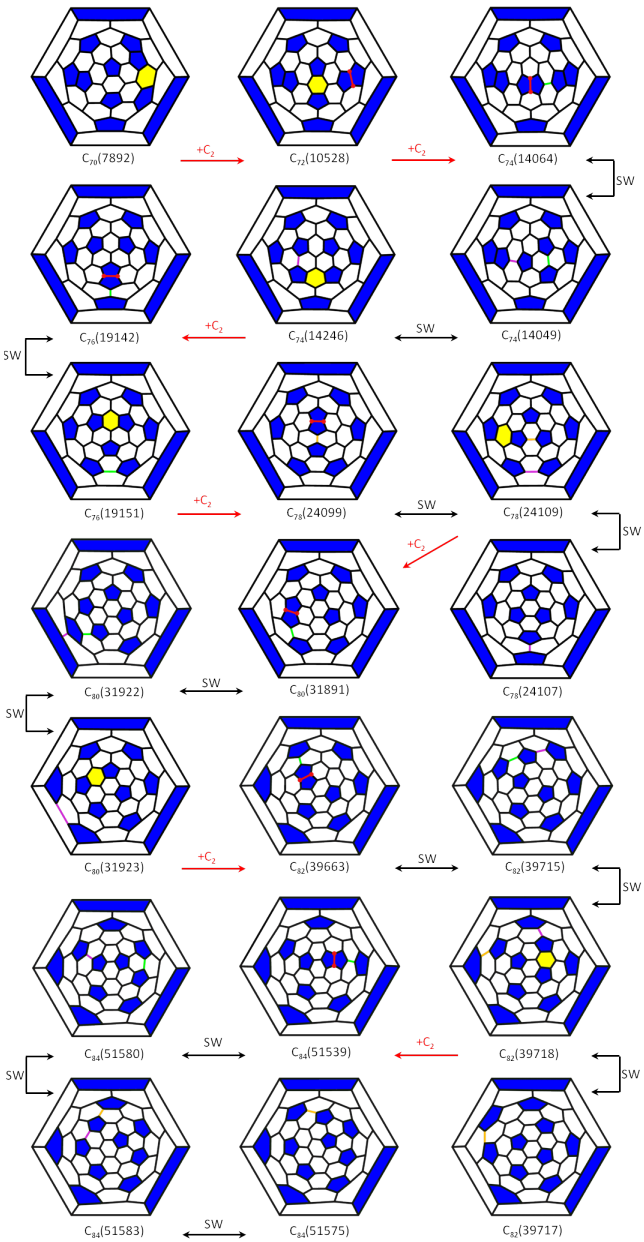

Figure 23. Schlegel diagrams connecting the isomers of $Sc_2O@C_{2n}$ family. The hexagons where C_2 inserts are highlighted in yellow, the formed C-C bonds are in red and the bonds that rearrange (Stone-Wales) are in green, purple and orange.

5.6.4. Comparison $Sc_2O@C_{2n}$ versus $Sc_2S@C_{2n}$

Sulfur and oxygen belong to the same group of the periodic table (chalcogens) and, consequently, they have the same number of valence electrons. Therefore, the clusters that they can form by combination with metals can be very similar. Indeed, just before Stevenson, Poblet and Balch characterized the structure of the first Sc_2O-based OCF, $Sc_2O@C_s$-C_{82}(39715),[35] in 2010 Yang, Popov and Dunsch had isolated and characterized the family of sulfide clusterfullerenes (SCFs) $M_2S@C_{3v}$-C_{82}(39717) with M = Sc, Y, Dy and Lu by using solid guanidinium thiocyanate as sulfur source.[23] In 2011, a collaboration between the groups of Stevenson, Echegoyen, Poblet and Balch resulted in the synthesis (SO_2 as sulfur source) and characterization of the electrochemical properties and the structures of $Sc_2S@C_s$-C_{82}(39715) and its isomer $Sc_2S@C_{3v}$-C_{82}(39717).[44] Later in 2012, Balch, Poblet and Echegoyen isolated and characterized $Sc_2S@C_s$-C_{72}(10528), which was the first dimetallic sulfide clusterfullerene with a non-IPR cage, as shown by X-ray crystallography.[38] Finally, in 2013, Poblet and Echegoyen found that the Sc_2S cluster could also be encapsulated in another small and non-IPR C_{70} cage, $Sc_2S@C_2$-C_{70}(7892).[22] Even though the structure was not determined by X-ray crystallography, electrochemical and spectroscopic characterization, as well as complementary DFT calculations doubtlessly pointed to C_2-C_{70}(7892) to be the cage present in this SCFs. Besides these isolated SCFs, the mass spectra showed peaks for a large number of members within the $Sc_2S@C_{2n}$ family, ranging from 2n = 68 to 100.[21] Structures for some of these peaks have been proposed from computations.[41,66]

Sulfide and oxide clusterfullerenes of the type $Sc_2X@C_{2n}$ (X = O, S) share identical electronic structures with formal electron transfers of four electrons from the cluster to the cage.[36,53] Therefore, the most favored fullerene cages that are predicted to encapsulate Sc_2O and Sc_2S are, according to the ionic model, the same. In fact, most of the cages that have been observed to contain Sc_2S they have been also found for Sc_2O. Since the sulfide anion is larger than the oxide anion, the Sc-S distances within the cluster are larger than the corresponding Sc-O distances. Therefore, the larger Sc_2S cluster has to bend more the Sc-S-Sc angle to fit well inside the same cages that encapsulate the smaller Sc_2O cluster. Hence, Sc-S-Sc angles in SCFs are significantly smaller than Sc-O-Sc angles in OCFs. Finally, the predicted very similar electronic structure for $Sc_2S@C_{2n}$ and $Sc_2O@C_{2n}$ was confirmed by computations of the frontier molecular orbital energies. The HOMO energies of SCFs and OCFs, as well as their LUMO energies, are quite similar with differences smaller than 40 mV that are consequence of the different nature of the cluster and interaction with the C_{2n} cage. Besides, the shapes of these frontier molecular orbitals are essentially the same for

sulfides and oxides (Figure 24). The calculated oxidation and reduction potentials are able to reproduce the small changes observed in the cyclic voltammetry experiments, i.e. it is somewhat easier to oxidize and reduce the oxide than the sulfide for C_2-C_{70}(7892) and C_s-C_{82}(39715), while it is slightly easier to oxidize and reduce the sulfide for C_{3v}-C_{82}(39717). Even though the electrochemical (EC) gaps are computed with a given error, which can be up to 230 mV for the $Sc_2X@C_2$-C_{70}(7892) systems, the differences between the EC gaps between the sulfide and the oxide CFs are very well reproduced in all the cases: +140 (calc) vs +120 mV (exp) for C_2-C_{70}(7892), +60 (calc) vs +60 mV (exp) for C_s-C_{82}(39715) and -150 (calc) vs -150 mV (exp) for C_{3v}-C_{82}(39717).[67]

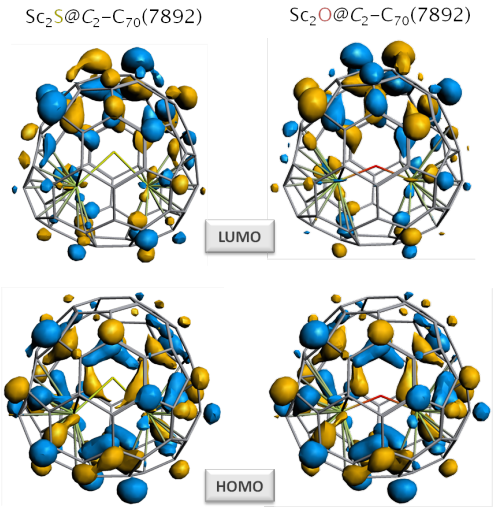

Figure 24. Representation of the HOMO and LUMO for $Sc_2S@C_2$-C_{70}(7892) and $Sc_2O@C_2$-C_{70}(7892), which are very similar in the two systems.

5.6.4.1. Redox Potentials and Correlation with the Electronic Structure

To predict the experimental reduction (or oxidation) potentials of $Sc_2O@C_{2n}$, their "absolute" reduction (or oxidation) potentials are first computed and then made relative to the normal hydrogen electrode (NHE), which has an estimated absolute reduction potential of +4.28 eV, value determined by Cramer and co-workers.[68] The

reduction potential E° of process (1) is related to its free energy change ΔG° by the Nernst equation.

$$Sc_2O@C_{2n\ (solv.)} + e^-(g) \rightarrow Sc_2O@C_{2n}{}^{-}{}_{(solv.)} \qquad \text{(Eq.1)}$$

Similarly, the oxidation process is associated to process (2)

$$Sc_2O@C_{2n\ (solv.)} \rightarrow Sc_2O@C_{2n}{}^{+}{}_{(solv.)} + e^-(g) \qquad \text{(Eq.2)}$$

The electrochemical measurements (cyclic voltammetries) are in general performed in a solution of o-dichlorobenzene (o-dcb). Therefore, solvation effects were taken into account by means of the continuum conductor-like screening model (COSMO) using o-dcb as solvent. If solvent effects are not included in the calculations, that is, gas phase calculations, meaningless predictions for reduction (and oxidation) potentials are obtained since the charged species, $Sc_2O@C_{2n}{}^{-}$ and $Sc_2O@C_{2n}{}^{+}$ are not well described in absence of their environment (solvent + counterions).

Table 13 collects the first anodic and cathodic potentials referenced versus the ferrocenium/ferrocene (Fc^+/Fc) potential. It has been observed that the electronic component of the free energy, that is, the reduction and electronic energies are able to describe rather well the redox properties of endohedral fullerenes.[52] This is important because the calculations of the harmonic frequencies are rather expensive. Calculated redox potentials in Table 13 are obtained from the reduction and oxidation energies. As expected from the low LUMOs of fullerene cages the energies associated to the reduction process are computed to be rather exothermic (between -3.4 and -4.0 eV). Consequently, the reduction potentials for endohedral fullerenes appear at not very negative potentials despite the electron transfer from the internal cluster to the carbon cage. HOMO and LUMO are mainly localized on the carbon cage and consequently the computed redox potentials correlates very well with the energy of the HOMO and LUMO computed in o-dcb (Figure 25). This figure also shows that the deviation of the computed reduction potential with respect to the observed values is very small (< 50 mV). However, for the first oxidation potential the deviation is larger (> 100 mV), indicating that the HOMOs are systematically computed above the real value, even though the shift is not very important. In endohedral metallofullerenes, cyclic voltammetry is an essential technique in the characterization of the different isomers. In particular, the excellent agreement between experimental and theoretical values allows one to discard many isomers when the X-ray structure is unknown.

Table 13. Computed and experimental (V vs Fc^+/Fc) first oxidation and reduction potentials, electrochemical (EC) gaps, HOMO and LUMO energies and HOMO-LUMO (H-L) gaps for some $Sc_2O@C_{2n}$ OCFs.[a]

OCF	E_{ox},	E_{red}	EC	E_{ox}[b]	E_{red}[b]	EC[b]	HOMO	LUMO	H-L gap
C_{70}(7892)	-0.02	-1.25	1.23	0.10	-1.36	1.46	-4.75	-3.88	0.86
C_{72}(10528)	0.15	-1.19	1.34	-	-	-	-4.90	-3.96	0.95
C_{74}(14246)	-0.08	-0.89	0.81	-	-	-	-4.67	-4.27	0.40
C_{76}(19151)	0.15	-1.00	1.15	0.32	-0.91	1.23	-4.93	-4.15	0.78
C_{78}(24107)	0.02	-1.13	1.15	0.16	-1.17	1.33	-4.77	-4.01	0.76
C_{78}(24109)	0.02	-0.70	0.72	0.18	-0.67	0.85	-4.79	-4.47	0.32
C_{80}(31922)	0.24	-0.92	1.16	0.24	-0.89	1.13	-5.02	-4.22	0.80
C_{82}(39715)	0.19	-0.98	1.17	0.35	-0.96	1.31	-4.98	-4.16	0.82
C_{82}(39717)	0.45	-1.19	1.64	0.54	-1.17	1.71	-5.19	-3.96	1.23
C_{84}(51575)	0.24	-1.06	1.30	-	-	-	-5.01	-4.09	0.92
C_{84}(51580)	0.12	-1.14	1.26	-	-	-	-4.89	-3.99	0.91

[a] All redox potentials are given in V and orbital energies in eV; computed values in o-dichlorobenzene. [b] Experimental values.

As shown in Figure 26, the energies of HOMO and LUMO of a given OCF and therefore their redox properties do not correlate with the size of the fullerene. In fact, they are related to the topology of the carbon cage. It was established from the initial studies on the endohedral metallofullerenes that cage C_{2v}-C_{82}(39717) has an optimal topology to encapsulate clusters or metal ions that involve the transfer of 4 electrons.[69] Thus, $Sc_2O@C_{2v}$-C_{82}(39717) exhibits an electronic structure with a very deep HOMO and a rather high LUMO, features that are at the origin of the observed electrochemical gap (1.71 eV), which is the largest among the $Sc_2O@C_{2n}$ series. In the opposite side, there is $Sc_2O@D_{3h}$-C_{78}(24109), that is an OCF with a cage that was initially detected hosting Sc_3N. The low energy of the LUMO for this OCF is a result of its electronic structure that is optimal for a 6-electron transfer. Accepting only 4e, D_{3h}-C_{78}(24109) is in some way an "electron deficient" species being able to be reduced at low potentials. In this line, it is worth mentioning that its second reduction potential ($^{Red}E_2$) was found at -0.86 V (vs $Fc^{0/+}$), only 0.19 V more negative than $^{Red}E_1$, suggesting that it is a system that can easily accept two electrons. Despite the small HOMO-LUMO gap, $Sc_2O@D_{3h}$-C_{78}(24109) could be isolated and its structure characterized by X-ray.[27] Among the endohedral fullerenes not yet observed, there is $Sc_2O@C_s$-C_{72}(10528), which is predicted to have a relatively large HOMO-LUMO gap and

therefore a presumably important stability. Although this cage has been observed encapsulating the homologous scandium sulfide, it has not been detected as scandium oxide yet. We presume that in the near future $Sc_2O@C_s$-C_{72}(10528) will likely be isolated and characterized.

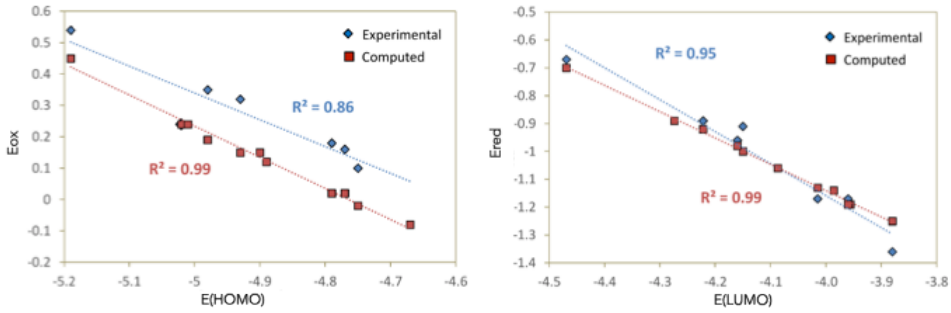

Figure 25. Correlations between first oxidation potentials and HOMO energies (left) and between first reduction potentials and LUMO energies (right) for the series of OCFs given in Table 13. Blue diamonds are used for experimental potentials whereas orange squares are for computed potentials.

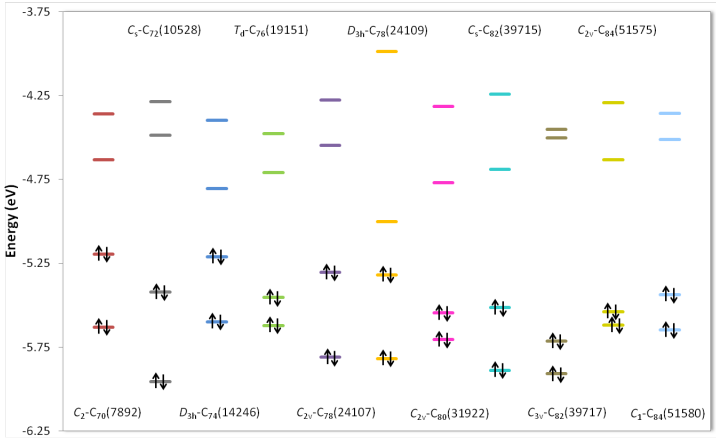

Figure 26. Frontier molecular orbitals for several $Sc_2O@C_{2n}$ fullerenes. Energies in eV.

5.7. The Trimetallic OCF $Sc_3O@I_h$-C_{80}(31924)

The trimetallic oxide clusterfullerene $Sc_3O@C_{80}$ has been obtained with rather high abundance in the raw soot. Most of the formed product, however, remained non-extracted in the soot so that only a small amount of it was isolated and purified. The tiny quantity of product acquired made only possible characterization by UV-vis-NIR spectroscopy. In this section, we report the computational studies of a unique trimetallic OCF, which is the first discovered neutral paramagnetic species within the OCF family. The polymerization process could explain the low yields obtained once the product is purified.

5.7.1. Preparation and Purification Studies

The OCFs were synthesized in a conventional Krätschmer-Huffman arc-discharge reactor under a He/CO_2 (10:1) atmosphere by Prof. Chen's group.[33] The soot was collected and refluxed in chlorobenzene under an argon atmosphere for 24 h. A mass peak with 1110.920 presents the highest intensity in the mass spectrum, which is much higher than that of C_{60} and C_{70} under the positive ion mode. The accurate mass analysis shows that this mass peak represents a novel trimetallic oxide clusterfullerene, $Sc_3O@C_{80}$. The notably high intensity indicates the rich abundance of $Sc_3O@C_{80}$ in the soot. After the extraction, in the mass spectrum of the extract, though remains to be the highest peak detected for endohedral fullerenes, the intensity of the peak for $Sc_3O@C_{80}$ significantly decreased. This difference indicates that $Sc_3O@C_{80}$ detected in the soot has low solubility and majority amount of it could not be extracted into organic solvent.

After extraction, they applied a multistage high-performance-liquid chromatography procedure to isolate and purify $Sc_3O@C_{80}$. Surprisingly, extremely low yield of purified $Sc_3O@C_{80}$ from the mass spectrum of the mixed fullerene solution is seen after the HPLC processes. It suggests that $Sc_3O@C_{80}$ is not stable in chlorobenzene and might decompose or polymerize during a period of time. Nevertheless, Prof. Chen obtained a very limited amount of the purified $Sc_3O@C_{80}$ after the HPLC procedures and carried MALDI-TOF spectrometry and UV-vis-NIR characterization on this sample.

5.7.2. Looking for the Most Suitable Candidates for $Sc_3O@C_{80}$

The charge transferred from the cluster to the cage is important when we have to determine the most suitable cages for the encapsulation of a selected cluster. Encapsulation of the Sc_3O oxide cluster inside a C_{80} cage led us to think about, within the ionic model, a formal transfer of six electrons from the cluster to the cage, i.e. $(Sc_3O)^{6+}@(C_{80})^{6-}$. Since the O in the oxide has a formal oxidation state of -2, the count of electrons shows that there remains an unpaired electron in the Sc ions (the total number of electrons in the molecule is odd). So, the Sc ions are not completely oxidized. $Sc_3O@C_{80}$ is isoelectronic with the anion $Sc_3N@C_{80}^-$, as well as the characteristic mixed-metal nitride $TiSc_2N@C_{80}$.

Isomers I_h(31924) and D_{5h}(31923), which satisfy the isolated pentagon rule, are the most suitable C_{80} cages for clusterfullerenes that show formal transfers of six electrons, i.e. they are the lowest-energy C_{80} hexaanions, as a consequence of their characteristic topology.[36,37] The cage I_h-C_{80}(31924) is found to encapsulate a large variety of clusters (M_3N, $M_{3-x}M'_xN$, TiM_2, Sc_3C_2, Sc_4C_2, Sc_4O_2, Sc_4O_3) and, in particular, $Sc_3N@I_h$-C_{80}(31924) is, under optimized conditions, the most abundant clusterfullerene.[42] Besides, the cage D_{5h}-C_{80}(31923) has been also found to encapsulate Sc_3N and other nitrides.[42] Therefore, we have only considered these two isomers as the most likely cages to encapsulate Sc_3O.Computations at BP86/TZP level show that the energies of different orientations of the Sc_3O cluster within each of these two cages are all rather similar, within 4 kcal mol^{-1} (Table 14).

Table 14. Relative energies (E_{rel}) (in kcal·mol^{-1}) for different orientations of the Sc_3O cluster inside the I_h(31924) and D_{5h}(31923) C_{80} cages.

$Sc_3O@I_h$-C_{80}(31924)	Erel	$Sc_3O@D_{5h}$-C_{80}(31923)	Erel
1	3.3	1	17.3
2	0.8	2	21.0
3	0.0	3	20.2
4	1.3	4	19.1
5	3.3	5	19.8
		6	20.7
		7	21.2
		8	20.4

Therefore, the cluster can rotate easily at rather low temperatures. The energy difference between $Sc_3O@I_h$-C_{80}(31924) and $Sc_3O@D_{5h}$-C_{80}(31923) is 17.3 kcal mol^{-1}, a value that is almost identical to that found for the energy difference in $Sc_3N@C_{80}$ (17.5 kcal mol^{-1}).[52] The optimized structures for the different orientations of the two isomers are shown in Figure 27 and 28.

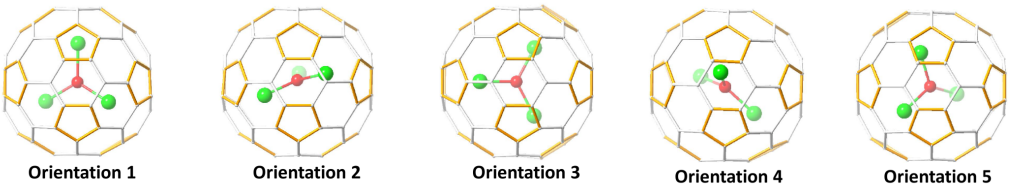

Figure 27. Representation of the optimized geometries for different orientations for $Sc_3O@I_h$-C_{80}(31924) isomer.

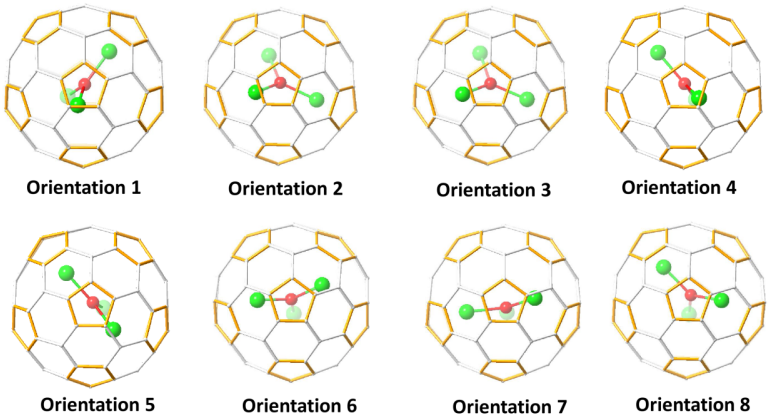

Figure 28. Representation of the optimized geometries for different orientations for $Sc_3O@D_{5h}$-C_{80}(31923) isomer.

5.7.3. Thermodynamic Control

In order to incorporate in our calculations the effect of the high temperatures at which fullerenes are formed, which can be critical to determine their relative stabilities and abundances, we have also computed the molar fractions of these two isomers as a function of the temperature (0 - 5000 K) using the rigid rotor and harmonic oscillator (RRHO) approximation and the related free-encapsulating model (FEM) as proposed by Slanina (Figure 29).[39,40] Since the internal cluster can rotate rather easily inside the cages, in principle the FEM model should be more appropriate to describe the abundances with respect to temperature. However, the behavior described by the two models is very similar.

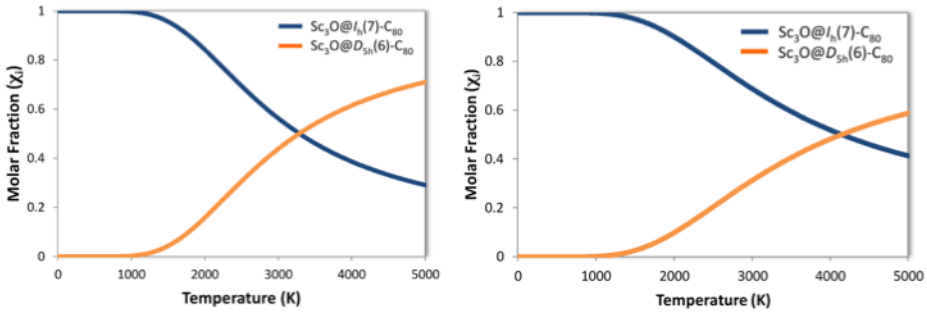

Figure 29. Predicted molar fractions for $Sc_3O@I_h$-C_{80}(31924) and $Sc_3O@D_{5h}$-C_{80}(31923) as a function of the temperature using the free-encapsulating model (FEM) (left) and the rigid rotor and harmonic oscillator (RRHO) approximation (right).

$Sc_3O@I_h$-C_{80}(31924) is predicted to be the most abundant isomer up to very high temperatures (around 3000 K for the FEM model and 4000 K for the RRHO, Figure 29). Therefore, we conclude that the OCF detected in experiments should be $Sc_3O@I_h$-C_{80}(31924).

5.7.4. Electronic Structure Properties

A detailed analysis of the electronic structure and the frontier molecular orbitals of $Sc_3O@I_h$-C_{80}(31924) confirms that there is a formal transfer of six electrons from the cluster to the cage and that the cluster remains with an unpaired electron (Figure 30).

Both the SOMO (singly occupied molecular orbital), which is the highest occupied molecular orbital in systems with unpaired electrons, and the LUMO (lowest unoccupied molecular orbital) are localized in the Sc_3O cluster (Figure 30). Therefore, both electrochemical oxidation and reduction are expected to take place in the endohedral oxide. This behavior is analogous to those found for the oxide clusterfullerene $Sc_4O_2@I_h$-C_{80}(31924) and the carbide $Sc_3C_2@I_h$-C_{80}(31924) with the HOMO and LUMO localized in the cluster.[31,44,70] It is, however, different to those observed for $Sc_4O_3@I_h$-C_{80}(31924) and $Sc_3N@I_h$-C_{80}(31924) with the HOMO localized in the cage.[44,52] In contrast to $Sc_4O_2@I_h$-C_{80}(31924), $Sc_3O@I_h$-C_{80}(31924) is magnetic in the neutral state. The spin density is mainly located on the cluster, with a shape that is essentially that of the SOMO and almost identical to that found for the isoelectronic $Sc_3N@I_h$-C_{80}(31924)$^-$ anion (Figure 31), albeit somewhat more localized on the Sc ions.

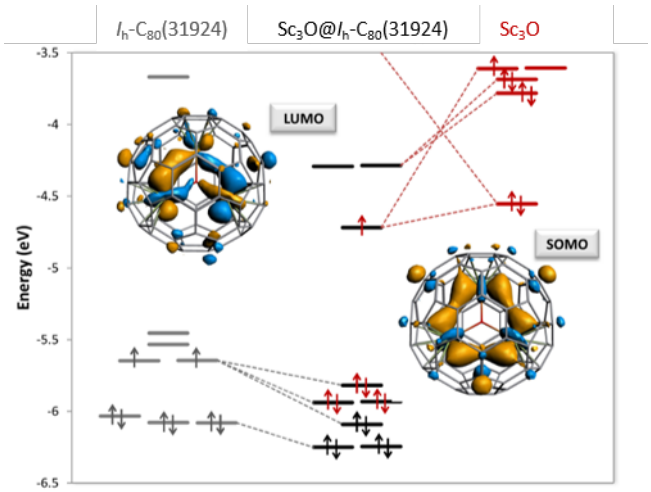

Figure 30. Orbital interaction diagram for $Sc_3O@I_h$-C_{80}(31924). The fragments Sc_3O and I_h-C_{80}(31924) are calculated with the geometry that they have in the OCF.

Compared to $Sc_3C_2@I_h$-C_{80}(31924), which is also magnetic in the neutral state with the spin density mainly located on the carbide C_2^{3-},[70] the spin density in $Sc_3O@I_h$-C_{80}(31924) is mostly located on the Sc ions.

We have computed the hyperfine coupling constants measured in ESR experiments for the three Sc ions, *a(Sc)*, in the isoelectronic oxide and nitride (anion) clusterfullerenes $Sc_3O@I_h$-C_{80}(31924) and $Sc_3N@I_h$-C_{80}(31924)$^-$. The average *a(Sc)* for the OCF, computed for the lowest-energy orientation, is 37.4 G, a value that almost doubles the one for the NCF anion, 22.4 G. Although care should be taken when the hyperfine coupling constant of a given center is used to make conclusions about the total spin density on that center,[31,71] we here find a correlation between these two magnitudes. The lower contributions of the Sc to the spin density in the carbide $Sc_3C_2@I_h$-C_{80}(31924) radical are reflected in a much lower hyperfine coupling constant, *a(Sc)* = -6.5 G. Figure 31 plots the spin density for $Sc_3O@I_h$-C_{80}(31924), $Sc_3N@I_h$-C_{80}(31924)$^-$ and $Sc_3C_2@I_h$-C_{80}(31924).

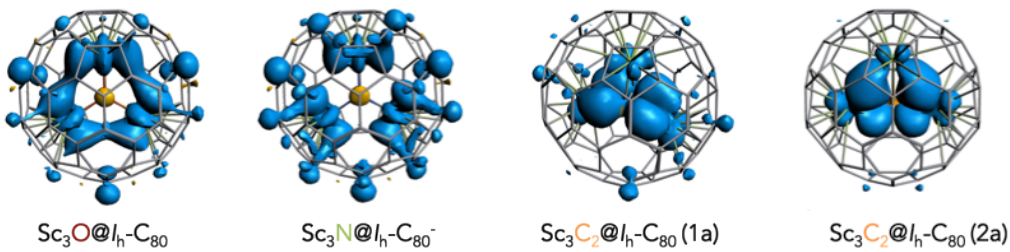

Figure 31. Representation of the spin densities for $Sc_3O@I_h$-C_{80}(31924), $Sc_3N@I_h$-C_{80}(31924)$^-$, $Sc_3C_2@I_h$-C_{80}(31924) (1a) and $Sc_3C_2@I_h$-C_{80}(31924) (2a) isomers.

5.7.5. Redox Properties

Given the shape and localization of the SOMO in the Sc_3O cluster, electrochemistry in this characteristic OCF should take place *in cavea*. In radicals, it is the SOMO orbital that is involved in both oxidation and reduction processes and, therefore, these species usually show low first oxidation and reduction potentials.[72]

The first oxidation potential for $Sc_3O@I_h$-C_{80}(31924) is predicted to be at -0.42 V, a very low value compared to other OCFs and more than 400 mV anodically shifted from the reference ferrocene. The lowest anodic potential for an OCF measured so far is 0.00 V for $Sc_4O_2@I_h$-C_{80}(31924) (the predicted value with the same computational settings is -0.09 V). In addition, this very low oxidation potential is almost 1 V anodically shifted with respect to the predicted first anodic peak in the analogous nitride $Sc_3N@I_h$-C_{80}(31924) (0.53 V). On the other side, the predicted reduction potential, -1.16 V, is comparable to those for $Sc_2O@C_{3v}$-C_{82}(39717) (-1.19 V) and $Sc_3N@I_h$-C_{80}(31924) (-1.17 V) and somewhat more cathodically shifted than for other OCFs. Consequently, the predicted EC gap for $Sc_3O@I_h$-C_{80}(31924), 0.74 V, which is significantly small, is the lowest gap among all the OCFs known so far.

It is interesting to remark at this point that first oxidation and reduction potentials are directly related to the HOMO and LUMO energies, respectively. The very low anodic potential found for $Sc_3O@I_h$-C_{80}(31924) is mainly dictated by the very high energy of its HOMO, -4.30 eV, almost 1 eV higher than for the analogous nitride $Sc_3N@I_h$-C_{80}(31924), -5.27 eV. The LUMO for $Sc_3O@I_h$-C_{80}(31924) shows a middle energy within the OCF family in line with its intermediate cathodic potential. A rather good correlation is also found between the experimental EC gaps and the H-L gaps (Figure 32), as for the family of NCFs.[52]

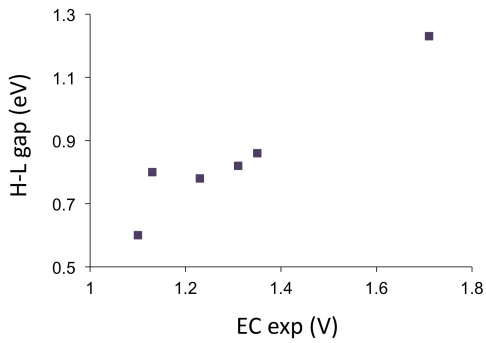

Figure 32. Plot of the HOMO-LUMO (H-L) gap (in eV) with respect to the experimental electrochemical (EC) gap (in V) for the OCFs characterized so far.

5.7.6. UV-vis-NIR Analysis

The purified sample has a brown colour in toluene. As shown in Figure 33, the overall UV-vis-NIR absorption of $Sc_3O@C_{80}$ presents a rather featureless pattern, similar to those of the I_h-C_{80} cage based clusterfullerenes, such as $Sc_3N@I_h$-C_{80},[73] and $Sc_3C_2@I_h$-C_{80}.[74] Nevertheless, broad absorption bands from 380 to 420 nm, 450 to 490 nm, 600 to 700 nm, and 780 to 880 nm are still visible on the absorption spectrum, which are rather similar to those of $Sc_3C_2@I_h$-C_{80}.[74] Due to limited sample amount, the UV-vis-NIR absorption can only be determined up to 1600 nm, which has not reached the absorption onset of $Sc_3O@C_{80}$. This shows that the absorption onset of $Sc_3O@C_{80}$ is beyond 1600 nm, suggesting a relatively narrow band gap comparable to that found for $Sc_2O@C_{2v}$-C_{80}(31922).[26]

We have computed the UV-vis-NIR spectrum for the $Sc_3O@I_h$-C_{80}(31924) isomer using time-dependent (TD) DFT. The predicted spectrum, which shows broad absorptions around 450, 600, 700 and 850 nm, is in reasonable agreement with the experimental one (Figure 33), despite the limitations of the methodology, as found for other OCFs.[25,26,28]

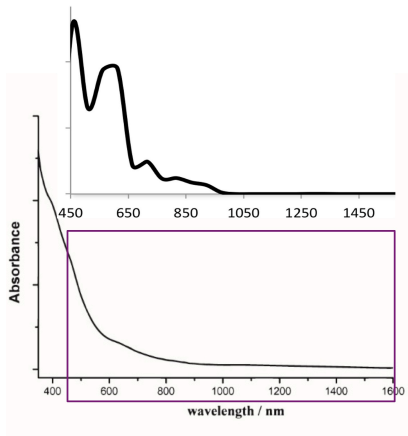

Figure 33. Experimental (bottom) and computational (top) UV-vis-NIR spectrum of $Sc_3O@C_{80}$ in toluene.

5.7.7. Mobility of the Sc_3O Moiety Inside the I_h-C_{80}(31924) Cage

Car-Parrinello simulations have been done to analyze the mobility of the cluster inside the cage. Trajectories at 298 K and at high temperatures that mimic the conditions of fullerene formation (2000 K) show that even at the low time scale of 25 ps the Sc_3O cluster rotates freely inside the I_h-C_{80}(31924) cage (Figure 34), thus confirming the appropriateness of the FEM model.

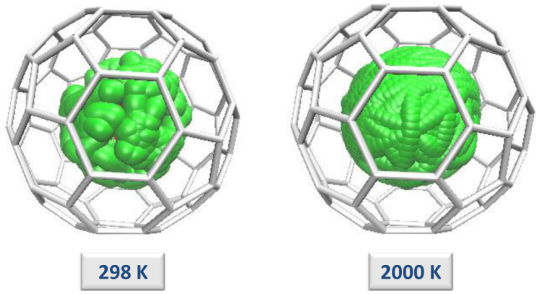

Figure 34. Cluster motion inside the I_h-C_{80}(31924) cage during the Car-Parrinello trajectories (25 ps) at 298 K and 2000 K.

Free rotation of the cluster makes the three Sc ions symmetry equivalent as in the prototypical $Sc_3N@I_h$-C_{80}(31924), which shows a single peak in the ^{45}Sc NMR spectrum. The variations of the three Sc-O-Sc angles and the Sc-O distances at 2000 K are presented in Figure 35. The angles oscillate around 120 degrees, which means that the Sc_3O remains essentially planar in average. At 2000 K, the Sc-O distances oscillate around 2.17 Å, a value that is somewhat longer than 2.08 Å, the average at 298 K (Figure 35 and Table 15); and longer than 2.05 Å, the average distance in the optimized structure (Table 15). The standard deviations for the Sc-O-Sc angles (around 10 degrees) and the Sc-O distances (around 0.09 Å) confirm that the Sc_3O cluster is rather flexible and that oscillations of the angles and distances are somewhat more important at higher temperatures (Figure 35 and Table 15).

Table 15. Mean values and standard deviations (in parenthesis) for the Sc-O distances (in Å) and Sc-O-Sc angles (in degrees) during the Car-Parrinello trajectories (25 ps) at room temperature and at 2000 K.

T	d(Sc1-O)	d(Sc2-O)	d(Sc3-O)	Angle (Sc1-O-Sc2)	Angle (Sc2-O-Sc3)	Angle (Sc1-O-Sc3)
298	2.072	2.083	2.080	117.4	114.0	118.3
	(0.045)	(0.038)	(0.040)	(9.9)	(10.2)	(9.8)
2000	2.166	2.171	2.171	120.3	118.0	119.2
	(0.087)	(0.089)	(0.087)	(10.1)	(10.4)	(10.3)

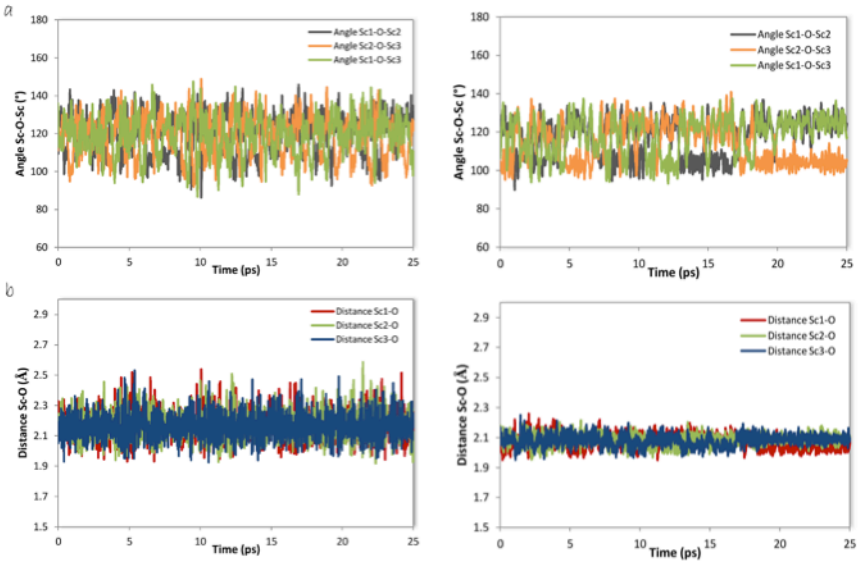

Figure 35. Oscillations of the three Sc-O-Sc angles (a) and Sc-O distances (b) at 2000 (left) and 298 K (right).

5.7.8. Polymerization of $Sc_3O@I_h$-C_{80}(31924)

Finally, we would like to discuss and provide a plausible explanation for the fact that this OCF is rather abundant in the soot, but isolated and purified in a tiny amount. It is known that some pristine fullerene cages that are free radicals or have small HOMO-LUMO (H-L) gaps, i.e. with kinetic instability, are prone to polymerize forming insoluble

products that are difficult to extract from raw soot using organic solvents.[72,75] Computed reaction energies for the formation of different $[Sc_3O@I_h\text{-}C_{80}(31924)]_2$ dimers show that dimerization is a favorable process for this radical OCF (Table 16). The dimerization energy can be as exothermic as -27 kcal·mol^{-1} when the bond is formed between two carbon atoms with high spin densities.

Different energies are predicted depending on the atoms that are bonded, being in many cases within -20 and -25 kcal mol^{-1}. Only the energies and H-L gaps for the lowest-energetic dimers are listed in Table 16. According to our results, this radical OCF might polymerize and, consequently, remain mainly in the soot when extracted with an organic solvent. Further isolation and purification by electrochemical reduction of the soot would improve the amount of purified OCF.[72] Likewise, if it were possible to quench the radical character of the OCF by addition of other radical species as phenyl, chlorine, etc. closed-shell systems with rather large band-gaps and much higher kinetic stabilities would be formed.

Table 16. Relative energies (E_{rel}), HOMO-LUMO (H-L) gaps and dimerization energies (E_{dim}) for several $[Sc_3O@I_h\text{-}C_{80}(31924)]_2$ dimers computed in this work.[a]

Dimer	E_{rel}	E_{dim}	H-L gap
1	0.0	-26.9	1.04
2	0.6	-26.3	1.10
3	1.1	-25.8	1.32
4	2.0	-24.9	1.01
5	3.3	-23.6	1.03
6	4.1	-22.8	1.14

[a] Energies in kcal·mol^{-1} and HOMO-LUMO gaps in eV.

H-L gaps of around 1 eV, at BP86/TZP level, are found for the magnetically-quenched $Sc_3O@I_h\text{-}C_{80}\text{-}CH_3(31924)$, $Sc_3O@I_h\text{-}C_{80}\text{-}Ph(31924)$ and $Sc_3O@I_h\text{-}C_{80}\text{-}Cl(31924)$ systems, which are larger than those found for most OCF characterized so far. The lowest-energy $[Sc_3O@I_h\text{-}C_{80}(31924)]_2$ dimer **1** also shows an enlarged H-L gap compared to the monomer (1.03 *vs* 0.29 eV). In addition, the HOMO and the LUMO remain quite localized on the Sc_3O clusters for the dimer as well as for the radical-quenched models (Figures 36). Therefore, all these functionalized $Sc_3O@I_h\text{-}C_{80}(31924)$ systems would also present electrochemistry *in cavea*, as the radical monomers.

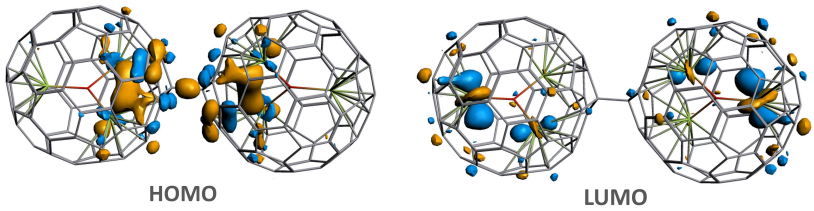

Figure 36. Representation of the HOMO and LUMO for the lowest-energy [$Sc_3O@I_h$-C_{80}(31924)]$_2$ dimer 1.

The same behaviour has the new superatomic crystal, [$Ni_{12}Te_{12}(PEt_3)_8$]$_2$[($Lu_3N@C_{80}$)$_2$], which Prof. Roy group at Columbia University discovered during their initial exploration of the reaction involving $Ni_9Te_6(PEt_3)_8$ and $Lu_3N@C_{80}$.[34] While polymerization could be a favourable process for $Sc_3O@I_h$-C_{80}(31924), here they found by using single crystal X-ray diffraction (SCXRD) that the anionic $Lu_3N@C_{80}$ is dimerized in the solid state, presumably as a consequence of the electron transfer from the electron-rich superatom. It selectively links the hexagon-hexagon-hexagon junctions (THJ) of neighboring C_{80} cages (Figure 37).

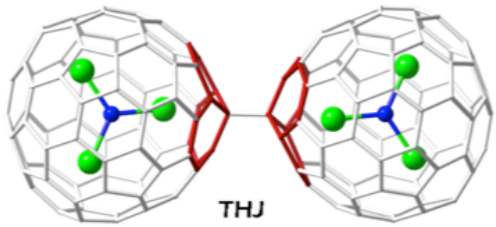

Figure 37. DFT-optimized geometries at PBE/TZ2P levels for the $Lu_3N@C_{80}$ dimers with a) THJ-THJ bonding with Lu_3N.

To evaluate the relevance of the stabilizing effect of the environment around the dianion we have represented the molecular electrostatic potential (MEP) distribution of the THJ dimer with and without solvent. Notice that in a continuum solvent model, both solvent and countercation effects are included in the calculations. In both cases, the region around the inter-cage bond has the highest electron density (shown in red

in Figure 38). Figure 38 shows that the electron density at the inter-cage junction increases significantly when the solvent environment is included in the calculation. These results suggest that the electrostatic environment surrounding the fullerenes can increase the stability of the dimer system by promoting the accumulation of electron density in the bonding hemispheres. A similar process could be at play in $[Ni_{12}Te_{12}(PEt_3)_8]_2[(Lu_3N@C_{80})_2]$ crystal as the cluster cations are located near the nucleophilic regions. In agreement with the spin density distribution,[34] the HOMO and the LUMO of the THJ $[Lu_3N@C_{80}]$ dimer are essentially localized on the cage, with the HOMO describing the bond formed between the two moieties (Figure 39).

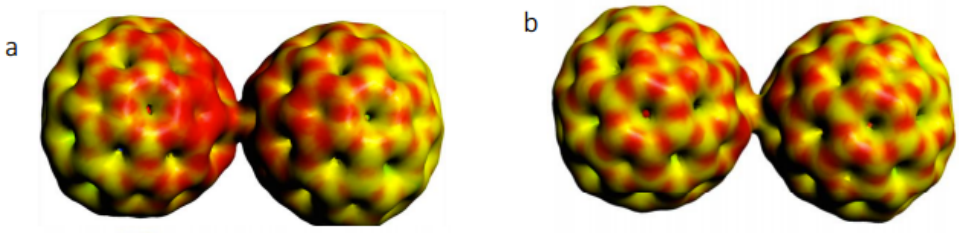

Figure 38. Molecular electrostatic potential distribution for the THJ dimer $[(Lu_3N@C_{80})_2]^{2-}$ (a) with and (b) without including the environment effects. More nucleophilic regions are displayed in red.

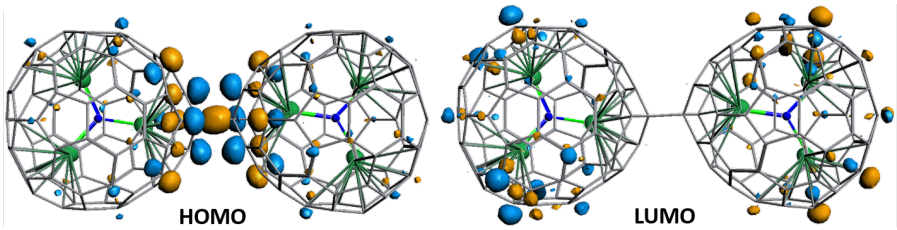

Figure 39. Representation of the HOMO and LUMO of the THJ $[Lu_3N@C_{80}]_2^{2-}$ dimer with Lu_3N in orientation 1.

Our results demonstrate that the nature of the encapsulated metal cluster controls the relative stability and orientation of the dimerization product, and our calculations agree

well with these results and predict that the THJ dimer becomes energetically flavored for $(Lu_3N@C_{80})_2^{2-}$.

5.8. Conclusions

The new metallic oxide clusterfullerenes, $Sc_2O@T_d$-C_{76}(19151), $Sc_2O@C_{2v}$-C_{80}(31922) and $Sc_2O@C_{3v}$-C_{82}(39717) have been isolated and characterized by mass spectrometry, UV-vis-NIR absorption spectroscopy, cyclic voltammetry, ^{45}Sc NMR spectroscopy, DFT calculations, and single-crystal X-ray diffraction. Computational studies show that the Sc_2O cluster transfers four electrons to the corresponding C_{2n} cage, $(Sc_2O)^{4+}@(C_{2n})^{4-}$.

$Sc_2O@T_d$-C_{76}(19151) is the most stable and abundant C_{76} cage in the whole range of temperatures. We suggest that the motion of the Sc_2O is more restrained inside the smaller T_d-C_{76}(19151) cage than in the C_s-C_{82}(39715) cage. This observation indicates that the cage size affects not only the shapes but also the cluster motion inside the carbon cages.

In case of $Sc_2O@C_{80}$, the $Sc_2O@C_{2v}$-C_{80}(31922) isomer was predicted to be the most abundant thermodynamic isomer at high temperatures (T > 1300 K), in agreement with the X-ray characterization, thus confirming again the relevant role that thermal and entropic effects play in the relative stabilization of OCFs.

Two isomers of $Sc_2O@C_{82}$ were isolated from the OCF mixtures synthesized by introducing CO_2 as the oxygen source during the arcing process. Besides the previously reported $Sc_2O@C_s$-C_{82}(39715), a new isomer, $Sc_2O@C_{3v}$-C_{82}(39717), was identified and fully characterized by mass spectrometry, UV−vis−NIR absorption, spectroscopy, cyclic voltammetry, ^{45}Sc NMR, DFT calculations, and single-crystal X-ray diffraction. Computational studies show that the cluster can rotate and change the Sc-O-Sc angle easily at rather low temperature.

$Sc_3O@I_h$-C_{80}(31924) has been detected in rather abundance in the raw soot, but isolated and purified with very low amounts. With the help of DFT computations, we predict $Sc_3O@I_h$-C_{80}(31924) as the isolated product and provide further characterization. A formal transfer of six electrons from the cluster to the cage explains the electronic structure of the compound, $(Sc_3O)^{6+}@(I_h$-$C_{80}(31924))^{6-}$. $Sc_3O@I_h$-C_{80}(31924) is isoelectronic to $Sc_3N@I_h$-$C_{80}(31924)^-$ and has a magnetic moment

different from zero in its neutral ground state. The predicted electrochemical gap, 0.74 V, is the lowest among all the OCFs isolated so far, which is in line with its low stability. Reaction energies for the formation of $[Sc_3O@I_h\text{-}C_{80}(31924)]_2$ dimers show that polymerization is a favorable process for this radical OCF and a plausible mechanism that might explain the significant drop in the yield once the product is extracted from the soot.

2.9. References

(1) Chai, Y.; Guo, T.; Jin, C.; Haufler, R. E.; Chibante, L. P. F.; Fure, J.; Wang, L.; Alford, J. M.; Smalley, R. E. *J. Phys. Chem.* **1991**, *95*, 7564.
(2) Li, F.-F.; Chen, N.; Mulet-Gas, M.; Triana, V.; Murillo, J.; Rodríguez-Fortea, A.; Poblet, J. M.; Echegoyen, L. *Chem. Sci.* **2013**, *4*, 3404.
(3) Wei, T.; Wang, S.; Lu, X.; Tan, Y.; Huang, J.; Liu, F.; Li, Q.; Xie, S.; Yang, S. *J. Am. Chem. Soc.* **2016**, *138*, 207.
(4) Junghans, K.; Schlesier, C.; Kostanyan, A.; Samoylova, N. A.; Deng, Q.; Rosenkranz, M.; Schiemenz, S.; Westerstrom, R.; Greber, T.; Buchner, B.; Popov, A. A. *Angew. Chem. Int. Ed. Engl.* **2015**, *54*, 13411.
(5) Wei, T.; Wang, S.; Liu, F.; Tan, Y.; Zhu, X.; Xie, S.; Yang, S. *J. Am. Chem. Soc.* **2015**, *137*, 3119.
(6) Zhang, Y.; Popov, A. A.; Schiemenz, S.; Dunsch, L. *Chem. Eur. J.* **2012**, *18*, 9691.
(7) Westerstrom, R.; Dreiser, J.; Piamonteze, C.; Muntwiler, M.; Weyeneth, S.; Brune, H.; Rusponi, S.; Nolting, F.; Popov, A.; Yang, S.; Dunsch, L.; Greber, T. *J. Am. Chem. Soc.* **2012**, *134*, 9840.
(8) Stevenson, S.; Rose, C. B.; Maslenikova, J. S.; Villarreal, J. R.; Mackey, M. A.; Mercado, B. Q.; Chen, K.; Olmstead, M. M.; Balch, A. L. *Inorg. Chem.* **2012**, *51*, 13096.
(9) Fu, W.; Xu, L.; Azurmendi, H.; Ge, J.; Fuhrer, T.; Zuo, T.; Reid, J.; Shu, C.; Harich, K.; Dorn, H. C. *J. Am. Chem. Soc.* **2009**, *131*, 11762.
(10) Duchamp, J. C.; Demortier, A.; Fletcher, K. R.; Dorn, D.; Iezzi, E. B.; Glass, T.; Dorn, H. C. *Chem. Phys. Lett.* **2003**, *375*, 655.
(11) Wang, Y.; Tang, Q.; Feng, L.; Chen, N. *Inorg. Chem.* **2017**, *56*, 1974.
(12) Chen, C.-H.; Abella, L.; Cerón, M. R.; Guerrero-Ayala, M. A.; Rodríguez-Fortea, A.; Olmstead, M. M.; Powers, X. B.; Balch, A. L.; Poblet, J. M.; Echegoyen, L. *J. Am. Chem. Soc.* **2016**, *138*, 13030.

(13) Feng, Y.; Wang, T.; Wu, J.; Feng, L.; Xiang, J.; Ma, Y.; Zhang, Z.; Jiang, L.; Shu, C.; Wang, C. *Nanoscale* **2013**, *5*, 6704.
(14) Kurihara, H.; Lu, X.; Iiduka, Y.; Mizorogi, N.; Slanina, Z.; Tsuchiya, T.; Akasaka, T.; Nagase, S. *J. Am. Chem. Soc.* **2011**, *133*, 2382.
(15) Kurihara, H.; Lu, X.; Iiduka, Y.; Nikawa, H.; Hachiya, M.; Mizorogi, N.; Slanina, Z.; Tsuchiya, T.; Nagase, S.; Akasaka, T. *Inorg. Chem.* **2012**, *51*, 746.
(16) Kurihara, H.; Lu, X.; Iiduka, Y.; Mizorogi, N.; Slanina, Z.; Tsuchiya, T.; Nagase, S.; Akasaka, T. *Chem. Commun. (Camb)* **2012**, *48*, 1290.
(17) Lu, X.; Nakajima, K.; Iiduka, Y.; Nikawa, H.; Tsuchiya, T.; Mizorogi, N.; Slanina, Z.; Nagase, S.; Akasaka, T. *Angew. Chem. Int. Ed. Engl.* **2012**, *51*, 5889.
(18) Chen, C.-H.; Ghiassi, K. B.; Cerón, M. R.; Guerrero-Ayala, M. A.; Echegoyen, L.; Olmstead, M. M.; Balch, A. L. *J. Am. Chem. Soc.* **2015**, *137*, 10116.
(19) Krause, M.; Ziegs, F.; Popov, A. A.; Dunsch, L. *ChemPhysChem* **2007**, *8*, 537.
(20) Yang, S.; Chen, C.; Liu, F.; Xie, Y.; Li, F.; Jiao, M.; Suzuki, M.; Wei, T.; Wang, S.; Chen, Z.; Lu, X.; Akasaka, T. *Sci. Rep.* **2013**, *3*, 1487.
(21) Chen, N.; Chaur, M. N.; Moore, C.; Pinzon, J. R.; Valencia, R.; Rodriguez-Fortea, A.; Poblet, J. M.; Echegoyen, L. *Chem. Commun. (Camb)* **2010**, *46*, 4818.
(22) Chen, N.; Mulet-Gas, M.; Li, Y. Y.; Stene, R. E.; Atherton, C. W.; Rodriguez-Fortea, A.; Poblet, J. M.; Echegoyen, L. *Chem. Sci.* **2013**, *4*, 180.
(23) Dunsch, L.; Yang, S. F.; Zhang, L.; Svitova, A.; Oswald, S.; Popov, A. A. *J. Am. Chem. Soc.* **2010**, *132*, 5413.
(24) Zhang, M.; Hao, Y.; Li, X.; Feng, L.; Yang, T.; Wan, Y.; Chen, N.; Slanina, Z.; Uhlík, F.; Cong, H. *The J. Phys. Chem. C* **2014**, *118*, 28883.
(25) Tang, Q.; Abella, L.; Hao, Y.; Li, X.; Wan, Y.; Rodríguez-Fortea, A.; Poblet, J. M.; Feng, L.; Chen, N. *Inorg. Chem.* **2016**, *55*, 1926.
(26) Tang, Q.; Abella, L.; Hao, Y.; Li, X.; Wan, Y.; Rodriguez-Fortea, A.; Poblet, J. M.; Feng, L.; Chen, N. *Inorg. Chem.* **2015**, *54*, 9845.
(27) Hao, Y.; Tang, Q.; Li, X.; Zhang, M.; Wan, Y.; Feng, L.; Chen, N.; Slanina, Z.; Adamowicz, L.; Uhlik, F. *Inorg. Chem.* **2016**, *55*, 11354.
(28) Yang, T.; Hao, Y.; Abella, L.; Tang, Q.; Li, X.; Wan, Y.; Rodriguez-Fortea, A.; Poblet, J. M.; Feng, L.; Chen, N. *Chem. Eur. J.* **2015**, *21*, 11110.
(29) Stevenson, S.; Mackey, M. A.; Stuart, M. A.; Phillips, J. P.; Easterling, M. L.; Chancellor, C. J.; Olmstead, M. M.; Balch, A. L. *J. Am. Chem. Soc.* **2008**, *130*, 11844.
(30) Stevenson, S.; Rice, G.; Glass, T.; Harich, K.; Cromer, F.; Jordan, M. R.; Craft, J.; Hadju, E.; Bible, R.; Olmstead, M. M.; Maitra, K.; Fisher, A. J.; Balch, A. L.; Dorn, H. C. *Nature* **1999**, *401*, 55.
(31) Popov, A. A.; Chen, N.; Pinzon, J. R.; Stevenson, S.; Echegoyen, L. A.; Dunsch, L. *J. Am. Chem. Soc.* **2012**, *134*, 19607.

(32) Mercado, B. Q.; Chen, N.; Rodriguez-Fortea, A.; Mackey, M. A.; Stevenson, S.; Echegoyen, L.; Poblet, J. M.; Olmstead, M. M.; Balch, A. L. *J. Am. Chem. Soc.* **2011**, *133*, 6752.
(33) Abella, L.; Tang, Q.; Zhang, X.; Wang, Y.; Chen, N.; Poblet, J. M.; Rodríguez-Fortea, A. *J. Phys. Chem. C* **2016**, *120*, 26159.
(34) Voevodin, A.; Abella, L.; Castro, E.; Paley, D. W.; Campos, L. M.; Rodríguez-Fortea, A.; Poblet, J. M.; Echegoyen, L.; Roy, X. *Chem. Eur. J.* **2017** (in press).
(35) Mercado, B. Q.; Stuart, M. A.; Mackey, M. A.; Pickens, J. E.; Confait, B. S.; Stevenson, S.; Easterling, M. L.; Valencia, R.; Rodríguez-Fortea, A.; Poblet, J. M.; Olmstead, M. M.; Balch, A. L. *J. Am. Chem. Soc.* **2010**, *132*, 12098.
(36) Rodriguez-Fortea, A.; Alegret, N.; Balch, A. L.; Poblet, J. M. *Nat. Chem.* **2010**, *2*, 955.
(37) Rodriguez-Fortea, A.; Poblet, J. M. *Faraday Discuss.* **2014**, *173*, 201.
(38) Chen, N.; Beavers, C. M.; Mulet-Gas, M.; Rodríguez-Fortea, A.; Munoz, E. J.; Li, Y.-Y.; Olmstead, M. M.; Balch, A. L.; Poblet, J. M.; Echegoyen, L. *J. Am. Chem. Soc.* **2012**, *134*, 7851.
(39) Slanina, Z. k.; Lee, S.-L.; UhlÃ-k, F.; Adamowicz, L.; Nagase, S. *Theor. Chem. Acc.* **2007**, *117*, 315.
(40) Slanina , Z.; Nagase, S. *ChemPhysChem* **2005**, *6*, 2060.
(41) Zhao, P.; Yang, T.; Guo, Y.-J.; Dang, J.-S.; Zhao, X.; Nagase, S. *J. Comput. Chem.* **2014**, *35*, 1657.
(42) Popov, A. A.; Yang, S.; Dunsch, L. *Chem. Rev.* **2013**, *113*, 5989.
(43) Chaur, M. N.; Melin, F.; Ortiz, A. L.; Echegoyen, L. *Angew. Chem. Int. Ed.* **2009**, *48*, 7514.
(44) Valencia, R.; Rodriguez-Fortea, A.; Stevenson, S.; Balch, A. L.; Poblet, J. M. *Inorg. Chem.* **2009**, *48*, 5957.
(45) Umemoto, H.; Ohashi, K.; Inoue, T.; Fukui, N.; Sugai, T.; Shinohara, H. *Chem. Commun.* **2010**, *46*, 5653.
(46) Yang, S.; Popov, A. A.; Dunsch, L. *J. Phys. Chem. B* **2007**, *111*, 13659.
(47) Car, R.; Parrinello, M. *Phys. Rev. Lett.* **1985**, *55*, 2471.
(48) Kurihara, H.; Lu, X.; Iiduka, Y.; Mizorogi, N.; Slanina, Z.; Tsuchiya, T.; Akasaka, T.; Nagase, S. *J. Am. Chem. Soc.* **2011**, *133*, 2382.
(49) Mercado, B. Q.; Olmstead, M. M.; Beavers, C. M.; Easterling, M. L.; Stevenson, S.; Mackey, M. A.; Coumbe, C. E.; Phillips, J. D.; Phillips, J. P.; Poblet, J. M.; Balch, A. L. *Chem. Commun.* **2010**, *46*, 279.
(50) Zhen, M. M.; Shu, C. Y.; Li, J.; Zhang, G. Q.; Wang, T. S.; Luo, Y.; Zou, T. J.; Deng, R. J.; Fang, F.; Lei, H.; Wang, C. R.; Bai, C. L. *SCMs* **2015**, *58*, 799.
(51) Tagmatarchis, N.; Shinohara, H. *Chem. Mat.* **2000**, *12*, 3222.

(52) Valencia, R.; Rodriguez-Fortea, A.; Clotet, A.; de Graaf, C.; Chaur, M. N.; Echegoyen, L.; Poblet, J. M. *Chem. Eur. J.* **2009**, *15*, 10997.
(53) Rodriguez-Fortea, A.; Balch, A. L.; Poblet, J. M. *Chem. Soc. Rev.* **2011**, *40*, 3551.
(54) Zhang, Q. L.; Obrien, S. C.; Heath, J. R.; Liu, Y.; Curl, R. F.; Kroto, H. W.; Smalley, R. E. *J. Phys. Chem.* **1986**, *90*, 525.
(55) Smalley, R. E. *Acc. Chem. Res.* **1992**, *25*, 98.
(56) Schwarz, H. *Angew. Chem. Int. Ed. Engl.* **1993**, *32*, 1412.
(57) Ueno, Y.; Saito, S. *Phys. Rev. B* **2008**, *77*, 085403.
(58) Wakabayashi, T.; Achiba, Y. *Chem. Phys. Lett.* **1992**, *190*, 465.
(59) Irle, S.; Zheng, G.; Wang, Z.; Morokuma, K. *J. Phys. Chem. B* **2006**, *110*, 14531.
(60) Saha, B.; Irle, S.; Morokuma, K. *J. Phys. Chem. C* **2011**, *115*, 22707.
(61) Dunk, P. W.; Kaiser, N. K.; Hendrickson, C. L.; Quinn, J. P.; Ewels, C. P.; Nakanishi, Y.; Sasaki, Y.; Shinohara, H.; Marshall, A. G.; Kroto, H. W. *Nat. Chem.* **2012**, *3*, 855.
(62) Mulet-Gas, M.; Abella, L.; Dunk, P. W.; Rodriguez-Fortea, A.; Kroto, H. W.; Poblet, J. M. *Chem. Sci.* **2015**, *6*, 675.
(63) Dunk, P. W.; Kaiser, N. K.; Mulet-Gas, M.; Rodriguez-Fortea, A.; Poblet, J. M.; Shinohara, H.; Hendrickson, C. L.; Marshall, A. G.; Kroto, H. W. *J. Am. Chem. Soc.* **2012**, *134*, 9380.
(64) Gan, L. H.; Wu, R.; Tian, J. L.; Fowler, P. W. *Phys. Chem. Chem. Phys.* **2017**, *19*, 419.
(65) Zhang, Y.; Ghiassi, K. B.; Deng, Q.; Samoylova, N. A.; Olmstead, M. M.; Balch, A. L.; Popov, A. A. *Angew. Chem. Int. Ed.* **2015**, *54*, 495.
(66) Guo, Y. J.; Gao, B. C.; Yang, T.; Nagase, S.; Zhao, X. *Phys. Chem. Chem. Phys.* **2014**, *16*, 15994.
(67) Abella, L.; Wang, Y.; Rodríguez-Fortea, A.; Chen, N.; Poblet, J. M. *Inorg. Chim. Acta* **2017** *(in press)*.
(68) Lewis, A.; Bumpus, J. A.; Truhlar, D. G.; Cramer, C. J. *J. Chem. Ed.* **2004**, *81*, 596.
(69) Valencia, R.; Rodriguez-Fortea, A.; Poblet, J. M. *J. Phys. Chem. A* **2008**, *112*, 4550.
(70) Tan, K.; Lu, X. *J. Phys. Chem. A* **2006**, *110*, 1171.
(71) Popov, A. A.; Dunsch, L. *J. Am. Chem. Soc.* **2008**, *130*, 17726.
(72) Rigorously, in unrestricted calculations where there is a set of alpha orbitals and a set of beta orbitals, oxidation takes place on the (alpha) SOMO and reduction on

the (beta) LUMO; these two orbitals are very similar, but they show somewhat different energy.

(73) Krause, M.; Dunsch, L. *ChemPhysChem* **2004**, *5*, 1445.

(74) Iiduka, Y.; Wakahara, T.; Nakahodo, T.; Tsuchiya, T.; Sakuraba, A.; Maeda, Y.; Akasaka, T.; Yoza, K.; Horn, E.; Kato, T. *J. Am. Chem. Soc.* **2005**, *127*, 12500.

(75) Diener, M. D.; Alford, J. M. *Nature* **1998**, *393*, 668.

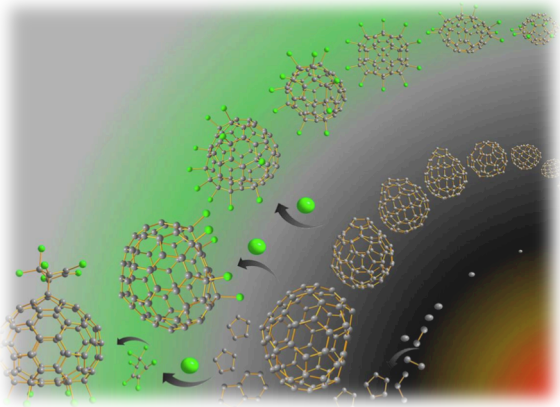

CHAPTER 6

On the Formation of Chlorofullerenes

Related Publications:

Different Factors Govern Chlorination and Encapsulation in Fullerenes: The Case of C_{66}
Alegret, N.; Abella, L.; Azmani, K.; Rodríguez-Fortea, A.; Poblet, J. M. *Inorg. Chem.* **2015**, 54, 7562.

Capturing the Fused-Pentagon C_{74} by Stepwise Chlorination
Gao, C. L.; Abella, L.; Tan, Y. Z.; Wu, X. Z.; Rodríguez-Fortea, A.; Poblet, J. M.; Xie, S. Y.; Huang, R. B.; Zheng, L. S. *Inorg. Chem.* **2016**, 55, 6861.

Double Functionalization of a Fullerene in Drastic Arc-Discharge Conditions: Synthesis and Formation Mechanism of $C_{2v}(2)$-$C_{78}Cl_6(C_5Cl_6)$
Gao, C. L.; Abella, L.; Tian, H. R.; Zhang, X.; Zhong, Y. Y.; Tan, Y. Z.; Wu, X. Z.; Rodríguez-Fortea, A.; Poblet, J. M.; Xie, S. Y.; Huang, R. B.; Zheng, L. S. **2017** (submitted for publication).

CHAPTER 6

On the Formation of Chlorofullerenes

This chapter tells about the interesting world of one kind of exohedral metallofullerenes; the chlorofullerenes. Chlorination has emerged as a powerful tool in fullerene derivatives. Several C_{2n} families (2n=50,60,66,68,etc.) have been found to show cages exohedrally chlorinated. The reaction sites where chlorines are attached, the chlorination pathways and how chlorofullerenes are formed are issues that have been considered in recent years. Part of this work was done during my stay at Xiamen University, in the group of Prof. Su-Yuan Xie.

6.1. Introduction

The rule per excellence governing the stability of fullerene cages is the well known Isolated Pentagon Rule.[1,2] The first fullerenes that did not satisfy this rule appeared in the 2000, with the simultaneous discovery of $Sc_2@C_{66}$ and $Sc_3N@C_{68}$.[3,4] With them, a second factor governing the fullerene's stability emerged: the instability of the non-IPR structures coming from the adjacent pentagons could be counterbalanced by charge transfer from an encapsulated metal atom or cluster.[5-7] It was not until 2004, when the first empty non-IPR cage $C_{50}Cl_{10}$ appeared;[8] a second way of breaking IPR by exohedral derivatization with halogens. Thus, non-IPR fullerenes can be obtained by insertion of metallic clusters inside the cavity or by external addition of halogenated species.

As an important branch of structurally investigated fullerene derivatives, fullerene chlorides have an irreplaceable advantage. They not only can serve as intermediates

for further derivatization of fullerenes, but also facilitate characterization of higher fullerenes. Derivatization of fullerene**s** is crucial in the development of new materials with potential applications in future technologies, and in the investigation of the role that any modification of the cage plays in tuning their properties.

Fullerenes can be chlorinated by introducing chlorines in the chaotic violent graphite arc discharge[9] or by reacting with inorganic chlorides (Cl_2,[10,11] ICl,[12] $SbCl_5$,[13-15] $TiCl_4$[16] and VCl_4[15,17]) at high temperature. Remarkable progress has been achieved in synthesis and investigation of fullerene chlorides in the last years. Numerous fullerenes chlorides, no matter whether IPR or non-IPR, have been produced.[18] In the presence of CCl_4, for example, a modified Krätschmer-Huffman arc discharge has been applied to synthesize smaller non-IPR chlorofullerenes such as D_{5h}-symmetric $C_{50}(271)Cl_{10}$, $C_{54}(540)Cl_8$, $C_{56}(864)Cl_{12}$, $C_{56}(913)Cl_{10}$.[8,19-21] Similar to arc-discharge technology, a number of chlorofullerenes such as $C_{56}(916)Cl_{12}$,[22] $C_{72}(11188)Cl_4$,[23] and $C_{68}(6094)Cl_8$[24] have been produced in radio-frequency furnace starting from graphite in the presence of CCl_4. In addition to chlorofullerenes, a few of exofullerenes functionalized with chlorinated carbon clusters (CCCs) were isolated as well.[25] Interestingly, the heretofore isolable fullerene chlorides can be exclusively classified into two types, i.e. chlorofullerenes functionalized with chlorine atoms and exo-fullerenes functionalized with CCCs. The introduction of chlorine atoms diminishes the strain caused by the presence of a delocalized double bond within a pentagon, makes the carbon atoms hybridizing from sp^2 to sp^3 and results in different aromatic fragments. The change of the distribution of surface charge of the cage brings into question the reactivity of the carbon sphere.

Other unconventional exohedral fullerene derivatives, such as $C_{66}H_4$, $C_{60}F_{18}$, $C_{60}F_{36}$ and $C_{60}F_{48}$ have been obtained.[26,27] Fluorinated fullerenes were shown to be more thermally stable and chemically inert than hydrogenated fullerenes. The reason lies in the relative strengths of the chemical bonds formed as a result of hydrogenation and fluorination: C-F bonds are stronger than C-H bonds. The effect of fluorine and chlorine atoms on the cage is very different because the former is much more electronegative than the latter, and the reactivity of the remaining sp^2-hybridized carbon atoms changes with the change of the number of halogen atoms and the size of the parent cage.

6.2. Factors that Govern the Chlorination: The Case of C_{66}

In 2010, Xie and Zheng reported a new isomer of C_{66} with 6 and 10 chlorine atoms attached on the fullerene surface.[28] The cage was characterized with the crystal structure as the C_{66}(4169) isomer (Figure 1), which was the first fullerene featuring triple sequentially fused pentagons (TSFP). This new characterized isomer arouse the curiosity of the fullerene community and, thus, the experiments to chlorinate C_{66}(4348) isomer, which was the first cage proposed to be detected in endohedral form, started. Recently, Xie and co-workers were able to identify by X-ray crystallography the halogenated C_{66}(4348)Cl_{10}, shown in Figure 1.[29]

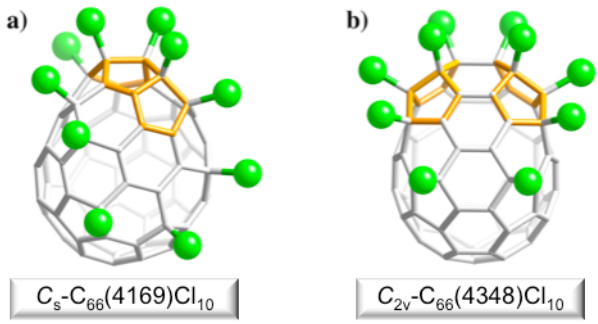

Figure 1. Computed structures of the experimental a) C_{66}(4169)Cl_{10} and b) C_{66}(4348)Cl_{10}.

Therefore, three isomers of C_{66} have been observed, two with exohedral derivatization and one with endohedral encapsulation: C_{66}(4348)Cl_{10}, C_{66}(4169)Cl_{10} and C_{66}(4169)Cl_6, and Sc_2@C_{66}(4059). In this work we have tried to understand (i) why endohedral and exohedral fullerenes show different cages; (ii) which is the main property that defines the cage selection.

6.2.1. Exploring the Most Appropriate C_{66} Cages

No possible IPR structures exist among the 4478 isomers of C_{66}.[2] In particular, none of them have one pair of fused pentagons (N_p=1); even more, only three of the isomers have two pentagon adjacencies: 4348 and 4169, both obtained experimentally as halogenated fullerenes (Figure 1), and 4466, proposed by Cui for Sc_2@C_{66}.[30] Most of the cages with 66 carbon atoms (176) show four pentagons adjacencies (N_p=4).

To analyse the chlorine-functionalized fullerenes we have evaluated the 4478 isomers at the neutral state. Table 1 shows the lowest-energetic neutral isomers. We do not consider the charged species since there is no electronic transfer present, but covalent bonding between the carbon atoms and the chlorines. The results, Table 1, show that the most stable and almost isoenergetic cages at the neutral state correspond to the two observed chlorinated isomers C_{66}(4348) and C_{66}(4169), followed by isomer C_{66}(4466)Cl_{10} at 7.3 kcal·mol^{-1}. All the other isomers appeared at more than 12 kcal·mol^{-1}. Note that the third experimental isomer C_{66}(4059), which was obtained as an endohedral fullerene, is placed within the first 100 with a relative energy of almost 48 kcal·mol^{-1}.

Table 1. Relative energies (E_{rel}) (in kcal·mol^{-1}), computed at the BP86/TZP level, symmetry and number of adjacent pentagons (N_p) for the most stable isomers of C_{66}.

Isomer	Symmetry	N_p	E_{rel}
#4169	C_s	2	0.0
#4348	C_{2v}	2	0.8
#4466	C_2	2	7.3
#4007	C_1	3	12.8
#3764	C_1	3	13.5
#4454	C_2	3	25.3
#4410	C_s	3	27.6
#4398	C_1	3	28.9
#4437	C_2	4	42.7
#4417	C_2	4	46.3
#4059	C_{2v}	4	47.8
#4407	C_2	4	52.3

The two lowest-energy neutral cages are the ones that have been identified as C_{66} chlorofullerenes, 4169 and 4348. Therefore, we could infer that halogenation has taken place once the cages are formed.

6.2.2. Building Several $C_{66}Cl_{10}$

We have considered the halogenated positions of the two experimental systems C_{66}(4348) and C_{66}(4169) as the model to build several $C_{66}Cl_{10}$ isomers and evaluate their energy differences. Structurally, these two fullerenes show N_p=2: C_{66}(4348) has a pair of fused pentagons, while C_{66}(4169) has a single TSFP. From deep analyses of the chlorine positions, we can outline that the main rule governing the halogenation is the release of surface strain, and that it is structurally achieved through several patterns: *(A)*

several chlorines are placed at the fused pentagons through one [5,5] bond in a zig-zag manner, 4 Cl at the pentalene motif and 5 at the TSFP; *(B)* the remaining chlorines are positioned on pentagons near the [5,5] bonds, and, in general, at (1,4) position one from each other; *(C)* finally, a closed belt of chlorines is formed along the surface.

Taking all these observations into account, we have used the $C_{66}(4059)Cl_{10}$ system to validate them and computed 50 different chlorine-patterned regioisomers.[31] We confirmed that the patterns designed according to the conditions A and B lead to the most stable structures. Then, we designed the chlorination patterns for isomers 3764, 4007, and 4466 by connecting the two adjacent-pentagon motifs while placing the chlorines at the fused pentagons (*condition A*) and at the pentagons near them at 1,4 distance (*condition B*). Once again, none of the three isomers reach a number of chlorines enough to close the belt around the cage (*condition C*). A complete list of the energies of the computed $C_{66}Cl_{10}$ isomers can be found in Table 2. At this point, it has to be noted that in all the cases studied, including the isomer 4059, the pentagon-fused motifs are not as close as in 4348, and thus there are many possibilities to connect them with chlorines. When more than one [5,5] bond is present, the relative position of the pentagon-fused motifs, and thus the connection between them using chlorines is, in some sense, an important factor that drives the chlorine addition. Therefore, the relative position of the fused-pentagon junctions plays a key role to determine the number of chlorines attached at each pentagon motif. Table 2 collects the relative energies of both the experimental and the low-lying computed chloroisomers. As for the neutral pristine cages, the experimental $C_{66}(4348)Cl_{10}$ remains the most stable isomer among all the calculated. Surprisingly, the second most stable isomer at 8.3 kcal·mol^{-1} is the computed $C_{66}(4466)Cl_{10}$. Above them, between 19.5 and 23.6 kcal·mol^{-1} a set of chlorofullerenes includes the $C_{66}(3764)Cl_{10}$, the experimental $C_{66}(4169)Cl_{10}$, and the regioisomers of $C_{66}(4007)Cl_{10}$. Quite higher, the $C_{66}(4059)Cl_{10}$ lays at more than 38 kcal·mol^{-1}. Such results are not conclusive enough to discard the possible formation of other $C_{66}Cl_{10}$ species.

Table 2. Relative energies (E_{rel}) (in kcal·mol^{-1}) for the lowest $C_{66}Cl_{10}$ isomers.

$C_{66}Cl_{10}$ Isomer	E_{rel}
4348	0.0
4466	8.3
3764	19.5
4169	21.1
4007-1	21.6
4007-2	21.8
4007-3	23.6
4059-1	38.7
4059-2	40.7

6.2.3. Thermal and Entropic Effects in C_{66} and $C_{66}Cl_{10}$

Maybe, other C_{66} species could be chlorinated, for that reason we have also evaluated the molar fractions of the lowest-energy isomers as a function of the temperature. We have used the rigid rotor and harmonic oscillator (RRHO) approximation.[32,33] As shown in Figure 2, the $C_{66}(4348)Cl_{10}$ is the most abundant chlorofullerene up to 1000K. At 2000 K and higher temperatures, isomer $C_{66}(4466)Cl_{10}$ achieve abundances up to 80%. The remaining isomers increase slightly their relative abundances with the temperature, although none of them exceed the 10%. It is surprising that, according to these results, the experimentally synthesized $C_{66}(4169)Cl_{10}$ should have never been obtained, and that $C_{66}(4466)Cl_{10}$ should have been observed instead. This could indicate either that isomer $C_{66}(4466)Cl_{10}$ is also feasible for halogenation, and it would be synthesized in a future, or that the halogenation of the cages takes place at relatively low temperatures and so the principal driving force to produce halogenated species is the formation of the pristine cages – note that the experimental $C_{66}(4348)$ and $C_{66}(4169)$ isomers are the most abundant neutral cages in the whole range of temperatures as shown in Figure 2.

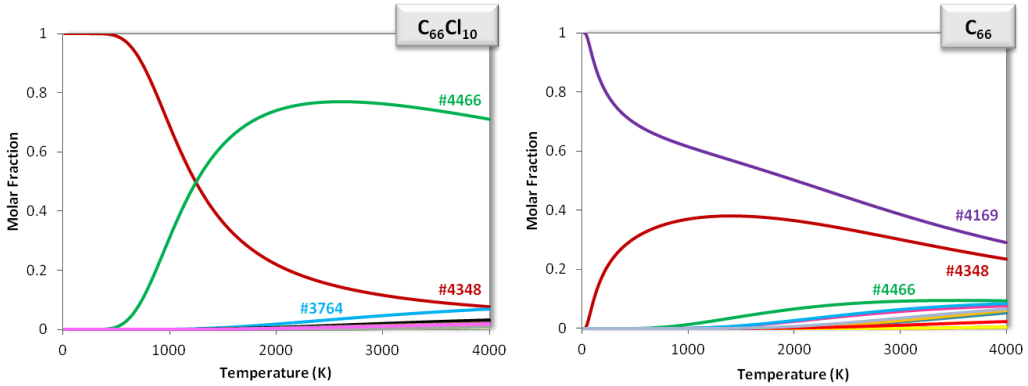

Figure 2. Representation of the molar fraction as a function of the temperature for the isomers of $C_{66}Cl_{10}$ and C_{66} using the RRHO approximation. Only the three most abundant isomers are labeled.

6.2.4. Behavior of Chlorines at High Temperatures

Car-Parrinello Molecular Dynamics simulations were also performed to provide more insight into the motion of chlorines at high temperatures. The trajectories at 2000 K for the experimental $C_{66}(4348)Cl_{10}$ cage show that chlorine atoms are lost after the first 4

ps. This result indicates that chlorination of fullerenes does not take place at 2000 K, but at lower temperatures. Trajectories at 1000 K and 800 K confirm that chlorines remain at their original positions at the rather short time scale simulated here (around 50 ps), as shown in Figure 3. Detachment and subsequent attachment of a single chlorine atom are rarely observed in some of these simulations, keeping the fullerene the total number of chlorines at the end of the trajectories. Therefore, chlorination should take place once the temperature in the arc is reduced (much lower than 2000 K) and the empty cages formed.

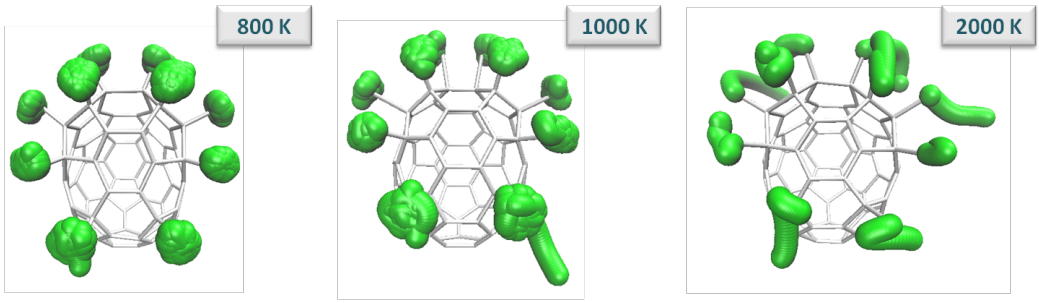

Figure 3. Representation of the motion of the Cl atoms in $C_{66}(4348)Cl_{10}$ during Car-Parrinello MD trajectories at 800 K, 1000 K and 2000 K.

6.3. The Stepwise Chlorination Path in $C_{74}Cl_{10}$

So far, all the clearly characterized structures of C_{74} derivatives are based on the same isomer of C_{74} with a D_{3h}-symmetry and a Fowler-Manolopoulos code of 14246,[2] namely the sole IPR-satisfying isomer among 14246 C_{74} isomers.[1] Although a number of non-IPR fullerenes have been stabilized by endohedral or exohedral derivatization in previous reports, the non-IPR structure in the family of C_{74} was unclear in experiments.

In this section, we report a hollow non-IPR C_{74} isomer, 14049,[2] which was captured by exohedral chlorination, extracted from toluene solution of carbon soot produced in a chlorine involving arc-discharge of graphite, definitely characterized as C_1-$C_{74}(14049)Cl_{10}$ by mass spectra and single-crystal X-ray diffraction, and studied by DFT methodology.

6.3.1. Experimental Data

The molecular composition of $C_{74}Cl_{10}$ was confirmed by mass spectrometry (MS) using an atmosphere pressure chemical ionization (APCI) source (Figure 4). The strong peak at 887.9 m/z confirms that the non-IPR C_{74} fullerene is produced in the graphite arc-discharge and existed in the gas phase.

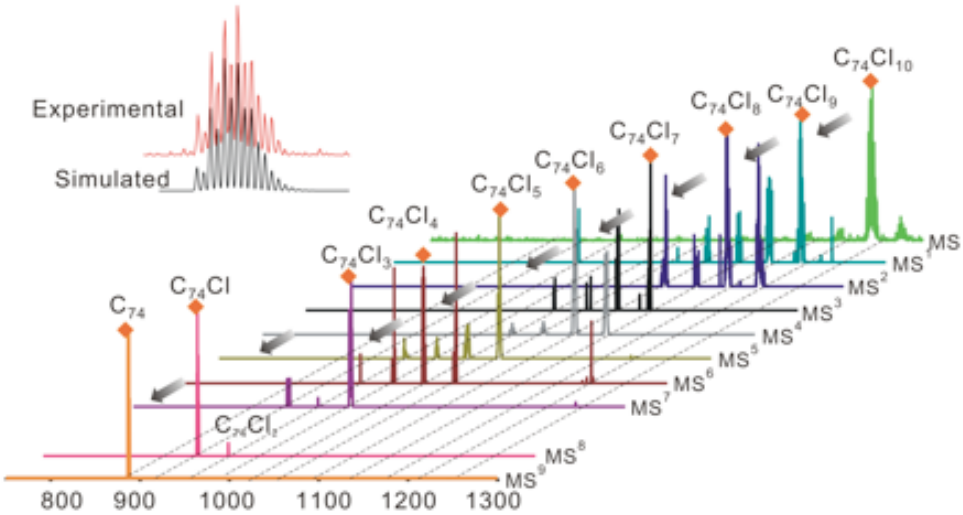

Figure 4. Multistage mass spectra (MS^n, n=1-9) *C*$_1$-C_{74}(14049)Cl_{10}. The mother ions of *C*$_1$-C_{74}(14049)Cl_{10} marked by rhombus are selected for the next dechlorination.

6.3.2. Comparison *D*$_{3h}$-C_{74}(14246)Cl_n *versus* *C*$_1$-C_{74}(14049)Cl_n

In principle, the kinetic stability of a molecule can be related with its H-L gap. The IPR *D*$_{3h}$-C_{74}(14246) isomer is elusive in the soot of graphite arc-discharge due to its small H-L gap.[34,35] In addition, this *D*$_{3h}$-C_{74}(14246) isomer is found to have an open-shell electronic structure according to computation at density functional theory level,[36] which confers it a radical-like character prone to polymerize. When we compare the H-L gaps of the non-IPR *C*$_1$-C_{74}(14049) and *C*$_1$-C_{74}(14049)Cl_{10}, we observe that chlorination of *C*$_1$-C_{74}(14049) induces a change in the H-L gap from 0.344 eV in the pristine structure to 1.727 eV in the chloride (at BP86/TZP level). The latter is even larger than that in C_{60} (1.658 eV), implying that the external chlorine atoms clearly increase the kinetic stability of the cage and stabilize the fullerene. The corresponding HOMO and LUMO of *C*$_1$-C_{74}(14049) and *C*$_1$-C_{74}(14049)Cl_{10} are shown in Figure 5. Even though the *C*$_1$-C_{74}(14049) is viable in the gas phase as inferred from the multistage mass spectra, the non-IPR *C*$_1$-C_{74}(14049) cage is assumed much more reactive to

chlorine than the IPR D_{3h}-C_{74}(14246) cage because of the enhanced reactivity of the pentalene [5,5] bond compared to the [5,6] and [6,6] bonds of the IPR structure. The IPR cage shows significantly lower energy than the non-IPR C_1-C_{74}(14049) one (21 kcal·mol^{-1} at BP86/TZP level), but the relative stability is already changed for the dichlorinated system. The energy of the non-IPR C_1-C_{74}(14049)Cl_2 isomer is 11 kcal·mol^{-1} lower than that of D_{3h}-C_{74}(14246)Cl_2 isomer (Figure 6). Therefore, we analyze below, using computational tools, the most favorable positions for the sequential chlorination steps of C_1-C_{74}(14049), which seems to be a plausible mechanism, among other possibilities, for the formation of C_1-C_{74}(14049)Cl_{10}.

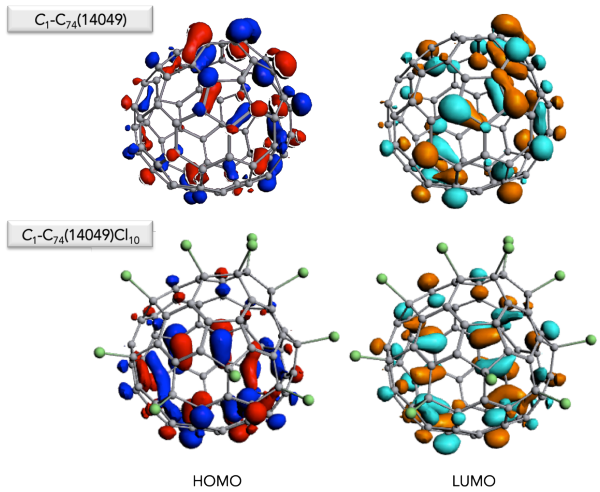

Figure 5. HOMO (left) and LUMO (right) orbitals of C_1-C_{74}(14049) and C_1-C_{74}(14049)Cl_{10}.

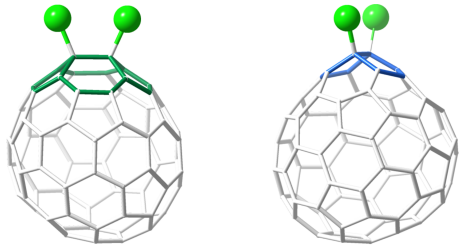

Figure 6. Representation of the non-IPR C_1-C_{74}(14049)Cl_2 isomer (right) with the two chlorines in the pentalene bond (pentalene motif highlighted in blue) and the IPR D_{3h}-C_{74}(14246)Cl_2 isomer with the two chlorines in one pyracylene [6,6] bond (left, pyracylene motif highlighted in green). The two cages are related by a Stone-Wales transformation on the [6,6] bond that is chlorinated in D_{3h}-C_{74}(14246)Cl_2.

6.3.3. Chlorination Pathway

Sometimes, the reactivity of a given fullerene can be rationalized easily from the simple inspection of energies and shapes of its molecular orbitals. In particular, the radical addition to a non-IPR fullerene can be understood from the atomic orbital contributions to the HOMO and the spin density distribution for cages with an odd number of Cl atoms. The shapes of the HOMOs for the closed-shell systems *C*1-C_{74}(14049), *C*1-C_{74}(14049)Cl_2, *C*1-C_{74}(14049)Cl_4, *C*1-C_{74}(14049)Cl_6, *C*1-C_{74}(14049)Cl_8, and *C*1-C_{74}(14049)Cl_{10} together with the spin densities for the radicals *C*1-C_{74}(14049)Cl_3, *C*1-C_{74}(14049)Cl_5, *C*1-C_{74}(14049)Cl_7, and *C*1-C_{74}(14049)Cl_9, are drawn in Figure 7 along with the stepwise chlorination pathway.

The first two chlorine atoms are added sequentially to the pentalene bond of the fused pentagons so that strain is maximally released.[31] The C atoms in these pentalene bonds are by far the two most pyramidalized atoms in the structure (pyramidalization angles of 16.25° and 14.89°). In addition, these two atoms show the highest atomic orbital contributions to the HOMO of C_{74} (Figure 7a). Once the first chlorine was added in any of the two C atoms of the pentalene bond, the two possible $C_{74}Cl$ radicals that could be generated show important values of the spin density on the other C atom of the pentalene. Therefore, both strain and electronic factors point to sequential addition to the pentalene bond for the first two chlorination steps. On the basis of the highest contribution to the HOMO of $C_{74}Cl_2$ the next position to be chlorinated is one [5, 6, 6] C atom contiguous to the pentalene bond, indicated by an arrow in $C_{74}Cl_2$ or as a black dot in the Schlegel diagram in Figure 7b. For the $C_{74}Cl_3$ radical, which shows several active sites with rather high spin densities, the most stable regioisomer was found to be that with the four chlorine atoms placed in the fused pentagons in a zigzag manner (Figure 7c). Therefore, analogous to C_{72}(11188)Cl_4 and other non-IPR chlorofullerenes, there are four Cl atoms placed at the fused pentagons through one [5, 5] bond in a zigzag manner.[23,37] Further chlorination on $C_{74}Cl_4$ was investigated. The fifth addition takes place again in the carbon atom with the highest HOMO contribution (Figure 7d), and the sixth addition is to the position with the highest spin density in $C_{74}Cl_5$ (Figure 7e). Chlorination up to $C_{74}Cl_{10}$ follows the same patterns: the lowest-energy regioisomers are those having highest HOMO (for systems with an even number of Cl atoms) or highest spin density contributions (for systems with an odd number of Cl atoms).

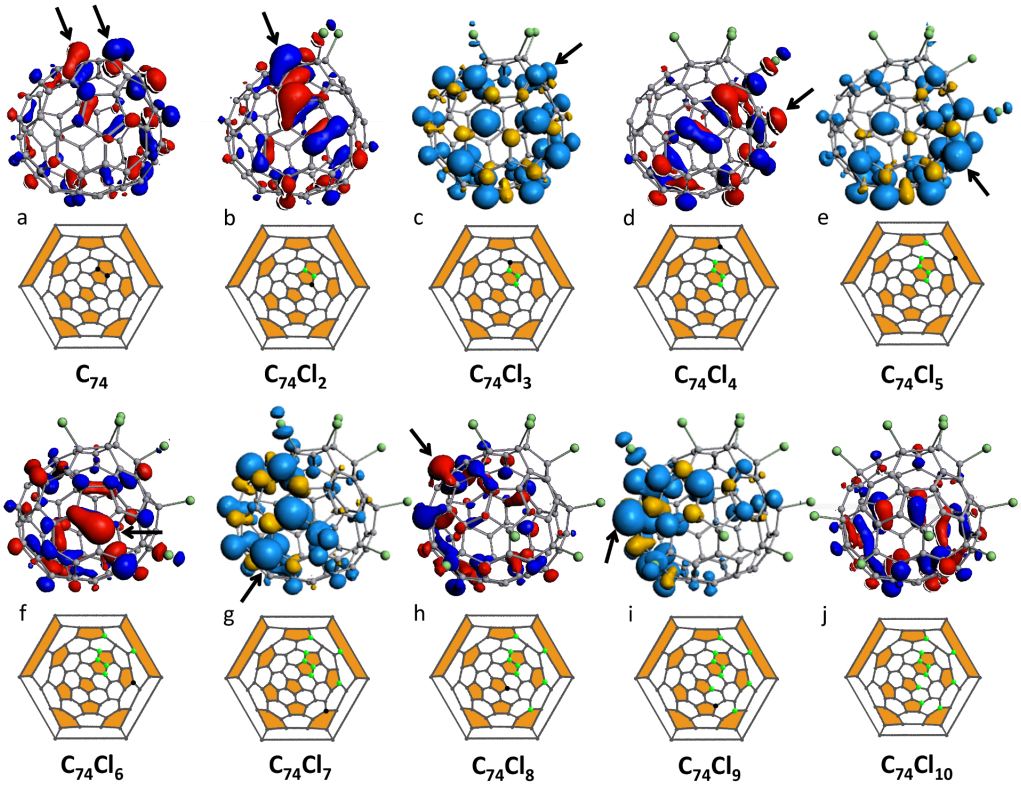

Figure 7. Representation of the HOMO (for C_{74}, $C_{74}Cl_2$, $C_{74}Cl_4$, $C_{74}Cl_6$, $C_{74}Cl_8$ and $C_{74}Cl_{10}$) or the spin density (for $C_{74}Cl_3$, $C_{74}Cl_5$, $C_{74}Cl_7$ and $C_{74}Cl_9$) distributions, along with the corresponding Schlegel diagrams, for different steps of the chlorination pathway. The green dots in the Schlegel diagrams indicate the positions of the chlorine atoms. The black arrows in the 3D structure and the black dots in the Schlegel diagrams show the position where the next chlorine atom is added.

6.3.3.1. Electronic Properties

Other positions that present high HOMO contributions or high spin densities were also analyzed, but in all cases the selected positions are the ones that led to the regioisomers with the lowest energy. Thus, stepwise chlorination from C_1-C_{74}(14049) to C_1-C_{74}(14049)Cl_{10} might take place following two simple rules; that is, (i) addition on structures with an even number of chlorines is directed by the highest atomic orbital contributions to the HOMO and (ii) addition on structures with an odd number of chlorines is governed by the topology of the spin densities. It is worth remarking here that these results are in good agreement with the chlorination patterns established so far[18,29,38] and with the experimental results as exemplified by dechlorination in the multistage mass spectra in negative ion mode (Figure 4). The introduction of chlorine

atoms effectively reduces reactive sites of the bare cage, preventing from polymerization and improving the solubility.

We observed that the H-L gaps show a gradual increase upon chlorination up to *C*1-C_{74}(14049)Cl_{10} (Table 3). In addition, bond energies between carbon and chlorine atoms in *C*1-C_{74}(14049) were found to be similar as in other chlorinated fullerenes detected so far (ca. – 50 kcal mol^{-1}). The bond energies for the first and second chlorines, which attach to the pentalene bond, are ca. −60 kcal mol^{-1}. We checked that the bond energies for dichlorination at other positions of the cage are much lower. The C−Cl bond energies for radicals *C*1-C_{74}(14049)Cl_x (x = 3, 5, 7, and 9) are significantly smaller than those for closed-shell species (x = 4, 6, 8, and 10). The bond energies for x = 6 and x = 8 are rather high (−58 kcal·mol^{-1}), but the energy for the addition of the 10th chlorine is by far the largest, which is related to the high stability of the formed product *C*1-C_{74}(14049)Cl_{10}. Despite the above analysis, we can not rule out that the *C*1-C_{74}(14049)Cl_{10} formation might also occur through chlorination of the isomeric *D*3h-C_{74}(14246), which is existent in the fullerene soot.[35,39-42] Topologically it is possible to undergo a single Stone−Wales rotation[43] from the IPR *D*3h-C_{74}(14246) to the non-IPR *C*1-C_{74}(14049), as stated in the caption of Figure 6.

The examples of isomeric transformations in chlorinated higher fullerenes as well as in inorganic systems have been observed under solvothermal conditions in seated vessel,[14,44-46] but the pressure of chlorine in the arc-discharge reaction is obviously lower than those in the solvothermal reactions.

Table 3. C-Cl bond energies (BE) and HOMO-LUMO (H-L) gaps (eV) for chlorinated systems at different stages of chlorination, *C*1-C_{74}(14049)Cl_x (x=0-10).[a,b]

System	C-Cl BE	H-L gap
C_{74}	-	0.344
$C_{74}Cl_1$	-59.5	
$C_{74}Cl_2$	-60.3	0.763
$C_{74}Cl_3$	-49.4	
$C_{74}Cl_4$	-51.5	0.813
$C_{74}Cl_5$	-45.8	
$C_{74}Cl_6$	-58.6	1.275
$C_{74}Cl_7$	-43.2	
$C_{74}Cl_8$	-58.2	1.297
$C_{74}Cl_9$	-44.4	
$C_{74}Cl_{10}$	-64.9	1.727

[a]BE in kcal mol^{-1} and H-L gaps in eV. [b] The BE are computed as BE = E(*C*1-C_{74}(14049)Cl_x)-E(*C*1-C_{74}(14049)-Cl_{x-1})-E(Cl). H-L gaps only for closed-shell systems.

6.4. Formation Mechanism of C_{2v}-$C_{78}(2)Cl_6(C_5Cl_6)$

Fullerene chlorides stand out due to their sustainable formation in the chlorine-involving carbon arc and feasible identification by crystallography. Interestingly, the heretofore isolable fullerene chlorides can be exclusively classified into two types, i.e. chlorofullerenes functionalized with chlorine atoms and exo-fullerenes functionalized with chlorinated carbon clusters (CCCs).[18,25,47] Numerous fullerenes chlorides, both with IPR or non-IPR cages, have been produced in the past dozen years.[18] In the presence of CCl_4, for example, a modified Krätschmer-Huffman arc discharge has been applied to synthesize smaller non-IPR chlorofullerenes such as D_{5h}-symmetric $C_{50}(271)Cl_{10}$ in 2004.[8] Larger fullerenes from C_{60} to C_{108} have been produced as chlorofullerenes in radio-frequency furnace[48] and solvothermal reactions[13,49] as well. In addition to chlorofullerenes, a few of exofullerenes functionalized with CCCs were also isolated.[50]

Unlike the previously produced chlorofullerenes functionalized with chlorine atoms or exofullerenes functionalized with CCCs, a meaningful C_{2v}-$C_{78}(2)Cl_6(C_5Cl_6)$ doubly functionalized with both chlorine atoms and CCCs has been isolated and characterized from the products of the chlorine-involving carbon arc. This structure is very valuable because it provides meaningful information about reaction venue for fullerene derivatization in the drastic conditions of the carbon arc. Note that truncated nomenclature for IPR structure is used here.

In this section, we make a qualitative prediction about the reaction temperatures and sequences for chlorination and exohedral derivatization with CCCs in the arc conditions.

6.4.1. Crystallography Results

The parent cage of the doubly functionalized chlorofullerene has been identified by crystallographic measurement as C_{2v}-symmetric IPR-satisfying C_{2v}-$C_{78}(2)$, which could be structurally linked to D_{3h}-$C_{78}(4)$, D_{3h}-$C_{78}(5)$, and C_{2v}-$C_{78}(3)$ by Stone-Wales transformations.[28,29] The two groups, chlorine atoms and perchlorinated cyclopentadiene, are shown to bind on two different sides of the C_{2v}-$C_{78}(2)$ cage (Figure 8).

The six chlorine atoms in the form of closed chain are respectively bound to the [5, 6, 6] atoms in the coronene motif of the C_{2v}-$C_{78}(2)$ isomer, transforming the fullerene cage into an isolated planar aromatic (benzenoid) ring and a curved C_{66} fragment.

The perchlorinated cyclopentadiene takes place on the [6,6] pyracylene bond in C_{2v}-$C_{78}(2)$ (C_{35}-C_{61} bond in Figure 8). The C35-C61 distance, 1.559 Å, is substantially

elongated if compared to the remaining C-C distances (1.337~1.410 Å) at [6, 6] pyracylene bonds.

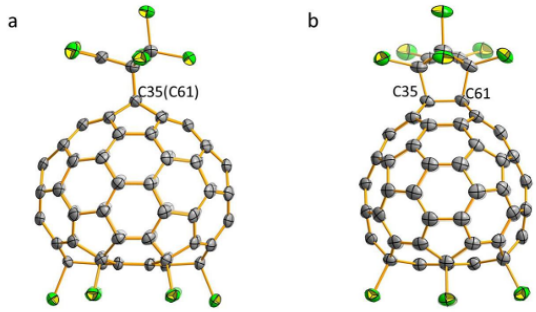

Figure 8. Two views of the crystallographic structure of C_{2v}-$C_{78}(2)Cl_6(C_5Cl_6)$. C35 and C61 atoms are shown.

6.4.2. Bond Energies

In order to predict quantitatively the stability of both groups, Cl_6 and C_5Cl_6, binding to the pristine cage, bond energies (BE) between C_{2v}-$C_{78}(2)$ cage and external groups were analysed.

The C-Cl bond energy per chlorine atom, $BE_{C\text{-}Cl}$, was calculated by equation [Eq.1] and the C-(C_5Cl_6) bond energy, $BE_{C\text{-}(C5Cl6)}$, by equation [Eq.2], where x is defined as the number of chlorine atoms.

$$BE_{C\text{-}Cl} = (E(C_{78}Cl_x) - E(C_{78}) - x\,E(Cl))/x \qquad [Eq.1]$$

$$BE_{C\text{-}(C5Cl6)} = E(C_{78}Cl_x(C_5Cl_6)) - E(C_{78}Cl_x) - E(C_5Cl_6) \qquad [Eq.2]$$

Table 4 shows the C-Cl bond energies ($BE_{C\text{-}Cl}$) and the HOMO-LUMO (H-L) gaps for several fullerene derivatives involved in the C_{2v}-$C_{78}(2)Cl_6(C_5Cl_6)$ formation and some other related species.[51] The $BE_{C\text{-}Cl}$ are comparable to those computed for other chlorinated fullerenes. For C_{2v}-$C_{78}(2)Cl_2$, with two Cl atoms attached to the coronene motif, the bond energy is -48.1 kcal·mol^{-1}, which is significantly larger (absolute value) than the bond energy for the perchlorinated cyclopentadiene C_5Cl_6, -17.1 kcal·mol^{-1}. Chlorination of the bond C35-C61 where the cycloaddition takes place at C35 and C61 atoms (Figure 8) to form C_{2v}-$C_{78}(2)Cl_2$* (Table 4), is not so exothermic (-43.8 kcal mol^{-1})

as chlorination in the coronene motif, but it is still much more favoured than cycloaddition of C_5Cl_6. Therefore, we conclude that the C-(C_5Cl_6) bond is appreciably much weaker than the C-Cl bond. For x > 2, the BE_{C-Cl} become progressively larger as the number of chlorine atoms increases up to x = 6 (-52.7 kcal mol^{-1}). For larger levels of chlorination, as in the experimentally detected C_{2v}-$C_{78}(2)Cl_{18}$[52] and C_{2v}-$C_{78}(2)Cl_{30}$,[53] a slight drop in BE_{C-Cl} is observed (Table 4).

Table 4. C-Cl bond energies (BE_{C-Cl}) and HOMO-LUMO (H-L) gaps for different systems related to C_{2v}-$C_{78}(2)Cl_6(C_5Cl_6)$ formation, and for experimentally detected C_{2v}-$C_{78}(2)Cl_{18}$ and C_{2v}-$C_{78}(2)Cl_{30}$.[a)]

System	BE_{C-Cl}	H-L gap[b)]
C_{2v}-$C_{78}(2)$		1.064
C_{2v}-$C_{78}(2)Cl$	-38.2	
C_{2v}-$C_{78}(2)Cl_2$	-48.1	1.059
C_{2v}-$C_{78}(2)Cl_2$[c)]	-43.8	1.187
C_{2v}-$C_{78}(2)Cl_3$	-46.8	
C_{2v}-$C_{78}(2)Cl_4$	-50.5	1.058
C_{2v}-$C_{78}(2)Cl_5$	-49.9	
C_{2v}-$C_{78}(2)Cl_6$	-52.7	1.167
C_{2v}-$C_{78}(2)Cl_{18}$	-51.2	2.373
C_{2v}-$C_{78}(2)Cl_{30}$	-48.9	2.575

[a)] BE_{C-Cl} in kcal mol^{-1} and H-L gaps in eV; b) H-L gaps only for closed-shell systems; c) The Cl atoms are not bonded to the coronene motif, but to C_{35} and C_{61} atoms where otherwise cycloaddition takes place as shown in Figure 8.

6.4.3. Formation Mechanism Proposal for C_{2v}-$C_{78}(2)Cl_6$

As the C-(C_5Cl_6) bond is much weaker than the C-Cl bond, we suggest that C_{2v}-$C_{78}(2)Cl_6$ is formed first than C_{2v}-$C_{78}(2)(C_5Cl_6)$. A plausible mechanism for the formation of C_{2v}-$C_{78}(2)Cl_6$ is based on successive chlorination steps. In particular, the stepwise chlorination pathway can be understood by the atomic orbital contributions to the HOMOs for C_{2v}-$C_{78}(2)$, $C_{78}Cl_2$ and $C_{78}Cl_4$, as well as the spin density distribution for $C_{78}Cl$, $C_{78}Cl_3$ and $C_{78}Cl_5$ (Figure 9), as in the previously case of $C_{74}Cl_{10}$.

Carbon atoms of the coronene motif of C_{2v}-$C_{78}(2)$ possess the largest contribution to HOMO. These carbon atoms represent the reactive sites of the prototypical fullerene and are those firstly bonded by chlorine atoms. On the other hand, the carbon atoms

where C_5Cl_6 is added, i.e. C35 and C61 (Figure 8) do not present significant contributions to the HOMO in line with the fact that chlorine atoms are added first to the coronene motif.

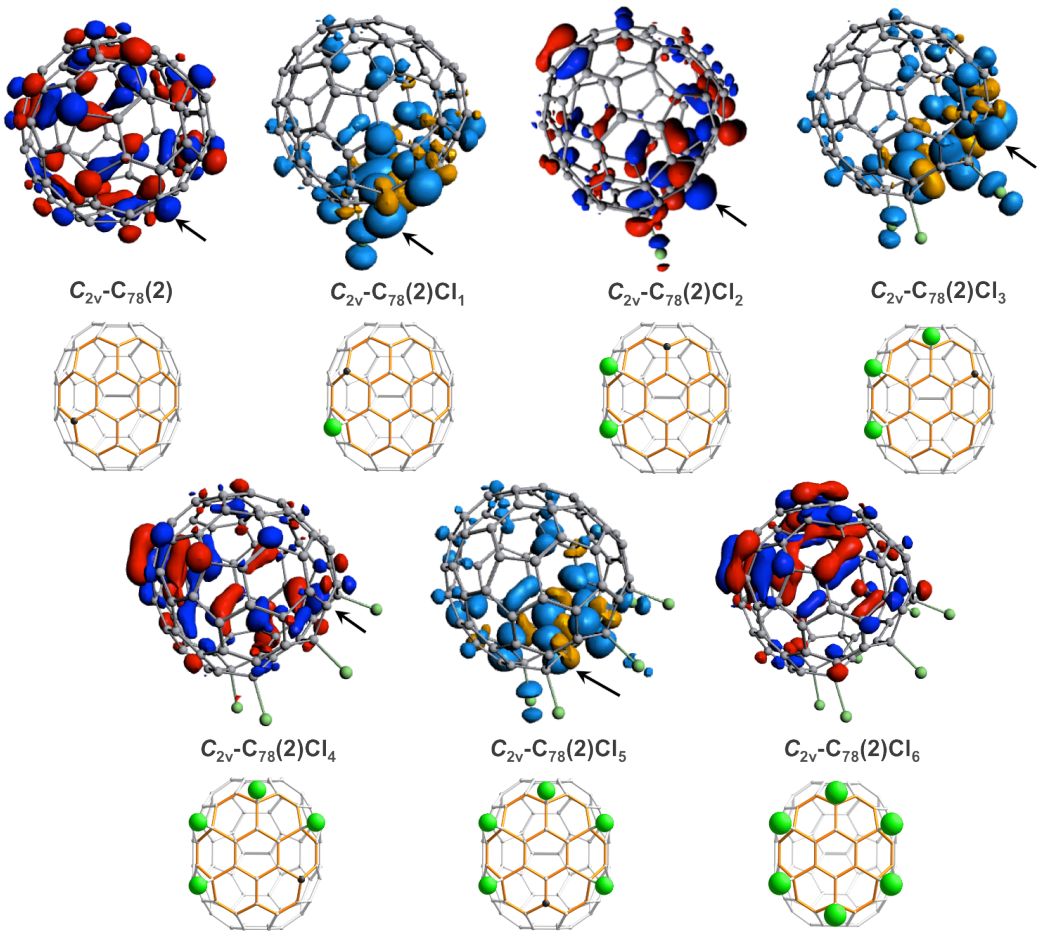

Figure 9. Chlorination pathway for C_{2v}-$C_{78}(2)Cl_6$ isomer. Representation of the HOMOs for C_{2v}-$C_{78}(2)$, $C_{78}Cl_2$ and $C_{78}Cl_4$, and the spin densities for $C_{78}Cl_1$, $C_{78}Cl_3$ and $C_{78}Cl_5$.

6.4.4. Formation Mechanism Proposal for C_{2v}-$C_{78}(2)Cl_6(C_5Cl_6)$

Once we had the C_{2v}-$C_{78}(2)Cl_6$ formed by radical addition, the last step in the reaction mechanism to obtain C_{2v}-$C_{78}(2)Cl_6(C_5Cl_6)$ was characterized to be a Diels-Alder reaction,

as fullerenes possess a reactive dienophile character derived from their electron-deficient properties. The addition pattern of the Diels-Alder reaction can be understood by the Woodward-Hoffmann rules[54] and the Frontier Molecular Orbital theory,[55,56] when kinetically controlled. In this context, the C_{2v}-$C_{78}(2)Cl_6$ acts as a dienophile and its LUMO is expected to play a key role in the interaction with the HOMO of C_5Cl_6, which acts as a diene. Addition sites are selected from those atoms that show large orbital contribution to the LUMO. The shape of the LUMO for C_{2v}-$C_{78}(2)Cl_6$ is represented in Figure 10. The largest contribution to the LUMO was found for C35 and C61, i.e. those carbon atoms where C_5Cl_6 was experimentally bonded. Thus, this simple qualitative theory predicts that the Diels-Alder reaction occurs on a [6,6] pyracylene bond, in good agreement with experiment and as in other experimental and computational studies previously published.[57]

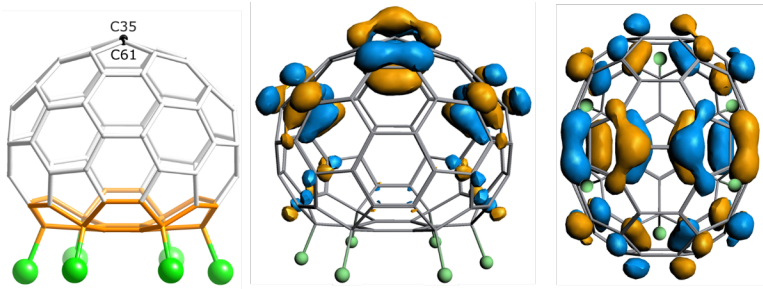

Figure 10. Representation of C_{2v}-$C_{78}(2)Cl_6$ (left) and its LUMO (middle). Top view of the LUMO to show that the 35-61 bond presents the largest contributions with the appropriate phase (antibonding) to interact with the HOMO of the diene C_5Cl_6 (right).

To gain more insight into the reactivity of the system and to check whether adduct on bond 35-61 is also one of the thermodynamic products, other bonds for the Diels-Alder reaction between C_5Cl_6 and C_{2v}-$C_{78}(2)Cl_6$ cage have also been analyzed. C_{2v}-$C_{78}(2)$ has four types of C-C bonds, namely, the so-called [6,6], [6,6]-pyracylene, [6,6]-pyrene and [5-6]-coranulene bonds (Figure 11). All of them have different reactivity, which can be rationalized by their different bond distances and pyramidalization angles, as shown in Table 5.

The lowest-energy adducts are those formed on three pyracylene bonds (75-80, 55-13 and 35-61), which are essentially degenerated. The pyracylene bonds show, in general, the lowest C-C distances (higher double bond character) and among the highest pyramidalization angles (lower deformation energies), which make them more reactive to diene attack than other bonds, as observed for other fullerenes.[58,59] Among them,

adduct on bond 35-61 show the largest HOMO-LUMO gap (1.541 eV). Interestingly, adduct on pyracylene bond 18-27 shows significantly higher energy than the others. Two reasons are behind such a different behavior: a lower pyramidalization angle due to its position next to the coronene motif (Figure 11) and a much higher steric hindrance between the chlorine atoms and the C_5Cl_6 group. Adducts on other [6,6] and [5,6] bonds are much higher in energy as well.

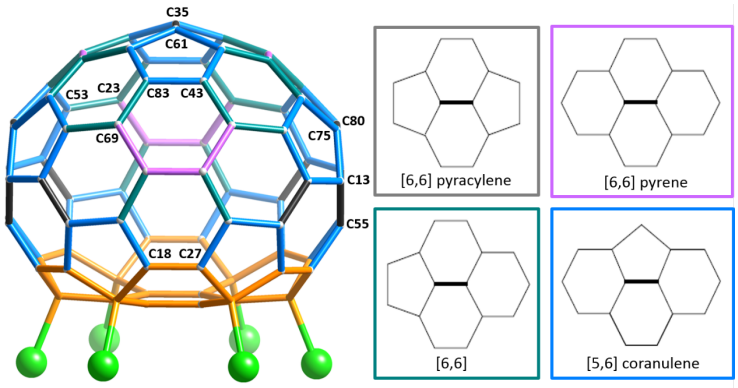

Figure 11. Structure and types of C-C bonds for C_{2v}-$C_{78}(2)Cl_6$. In the structure, each bond is coloured according to its type. Grey for the [6,6] pyracylene bond, pink for the [6,6] pyrene bond, green for the other [6,6] bond, and blue for the [5,6] coranulene bond. Coronene motif is highlighted in orange. Carbon atoms labelled in Table 5 are also represented in the structure.

Table 5. Relative energies (E_{rel}), HOMO-LUMO (H-L) gaps, C-(C_5Cl_6) bond energies (BE), C-C bond distances, pyramydalization angles and types of bonds for different sites of C_5Cl_6 addition on the C_{2v}-$C_{78}(2)Cl_6$ cage.[a)]

Bond	E_{rel}	H-L gap	BE	C-C reactant[b)]	C-C product[b)]	pyr angle[c)]	Type of bond
35-61	0.2	1.541	-17.2	1.380	1.571	11.1	[6,6] pyracylene
69-83	16.2	1.191	-1.3	1.412	1.609	8.8	[6,6]
43-83	24.0	0.735	6.6	1.453	1.606	9.7	[5,6] coranulene
75-80	0.0	1.350	-17.4	1.389	1.589	11.5	[6,6] pyracylene
55-13	0.1	1.071	-17.3	1.405	1.630	11.8	[6,6] pyracylene
53-23	17.4	0.860	0.0	1.428	1.638	9.1	[6,6]
82-72	30.8	1.192	13.3	1.464	1.733	8.8	[6,6] pyrene
18-27	28.7	0.966	11.2	1.360	1.566	9.1	[6,6] pyracylene

a) E_{rel} and BE in kcal mol^{-1}, H-L gaps in eV, bond distances in Å and pyramidalization angles in degrees. b) Computed bond distances on C_{2v}-$C_{78}(2)Cl_6$ and C_{2v}-$C_{78}(2)Cl_6(C_5Cl_6)$. c) Average pyramidalization angles of the two atoms that constitute the bond.

6.4.5. Stability of the Derivatized Groups at High Temperatures

Car-Parrinello MD simulations were also performed to provide more insight into the stability of both groups found in C_{2v}-$C_{78}(2)Cl_6(C_5Cl_6)$. Trajectories for C_{2v}-$C_{78}(2)Cl_6$, C_{2v}-$C_{78}(2)(C_5Cl_6)$ and C_{2v}-$C_{78}(2)Cl_6(C_5Cl_6)$ were analyzed at different temperatures. For example, motion of chlorine atoms of C_{2v}-$C_{78}(2)Cl_6$ at high temperature (1500 K) is shown in Figure 12. Chlorine atoms remain in their original positions during the short time of simulation (19 ps). Besides, simulations for C_{2v}-$C_{78}(2)(C_5Cl_6)$ done at different temperatures (300, 800 and 1000 K), show that C_5Cl_6 only remains on the cage at 300 K in the rather short time scale simulated here (around 15 ps). Trajectories at higher temperatures, 800 and 1000 K, show that the organic group is lost after 7 and 3 ps, respectively. Finally, molecular dynamics simulations for C_{2v}-$C_{78}(2)Cl_6(C_5Cl_6)$ at high temperatures (800, 1000 and 1500 K) indicated that the C_5Cl_6 group is lost before chlorine atoms after short time (4, 1 and less than 1 ps, respectively). It is also observed that the C_5Cl_6 group in C_{2v}-$C_{78}(2)Cl_6(C_5Cl_6)$ leaves faster than in C_{2v}-$C_{78}(2)(C_5Cl_6)$.

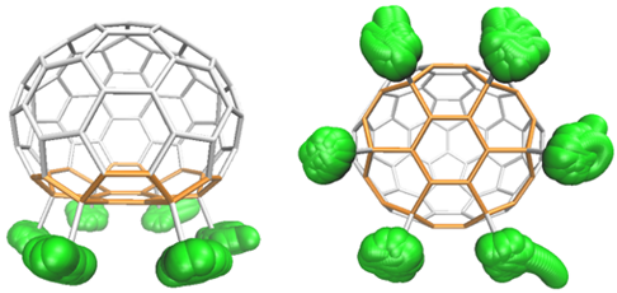

Figure 12. Representation of the motion of the Cl atoms in C_{2v}-$C_{78}(2)Cl_6$ during Car-Parrinello MD trajectories at 1500 K. Coronene motif is shown in orange.

Stepwise mass spectra of C_{2v}-$C_{78}(2)Cl_6(C_5Cl_6)$ at different ionization temperatures confirm the Car-Parrinello MD results. As shown in Figure 13, only mass peaks at m/z 936 and 1149 respectively corresponding to C_{78} and $C_{78}Cl_6$ appeared when the vaporization/ionization temperature was 573 K. A single and strong peak at m/z 1149 occurred when the temperature was 523 K. Only when the temperatures drop to 423 K, the mother peak at m/z 1419 corresponding to $C_{78}Cl_6(C_5Cl_6)$ gradually dominated the mass spectrum. It is worth remarking here that the results of multi-stage mass spectra (Figure 13) are in good agreement with the Car-Parrinello MD simulations and the computations of bond energies, i.e. C-(C_5Cl_6) bond is weaker than C-Cl bond. Therefore, it can be clearly concluded that C_5Cl_6 is lost before Cl atoms at high

temperatures. The synthesis of C_{2v}-$C_{78}(2)Cl_6(C_5Cl_6)$ can be seen just like a travel of C_{2v}-$C_{78}(2)$ in the complex arc discharge system from the high temperature central zone to the low temperature peripheral zone. Therefore, the formation of C_{2v}-$C_{78}(2)Cl_6(C_5Cl_6)$ is proposed to take place in three steps, where first the carbon cage is formed at very high temperatures in a zone very near to the arc center, then six Cl are attached to the coronene motif of C_{2v}-$C_{78}(2)$ in a zone still near to the arc center but at lower temperatures, and later C_5Cl_6 is added to the corresponding C35-C61 bond further from the center at a much lower temperature.

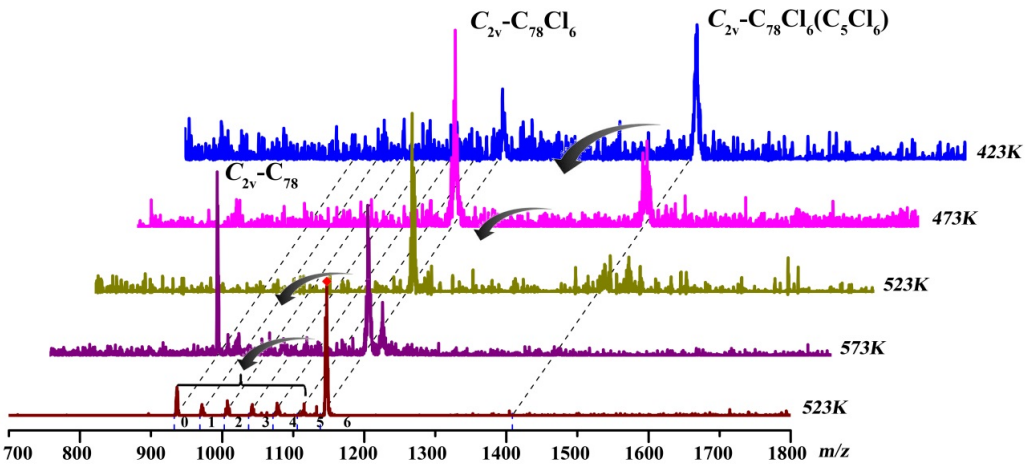

Figure 13. Mass spectra of C_{2v}-$C_{78}(2)Cl_6(C_5Cl_6)$ obtained at different ionization temperatures and multi mass spectrum for the fragments ions of C_{2v}-$C_{78}(2)Cl_6$ at 523 K.

6.5. Conclusions

Up to now, exohedral as well as endohedral derivatives are found in the C_{66} fullerene family, but those isomers that get chlorinated, $C_{66}(4348)$, $C_{66}(4169)$, are not able to encapsulate metal atoms, as $C_{66}(4059)$, and *viceversa*. According to our results, low-energy neutral cages are the ones that are functionalized when a chlorine source is introduced in the arc. Chlorination would take place at a temperature significantly lower than 2000 K, once the neutral isomers were formed. Chlorination patterns follow the trend of maximizing strain release on the cage surface, with chlorines at the highly

pyramidalized C atoms of the adjacent pentagons. In addition, the relative position of the adjacent pentagons may also play an important role.

The reactive small band gap fullerene C_1-C_{74}(14049), representing the first non-IPR isomer of C_{74} characterized by X-ray single-crystal diffraction, was successfully stabilized by regioselective chlorination in the graphite arc-discharge. The stabilization of pristine fused-pentagon C_1-C_{74}(14049) by stepwise chlorination to C_1-C_{74}(14049)Cl_{10} has been clarified in both theoretical simulation with DFT calculations and experimental fragmentation with multistage mass spectrometry.

The $C_{78}Cl_6(C_5Cl_6)$ with prototypical C_{2v}-C_{78}(2) cage doubly functionalized by both chlorine atoms and perchlorinated cyclopentadiene has been trapped, isolated, and accurately determined by single-crystal X-ray diffraction. Taking into account that C-C_5Cl_6 bond is weaker than C-Cl bond, the former shows lower bond energy and leaves earlier than the six chlorine atoms at high temperature based on Car-Parrinello MD simulations. Results from computations are also in accord with the mass spectra of C_{2v}-C_{78}(2)$Cl_6(C_5Cl_6)$ at different ionization temperatures. Accordingly, the formation mechanism for C_{2v}-C_{78}(2)$Cl_6(C_5Cl_6)$ has been elucidated. The nascent C_{2v}-C_{78}(2) reacts first with chlorine atoms by free radical addition considering the HOMO and the spin density distributions of the pristine cage and intermediates, and then with perchlorinated cyclopentadiene by 1,4-cycloaddition.

6.6. References

(1) Kroto, H. W. *Nature* **1987**, *329*, 529.
(2) Fowler, P. W.; Manolopoulos, D. E. *An Atlas of Fullerenes*; Oxford Univ. Press: Oxford (UK), 1995.
(3) Wang, C.-R.; Kai, T.; Tomiyama, T.; Yoshida, T.; Kobayashi, Y.; Nishibori, E.; Takata, M.; Sakata, M.; Shinohara, H. *Nature* **2000**, *408*, 426.
(4) Stevenson, S.; Fowler, P. W.; Heine, T.; Duchamp, J. C.; Rice, G.; Glass, T.; Harich, K.; Hajdu, E.; Bible, R.; Dorn, H. C. *Nature* **2000**, *408*, 427.
(5) Popov, A. A.; Yang, S.; Dunsch, L. *Chem. Rev.* **2013**, *113*, 5989.
(6) Rodríguez-Fortea, A.; Alegret, N.; Balch, A. L.; Poblet, J. M. *Nat. Chem.* **2010**, *2*, 955.
(7) Rodriguez-Fortea, A.; Balch, A. L.; Poblet, J. M. *Chem. Soc. Rev.* **2011**, *40*, 3551.
(8) Xie, S.-Y.; Gao, F.; Lu, X.; Huang, R.-B.; Wang, C.-R.; Zhang, X.; Liu, M.-L.; Deng, S.-L.; Zheng, L.-S. *Science* **2004**, *304*, 699.

(9) Gao, F.; Xie, S.-Y.; Huang, R.-B.; Zheng, L.-S. *Chem. Commun.* **2003**, 2676.
(10) Tebbe, F. N.; Becker, J. Y.; Chase, D. B.; Firment, L. E.; Holler, E. R.; Malone, B. S.; Krusic, P. J.; Wasserman, E. *J. Am. Chem. Soc.* **1991**, *113*, 9900.
(11) Olah, G. A.; Bucsi, I.; Lambert, C.; Aniszfeld, R.; Trivedi, N. J.; Sensharma, D. K.; Prakash, G. K. S. *J. Am. Chem. Soc.* **1991**, *113*, 9385.
(12) Birkett, P. R.; Avent, A. G.; Darwish, A. D.; Kroto, H. W.; Taylor, R.; Walton, D. R. M. *J. Chem. Soc., Chem. Commun.* **1995**, 0, 683.
(13) Troshin, P. A.; Lyubovskaya, R. N.; Ioffe, I. N.; Shustova, N. B.; Kemnitz, E.; Troyanov, S. I. *Angew. Chem. Int. Ed.* **2005**, *44*, 234.
(14) Ioffe, I. N.; Goryunkov, A. A.; Tamm, N. B.; Sidorov, L. N.; Kemnitz, E.; Troyanov, S. I. *Angew. Chem. Int. Ed.* **2009**, *48*, 5904.
(15) Käß, M.; Hohenberger, J.; Adelhardt, M.; Zolnhofer, E. M.; Mossin, S.; Heinemann, F. W.; Sutter, J.; Meyer, K. *Inorg. Chem.* **2014**, *53*, 2460.
(16) Hayashi, Y.; Gotoh, H.; Hayashi, T.; Shoji, M. *Angew. Chem. Int. Ed.* **2005**, *44*, 4212.
(17) Troyanov, S. I.; Shustova, N. B.; Popov, A. A.; Sidorov, L. N.; Kemnitz, E. *Angew. Chem. Int. Ed.* **2005**, *44*, 432.
(18) Tan, Y. Z.; Xie, S. Y.; Huang, R. B.; Zheng, L. S. *Nat. Chem.* **2009**, *1*, 450.
(19) Tan, Y.-Z.; Han, X.; Wu, X.; Meng, Y.-Y.; Zhu, F.; Qian, Z.-Z.; Liao, Z.-J.; Chen, M.-H.; Lu, X.; Xie, S.-Y.; Huang, R.-B.; Zheng, L.-S. *J. Am. Chem. Soc.* **2008**, *130*, 15240.
(20) Tan, Y.-Z.; Li, J.; Zhu, F.; Han, X.; Jiang, W.-S.; Huang, R.-B.; Zheng, Z.; Qian, Z.-Z.; Chen, R.-T.; Liao, Z.-J.; Xie, S.-Y.; Lu, X.; Zheng, L.-S. *Nat. Chem.* **2010**, *2*, 269.
(21) Zhou, T.; Tan, Y.-Z.; Shan, G.-J.; Zou, X.-M.; Gao, C.-L.; Li, X.; Li, K.; Deng, L.-L.; Huang, R.-B.; Zheng, L.-S.; Xie, S.-Y. *Chem. Eur. J.* **2011**, *17*, 8529.
(22) Ziegler, K.; Mueller, A.; Amsharov, K. Y.; Jansen, M. *Chem. Asian J.* **2011**, *6*, 2412.
(23) Ziegler, K.; Mueller, A.; Amsharov, K. Y.; Jansen, M. *J. Am. Chem. Soc.* **2010**, *132*, 17099.
(24) Amsharov, K. Y.; Ziegler, K.; Mueller, A.; Jansen, M. *Chem. Eur. J.* **2012**, *18*, 9289.
(25) Mueller, A.; Ziegler, K.; Amsharov, K. Y.; Jansen, M. *Chem. Eur. J.* **2011**, *17*, 11797.
(26) Chilingarov, N. S.; Nikitin, A. V.; Rau, J. V.; Golyshevsky, I. V.; Kepman, A. V.; Spiridonov, F. M.; Sidorov, L. N. *J. Fluor. Chem.* **2002**, *113*, 219.
(27) Bulusheva, L. G.; Okotrub, A. V.; Boltalina, O. V. *J. Phys. Chem. A* **1999**, *103*, 9921.
(28) Tan, Y. Z.; Li, J.; Zhu, F.; Han, X.; Jiang, W. S.; Huang, R. B.; Zheng, Z.; Qian, Z. Z.; Chen, R. T.; Liao, Z. J. *Nat. Chem.* **2010**, *2*, 269.
(29) Gao, C.-L.; Li, X.; Tan, Y.-Z.; Wu, X.-Z.; Zhang, Q.; Xie, S.-Y.; Huang, R.-B. *Angew. Chem. Int. Ed.* **2014**, *53*, 7853.

(30) Cui, Y. H.; Tian, W. Q.; Feng, J. K.; Chen, D. L. *J. Nano. Res.* **2010**, *12*, 429.
(31) Alegret, N.; Abella, L.; Azmani, K.; Rodríguez-Fortea, A.; Poblet, J. M. *Inorg. Chem.* **2015**, *54*, 7562.
(32) Slanina, Z. k.; Lee, S.-L.; UhlÃ-k, F.; Adamowicz, L.; Nagase, S. *Theor. Chem. Acc.* **2007**, *117*, 315.
(33) Slanina , Z.; Nagase, S. *ChemPhysChem* **2005**, *6*, 2060.
(34) Zhang, B. L.; Wang, C. Z.; Ho, K. M.; Xu, C. H.; Chan, C. T. *J. Chem. Phys.* **1993**, *98*, 3095.
(35) Diener, M. D.; Alford, J. M. *Nature* **1998**, *393*, 668.
(36) Kovalenko, V. I.; Khamatgalimov, A. R. *Chem. Phys. Lett.* **2003**, *377*, 263.
(37) Tan, Y.-Z.; Zhou, T.; Bao, J.; Shan, G.-J.; Xie, S.-Y.; Huang, R.-B.; Zheng, L.-S. *J. Am. Chem. Soc.* **2010**, *132*, 17102.
(38) Tan, Y. Z.; Li, J.; Du, M. Y.; Lin, S. C.; Xie, S. Y.; Lu, X.; Huang, R. B.; Zheng, L. S. *Chem. Sci.* **2013**, *4*, 2967.
(39) Yeretzian, C.; Wiley, J. B.; Holczer, K.; Su, T.; Nguyen, S.; Kaner, R. B.; Whetten, R. L. *J. Phys. Chem.* **1993**, *97*, 10097.
(40) Goryunkov, A. A.; Markov, V. Y.; Ioffe, I. N.; Bolskar, R. D.; Diener, M. D.; Kuvychko, I. V.; Strauss, S. H.; Boltalina, O. V. *Angew. Chem. Int. Ed.* **2004**, *43*, 997.
(41) Shustova, N. B.; Kuvychko, I. V.; Bolskar, R. D.; Seppelt, K.; Strauss, S. H.; Popov, A. A.; Boltalina, O. V. *J. Am. Chem. Soc.* **2006**, *128*, 15793.
(42) Shustova, N. B.; Newell, B. S.; Miller, S. M.; Anderson, O. P.; Bolskar, R. D.; Seppelt, K.; Popov, A. A.; Boltalina, O. V.; Strauss, S. H. *Angew. Chem. Int. Ed.* **2007**, *46*, 4111.
(43) Stone, A. J.; Wales, D. J. *Chem. Phys. Lett.* **1986**, *128*, 501.
(44) Liu, J. L.; Liu, W.; Huang, G. Z.; Tong, M. L. *Sci. Bull.* **2015**, *60*, 447.
(45) Ioffe, I. N.; Chen, C. B.; Yang, S. F.; Sidorov, L. N.; Kemnitz, E.; Troyanov, S. I. *Angew. Chem. Int. Ed.* **2010**, *49*, 4784.
(46) Ioffe, I. N.; Mazaleva, O. N.; Sidorov, L. N.; Yang, S. F.; Wei, T.; Kemnitz, E.; Troyanov, S. I. *Inorg. Chem.* **2012**, *51*, 11226.
(47) Troyanov, S. I.; Popov, A. A. *Angew. Chem. Int. Ed.* **2005**, *44*, 4215.
(48) Mueller, A.; Ziegler, K.; Amsharov, K. Y.; Jansen, M. *Eur. J. Inorg. Chem.* **2011**, *2*, 268.
(49) Wang, S.; Yang, S.; Kemnitz, E.; Troyanov, S. I. *Inorg. Chem.* **2016**, *55*, 5741.
(50) Tan, Y.-Z.; Chen, R.-T.; Liao, Z.-J.; Li, J.; Zhu, F.; Lu, X.; Xie, S.-Y.; Li, J.; Huang, R.-B.; Zheng, L.-S. *Nat. Commun.* **2011**, *2*, 420.
(51) Gao, C.-l.; Abella, L.; Tan, Y.-Z.; Wu, X.-Z.; Rodríguez-Fortea, A.; Poblet, J. M.; Xie, S.-Y.; Huang, R.-B.; Zheng, L.-S. *Inorg. Chem.* **2016**, *55*, 6861.
(52) Kemnitz, E.; Troyanov, S. I. *Mendeleev Commun.* **2010**, *20*, 74.
(53) Sergeyi, T.; Nadezhdab, T.; Chen, C.; Yang, S.; Erhard, K. *Anorg. Allg. Chem.* **2009**, *635*, 1783.
(54) Woodward, R. B.; Hoffmann, R. *Angew. Chem.* **1969**, *8*, 781.

(55) Fukui, K. *Acc. Chem. Res.* **1971**, *4*, 57.
(56) Fukui, K.; Yonezawa, T.; Shingu, H. *J. Chem. Phys.* **1952**, *20*, 722.
(57) Fernández, I.; Solà, M.; Bickelhaupt, M. *Chem. Eur. J.* **2013**, *19*, 7416.
(58) Osuna, S.; Swart, M.; Campanera, J. M.; Poblet, J. M.; Solà, M. *J. Am. Chem. Soc.* **2008**, *130*, 6206.
(59) Osuna, S.; Valencia, R.; Rodríguez-Fortea, A.; Swart, M.; Solà, M.; Poblet, J. M. *Chem. Eur. J.* **2012**, *18*, 8944.

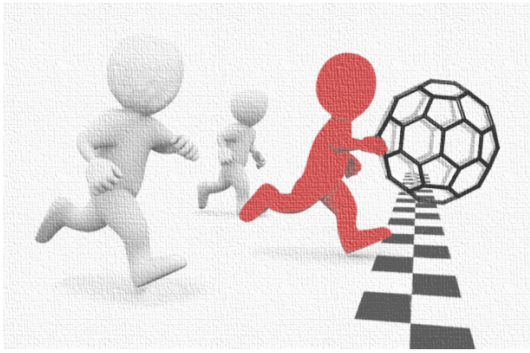

CHAPTER 7

Concluding Remarks

UNIVERSITAT ROVIRA I VIRGILI
COMPUTATIONS ON FULLERENES: CHARACTERIZATION, REACTIVITY AND GROWTH
Laura Abella Guzman

CHAPTER 7

Concluding Remarks

The last chapter summarizes the most important achievements and conclusions presented along this Thesis. Although computational studies are not as easy as it might seem, we have succeeded in most of the goals we have faced. In addition, most of the projects resulted in agreement with experiments. A brief chapter-by-chapter summary of the concluding remarks for each project is contained in the following pages.

Chapter 4 | Growth of Endohedral Metallofullerenes

The experimental detection of new families of endohedral metallofullerenes led us to think about the way that they are formed. Thus, we have performed the computational studies in $Ti@C_{2n}$ (2n=26-50), $Sc_2C_2@C_{2n}$ (2n=86-90) and $Sc_3N@C_{2n}$ (2n=68-80) families that provide strong support for the CNG mechanism. The main conclusions after this work are the following:

- ✗ The insertion of a C_2 unit to already formed EMF is always an exothermic/exergonic process, independent of the size, insertion site, or symmetry of the cage.

- ✗ The free energy barriers for each step are attainable considering the high temperature at which the processes occur.

- ✗ The most abundant $Ti@C_{2n}$ (2n=26-48) isomers are formally linked by direct C_2 insertions and in a few cases by additional Stone-Wales transformations.

- ✗ Car-Parrinello MD simulations show that after the attack of a C_2 unit to one of the C atoms of the Ti@C_{2n} system, the formation of the second C-C bond that closes the cage is a very unlikely event at the time scale of our simulations, and must be accelerated using metadynamics or via an external collision.

- ✗ Sc_2C_2@C_s(hept)-C_{88} is the first example of an endohedral carbide fullerene with a heptagon ring on the carbon cage and only the second endohedral fullerene to contain a heptagon. Calculations suggest that Sc_2C_2@C_s(hept)-C_{88} could be a kinetically-trapped species derived from the recently reported Sc_2C_2@C_{2v}-C_{86}(9) via a direct C_2 insertion.

- ✗ A simplified growth mechanism that proceeds by simple C_2 insertion reactions and rearrangements from Sc_3N@D_3-C_{68} to Sc_3N@I_h-C_{80} has been found.

- ✗ A diverse range of reaction paths are possible, however, in the presence of C_2, a closed fullerene tends to always capture carbon units.

- ✗ The iconic I_h-C_{80} cage can be formed from the much smaller D_3-C_{68} species via several routes that involve classical and heptagon-containing intermediates, and a minimal number of C_2 rearrangements.

- ✗ The extent of cages formed is related to the carbon cage closure step, in which He gas is expected to play a significant role.

- ✗ As the size of the carbon cages increases, the free energy barriers associated with C_2 insertion decrease and the collision kinetic energy required to close the cages also become smaller.

- ✗ Growth should be controlled by carbon density of the atmosphere surrounding a cage.

- ✗ In the presence of C_2 units, a closed fullerene will tend to grow and the mechanism may depend significantly on carbon density. At a low carbon concentration the insertion of C_2 could occur, where C_2 insertions and rearrangements may be sequential. When the carbon density is very high, however, our molecular dynamics simulations suggest that the growth can be more chaotic.

✗ These results do not exclude shrinkage of fullerenes as an important process when the fullerenes abundance are high and the carbon vapour density is low, as Irle and Morokuma have demonstrated.

Chapter 5 | Identifying an Extended Oxide Clusterfullerene Family

We were able to characterize combining experiments and theory a new endohedral oxide metallofullerene family. The main conclusions are:

✗ The new metallic oxide clusterfullerenes $Sc_2O@C_{2n}$, $Sc_2O@T_d$-C_{76}(19151), $Sc_2O@C_{2v}$-C_{80}(31922) and $Sc_2O@C_{3v}$-C_{82}(39717), have been isolated and characterized by mass spectrometry, UV-vis-NIR absorption spectroscopy, cyclic voltammetry, ^{45}Sc NMR spectroscopy, DFT calculations, and single-crystal X-ray diffraction.

✗ Computational studies show that the Sc_2O cluster transfers four electrons to the corresponding C_{2n} cage, $(Sc_2O)^{4+}@(C_{2n})^{4-}$.

✗ $Sc_2O@T_d$-C_{76}(19151) is the most stable and abundant C_{70} cage in the whole range of temperatures.

✗ The cage size affects not only the shapes but also the cluster motion inside the carbon cages.

✗ The $Sc_2O@C_{2v}$-C_{80}(31922) isomer was predicted to be the most abundant thermodynamic isomer at high temperatures (T > 1300 K), in agreement with the X-ray characterization.

✗ Thermal and entropic effects play a role in the relative stabilization of OCFs.

✗ Besides the previously reported $Sc_2O@C_s$-C_{82}(39715), a new isomer, $Sc_2O@C_{3v}$-C_{82}(39717), was identified and computationally characterized.

✗ The cluster of Sc_2O in C_{3v}-C_{82}(39717) cage can rotate and change the Sc-O-Sc angle easily at rather low temperature.

✗ A formal transfer of six electrons from the Sc_3O cluster to the I_h-C_{80}(31924) cage explains the electronic structure of the compound, $(Sc_3O)^{6+}@(I_h$-$C_{80}(31924))^{6-}$.

- ✗ $Sc_3O@I_h$-C_{80}(31924) is isoelectronic to $Sc_3N@I_h$-C_{80}(31924)$^-$ and has a magnetic moment different from zero in its neutral ground state.

- ✗ The predicted electrochemical gap of $Sc_3O@I_h$-C_{80}(31924), 0.74 V, is the lowest among all the OCFs isolated so far, which is in line with its low stability.

- ✗ Reaction energies for the formation of $[Sc_3O@I_h(7)\text{-}C_{80}]_2$ dimers show that polymerization is a favorable process for this radical OCF and a plausible mechanism that might explain the significant drop in the yield once the product is extracted from the soot.

- ✗ The nature of the encapsulated metal cluster controls the relative stability and orientation of the dimerization product.

- ✗ The THJ dimer becomes energetically favoured for $[Lu_3N@C_{80}]_2^{2-}$ in very good agreement with experiments.

Chapter 6 | On the Formation of Chlorofullerenes

We reported the computational data about the formation of chlorofullerenes. Some systems have been studied and several conclusions emerged:

- ✗ Low-energy neutral cages are the ones that are functionalized when a chlorine source is introduced in the arc.

- ✗ Chlorination would take place at a temperature significantly lower than 2000 K, once the neutral isomers were formed.

- ✗ Chlorination patterns follow the trend of maximizing strain release on the cage surface, with chlorines at the highly pyramidalized C atoms of the adjacent pentagons.

- ✗ The relative position of the adjacent pentagons may also play an important role.

- ✗ The reactive small band gap fullerene C_1-C_{74}(14049) was successfully stabilized by regioselective chlorination in the graphite arc-discharge.

- ✗ The stabilization of pristine fused-pentagon C_1-C_{74}(14049) by stepwise chlorination to C_1-C_{74}(14049)Cl_{10} has been clarified in both theoretical simulation with DFT calculations and experimental fragmentation with multistage mass spectrometry.

- ✗ The C-C_5Cl_6 bond is weaker than C-Cl bond, the former shows lower bond energy and leaves earlier than the six chlorine atoms at high temperature based on Car-Parrinello MD simulations.

- ✗ Computational results are also in accord with the mass spectra of C_{2v}-C_{78}(2)Cl_6(C_5Cl_6) at different ionization temperatures.

- ✗ The formation mechanism for C_{2v}-C_{78}(2)Cl_6(C_5Cl_6) has been elucidated; the nascent C_{2v}-C_{78}(2) reacts first with chlorine atoms by free radical addition considering the HOMO and the spin density distributions of the pristine cage and intermediates, and then with perchlorinated cyclopentadiene by 1,4-cycloaddition.

UNIVERSITAT ROVIRA I VIRGILI
COMPUTATIONS ON FULLERENES: CHARACTERIZATION, REACTIVITY AND GROWTH
Laura Abella Guzman

List of Publications

Related to this Thesis:

[1] Double Functionalization of a Fullerene in Drastic Arc-Discharge Conditions: Synthesis and Formation Mechanism of $C_{2v}(2)$-$C_{78}Cl_6(C_5Cl_6)$
Gao, C. L.; Abella, L.; Tian, H. R.; Zhang, X.; Zhong, Y. Y.; Tan, Y. Z.; Wu, X. Z.; Rodríguez-Fortea, A.; Poblet, J. M.; Xie, S. Y.; Huang, R. B.; Zheng, L. S. **2017** (submitted for publication).

[2] Transformation of Graphite into Cluster-Encapsulated Cages
Mulet-Gas, M.; Abella, L.; Cerón, M. R.; Castro, E.; Marshall, A. G.; Rodríguez-Fortea, A.; Echegoyen, L.; Poblet, J. M.; Dunk, P. W. *Nat. Commun.* **2017** (in press).

[3] Dimerization of endohedral fullerene in a superatomic crystal
Voevodin, A. A.; Abella, L.; Castro Portillo, E.; Paley, D. W.; Campos, L. M.; Rodríguez-Fortea, A.; Poblet, J. M.; Echegoyen, L.; Roy, X. *Chem. Eur. J.*, **2017** (in press).

[4] Current Status of Oxide Clusterfullerenes
Abella, L.; Wang, Y.; Rodríguez-Fortea, A.; Chen, N.; Poblet, J. M. *Inorg. Chim. Acta* **2017** (in press).

[5] $Sc_3O@I_h(7)$-C_{80}: A Trimetallic Oxide Clusterfullerene Abundant in the Raw Soot
Abella, L.; Tang, Q.; Zhang, X.; Wang, Y.; Chen, N.; Poblet, J. M.; Rodríguez-Fortea, A. *J. Phys. Chem. C* **2016**, 120, 26159.

[6] A Zigzag Sc_2C_2 Carbide Cluster inside a [88]Fullerene Cage with One Heptagon $Sc_2C_2@C_s$(hept)-C_{88}: A Kinetically-Trapped Fullerene Formed by C_2 Insertion?
Chen, C.H.; Abella, L.; Cerón, M. R.; Guerrero-Ayala, M.; Rodríguez-Fortea, A.; Olmstead, M. M.; Powers, X. B.; Balch, A.; Poblet, J. M.; Echegoyen, L. *J. Am. Chem. Soc.* **2016**, 138, 13030.

[7] Capturing the Fused-Pentagon C_{74} by Stepwise Chlorination
Gao, C. L.; Abella, L.; Tan, Y. Z.; Wu, X. Z.; Rodríguez-Fortea, A.; Poblet, J. M.; Xie, S. Y.; Huang, R. B.; Zheng, L. S. *Inorg. Chem.* **2016**, 55, 6861.

[8] $Sc_2O@C_{3v}(8)$–C_{82}: A Missing Isomer of $Sc_2O@C_{82}$
Tang, Q.; Abella, L.; Hao, Y.; Li, X.; Wan, Y.; Rodríguez-Fortea, A.; Poblet, J. M.; Feng, L.; Chen, N. *Inorg. Chem.* **2016**, 55, 1926.

[9] $Sc_2O@C_{2v}(5)$-C_{80}: Dimetallic Oxide Cluster Inside a C_{80} Fullerene Cage
Tang, Q.; Abella, L.; Hao, Y.; Li, X.; Wan, Y.; Rodríguez-Fortea, A.; Poblet, J. M.; Feng, L.; Chen, N. *Inorg. Chem.* **2015**, 54, 9845.

[10] Different Factors Govern Chlorination and Encapsulation in Fullerenes: The Case of C_{66}
Alegret, N.; Abella, L.; Azmani, K.; Rodríguez-Fortea, A.; Poblet, J. M. *Inorg. Chem.* **2015**, 54, 7562.

[11] $Sc_2O@T_d(19151)$-C_{76}: Hindered Cluster Motion Inside a Tetrahedral Carbon Cage Probed by Crystallographic and Computational Studies
Yang, T.; Hao, Y.; Abella, L.; Tang, Q.; Li, X.; Wan, Y.; Rodríguez-Fortea, A.; Poblet, J. M.; Feng, L.; Chen, N. *Chem. Eur. J.* **2015**, 21, 1.

[12] Small Endoheral Metallofullerenes: Exploration of the Structure and Growth Mechanisms in the Ti@C_{2n} (2n=26-50) Family
Mulet-Gas, M.; Abella, L.; Dunk, P. W.; Rodríguez-Fortea, A.; Kroto, H.; Poblet, J.M. *Chem. Sci.* **2015**, 6, 675.

Non-Related to this Thesis:

[13] Formation of Curvature Subunit of Carbon in Combustion
Wu, X. Z.; Yao, Y. R.; Chen, M. M.; Tian, H. R.; Xiao, J.; Xu, Y. Y.; Lin, M. S.; Abella, L.; Tian, C. B.; Gao, C. L.; Zhang, Q.; Xie, S. Y.; Huang, R. B.; Zheng, L. S. *J. Am. Chem. Soc.* **2016**, 138, 9629.

[14] $La_3N@C_{92}$: An Endohedral Metallofullerene Governed by Kinetic Factors?
Abella, L.; Mulet-Gas, M.; Rodríguez-Fortea, A.; Poblet, J. M. *Inorg. Chem.* **2016**, 55, 3302.

[15] Cubane oxides inside middle-size fullerenes: the next endohedrals to be detected?
Alegret, N.; Abella, L.; Rodríguez-Fortea, A.; Poblet, J. M. *Theor. Chem. Acc.* **2015**, 134, 5.

Posters and Oral Presentations

On the Formation of Chlorofullerenes
2nd International Symposium on NanoCarbons (ISNC2017)
Wuhan (China) | June 2017
Poster presentation

A Theoretical Exploration of the Growth Mechanism in the Ti@C_{2n} (2N=26-48) Family
10th European Conference on Computational Chemistry
Fulda (Germany) | September 2015
Poster presentation

Small Endohedral Metallofullerenes: Growth Mechanism in the Ti@C_{2n} (2N=26-48) Family
XXXI Annual Meeting of the Reference Network of R+D+i on Theoretical and Computational Chemistry
Girona (Spain) | June 2015
Oral presentation

A Theoretical Exploration of the Growth Mechanism in the Ti@C_{2n} (2N=26-48) Family
XI Girona Seminar on Carbon, Metal, and Carbon-Metal Clusters: From Theory to Applications
Girona (Spain) | July 2014
Poster presentation

UNIVERSITAT ROVIRA I VIRGILI
COMPUTATIONS ON FULLERENES: CHARACTERIZATION, REACTIVITY AND GROWTH
Laura Abella Guzman

Collaborations

Florida State University
Prof. Sir Harold W. Kroto
and Prof. Paul Dunk

University of Texas at El Paso
Prof. Luis Echegoyen

Xiamen University
Prof. Su-Yuan Xie

Soochow University
Prof. Ning Chen

Research Abroad

XIAMEN UNIVERSITY

Project	*Experimental and Theoretical Study of Chlorofullerenes*
Supervisor	Prof. Su-Yuan Xie
Center	Xiamen University
Period	September 2015 - January 2016

UNIVERSITAT ROVIRA I VIRGILI
COMPUTATIONS ON FULLERENES: CHARACTERIZATION, REACTIVITY AND GROWTH
Laura Abella Guzman

Notes & Comments

UNIVERSITAT ROVIRA I VIRGILI
COMPUTATIONS ON FULLERENES: CHARACTERIZATION, REACTIVITY AND GROWTH
Laura Abella Guzman

UNIVERSITAT ROVIRA I VIRGILI
COMPUTATIONS ON FULLERENES: CHARACTERIZATION, REACTIVITY AND GROWTH
Laura Abella Guzman

UNIVERSITAT
ROVIRA i VIRGILI